

# **Modeling of polythermal preferential crystallization**

**Dissertation**

zur Erlangung des akademischen Grades

**Doktoringenieur  
(Dr. Ing.)**

von Dipl.-Ing. Felix Czapla

geb. am 18.03.1979 in Rinteln

genehmigt durch die Fakultät für Verfahrens- und Systemtechnik  
der Otto-von-Guericke Universität Magdeburg

Gutachter: Professor Dr. Ing. habil. Andreas Seidel-Morgenstern  
Professor Dr. Ing. habil. Joachim Ulrich

eingereicht am: 01.12.2009

Promotionskolloquium am 19.03.2010



## **Schriftliche Erklärung**

Ich erkläre hiermit, dass ich die vorliegende Arbeit ohne unzulässige Hilfe Dritter und ohne Benutzung anderer als der angegebenen Hilfsmittel angefertigt habe. Die aus fremden Quellen direkt oder indirekt übernommenen Gedanken sind als solche kenntlich gemacht.

Insbesondere habe ich nicht die Hilfe einer kommerziellen Promotionsberatung in Anspruch genommen. Dritte haben von mir weder unmittelbar noch mittelbar geldwerte Leistungen für Arbeiten erhalten, die im Zusammenhang mit dem Inhalt der vorgelegten Dissertation stehen.

Die Arbeit wurde bisher weder im Inland noch im Ausland in gleicher oder ähnlicher Form als Dissertation eingereicht und ist als Ganzes auch noch nicht veröffentlicht.

Braunschweig, \_\_\_\_\_

\_\_\_\_\_  
(Unterschrift)

# Publications

## Journals

Czapla, F., Polenske, D., Klukas, L., Lorenz, H., Seidel-Morgenstern, A. (2010). Cyclic auto seeded polythermal preferential crystallisation – Effect of impurity accumulation. *Chem. Eng. & Proc: Proc. Intensification*, 49(1), 22-28.

Czapla, F., Lorenz, H. & Seidel-Morgenstern, A. (2009). Modellierung und Vergleich von polythermen autoseeded Prozessvarianten der Bevorzugten Kristallisation. *Chemie Ingenieur Technik*, 6, 839-848.

Czapla, F., Haida, H., Elsner, M. P., Lorenz, H. & Seidel-Morgenstern, A. (2008). Parameterization of population balance models for polythermal auto seeded preferential crystallization of enantiomers. *Chemical Engineering Science*, 64(4), 753-763.

Czapla, F., Lorenz, H., Elsner, M. P. & Seidel-Morgenstern, A. (2007). Einfluss der Prozessführungsstrategie auf Produktivität und Produkteigenschaften einer “Bevorzugten Kristallisation”. *Chemie Ingenieur Technik*, 79(3), 281-286.

Lorenz, H., Elsner, M. P., Polenske, D., Czapla, F., Seidel-Morgenstern, A. (2007). Gut kombiniert – Online-Monitoring kristallisationsbasierter chiraler Trennungen. *Process*, 07/08, 40-41.

Lorenz, H., Czapla, F., Elsner, M. P., Polenske, D., Seidel-Morgenstern, A. (2007). Crystallisation based separation of enantiomers. *Journal of the University of Chemical Technology and Metallurgy*, 42, 1, 5-16.

## Conference proceedings

Czapla, F., Lorenz, H. & Seidel-Morgenstern, A. (2008): Efficient design of preferential crystallization processes. In “17<sup>th</sup> International Symposium on Industrial Crystallization” - ISIC 17<sup>th</sup>, Maastricht, 803-810.

Haida, H., Czapla, F., Lorenz, H. & Seidel-Morgenstern, A. (2008) In “15<sup>th</sup> Bremer International Workshop on Industrial Crystallization” - *BIWIC 15<sup>th</sup>*, (Eds, H. Lorenz & H. Kaemmerer) Shaker, Magdeburg, 288-295.

Czapla, F., Lorenz, H. & Seidel-Morgenstern, A. (2008). Einstellen der Partikelgrößenverteilung bei der Bevorzugten Kristallisation unter Berücksichtigung von Produktivitäts- und Reinheitsanforderungen. In U. Teipel (Ed.), *Produktgestaltung in der Partikeltechnologie Bd. 4*. Pfinztal: Fraunhofer IRB Verlag, 235-249.

Czapla, F., Elsner, M.P., Lorenz, H., Joshi, M., Seidel-Morgenstern, A. (2007) Parameterization of population balance models for polythermal auto seeded “preferential crystallization” of enantiomers. In *PBM 2007: 3<sup>rd</sup> international conference on population balance modeling*, Quebec City, Canada.

Czapla, F., Lorenz, H., Elsner, M. P. & Seidel-Morgenstern, A. (2006) In “13<sup>th</sup> Bremer International Workshop on Industrial Crystallization” - *BIWIC 13<sup>th</sup>* (Eds, P. J. Jansens, J. H. ter Horst & S. Jiang) IOS Press BV, Delft, 98-104.

Czapla, F., Lorenz, H., Elsner, M. P. & Seidel-Morgenstern, A. (2006). Einfluss unterschiedlicher Prozessführungsstrategien auf die Produktivität und Produkteigenschaften bei der "Bevorzugten Kristallisation" In U. Teipel (Ed.), *Produktgestaltung in der Partikeltechnologie Bd. 3*. Pfinztal: Fraunhofer IRB Verlag, 219-235.

## Kurzzusammenfassung

Die Bevorzugte Kristallisation ist ein kostengünstiges Verfahren zur Trennung von Enantiomergemischen. Insbesondere in der Pharmazie wächst die Bedeutung der Trennung dieser speziellen Klasse von Isomeren. Trotz des relativ geringen apparativen Aufwandes wird das Verfahren in der industriellen Praxis selten angewendet.

Eine Ursache könnte in der vermeintlichen Störungsanfälligkeit des kinetisch kontrollierten Trennprozesses liegen. Die vorliegende Arbeit leistet einen Beitrag zum Verständnis des Prozesses und bietet einen Leitfaden zur modellgestützten Prozessauslegung. Damit soll dazu beigetragen werden, dass die Bevorzugte Kristallisation stärker als bisher als alternatives Trennverfahren den Weg in die industrielle Praxis findet. Daneben können die verwendeten und entwickelten Methoden teilweise auch auf andere Prozesse übertragen werden.

Zunächst wird ein Konzept für die a priori Prozessevaluierung vorgestellt, das auf Löslichkeitsdaten und metastabilen Breiten der betrachteten Stoffsysteme beruht. Die Anwendung dieses einfachen Konzeptes ermöglicht es, für zwei untersuchte Beispielstoffsysteme Prozessbedingungen zu identifizieren, bei denen ein Trennprozess Erfolg versprechend ist und eine maximale Ausbeute und/oder Produktivität erzielt werden kann. Die Prozessevaluierung wird dabei am Beispiel der Stoffsysteme DL-Threonin/Wasser (Konglomerat) und R,S-Mandelsäure/Wasser (verbindungs bildend) vorgenommen.

Weiterhin wird am Beispiel des Stoffsystems DL-Threonin/Wasser, basierend auf dem Konzept der Populationsbilanzen, eine ausführlichere dynamische Modellierung vorgenommen. Unter Verwendung der gemessenen Daten von Trennprozessverläufen werden freie kinetische Parameter für die verwendeten Modelle abgeschätzt. Die Bewertung der Abschätzungsgüte erfolgt mit gängigen statistischen Methoden unter Verwendung der Fisher-Informationsmatrix sowie eines Bootstrap-Verfahrens. Zusätzliche Versuche werden mit Hilfe der entwickelten Modelle so geplant, dass sie ein Maximum an Information für die Identifizierung der kinetischen Parameter bieten (dynamisches experimentelles Design).

Neben der Prozessmodellierung wird eine Online- und Inlineanalytik etabliert, die nach entsprechender Kalibrierung in der Lage ist, die untersuchten Prozesse sowohl

hinsichtlich der Flüssigphasenzusammensetzung, als auch bezüglich der festen Phase zu verfolgen.

Je nachdem, ob aus den Messungen Informationen bezüglich der Partikelgrößenverteilung vorhanden sind, können ein voll diskretisiertes oder ein auf die Momente der Verteilung reduziertes Modell gelöst werden. Das reduzierte Modell bietet den Vorteil geringerer Rechenzeit.

Das entwickelte kinetische Modell wird einerseits in Matlab<sup>®</sup> implementiert, andererseits mit Hilfe eines kommerziellen Simulationstools, Parsival<sup>®</sup>, gelöst. Der Vergleich der verschiedenen Simulationsansätze ermöglicht es für eine spezifische Anwendung die geeignete Simulationsstrategie auszuwählen.

Abschließend wird ein in Parsival<sup>®</sup> implementiertes, parametrisiertes und validiertes Modell verwendet, um eine Prozessoptimierung hinsichtlich der Produktivität vorzunehmen.

## **Abstract**

Preferential crystallization is a rather cheap alternative to separate mixtures of enantiomers into the pure chiral species. Especially in the pharmaceutical industry the separation of enantiomers is of growing importance. Despite its rather low costs compared with other separation methods (e.g. chromatography, membrane processes) the application of the method in the industrial practice is scarce.

One reason for this could be the assumed liability to disturbances of the process due to its kinetically controlled nature. In this context the thesis provides a contribution to the understanding of the process as well as a guideline to process design.

One goal of the work is to increase the usage of the preferential crystallization process as an alternative to other separation methods. Apart from that the methods introduced can also be applied to other (crystallization) processes.

At first a concept for an a priori process evaluation based on solubilities and metastable zone width is introduced. The process concept is then tested and evaluated for two different systems. Using the example of the conglomerate forming system DL-threonine/water a more complex dynamic modeling approach based on population balances is introduced. Based on measured separation runs the free kinetic parameters of the used models are estimated. The reliability of the parameter estimates is evaluated using the Fisher information matrix or a Bootstrap method respectively.

Additional experiments are designed based on the developed models using a dynamic experimental design. Using this approach the number of experimental runs can be minimized. As a prerequisite for process modeling and optimization an online and inline analytic is established and calibrated which is used to investigate the liquid phase composition as well as properties of the particle size distribution.

Depending on the available information and the process design goal a reduced moment model or a fully discretized model is used. The reduced model offers the advantage of increased computational speed, whereas the fully discretized model does not only provide information with respect to the moments of the particle size distribution but provides the full particle size distribution at every time point. The developed kinetic model is implemented into Matlab<sup>®</sup> as well as into Parsival<sup>®</sup>. The different model solution strategies are compared and therefore different options for model simulation are provided.

Finally the parameterized and validated model implemented into Parsival<sup>®</sup> is used to optimize the process in terms of productivity. Additionally the model can be used to predict the mean diameter of the product crystals and the variance of the particle size distribution for different experimental conditions.

## Acknowledgements

This thesis originated while I was working at the Max-Planck institute for dynamics of complex technical systems in Magdeburg.

Several people have contributed to the success of this work. At first I would like to thank Professor A. Seidel-Morgenstern for offering me a research position at the Max-Planck institute and for his constant support in many ways throughout the years. I appreciated his trust in my capabilities, his calmness, his guidance and courtesy accompanied with a good sense of humor a lot.

Further on I would like to thank Dr. Heike Lorenz for many fruitful discussions and her inspiring ideas and support especially in the beginning of the work, where she was introducing me into the world of crystallization.

I also would like to thank Professor J. Ulrich for acting as a second referee for this thesis.

Most of the work done would have been impossible without the support of our lab technicians Jaqueline Kauffmann and Luise Borchert who helped a lot during the experimental part of this work. A great part of the experiments used in the final version of the thesis have been carried out by students. I would like to thank Martina Naumann, Polina Peeva, Luis Guilherme Medeiros de Souza, Pinatcha Supapich, Nicole Michaluk, Linzhu Klukas, Kathleen Müller and Anita Hildebrandt for providing valuable results and ideas for this work and wish them all the best for their future.

Without support from my doctoral colleagues I would have given up along the way for sure. Special thanks among many others to Henning Haida, Henning Kaemmerer and Daniel Polenske for the interesting projects we undertook and the conferences we visited together.

I also would like to thank Dr. Heiko Briesen, Dr. Milind Joshi, Dr. Martin Peter Elsner, Alper Öncül and Ivan Angelov for their consultancy during parts of my thesis work.

Many thanks also to Dr. Matthias Rauls who offered me the possibility to contribute to a project from industry and who showed me the mediterranean side of Ludwigshafen.

In the Max-Planck Institute I would like to thank the people from the IT department and the mechanical workshop for their constant support throughout the years.

Additionally I would like to thank all the people from our lunch group for the inspiring and stimulating discussions.

At the end I would like to thank my parents and my brother for their constant support in many ways during the time not only of the PhD-work but during my whole education.

As this list will never be completed I would like to thank all other people not mentioned explicitly here who contributed to this work and made the time in Magdeburg a pleasant and thrilling experience.

## Contents

Modeling of polythermal preferential crystallization .....	1
1 Introduction.....	13
1.1 Motivation.....	13
1.2 Goal and structure of the thesis.....	15
2 Theoretical aspects.....	18
2.1 Basics of crystallization .....	18
2.1.1 <i>Crystal nucleation and the metastable zone</i> .....	19
2.1.2 <i>Crystal growth</i> .....	21
2.1.3 <i>Binary and ternary phase diagrams and system types</i> .....	23
2.1.4 <i>Modeling of phase equilibria</i> .....	26
2.1.5 <i>Population balance modeling</i> .....	27
2.1.6 <i>Model reduction using the method of moments</i> .....	30
2.2 Crystallization of enantiomers and preferential crystallization .....	31
2.2.1 <i>Process concept „nucleation seeding“</i> .....	34
2.2.2 <i>Process concept „milled seeds“</i> .....	40
2.2.3 <i>Process concept „defined seeding“</i> .....	42
2.2.4 <i>Crystallization kinetics for enantiomeric systems</i> .....	42
2.3 Parameter estimation.....	44
2.3.1 <i>Sensitivity analysis</i> .....	45
2.3.2 <i>Fisher Information Matrix</i> .....	46
2.3.3 <i>Bootstrap method</i> .....	48
2.3.4 <i>Experimental design</i> .....	50
2.3.5 <i>Reparameterization of crystallization kinetics</i> .....	51
3 Experimental .....	53
3.1 Model system DL-threonine/water .....	53
3.2 Model system R,S-mandelic acid/water .....	55
3.3 Experimental setup.....	57
3.4 Online monitoring and analytical methods.....	58
3.4.1 <i>Fluid phase monitoring</i> .....	58
3.4.2 <i>Solid phase monitoring</i> .....	59
3.5 Experimental reproducibility .....	63
3.6 Preparation of seed crystals .....	66
3.7 Summary of data sets used in further analysis.....	68
4 Results and discussion .....	69
4.1 Calibration of polarimeter and densitometer .....	69
4.2 FBRM-probe calibration.....	71
4.3 Solubility and metastable zone width .....	74
4.3.1 <i>DL-threonine/water</i> .....	74
4.3.2 <i>R,S-mandelic acid/water</i> .....	77
4.4 Short-cut process evaluation .....	81
4.4.1 <i>Equilibrium analysis DL-threonine</i> .....	82
4.4.2 <i>Evaluation using MSZW-data (DL-threonine)</i> .....	86
4.4.3 <i>Equilibrium analysis R,S-mandelic acid</i> .....	90
4.4.4 <i>Evaluation using MSZW-data (R,S-mandelic acid)</i> .....	94
4.5 Model solution strategies .....	97

4.6	Parameterization of the model .....	103
4.6.1	<i>Parameter estimation using second moments and optical rotation...</i>	105
4.6.2	<i>Parameter estimation using FBRM data and optical rotation .....</i>	112
4.6.3	<i>Parameter estimation using mass fractions and PSDs .....</i>	123
4.6.4	<i>Possible improvements of parameter estimation – experimental design</i> .....	127
4.6.5	<i>Comparison of parameter estimation approaches.....</i>	132
4.6.6	<i>Comparison of confidence intervals obtained with different methods</i> .....	134
4.7	Parametric studies – Trends for product design.....	139
4.8	Illustration of process optimization .....	143
5	Conclusions and outlook.....	149
6	Nomenclature.....	152
7	Literature.....	155
	Appendix A - Data and settings .....	162
	Appendix B - Parameter estimates.....	169
	Lebenslauf.....	181

# 1 Introduction

## 1.1 Motivation

Enantiomers are molecules that are mirror images of one another. They have very similar physicochemical properties (Jaques et al., 1994). However, within most organisms the two enantiomers of a species have different effects. This is due to the many chiral centers that most of the proteins and enzymes in organisms have. In some cases the differences can be extreme. One molecule can be a potent pharmaceutical drug while the stereoisomer is poisonous (Knabe, 1989). Additionally, even if the stereoisomer has no harmful effect, it is advantageous to separate the Enantiomers in order to minimize the amount of pharmaceutical substance to use for a single dosage (Ariens, 1984). Because of these facts the separation of enantiomers into the pure chiral species has gained attractiveness and importance during the last decades (Collins et al., 1997; Collins et al., 2000). The market volume for chiral drugs (single enantiomers) rose from 26% in 1983 to 55% in 2004 (Caner et al., 2004). The volume of the market for single enantiomer chiral drugs was approximately 100 billion US\$ in 2000 (Maier et al., 2001) and was assumed to reach a volume of 200 billion US\$ in 2008. These numbers show that the separation of enantiomers has gained increasing importance in the last decade.

Preferential crystallization is a process concept to separate enantiomers into the pure chiral species in a cyclic operation mode (Jaques et al., 1994) crystallizing the two species in sequel batches respectively. The mother liquor is recycled while before each batch fresh racemate is added to obtain the initial concentration. The basic process concept has already been known for a long time (Amiard, 1956) as a rather cheap alternative to other separation techniques. However it still lacks wider industrial application (Jaques et al., 1994; Sakai & Coquerel, 2007). One reason for this might be the complexity of the kinetically controlled process. Without a profound knowledge of the process kinetics and the thermodynamic data it is very difficult to evaluate, design or even optimize the process (Angelov et al., 2006; Elsner et al., 2005; Lorenz et al., 2006a; Wang & Ching, 2006). Due to the cyclic operation mode and the usually rather high product prices for pure chiral substances the optimal design of the individual batch has a large influence on the overall process

performance. A basis for these classical engineering tasks is a model framework that is capable of describing the dynamics of the process in a quantitative manner.

The motivation for the thesis in the context described is twofold. On the one hand it shall give a guideline on how to design and optimize certain aspects such as productivity or the particle size of the product of a preferential crystallization process based on simple models. Simple should mean as complex as necessary to fulfill the tasks mentioned. Another degree of freedom for process implementation and design are different process variants of the basic concept of preferential crystallization that have come up during the last years (Sakai & Coquerel, 2007). When looking at process optimization polythermal process variants such as the so called “auto seeded polythermal programmed preferential crystallization” (Coquerel et al., 2000) or variants thereof (Czapla et al., 2008b) give additional degrees of freedom due to different seeding concepts and the possibility of temperature profile variations.

In another way the preferential crystallization process concept with its inherent complexity acts as a test system for the interplay of modeling and experiment/process. Especially the problem of limited access to data is often one of the bottlenecks in validating process models in the industrial practice (Brun, 2002; Dochain & Vanrolleghem, 2001). Kinetic parameter estimation based on data gathered during production runs is an important part in obtaining a model that is capable of predicting the process behavior in the region of interest. The procedure followed is related to model based experimental analysis (Marquardt, 2005). This field has gained increasing importance during the last decade. The mathematical methods used are interdisciplinary tools applied in many fields of research. In the context of crystallization processes these techniques are only scarcely used up to now, with some notable exceptions (for example (Diez et al., 2006; Heinrich, 2008) or (Togkalidou et al., 2004), (Togkalidou et al., 2001)).

Once a reliable model has been identified and validated it can be used to evaluate and optimize the process with respect to product purity, yield, productivity (Angelov et al., 2006; Angelov et al., 2007) or particle size (Braun et al., 2004; Chow et al., 2008).

## 1.2 Goal and structure of the thesis

The goal of the thesis is to use experimental data for model building and subsequent process optimization of a complex kinetically controlled process for the separation of enantiomers (preferential crystallization). The presented approaches differ in terms of complexity and the type of data used to parameterize the individual models. The simplest approach is an equilibrium model that is based on mass balances and solubility data. This approach can be enhanced if data regarding the metastable zone width of the investigated system is available. The more complex approach uses data from actual production runs and a dynamic population balance model. The runs are monitored with state of the art analytical devices. The devices have to be calibrated in order to extract useful information regarding the fluid phase mass fractions and the moments of the particle size distribution or the complete distribution, respectively. The process trajectories followed experimentally during the runs can be analyzed and used as a basis for model building, model validation and subsequent process evaluation and optimization.

Three different process concepts of polythermal preferential crystallization (Sakai & Coquerel, 2007) are introduced and investigated. The model systems DL-threonine and R,S-mandelic acid with water as a solvent were chosen for experimental investigations. As a conglomerate forming system (Jaques et al., 1994) DL-threonine is suitable for the classical preferential crystallization. Preliminary research showed that it can be crystallized out of water (Elsner et al., 2005; Lorenz et al., 2006a) without formation of polymorphs or solvates. In contrast, R,S-mandelic acid is a representative of the large group of compound forming systems (Jaques et al., 1994) that is capable to crystallize out of water as well.

Throughout the thesis different aspects related to process evaluation and optimization are covered. Following the introduction the second chapter deals with the basic theory of crystallization, (chapters 2.1.1, 2.1.2, 2.1.3), different process concepts of preferential crystallization (chapter 2.2) as well as basic mathematical process models (chapter 2.1.5) and the theory used in the field of kinetic parameter estimation (chapter 2.3). Another focus within chapter 2 is set on the representation and modeling of binary and ternary systems in phase diagrams (chapter 2.1.3).

Chapter 3 deals with the experimental setup and the measurement devices used. The measurement principles of each device along with possible measurement artifacts/errors of the individual apparatus are discussed. In chapter 3.5 the experimental reproducibility is addressed. The preparation of seed crystals, that are needed for one of the process concepts (“defined seeding”) is explained in chapter 3.6. A summary of the experimental data used as a basic set to test and develop process models concludes chapter 3.

In chapter 4 the main results of the thesis are presented and discussed. The chapter starts with the calibration of the analytical devices to monitor the fluid phase composition (chapter 4.1). As a second analytical tool a FBRM-probe is evaluated to monitor the course of the moments of the particle population in the crystallizer (chapter 4.2).

Then correlation functions for the solubility and metastable zone width of the two investigated systems in the regions of interest are provided (chapter 4.3).

Based on the solubility and metastable zone width data an estimation method to evaluate the yield and productivity of the two model systems is introduced. It can be used to quickly identify process regions of potentially high yield and productivity (chapter 4.4).

To enhance the accuracy of the prediction of the process outcome, different dynamic modeling strategies are introduced and compared in chapter 4.5. The goal is here to estimate the free parameters governing different kinetic phenomena as nucleation, crystal growth and dissolution simultaneously using the available data. In that way kinetics are sort of lumped together. However in practice it is very tedious to measure kinetics such as primary and secondary nucleation separately.

In chapter 4.6 the estimation of the free parameters using the dynamic model is performed. One subchapter deals with parameter estimation using a reduced moment model (chapter 4.6.1). During the parameter identification procedure additional experiments were undertaken using a dynamic experimental design (chapter 4.6.4) in order to maximize the information content of the individual experiments with respect to the parameter estimation task.

A second parameter estimation approach uses the full population balance and a model of the FBRM-probe to transform the calculated particle size distribution into a chord length distribution that can be compared with the measured chord-length distribution in order to estimate free kinetic model parameters (chapter 4.6.2). This approach was

found to enhance the quality of the data regarding the moments of the particle size distribution in comparison with the empirical probe calibration procedure presented in chapter 4.2.

The third parameter estimation approach for modeling of the preferential crystallization process is to use the commercial program Parsival<sup>®</sup> to determine a subset of free model parameters and optimize the three different process concepts in terms of productivity. After these calculations additional experiments were performed realising the proposed regime in order to compare the results with the model predictions (chapter 4.6.3).

When the fully discretized population balance is solved the model can be used to modify certain aspects of the particle size distribution of the product such as mean diameter or variance (chapter 4.7).

Finally the parameterized model is used to optimize the different process concepts in terms of productivity (chapter 4.8).

## 2 Theoretical aspects

### 2.1 Basics of crystallization

Crystallization is the conversion of one or several substances from an amorphous solid, liquid, or gaseous state to the crystalline state (Mersmann, 1995). The crystalline state describes a structured solid in which the molecules of one or several substances are arranged in a certain, defined manner which is called the crystal lattice. In the processes investigated in this thesis crystallization takes place from solution. The formation of a solid out of a solution is a thermodynamic process. The driving force for the solid formation is the difference in the chemical potential of the liquid and solid states at a certain temperature. In engineering practice it is more convenient to use the difference or the ratio between the saturation concentration and the actual concentration as the driving force for the crystallization. The saturation concentration is the concentration at thermodynamic equilibrium, which is usually called solubility. It is a quantity that describes the maximal amount of a substance that can be solved in another substance (the solvent) at a certain temperature and pressure. The influence of the system pressure is usually negligible and will not be considered for the systems studied in this thesis. Throughout the thesis the fluid compositions are expressed in the form of mass fractions. The thermodynamic driving force for the crystallization, which is called supersaturation, can be expressed using relative supersaturations:

$$s = \frac{w}{w_{sat}} \quad \text{Equation 1}$$

Or:

$$\sigma = 1 - \frac{w}{w_{sat}} \quad \text{Equation 2}$$

In the process of crystallization from solution there are two main distinguishable mechanisms: crystal growth and nucleation. Nucleation is the formation of the first stable solid particles from molecular aggregates that later grow from the supersaturated solution to larger crystals. Within these two main mechanisms there

exist several theories that describe more specific aspects. Some of these aspects will be explained in the following. An overview is given e.g. in the books of (Mersmann, 1995) and (Mullin, 2001) to mention just two examples out of the growing field of crystallization literature.

### 2.1.1 *Crystal nucleation and the metastable zone*

Crystal nucleation is the formation of new crystalline material. Primary nucleation is the formation of a new crystal directly out of solution. Within the mechanism of primary nucleation one distinguishes between homogeneous and heterogeneous primary nucleation. Primary homogeneous nucleation refers to a nucleation out of the clear solution while primary heterogeneous nucleation occurs at foreign surfaces. Different mechanisms that can provide new crystalline material at generally lower supersaturations compared to primary nucleation is the so called secondary nucleation. Here other already present crystals act as the source for the new crystalline particles. The mechanisms leading to secondary nucleation are manifold. Figure 1 gives an overview of the different mechanisms leading to nucleation.

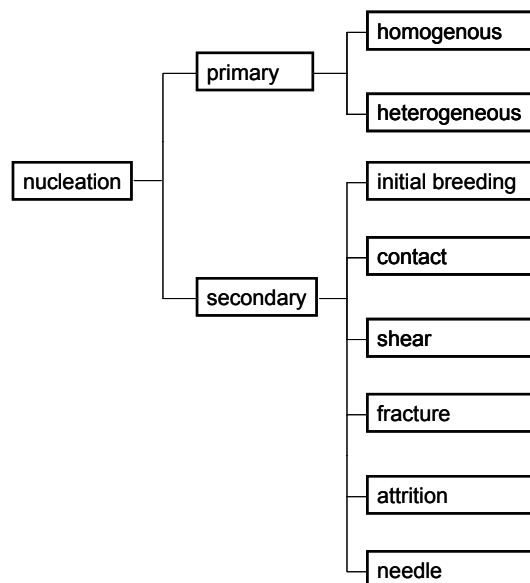


**Figure 1:** Overview of different nucleation mechanisms adapted from (Mersmann, 1995).

Depending on the system being studied at certain process conditions some or all of the mechanisms can take place at the same time. That makes the understanding and modeling of nucleation a difficult and controversy task (Kashiev, 2000). Most crystallization processes take place in stirred vessels. Therefore usually no primary homogeneous nucleation will occur but instead primary heterogeneous nucleation.

This is due to intensive contact of the liquid to the surfaces of the vessel and stirrer as well as the turbulence induced by the stirring. Additionally all of the above mentioned mechanisms for secondary nucleation can take place. *Initial breeding* refers to the generation of secondary nuclei due to dust adhering at the surface of seed particles. The dust particles stick to the dry crystals and acts as nuclei when the seeds are introduced into the vessel and the dust particles get washed off. *Contact nucleation* is mentioned as the most important source of secondary nucleation in stirred vessels (Randolph & Larson, 1988). It occurs, when crystals get in contact with the vessel equipment or other crystals and parts of the adhering adsorption layer at the crystal surface get washed off and grow in solution. *Shear* refers to removal of the adsorption layer by fluid shear due to the relative velocity of crystal and liquid. *Fracture* refers to the fragmentation of individual crystals into two or more pieces due to mechanical stress. *Attrition* is also related to fracture with the difference that the attrited particles are small compared to the almost intact “mother” particles. The reason for attrition is also mechanical stress such as crystal-stirrer collisions.

*Needle breeding* refers to dendritic crystal growth. It occurs in some systems at higher supersaturation and fast crystal growth velocities. Starting from an initial crystal, needles will grow into all directions and eventually break off if they reach a certain length.

Modeling all these partly related effects is a very challenging task. Usually lumped models are used that incorporate more than one of the mentioned mechanisms for secondary nucleation (see chapter 2.2.4 for more details regarding the kinetic equations used in the models of this work).

An important kinetic quantity in the field of nucleation is the so called metastable zone. The width of the metastable zone describes a region within a system of solute and solvent where the system is supersaturated but no crystals will form for a certain period of time. Depending on the system under investigation and the supersaturation level this nucleation delay can range from seconds to years (Mullin, 2001). The difference in concentration between the solubility and the metastable zone width depends on many factors such as cooling rate, stirring rate, vessel size and type, etc.. Therefore *the* metastable zone width is not a fixed thermodynamic quantity but varies depending on the conditions.

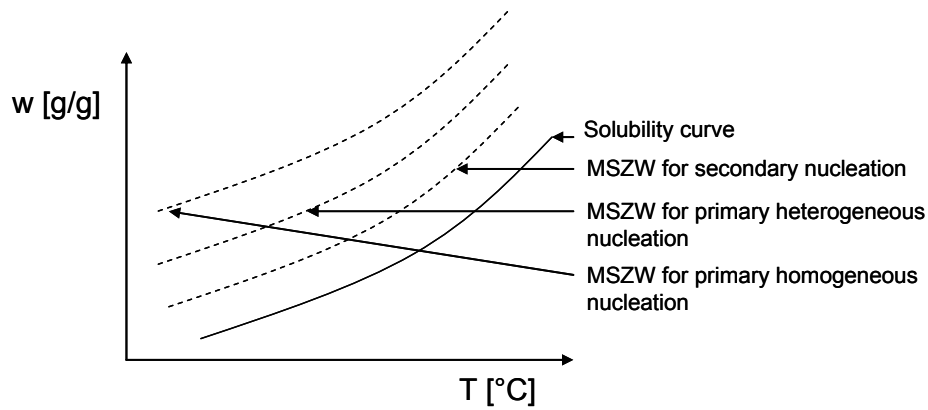


**Figure 2:** Schematic illustration of the different metastable zone widths (MSZW) for different types of nucleation.

The width of the metastable zone usually also varies depending on the different mechanisms illustrated earlier in Figure 1. Typical courses of solubility and metastable zone width curves are drawn in Figure 2 (adapted from (Mersmann, 1995)). The situation depicted is valid for most systems: Usually the metastable zone for the formation of secondary nuclei is smaller than the metastable zone for primary heterogeneous nucleation which again is smaller than the metastable zone for primary homogeneous nucleation. The metastable zone width is a quantity which is difficult to measure but is very important for the design and understanding of preferential crystallization processes (see chapter 2.2).

### 2.1.2 Crystal growth

Crystal growth from solution is a very complex and not fully understood process. It can be roughly divided into two parts: Mass transfer through a boundary layer on the surface of crystals followed by an integration of clusters or individual molecules into the crystal lattice. Depending on the process conditions growth can be mass transfer limited or integration limited or both (Mersmann, 1995). This and the multitude of crystal shapes and lattice structures lead to very different growth behaviors and theories. For the one dimensional case a general definition of a growth rate  $G$  can be formulated as:

$$G = \frac{dL}{dt} \tag{Equation 3}$$

That is a change of a crystal length  $L$  over time. To define what exactly the crystal length is, can be challenging if the crystals have a rather unstructured appearance with many faces, dendrites etc.. Usually the growth rate  $G$  is a function of the

supersaturations. If the growth is mass transfer limited the equation for the growth rate takes the form (Mullin, 2001):

$$G = k_g \cdot \sigma \quad \text{Equation 4}$$

If the crystal growth is integration and mass transfer limited an exponent  $g$  can be introduced along with a modified  $k_g$  leading to a non linear proportionality of the growth rate to the supersaturation.

$$G = k_g \cdot \sigma^g \quad \text{Equation 5}$$

This simple model modification allows accounting for a reaction step at the crystal surface which may not be directly proportional to the supersaturation. Usually the values of the exponent  $g$  lie in the range of 1 to 2 (Randolph & Larson, 1988).

If the growth is totally limited by the integration of molecules into the crystal lattice more complex theories are available. Two of the most important ones are the Burton-Cabrera-Frank theory (BCF-theory) and the Birth and Spread theory (B+S-theory) (see (Burton et al., 1951) and (O'Hara & Reid, 1973)), which will be explained briefly in the following. The BCF-theory assumes that crystal growth takes place at so called screw dislocations, kinks or steps at the surface of the crystal. At such spots the energy for integration into the crystal lattice is lowest and therefore the formation of a new layer should start here. The mathematical description of the corresponding model is given by Equation 6:

$$G_{BCF} = A \cdot \frac{\sigma^2}{B} \cdot \tanh\left(\frac{B}{\sigma}\right) \quad \text{Equation 6}$$

The B+S theory assumes that two dimensional nuclei are formed at a crystal surface and then spread over the surface starting from different points. The corresponding model is sometimes also referred to as polynuclear growth model. It is mathematically described by Equation 7:

$$G_{B+S} = C \cdot \sigma^{5/6} \exp\left(\frac{-D}{\sigma}\right) \quad \text{Equation 7}$$

More details about these and other models for crystal growth can be found among others in the books by (Mersmann, 1995), (Mullin, 2001) and (Myerson, 2002) (to name just a few examples in Literature).

### 2.1.3 Binary and ternary phase diagrams and system types

The crystallization processes are investigated in ternary systems consisting of two enantiomers and a suitable solvent. The equilibria in such systems are usually characterized and illustrated with the help of ternary phase diagrams. To understand the different process concepts presented below in this thesis, a basic knowledge about ternary phase diagrams is useful. A short introduction to this topic will be given in the following starting with binary melting phase diagrams describing the phase behavior of just the two enantiomers without any solvent. At the start of process design or research respectively it can be very useful to look at the binary phase diagram at first. Usually valuable information about the type of system (conglomerate, compound, solid solution) along with information about the enthalpy of melting, the melting point temperature and the eutectic composition can be obtained.

The general system types found for enantiomer systems are depicted in Figure 3.

Preferential crystallization studied in this work takes place in solution. Therefore a suitable solvent is present leading to a ternary system as depicted schematically in Figure 4. In many cases the system type characterizing the binary system is not altered by the addition of a solvent.

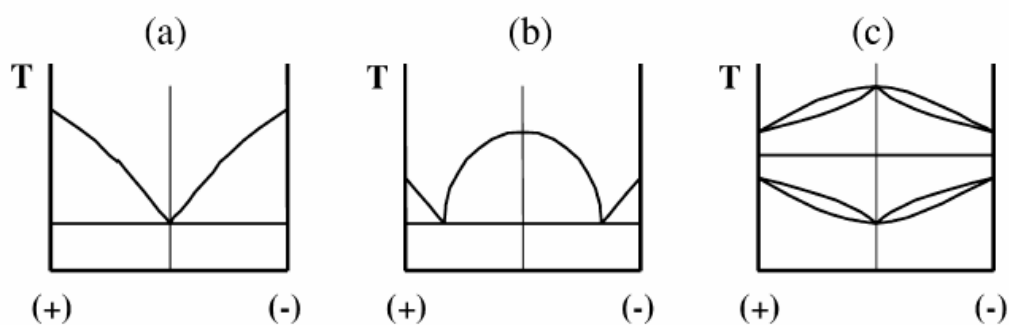


**Figure 3:** Different types of enantiomer systems represented by binary phase diagrams. (a): conglomerate, (b): compound forming systems, (c): the three types of solid solution forming systems.

Considering the mass fractions of the three species and the temperature as system coordinates the situation depicted in Figure 4 is obtained. Since the 3D representation is not very useful for process design and illustration, usually isothermal planar cuts are used. An example of such a cut is the hatched surface in Figure 4.

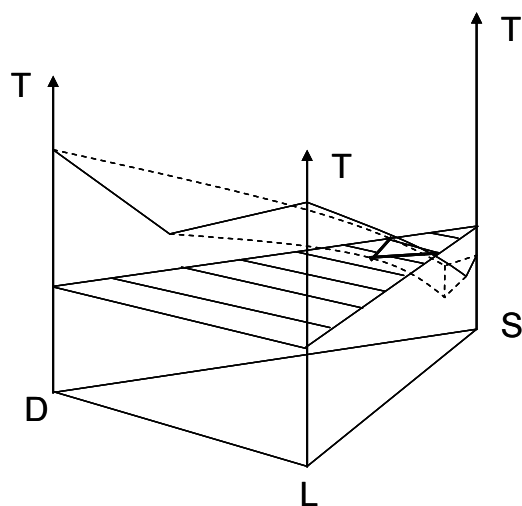


**Figure 4:** Schematic 3D-representation of a ternary system of two enantiomers labeled D and L and the solvent S.

In such a cut the temperature axis is omitted but different solubility isotherms can be plotted in order to show the temperature dependency of the saturation concentrations on composition.

From the ternary phase diagrams represented as isothermal planar cuts illustrated in Figure 5 the thermodynamically stable phases can be identified for the different regions labeled in the diagram. The left diagram in Figure 5 (a) represents a so called conglomerate. Here the two enantiomers crystallize separately. That means that one crystal contains only molecules of one enantiomer. Approximately five percent of the enantiomeric systems exhibit this behavior (Jaques et al., 1994).

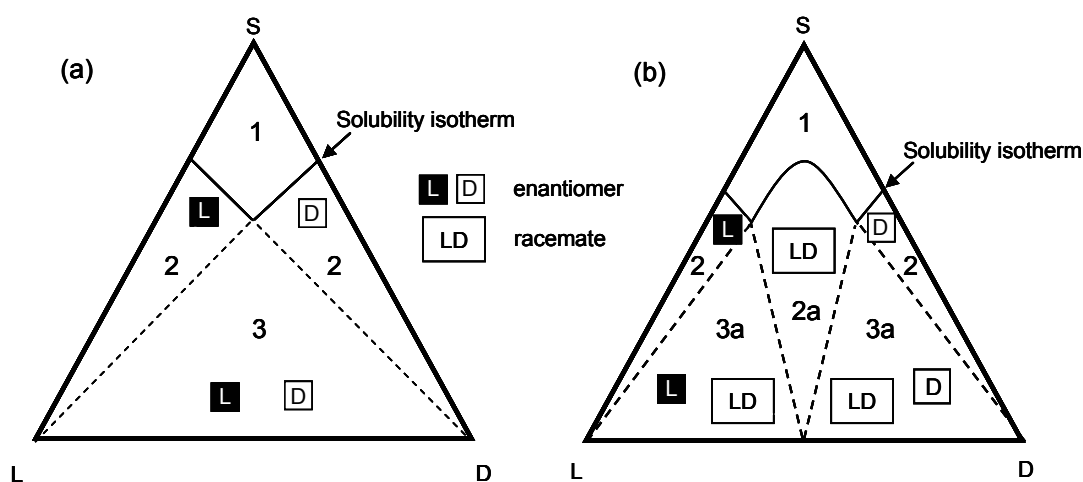


**Figure 5:** The two types of ternary systems investigated in this thesis: (a), conglomerate, (b) racemic compound. The rectangles designate the thermodynamically stable solid phases in certain parts of the phase diagram.



In Figure 6 the well known principle of quantitative evaluation of composition using a ternary phase diagram is illustrated. In the diagram the mass fractions of all three components can be derived from the corresponding point coordinates. This is done as shown in the Figure, by connecting the point (P in the Figure) with lines parallel to the sides opposing the corner of the species in question.

### 2.1.4 Modeling of phase equilibria

Solubilities and equilibrium phase composition are an important basis for modeling crystallization processes. There are several mathematical models available that can be used to mathematically describe the phase behavior of ternary systems (Prausnitz et al., 1986; Predel, 1982; Sandler & Stanley, 1999). A basic equation for modeling the temperature and composition dependency of solubilities is the van't Hoff equation (Equation 8):

$$\ln(x_{m,i} \cdot \gamma) = \int_{T_{m,i}}^T \frac{\Delta h_{m,i}}{R \cdot T^2} dT \quad \text{Equation 8}$$

Derived from Equation 8 is the so called Schröder-van Laar equation ((Jaques et al., 1994)):

$$\ln(x_{m,i}) = \frac{\Delta h_{m,i}}{R} \left( \frac{1}{T_{m,i}} - \frac{1}{T_{m,i}} \right) - \frac{C^l - C_{m,i}^i}{R} \cdot \left( \ln \left( \frac{T_{m,i}}{T_{m,i}} \right) + 1 - \frac{T_{m,i}}{T_{m,i}} \right) \quad \text{Equation 9}$$

The validity of Equation 9 rests upon some idealizing conditions. It is assumed that the enantiomers are immiscible in the solid state (conglomerates only). The mixture is ideal in the liquid state. The difference of the heat capacities  $C^l - C_m^i$  is assumed to be independent of temperature. In many cases the second term of Equation 9 can be neglected (Jaques et al., 1994). This simplification leads to the frequently used formulation given in Equation 10:

$$\ln(x_{m,i}) = \frac{\Delta h_{m,i}}{R} \left( \frac{1}{T_{m,i}} - \frac{1}{T_{m,i}} \right) \quad \text{Equation 10}$$

To account for non idealities the activity coefficient  $\gamma_i$ , present in Equation 8, can be reintroduced into Equation 10. If solvent-solute interactions or a complex phase behavior has to be modeled non constant activity coefficients are introduced as a function of the partial molar excess Gibbs energies.

$$G_i^E = R \cdot T \cdot \ln(\gamma_i) \quad \text{Equation 11}$$

For an ideal solution  $G_i^E = 0$  and therefore  $\gamma_i = 1$ . There exist a number of different models to calculate  $G_i^E$  (Prausnitz et al., 1986). A rather simple method is the one constant Margules equation (van Ness & Abbott, 1982):

$$G_i^E = A \cdot x_{m,i}^2 \quad \text{Equation 12}$$

More sophisticated methods for modeling of phase equilibria are available. The literature on this field is extensive. The Wilson model (Orye & Prausnitz, 1965) as well as the NRTL-model (Renon & Prausnitz, 1968) are quite popular. Group contribution methods such as the UNIQUAC models (Abrams & Prausnitz, 1975) are more recent and are also frequently applied. A group of methods that rely just on the molecular structure of a substance are the COSMO-RS and derived methods (Klamt, 1995).

A simple model capable to describe the solid-liquid phase behavior of the studied systems will be introduced in chapter 4.3 and is used throughout the work to model the solubilities of the investigated systems.

### **2.1.5 Population balance modeling**

As addressed in the introduction of the thesis one goal is to model different concepts for preferential crystallization in a reliable way. For crystallization systems usually the population balance approach is chosen ((Randolph & Larson, 1988), (Ramkrishna, 2000), (Gerstlauer et al., 2006), (Ramkrishna & Mahoney, 2002)).

In the population balance concept a distributed system, represented by a number density function  $F$  is modeled in order to describe changes of the distributed property coordinate or coordinates. In our study a one dimensional representation of the distributed particle property length  $L$  will be chosen. The goal is to describe the changes in this distributed system with a mathematical model consisting of integro-differential and algebraic equations. The change of the particle size distribution has to be coupled with the change of the fluid phase composition via a mass balance. Inside

these models algebraic expressions for the underlying kinetic phenomena (nucleation, growth,...) have to be formulated (see (Mersmann et al., 2002) and (Garside & Shah, 1980) for overviews).

The general population balance equation for an one dimensional case can be stated as (Randolph & Larson, 1988):

$$\underbrace{\frac{\partial F(L,t)}{\partial t}}_{(1)} + \underbrace{\frac{\partial(G \cdot F(L,t))}{\partial L}}_{(2)} + \underbrace{F \cdot \frac{\partial V}{V \cdot \partial t}}_{(3)} - \underbrace{B(L)}_{(4)} + \underbrace{D(L)}_{(5)} + \sum \left( \underbrace{\frac{\dot{V}_{out} \cdot F_{out}}{V}}_{(6)} - \underbrace{\frac{\dot{V}_{in} \cdot F_{in}}{V}}_{(7)} \right) = 0$$

**Equation 13**

The individual numbered terms in Equation 13 have the following meaning:

- (1) Change of the number density function with respect to time
- (2) Change of the number density function with respect to length assuming a general growth law
- (3) Change of the number density function due to changes in the size of the control volume
- (4) Particle birth rate
- (5) Particle death rate
- (6) Distribution changes due to outgoing fluxes
- (7) Distribution changes due to incoming fluxes

The coupling of the change in the particle density function with the change of the fluid phase mass  $m_l$  is done by integrating the particle size distribution with respect to the length coordinate and introducing a system dependent crystal shape factor  $k_v$ :

$$\frac{dm_{l,r}}{dt} = \rho_{solid} \cdot \frac{dV_{solid,r}}{dt} = \frac{d \left( k_v \cdot \rho_{solid} \cdot \int_0^{L_{max}} L^3 \cdot F_r(L,t) \cdot dL \right)}{dt} \quad \text{Equation 14}$$

Applying partial integration (Meyberg & Vachenaer, 1991) and the definition of the growth rate as given in Equation 3 the following relationship for the liquid phase mass balance results if a size independent growth rate  $G$  is assumed (Randolph & Larson, 1988):

$$\frac{dm_{l,r}}{dt} = 3 \cdot \rho \cdot k_v \cdot G_r \cdot \underbrace{\int_0^{L_{\max}} L^2 \cdot F_r(L,t) \cdot dL}_{\mu_{2,r}} \quad \text{Equation 15}$$

If it is assumed that particles enter the system only due to nucleation and the system is closed (batch mode), Equation 13 can be simplified. If it is further on assumed, that the change in volumes of the phases accounted for in Equation 13 is negligible, the population balance function reduces to the partial differential Equation 16.

$$\frac{\partial F(L,t)}{\partial t} + G \cdot \frac{\partial(F(L,t))}{\partial L} = 0 \quad \text{Equation 16}$$

These boundary and initial conditions depend on the process scheme chosen. If no seeds are present at the beginning of a batch, Equation 17 and 18 describe typical conditions.

$$F(L, t = 0) = 0 \quad \text{Equation 17}$$

$$F(L = 0, t) = \frac{B}{G} \quad \text{Equation 18}$$

The boundary condition presented in Equation 18 implies the assumption of zero size nuclei entering the system. If seeds of a certain size distribution  $F_{seeds}$  are used Equation 17 has to be replaced by Equation 19.

$$F(L, t = 0) = F_{seeds} \quad \text{Equation 19}$$

In order to solve the population balance (Equation 16), a suitable discretization scheme has to be used. There are a number of more or less sophisticated discretization schemes available ((Hu et al., 2005; Motz et al., 2002; Qamar et al., 2008; Qamar et al., 2007; Qamar et al., 2006). Due to its simplicity, a simple forward finite difference discretization scheme for the length coordinate was chosen in this work. For the time domain the matlab solver ode23 was used (Shampine & Reichelt, 1997). Different solvers were tested (ode15s, ode45) and ode23 delivered reliable results with a high computational speed. As an alternative method also the method of characteristics was used to solve the population balance (Kumar & Ramkrishna, 1997). It is easily implemented if it is assumed that during a separation run no nucleation of the counter enantiomer occurs.

As another alternative for solving the population balance model the commercial software Parsival<sup>®</sup> was used, which is based on a h,p-moving grid Galerkin scheme

applicable for solving the model equations (M.Wulkow, 2001), was used (chapter 4.5).

### 2.1.6 Model reduction using the method of moments

For optimization and parameter estimation, where a model usually has to be solved repeatedly, a model reduction is advantageous to reduce calculation times. A problem might be that, due to this model reduction, the accuracy or information content of the model will decrease. In this work a model reduction was applied based on the method of moments ((Hulburt & Katz, 1964), (Czapla et al., 2008b)).

The distributed model introduced above can be greatly simplified by converting it into a moment model. Hereby the  $k$ -th moment of the number density distribution of enantiomer  $r$ ,  $\mu_{k,r}$  is defined as follows:

$$\mu_{k,r}(t) = \int_0^{\infty} L^k \cdot F_r(L,t) dL \quad \text{Equation 20}$$

To ease matrix operations and matrix inversions, a scaling of the moments with the scaling factors  $A_k$  is expedient:

$$\mu_{k,r}^* = A_k \cdot \mu_{k,r}(t) \quad \text{Equation 21}$$

Using this scaling and the conversion into moments a set of ODEs can be derived for the first four moments (namely the zero, first, second and third moment) of the particle population for each component  $r=1,2$ . For the zero moment:

$$\frac{d\mu_{0,r}^*}{dt} = A_{0,r} \cdot B_r \quad \text{Equation 22}$$

and for the other moments:

$$\frac{d\mu_{k,r}^*}{dt} = A_{k,r} \cdot [k_v \cdot G_r \cdot \mu_{k-1,r}] \quad \text{Equation 23}$$

where  $B$  is the nucleation rate. A problematic aspect within this model reduction technique is the fact that, due to the reduction of the particle size distribution to its moments, information of the total particle size distribution is lost. This is especially problematic if this complete particle size distribution is needed (e.g. for some of the crystallization kinetics). The classical moment equation for the change of the zero moment (Equation 23) has to be replaced by a slightly different expression if the solution is undersaturated and dissolution with a dissolution rate  $D$  takes place:

$$\frac{d\mu_{0,r}}{dt} = -D_r \cdot F_r(0,t) \quad \text{Equation 24}$$

Since a moment model has been used, the value of the population  $F_r$  at the boundary  $L=0$  is unknown. This leads to a closure problem for the set of moment equations. However, the first four moments of the distribution are known from the calculations performed up to the point where dissolution of the solids begins. Assuming a certain shape of the particle size distribution the population can be approximated by fitting a series of polynomials to the known moments of the population balance (John et al., 2007; Motz, 2004). In this study an approach from Motz ((Motz, 2004) is used, assuming that the population at this point can be approximated using the first four polynomials of a Bernstein series (Grosche et al., 1995):

$$F_r(L) \approx \sum_j q_j \cdot F_{basis,j}(L) \quad \text{Equation 25}$$

$$F_{basis,j}(L) = Bern_i^n(L) \quad \text{Equation 26}$$

$$Bern_i^n(L) = \frac{1}{(L_{\max} - L_{\min})^n} \cdot \binom{n}{i} \cdot (L - L_{\min})^i \cdot (L_{\max} - L)^{n-i} \quad \text{Equation 27}$$

With this approximation function, Equation 24 can be solved. However, it has to be carefully checked if the solution of the reduced model is comparable to the solution of the fully discretized model (see chapter 4.5 for a comparison of different model solution strategies).

## 2.2 Crystallization of enantiomers and preferential crystallization

As mentioned before the process of preferential crystallization is an interesting method for the separation of enantiomer mixtures into the pure enantiomers by crystallization. It is a method to separate ternary mixtures of two enantiomers and solvent as it was introduced in Chapter 2.1.3.. The technique is also referred to as resolution by entrainment (Amiard, 1956). Formerly it was thought that the process would only work for systems of the conglomerate forming type. However in a recent investigation (Lorenz et al., 2006c) it was shown that the process concept is also applicable to resolve systems of the compound forming type, when starting from an already enriched solution.

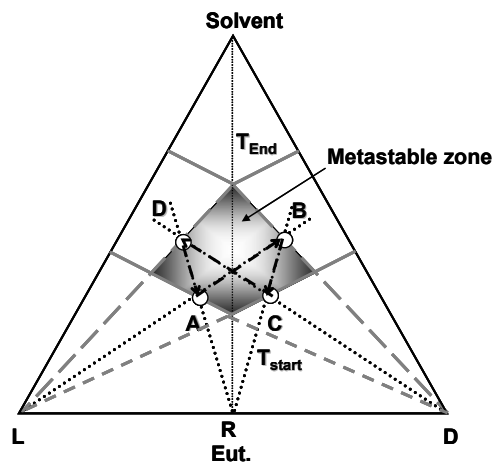


**Figure 7:** Schematic illustration of a periodically operated preferential crystallization process in a ternary phase diagram for a conglomerate forming system.

For reasons of simplification the basic concept of preferential crystallization will be explained below on the basis of the at present more typical and relevant case of conglomerate systems separation. The concept is illustrated in Figure 7 using the corresponding ternary phase diagram. At point A and temperature  $T_{Start}$  the solution contains a slight excess of the enantiomer L. This solution is cooled down to  $T_{End}$ . Thereby the system is inside the metastable zone with respect to both enantiomers. This means that the solution is supersaturated but no crystallization will occur for a certain period of time. Now enantiopure seed material of L is added to the vessel. These seeds will induce a crystallization of the L enantiomer. Since molecules of L are consumed from the mother liquor, the concentration of the liquid phase will decrease along the trajectory A-B until point B is reached. At B the process is stopped and the crystals of L are harvested via a solid-liquid separation. Since the process is cyclic, the mother liquor is heated up again and a defined quantity of eutectic material is added to the solution so that after an intermediate complete dissolution point C is reached. Starting from point C the solution is cooled down again to  $T_{End}$  and seeds of D are added. D crystallizes and the composition changes along the trajectory C-D until point D is reached. Subsequently the D crystals are harvested via a solid-liquid separation. With the addition of eutectic feed material the solution again reaches point A and the cyclic process scheme can be repeated. That way, with two sequential batches, a certain amount of eutectic feed material can be separated into pure D and L crystals.

Ideally the process could be continued infinitely. In practice there exist certain limitations. Due to the recycling of the mother liquor, impurities will accumulate. When the impurities start to affect the crystallization kinetics or change the solubility of the system the cyclic process can collapse (Klukas, 2008).

Since the whole process takes place inside the not very well defined metastable zone the crystallization kinetics control the process applicability and productivity.

As mentioned earlier the process scheme has been recently applied to compound forming systems. Since this slightly modified process concept will also be investigated in the thesis it is explained with the help of Figure 8.

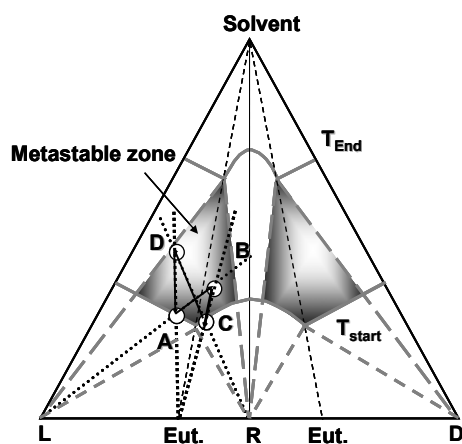


**Figure 8:** Schematic illustration of a periodically operated preferential crystallization process in a ternary phase diagram for a compound forming system.

Here the process also starts at point A. At this point the mother liquor is enriched with the L enantiomer with a concentration exceeding the one at eutectic composition. The solution is cooled down to  $T_{End}$  and enantiopure seeds of L are added. Due to the enantioselective crystallization that takes place inside the metastable zone the solution concentration changes along the trajectory A-B and crosses the eutectic line. At point B the crystals of the first batch are harvested via a solid-liquid separation. Then the solution is heated up again and solid material with eutectic composition is added to the vessel and is completely dissolved so that point C is reached. At point C racemic seeds are added. The solution is then cooled down to  $T_{End}$  and molecules of both enantiomers are incorporated into the crystals. Due to the growth of the seed crystals the concentration changes along a trajectory C-D. At point D the crystals of the racemate are harvested. After addition and dissolution of eutectic feed material the cyclic process scheme again reaches point A.

The main difference between the processes applied to a conglomerate forming system (Figure 7) and to a compound forming system (Figure 8) is that for the compound forming system only one enantiomer can be obtained as a pure substance. Of course another important difference is the necessity of a preceding enrichment step in case of the compound forming system (Figure 8) (see also (Lorenz et al., 2006c)). The racemate collected in the other batch of one cycle can be recycled to the required enrichment step (e.g. chiral membrane separation or chromatographic separation).

### **2.2.1 Process concept „nucleation seeding“**

The process concept “nucleation seeding” is a variant of the so called auto seeded polythermal programmed preferential crystallization (AS3PC) process (Coquerel et al., 2000; Czaplá et al., 2008b). The most important and interesting aspect of this process concept is the “auto seeding”. Auto seeding refers here to the generation of seed crystals inside the crystallization vessel. “Nucleation seeding” will be introduced as follows with the help of Figure 9 .

A clear solution that contains the target enantiomer in excess (point (1)) is cooled down from  $T_{\text{start}}$  to a temperature  $T_0$  (2). Around point (2) primary nucleation of both enantiomers occurs (3). These crystals grow for a while. Then the solution is heated up to a temperature  $T_{\text{annealing}}$  (5). During this heating process at first racemate dissolves up to a point (4) at  $T_{\text{intermediate}}$ . Then the two phase region of the target enantiomer is reached and the course of the trajectory shifts while crystals of the L-enantiomer dissolve. This dissolution stops at point (5) when the annealing temperature  $T_{\text{annealing}}$  is reached. The temperature  $T_{\text{annealing}}$  has to be chosen carefully based on the knowledge of the phase diagram so that all crystals of the unwanted enantiomer are dissolved at the end of the “annealing” period (point 5) and a certain amount of crystals of the target enantiomer remain. Ideally the process could already be started at point (4) at  $T_{\text{intermediate}}$ . In practice it is wise to heat up the suspension to a temperature  $T_{\text{annealing}}$  inside the two phase region in order to make very sure that only crystals containing the target enantiomer remain in the solid phase, acting now as seed material for the preferential cooling crystallization that follows shifting the liquid phase composition (5) up to point (6).

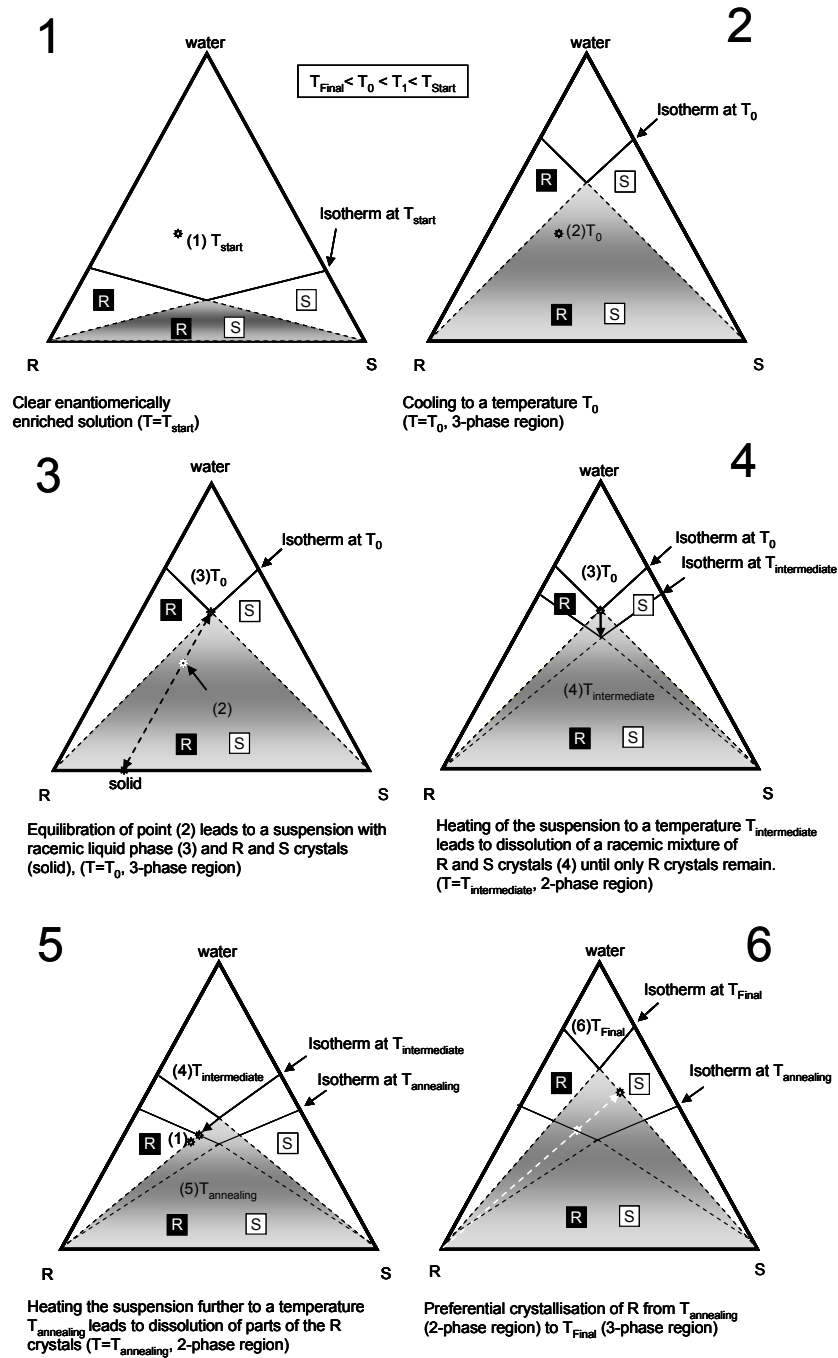


**Figure 9:** Process concept of auto seeded polythermal preferential crystallization. The seeds are generated by primary nucleation followed by dissolution of the crystals of the unwanted enantiomer. Ternary phase diagrams are used to illustrate the process concept.

The schematic course of the temperature is depicted in Figure 10. The different stages of the process are explained below the Figure. The numbers correspond to the points illustrated in the ternary phase diagrams shown in Figure 9.

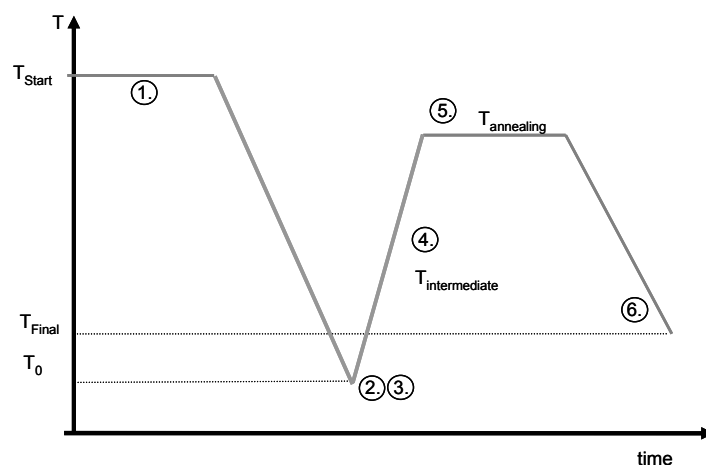


**Figure 10:** Schematic temperature profile for the Process concept „nucleation seeding“.

1. Clear solution
- 2./3. Primary nucleation
4. Dissolution
5. Annealing
6. Preferential cooling crystallization

Usually now eutectic feed material is added and the other enantiomer is seeded. This way a cyclic operation where racemate is separated into the pure enantiomers can be realized.

The principle of this cyclic process can also be applied to resolve compound forming systems (Lorenz et al., 2006b). In the adopted scheme the two batches are different in that way, that in one batch the pure enantiomer is harvested, while in the other batch the racemate is crystallized in order to close the cycle.

Here also the so called “nucleation seeding” will be applied and described in detail with the help of Figure 11 and Figure 12. In Figure 11 the course of the process is illustrated with the help of ternary phase diagrams. The numbers and temperatures given in Figure 12 represent the temperature profile of the process and correspond to the numbers shown in Figure 11.

A clear solution that has an enantiomeric excess, e.g. of R, higher than the one for the eutectic composition is cooled down from  $T_{start}$  (1) to a temperature  $T_0$ . Around point (2) primary nucleation of racemate and pure enantiomer occurs and the liquid phase composition turns to the eutectic one (2). The nucleated crystals grow for a while.

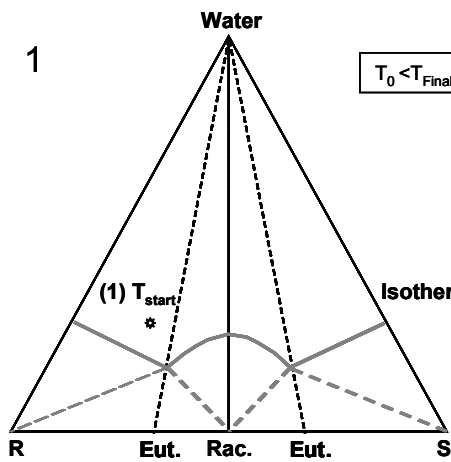
Then the solution is heated up to a temperature  $T_{annealing}$  (3). After complete dissolution of the racemate crystals the two phase region of the target enantiomer is reached and pure R-enantiomer crystals remain. The temperature  $T_{annealing}$  has to be chosen carefully based on the knowledge of the phase diagram in such a way that all crystals of the racemate have been dissolved at the end of the “annealing” period (3) and crystals of the wanted enantiomer remain, acting as seed crystals for the follow up preferential cooling crystallization (4).

After the temperature  $T_{final}$  (4) is reached the process is stopped and a solid-liquid separation is performed.  $T_{final}$  has also to be chosen carefully in order to avoid a nucleation of the unwanted enantiomer.

The width of the metastable zone, which is needed to accurately predict  $T_{final}$ , can be approximated based on the solubility isotherms as illustrated in Figure 11 (pictures 5 and 8) by connecting the eutectic solubility at  $T_{final}$  with the racemate composition on the lower edge of the phase diagram (Czapla et al., 2008a).

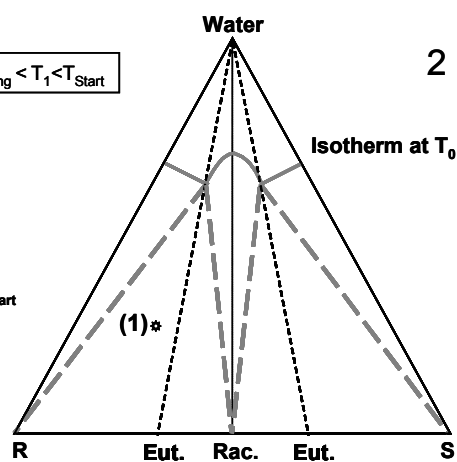
In order to complete the cycle, eutectic feed material has to be added to the vessel in order to reach (5). The seeds for the racemate batch are now produced by a subcooling from  $T_1$  (5) to a temperature  $T_{annealing}$  (6). The temperature difference should be chosen large enough in order to induce nucleation of the racemate.

The nucleated crystals now act as seeds for the racemate crystallization up to (7). Again the position of (7) in the ternary phase diagram is calculated assuming that the metastable zone width can be approximated by the connecting line from the eutectic solubility at  $T_0$  to the enantiomer corner of the phase diagram (Czapla et al., 2008c) (Figure 11, picture 8). When eutectic feed is added to the solution in an amount so that point (1) or (1') respectively is reached the cycle is completed and a new one can be started.

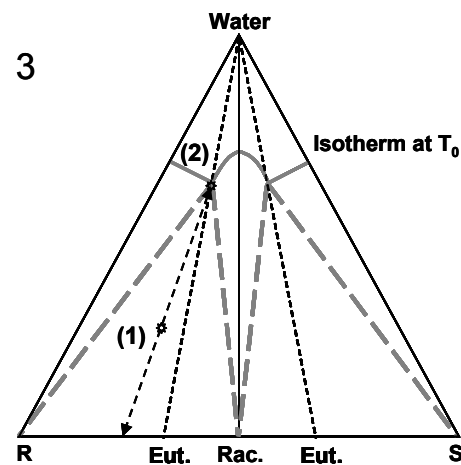


Clear enantiomerically enriched (above eutectic composition) solution ( $T=T_{start}$ )

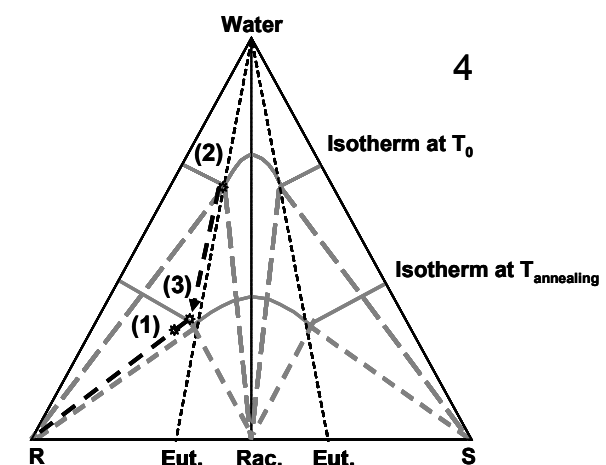
$$T_0 < T_{Final} < T_{Annealing} < T_1 < T_{Start}$$



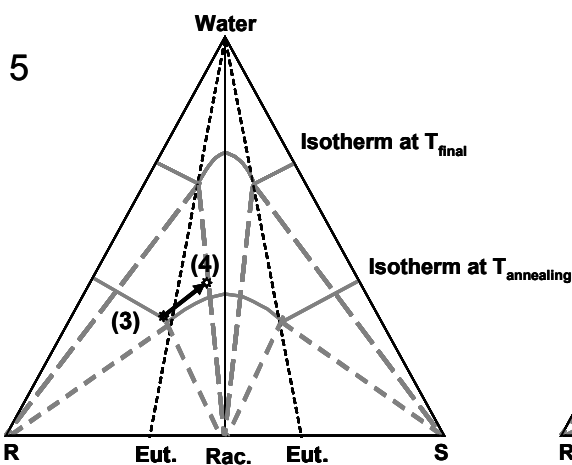
Cooling to a temperature  $T_0$  ( $T=T_0$ , 3-phase region)



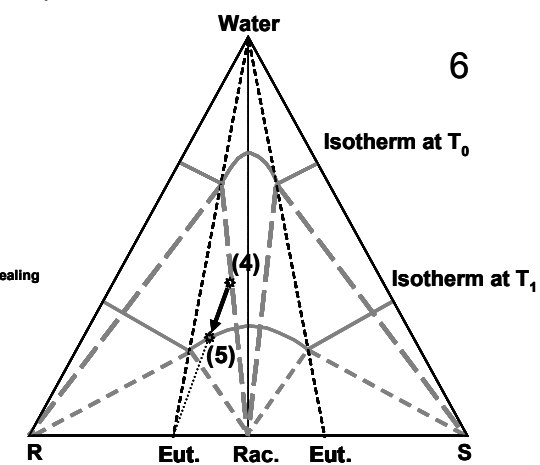
Equilibration of point (1) leads to a suspension containing racemic and pure R-MA crystals. The liquid phase has eutectic composition (2). ( $T=T_0$ , 3-phase region)



Heating of the suspension to a temperature  $T_{annealing}$  leads first to a dissolution of a mixture of R-MA and racemic MA crystals (2)-(3). ( $T=T_{annealing}$ , 3-phase region). At point (3) the two phase region is reached and only R-MA Crystals remain, acting as seeds for the follow up preferential cooling crystallization.



Cooling crystallization of R-MA inside the metastable zone to  $T_{Final}$  starting from point (3) to point (4).



Heating to a temperature  $T_1$ . Addition of eutectic feed and complete dissolution leads to (5).

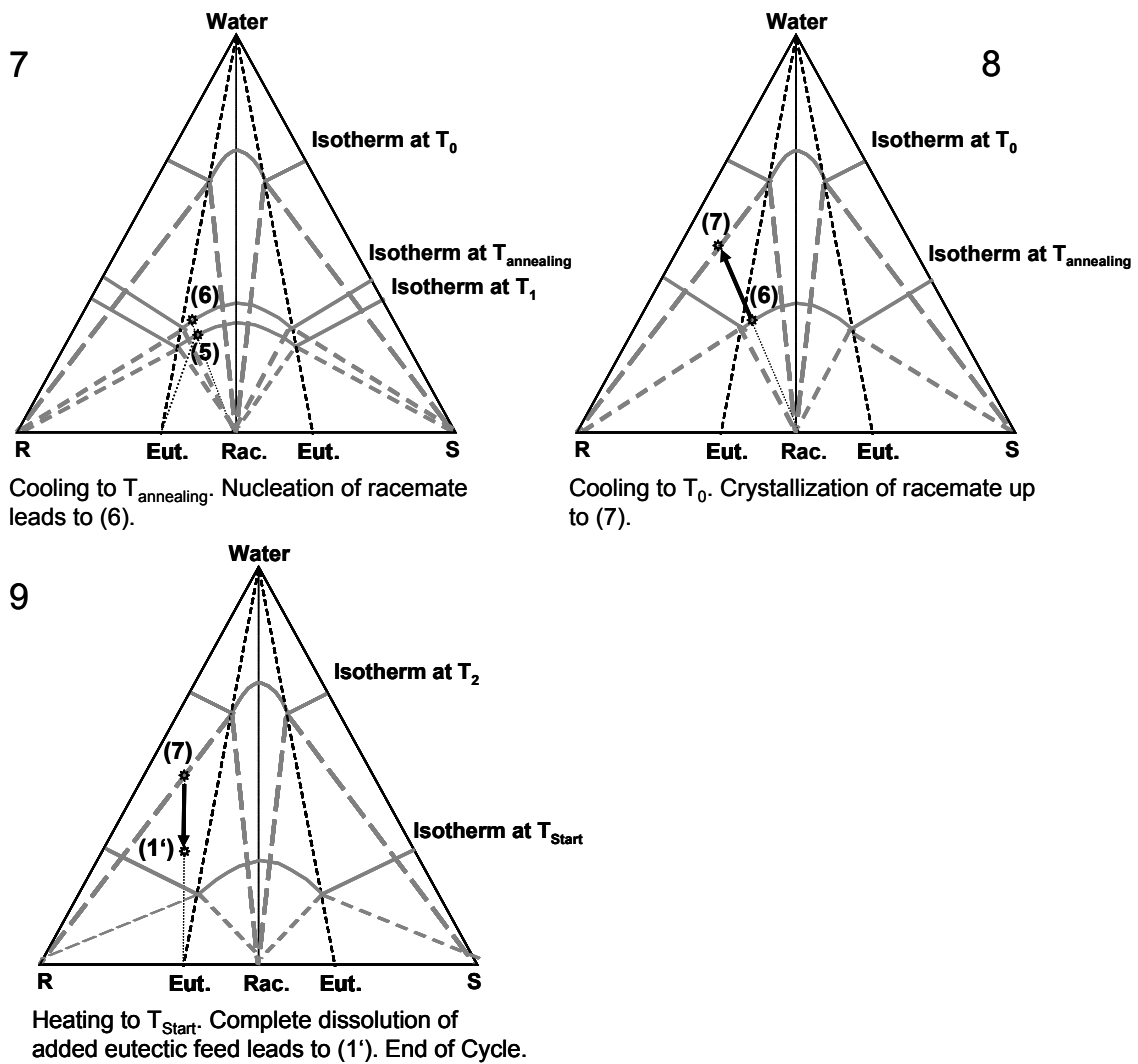


**Figure 11:** Illustration of the AS3PC nucleation process concept “Nucleation seeding” in a series of ternary phase diagrams. The seeds of the pure enantiomer are generated through primary nucleation followed by dissolution of the crystals of the racemate. The seeds for the racemate batch are generated by primary nucleation only.

In practice limitations exist on the maximal number of cycles that can be performed due to an accumulation of impurities in the mother liquor, decomposition of the educt molecules, etc..

The maximum yield of the process can be estimated solely using the solubility data and the simplifying assumptions made with respect to the metastable zone width.

If experimental data for the metastable zone width are available a more sophisticated procedure for process evaluation can be followed. This concept will be illustrated later (chapter 4.4) to estimate the process yield and productivity if a linear cooling with a constant cooling rate is used.

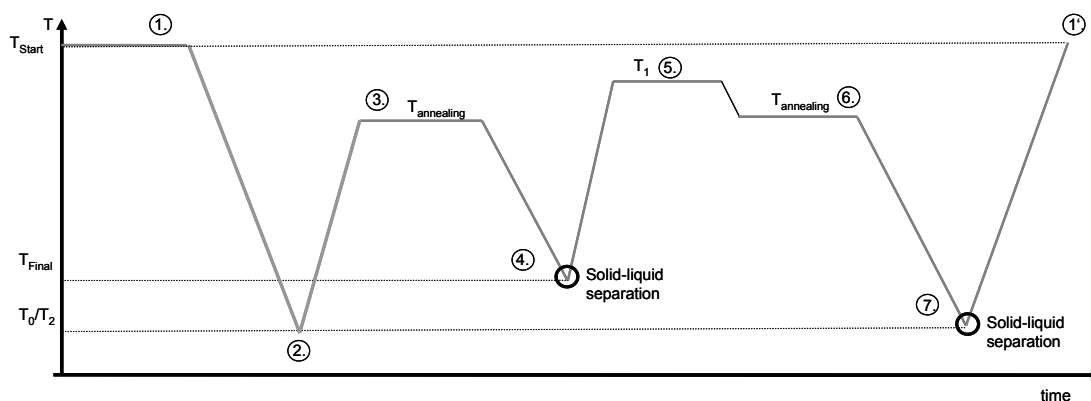


**Figure 12:** Schematic illustration of the temperature profile corresponding to the process illustrated in Figure 11. The temperature profile illustrates one complete cycle with an enantiomer and a racemate batch.

1. Clear solution
2. Primary nucleation and growth
3. Annealing
4. Preferential cooling crystallization of the enantiomer followed by a solid –liquid separation and addition of a mixture of crystalline material with eutectic composition
5. Complete dissolution of the added crystals
6. Primary nucleation of the racemate and subsequent annealing
7. Preferential cooling crystallization of the racemate followed by a solid –liquid separation and addition of a mixture of crystalline material with eutectic composition.
- 1.' Clear solution with the starting composition, end of cycle

The method described might not work for all systems and depends on the primary nucleation kinetics. Sometimes it might be hard to get any crystalline material at all without the help of prepared seed material added additionally. Thus an alternative method which uses milled racemic material to generate the seed crystals is used. This concept labeled as “milled seeds” will be introduced in the next chapter.

### **2.2.2 Process concept „milled seeds“**

The process concept “milled seeds” is the second variant of the AS3PC process studied in this thesis. Also here the most important and interesting aspect is the realization of the so called “auto seeding”. The process starts from a clear solution containing both enantiomers heated slightly above the saturation temperature at  $T_{Start}$ . Thus the solution is undersaturated. One of the enantiomers, the target enantiomer (e.g. R in Figure 13) is present in excess. The solution is then cooled down to a temperature  $T_1$  (point (1)) which has to be chosen carefully based on the knowledge

of the phase diagram. Milled racemate is added to the solution. The racemate now dissolves, but due to the excess of R and the correct amount of the solid racemate added the two phase region of the target enantiomer is reached. The milling of the seeds is done in order to homogenize the material and provide a fast dissolution. In this manner all crystals of the S-enantiomer should have dissolved and a certain amount of the R-enantiomer crystals remains in suspension. These crystals now act as seed material for the follow up preferential cooling crystallization depicted in part (2) of Figure 13. The process is stopped with a solid-liquid separation at  $T_{Final}$ . The choice of  $T_{Final}$  is crucial to obtain a pure product. If the metastable limit of the counter enantiomer is crossed it will nucleate and thus contaminate the product.

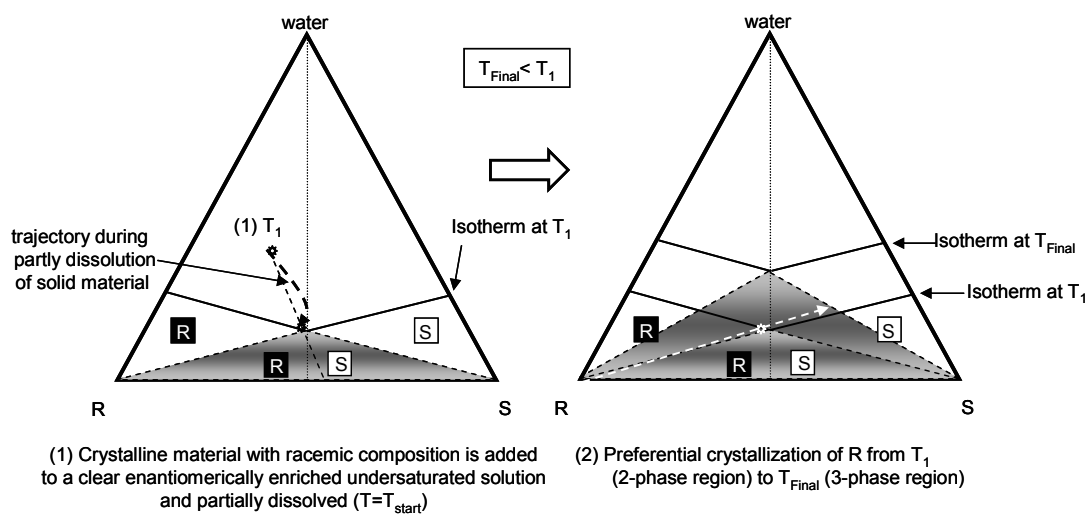


**Figure 13:** Illustration of the process concept „milled seeds“ in two ternary phase diagrams.

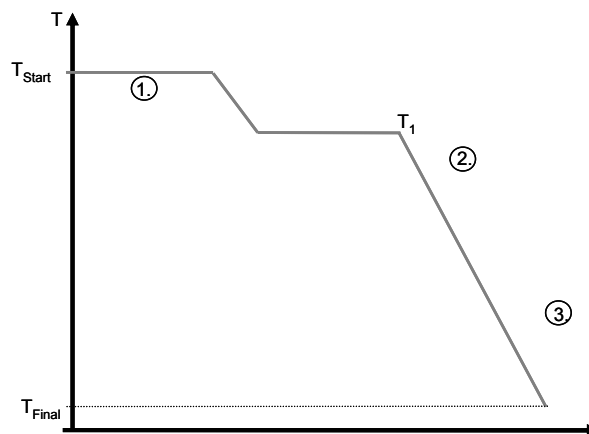


**Figure 14:** Schematic illustration of the temperature profile for the Process concept „milled seeds“

1. Clear solution
2. Annealing
3. Preferential cooling crystallization

The course of a typical temperature trajectory for this process concept is illustrated in Figure 14.

### **2.2.3 Process concept „defined seeding“**

The third process concept that is investigated in this work uses the classical seeded approach. Here seed material is added in defined amounts to a supersaturated solution at the beginning of a batch.

The temperature profile used during the seeded runs is similar to the one depicted in Figure 14 for the “milled seeding” concept. The seed material is inserted where the final cooling starts (start of step 3.).

Depicted in a ternary phase diagram the process looks similar to the last process step depicted in Figure 13 (right illustration).

### **2.2.4 Crystallization kinetics for enantiomeric systems**

The crystallization kinetics describe the rates for the different phenomena that govern the dynamics of the particle size distributions  $F_r$ . The index  $r$  accounts for the two different distributions of the two enantiomers or enantiomer and racemate, respectively.

There exist a multitude of empirical, semi empirical and physically based expressions to model different kinetic phenomena (Garside et al., 2002). For the models used in this work the kinetics of crystal growth, secondary and primary nucleation and dissolution are needed. Typical expressions suggested are summarized below.

Crystal growth (Mersmann, 1995):

$$G_r = k_g \cdot \left( \frac{w_r}{w_{r,sat}} - 1 \right)^g \quad \text{Equation 28}$$

Dissolution (Saenz de Jubera, 2006):

$$D_r = k_d \cdot \frac{2}{3 \cdot \rho \cdot Elo} \cdot (w_r^+ - w_r) \quad \text{Equation 29}$$

Primary nucleation:

$$B_r = k_b \cdot (w_r + w_{r\pm 1})^{7/3} \cdot \sqrt{\ln\left(\frac{1}{w_{r,sat}}\right)} \cdot e^{\frac{-k_{prim} + k_{prim2} \cdot \frac{\mu_{2,r\pm 1}}{V}}{\ln(T^3) \left(\ln\left(\frac{w_r}{w_{r,sat}}\right)\right)^2}} \quad \text{Equation 30}$$

Secondary nucleation (Garside et al., 2002):

$$B_r = k_{bsek} \cdot \left(\frac{w_r}{w_{r,sat}} - 1\right)^b \cdot k_v \cdot \left(\frac{\mu_{3,r}}{V}\right) \quad \text{Equation 31}$$

The temperature dependence of the processes is modeled with Arrhenius laws. This is the case e.g. for the prefactors of the crystal growth and dissolution rates as well as for the secondary nucleation rates (A.Tadayon, 2002):

$$k_g = k_{g,pre} \cdot e^{\frac{-E_g}{R \cdot T}} \quad \text{Equation 32}$$

$$k_d = k_{d,pre} \cdot e^{\frac{-E_d}{R \cdot T}} \quad \text{Equation 33}$$

$$k_d = k_{d,pre} \cdot e^{\frac{-E_d}{R \cdot T}} \quad \text{Equation 34}$$

**Equation 35**

The chosen expression for the crystal growth rate as well as the rate equation for the secondary nucleation are classical semi-empirical formulations that were frequently used for other systems. The formulation for the primary nucleation rate is more sophisticated. It is based on the classical nucleation theory (Mersmann, 1995), (Mersmann et al., 2002), (Mullin, 2001) with a modification made by the author to account for the fact that the activation energy for nucleation will decrease when the structurally quite similar counter enantiomer is already present in solution. Therefore a term is included in the exponential part of the function given in Equation 30. This term assumes a higher primary nucleation rate with a linear proportionality to the second moment of the particle size distribution of the counter enantiomer relative to the total suspension volume. Compared to simpler models this formulation of the rate equation performed superior representing the experimental data. The assumed mechanism of surface nucleation is supported by the findings of Ito and Matsuoka (Ito & Matsuoka, 2008). Inside the classical equations for the description of the primary

nucleation kinetics there are some physical constants like the surface tension or kinematic viscosity of the liquid phase. These constants are all lumped into the pre exponential factor  $k_b$  since they are often not known for the system studied and the direct measurement of these constants is sometimes tedious and time consuming. In general, in order to describe the dynamics of the different process schemes many free kinetic parameters have to be estimated.

### 2.3 Parameter estimation

In this chapter selected aspects in the context of parameter evaluation are presented and discussed. One section is dedicated to experimental design in order to determine experimental conditions that minimize certain experimental design criteria.

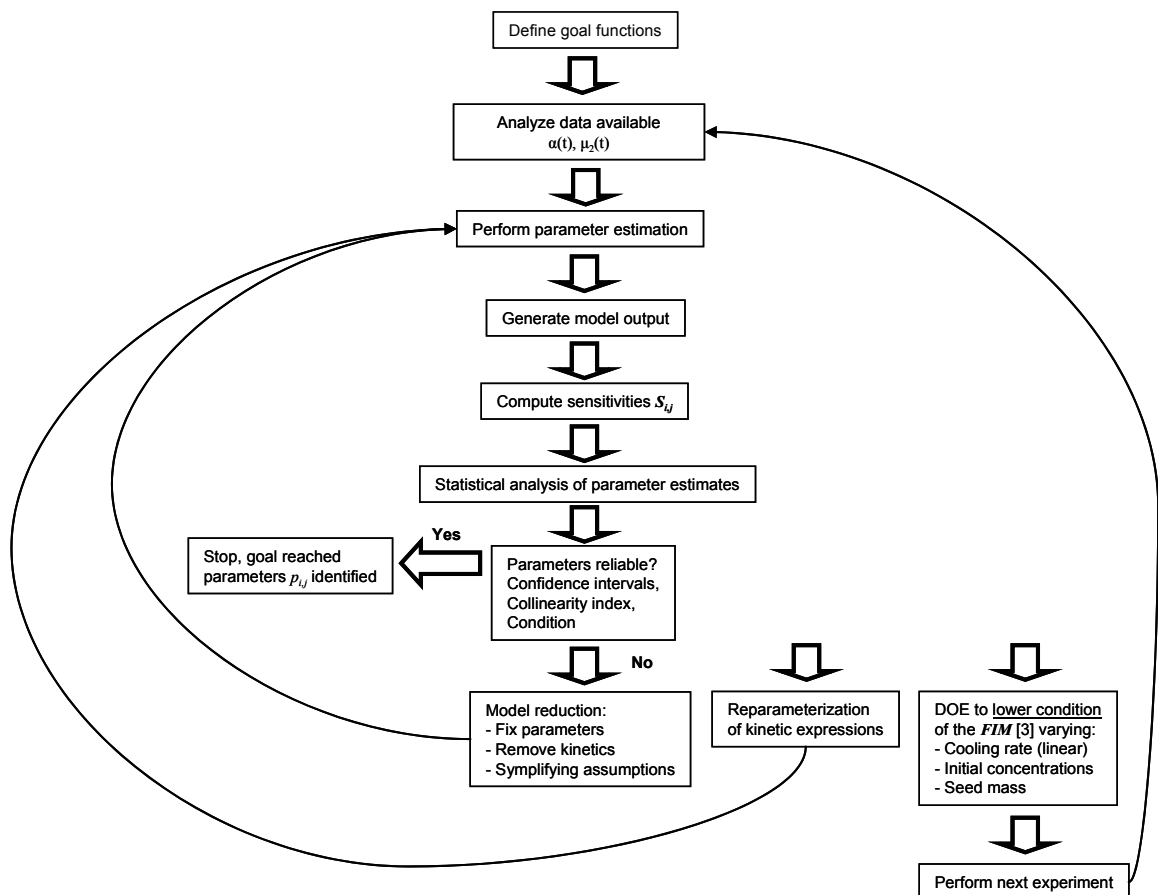


**Figure 15:** Schematic illustration of an approach to model parameterization (adapted from (Brun, 2002))

As the result of the chosen parameter estimation procedure one gets a set of parameters that minimize the difference between measured and calculated trajectories

according to the definition of the goal function. However using a given data set it is not always clear if the estimated parameters are reliable. That means if they are unique and what confidence interval each parameter has. There are some statistical methods available that can be used to quantify parameter cross correlation, estimate confidence intervals and check for general model identifyability. The approaches applied in this work are briefly explained in the following chapters. A typical approach to parameterize a model is shown in Figure 15.

### 2.3.1 Sensitivity analysis

Sensitivities of the observed variables with respect to the parameters of interest as defined in Equation 36 are useful to analyze the model structure and the impact of single parameters on the model output.

In the investigations performed below the method of internal numerical differentiation (Matlab function `sens_ind.m`, (Mollá & Padilla, 2002), (Bock, 1981)) is used to determine local sensitivities  $S_{ij}$ :

$$S_{ij}(t) = \frac{\partial x_i(t)}{\partial p_j} \quad \text{Equation 36}$$

With the functional relation

$$\vec{f}(t, x, p) = \frac{\partial \vec{x}(t)}{\partial t} \quad \text{Equation 37}$$

a time variant sensitivity matrix can be built:

$$\frac{d}{dt} \hat{S} = \nabla_p \vec{f} + \hat{S} \cdot \nabla_x \vec{f} \quad \text{Equation 38}$$

From the time variant sensitivity matrix a non dimensional sensitivity matrix can be built.

$$\hat{S}_{\text{dim}} = \frac{p_j}{A(x_i)_{\text{scal}}} \cdot \frac{\partial x_i}{\partial p_j} \quad \text{Equation 39}$$

The preterm  $\frac{p_j}{A(x_i)_{\text{scal}}}$  in Equation 39 is introduced for normalization with respect to the different units of the parameters and the experimental signals measured.

From this a normed sensitivity matrix can be defined by division of the non dimensional sensitivity with the Euclidian norm of the matrix (Brun, 2002).

$$\tilde{S}_{norm} = \frac{\hat{S}_{dim}}{\|\hat{S}_{dim}\|} \quad \text{Equation 40}$$

If the sensitivities are plotted against time for dynamic processes it can be seen which parameter is the most sensitive one and at what process time the sensitivities are highest. To quantify and rank the parameters in terms of sensitivity a sensitivity measure was introduced (Brun, 2002):

$$\delta_j = \sqrt{\frac{1}{n} \cdot \sum_{i=1}^n s_{ij}^2} \quad \text{Equation 41}$$

Based on the sensitivity measure  $\delta$  the parameters can be ranked according to their importance. If a sensitivity measure of a parameter is close to zero it cannot be estimated with the measured data and should be fixed to a suitable value. Also if certain parameters have a much lower sensitivity measure than others it should be checked if they can be fixed without a loss of degrees of freedom when the model is adjusted to represent experimental data.

### 2.3.2 Fisher Information Matrix

The Fisher information matrix is used to calculate uncertainties for parameter estimates (Peterson, 2000). As a basis for the calculation, parameter sensitivities have to be calculated using the considered model of the process. Based on the non dimensional form of the Sensitivity matrix (Equation 40) along with the variance covariance matrix of the measurements finally the Fisher information matrix can be calculated (Kay, 1993).

$$FIM = \sum \hat{S}_{dim}^T \cdot C^{-1} \cdot \hat{S}_{dim} \quad \text{Equation 42}$$

Based on two experimental signals  $w_{ij}$  and  $\mu_{2,ij}$  the variances and the covariance of the 2x2 variance-covariance matrix are defined as follows (Chen et al., 2004):

$$c_{11} = \frac{1}{df} \cdot \sum_{j=1}^{N_{Exp}} \sum_{i=1}^{N_{data}} (w_{ij}^{exp} - w_{ij}^{mod}) \quad \text{Equation 43}$$

$$c_{22} = \frac{1}{df} \cdot \sum_{j=1}^{N_{Exp}} \sum_{i=1}^{N_{data}} \left( \frac{\mu_{2,ij}^{*,exp}}{\max(\mu_{2,ij}^{*,exp})} - \frac{\mu_{2,ij}^{*,mod}}{\max(\mu_{2,ij}^{*,mod})} \right)^2 \quad \text{Equation 44}$$

$$c_{12} = c_{21} = \frac{1}{df} \cdot \sum_{j=1}^{N_{Exp}} \sum_{i=1}^{N_{data}} (w_{ij}^{exp} - w_{ij}^{mod}) \cdot \left( \frac{\mu_{2,ij}^{*,exp}}{\max(\mu_{2,ij}^{*,exp})} - \frac{\mu_{2,ij}^{*,mod}}{\max(\mu_{2,ij}^{*,mod})} \right) \quad \text{Equation 45}$$

The degree of freedom  $df$  is defined as the total number of experiments (data points) minus the number of parameters. The inverse of the Fisher Information Matrix  $FIM^{-1}$  leads to a matrix  $\Omega$  of coefficients measuring parameter cross correlations. Absolute values of 1 ( $|\Omega_{kk}| = 1$ ) denote total correlation between a pair of parameters  $p_h$  and  $p_k$ . A value of zero implies no correlation at all. In practice values greater than 0.9 represent significant correlations (Beck, 1977).

$$\Omega_{hk} = \begin{cases} 1 & \text{if } h = k \\ \text{else} & \frac{(FIM^{-1})_{hk}}{\sqrt{(FIM^{-1})_{kk}} \cdot \sqrt{(FIM^{-1})_{hh}}} \end{cases} \quad \text{Equation 46}$$

In addition to correlation coefficients the Fisher Information Matrix is used to evaluate the confidence of the estimated parameters. Following the Cramér-Rao inequality the lower bound of the parameter variance is equal to the diagonal element of the inverse of the  $FIM$  (Kay, 1993; Ljung, 1999):

$$\sigma^2 \geq FIM^{-1} \quad \text{Equation 47}$$

Then the confidence intervals can be calculated by means of a quantile  $t_{\alpha/2}^{df}$  of the Student's t-distribution for a given degree of freedom  $df$  and confidence  $\alpha$ .

$$p_h - t_{\alpha/2}^{df} \cdot \sigma \leq p_h^* \leq p_h + t_{\alpha/2}^{df} \cdot \sigma \quad \text{Equation 48}$$

Typically for  $\alpha$  a value of 90%, 95% or 99% is chosen. Here  $\alpha = 0.95$ .

An additional useful measure to quantify the identifiability of the parameters with respect to given data is the condition number of the inverse of the  $FIM$ . The condition is defined as the ratio of the largest to the smallest eigenvalue of  $FIM^{-1}$ . A condition greater than 1000 indicates severe problems to estimate the free model parameters with a given set of data (Beck, 1977). Another method to quantify the reliability of the estimated parameters is via the so called collinearity index  $\gamma$  that is a measure for the linear dependence of the columns of the Fisher information matrix:

$$\gamma = \frac{1}{\sqrt{\tilde{\lambda}_{\min}^{norm}}}$$

**Equation 49**

It is unity if the matrix is orthogonal and it tends to infinity if the columns are linearly dependent (singular matrix). To consider a model as identifiable a collinearity index below 20 should be obtained (Brun, 2002). A collinearity index of 20 can be interpreted in such a way that the effect of a change of one parameter on the model output can be compensated to 5% by appropriate changes of other model parameters. If the collinearity index exceeds a value of 100 severe problems to estimate parameters have to be expected (Brun, 2002).

### **2.3.3 Bootstrap method**

The Bootstrap method was originally introduced by Efron in 1979 (Efron, 1979) as a new computer based method to estimate confidence intervals, means and standard errors of samples that should be more accurate than those obtained from the Fisher information matrix (see (Efron & Tibshirani, 1993)). It is a Monte Carlo based method that since its introduction had many useful applications in a variety of fields (see (Joshi et al., 2006)). This is especially true for models with a high degree of nonlinearity with respect to the parameters. Here the analysis of the Fisher information will sometimes give unsatisfying results for the confidence intervals. Due to the Cramer-Rao inequality the FIM provides only a lower bound of the confidence intervals for the parameter estimates (Equation 47). Another advantage of the bootstrap method is that distributions of the parameter estimates are obtained that can be analyzed by means of classical statistical methods.

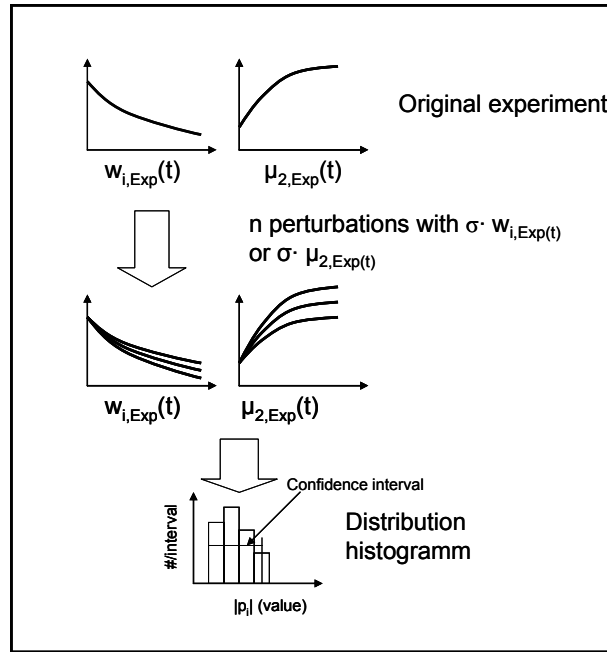


**Figure 16:** Illustration of the procedure to obtain confidence intervals for parameters estimated based on the bootstrap approach.

In order to perform a bootstrap analysis new experiments are generated with random perturbations of the original experimental data based on a priori knowledge on experimental variances. Afterwards parameter estimations are carried out based on each of the newly obtained data sets. The procedure is schematically illustrated in Figure 16. The obtained new samples directly relate the uncertainty in the data to the uncertainty in the parameters without any special mathematical operation or assumptions. The disadvantage of the method is the usually quite high computational burden of the multiple parameter estimations to be carried out. If the model is complex and the time to solve the model is large the calculations can be very time consuming.

The bootstrap method starts in a mathematical formulation. Based on an original experimental data set  $y$  a new data set  $y^*$  is generated according to:

$$y^* = y + \sigma_{\text{exp}} \cdot \text{randn} \quad \text{Equation 50}$$

Where  $\text{randn}$  is a normally distributed random number with mean 0 and standard deviation of 1. If insufficient experimental data is available a common assumption for the experimental variance is presented in Equation 51 (Box et al., 1978):

$$\sigma_{\text{exp}} = \sqrt{\frac{\sum_0^{t_{\text{Ende}}} (x_i - x_{i,\text{exp}})^2}{df}}$$

**Equation 51**

Here it is assumed that the experimental standard deviation can be approximated by the square root of the square of the difference between model output and experimental data divided by the degree of freedom  $df$ . Again the degree of freedom  $df$  is defined as the total number of experiments (data points) minus the number of parameters.

### **2.3.4 Experimental design**

Experimental design or design of experiments (DOE) has attracted increasing attention throughout the last years (e.g. (Arellano-Garcia et al., 2007)). It is applied in many fields of research. Basically it is an approach to perform experiments containing a maximum of information with respect to the goals of the research. That way, in many cases, the experimental effort can be greatly reduced (Hintermaier, 1948), (Smallwood, 1947). Two general approaches to the concept can be distinguished:

- factorial design
- dynamic design

Factorial design is a design method that emphasizes on detecting which experimental factors have influences on the outcome or research goal and what influences they have. A good overview over the principles and their applications is given for example in the books by (Box et al., 1978) and (Morgan, 1995).

The dynamic design approach uses information of the sensitivity matrix and variance-covariance matrix to design experiments that maximize the sensitivity and thus the information content with respect to certain design goals based on a mathematical model. In our case discussed below the design goal is the identification of the free model parameters. Examples for the dynamic design approach in the field of crystallization process modeling are given by (Chung et al., 2000). More general information about the available methods can be found in the books by Bard (Bard, 1974) or more recently Vanrolleghem (Dochain & Vanrolleghem, 2001). Within the dynamic design approach it can be distinguished between different design criteria that are all based on local sensitivities or the *FIM* respectively (Chen et al., 2004), (Chen & Asprey, 2003), (Walter & Pronzato, 1997), (Walter & Pronzato, 1990):

A-optimal design:  $\min[\text{tr}(FIM^{-1})]$  Equation 52

D-optimal design:  $\min[\det(FIM^{-1})]$  Equation 53

E-optimal design:  $\min[\lambda_{\max}(FIM^{-1})]$  Equation 54

Modified E-optimal design:  $\min\left[\frac{\lambda_{\max}(FIM^{-1})}{\lambda_{\min}(FIM^{-1})}\right]$  Equation 55

The design criteria applied in this thesis will be the modified E-optimal design criterion (Equation 55).

### 2.3.5 Reparameterization of crystallization kinetics

The model kinetics presented in chapter 2.2.4 are usually strongly nonlinear with respect to supersaturation and temperature. A method to reduce the intrinsic nonlinearity of these equations as well as the cross correlation between prefactors and exponents or prefactors and exponential terms is reparameterization (Ratkowsky, 1989).

Reparameterization refers to finding a new mathematical function containing different parameters but providing the same output (at least in the region of interest) while the sensitivities of the new parameters with respect to the function values are different.

A recommendation coming from the field of reaction engineering is to reparameterize the Arrhenius-type equations for the temperature dependency of the kinetic constants (Equation 34, Equation 35) (Mezaki & Kittrell, 1967; Park & Froment, 2001). The method will be illustrated with the rate law for the formation of secondary nuclei (Equation 31, Equation 35). Instead of using the relation of Equation 35 a new relation is formulated showing the same general mathematical form:

$$k_{b,sec} = k'_{b,sec,pre} \cdot e^{\frac{-E_{sec}}{R} \left( \frac{1}{T} - \frac{1}{T_{mean}} \right)}$$
 Equation 56

The parameters of the original law (Equation 35) can be easily obtained by resubstitution:

$$k'_{b,sec,pre} = \frac{k_{b,sec,pre}}{e^{\left( \frac{-E_{sec}}{R \cdot T_{mean}} \right)}}$$
 Equation 57

This method is also referred to as temperature mean centering. The mean or reference temperature  $T_{mean}$  can be taken e.g. as an average temperature of the temperature range under investigation. Instead of estimating,  $k_{b,sec,pre}$ , now  $k'_{b,sec,pre}$  will be estimated. The principle illustrated in Equation 56 and Equation 57 for the example of secondary nucleation is also applied to the Arrhenius-type laws for crystal growth and dissolution (Equation 33, Equation 34).

The power laws used to model the kinetics of crystal growth and secondary nucleation (Equation 28, Equation 31) can be reparameterized using a suggestion of Ratkowsky (Ratkowsky, 1989) for these types of functions. Point values are calculated for the growth rate with arbitrarily chosen supersaturations  $s_1$  and  $s_2$ . They could be the lowest and highest supersaturation values expected in the process. A value of zero would not work because of the logarithmic functions in Equation 59 and Equation 61. With these values point estimates of the rate laws for crystal growth and secondary nucleation can be calculated according to Equation 58 and Equation 60.

$$\begin{aligned} G_1 &= k_{g,pre} \cdot (s_1)^g \\ G_2 &= k_{g,pre} \cdot (s_2)^g \end{aligned} \quad \text{Equation 58}$$

$$G = G_1 \cdot (G_1 / G_2)^{\frac{\log\left(\left(\frac{c_i}{c_i^+} - 1\right) / s_1\right)}{\log\left(\frac{s_1}{s_2}\right)}} \cdot e^{\frac{-E}{R} \cdot \left(\frac{1}{T} - \frac{1}{T_{mean}}\right)} \quad \text{Equation 59}$$

$$\begin{aligned} B_1 &= k_{b,sek} \cdot (s_1)^b \\ B_2 &= k_{b,sek} \cdot (s_2)^b \end{aligned} \quad \text{Equation 60}$$

$$B_{sek} = B_1 \cdot (B_1 / B_2)^{\frac{\log\left(\left(\frac{c_i}{c_i^+} - 1\right) / s_1\right)}{\log\left(\frac{s_1}{s_2}\right)}} \cdot k_v \cdot \frac{\mu_3(t)}{V_{total}} \cdot e^{\frac{-E}{R} \cdot \left(\frac{1}{T} - \frac{1}{T_{mean}}\right)} \quad \text{Equation 61}$$

The effect of such reparameterizations is evaluated and further discussed in chapter 4.6.4.

### 3 Experimental

Experiments and analysis of the results are a major part of this thesis. They are needed to parameterize the models, validate them and to show the feasibility of the new process concepts described above.

In this chapter the basic experimental setup used for nearly all experiments and the analytical methods applied are described. A special chapter is dedicated to particle size analysis. Different methods were tried and compared to find a suitable mode of analysis that would provide the best information about the dynamics of the process. In the last subchapter typical experimental data gathered during an experimental run are shown and the reproducibility is illustrated for repeated experimental runs under comparable conditions.

#### 3.1 Model system DL-threonine/water

DL-threonine is an essential amino acid. It has importance in the food industry and as an additive to animal feed. When crystallized from water it forms a thermodynamic system of the conglomerate type. It has a rather high solubility in water (Sapoundjiev et al., 2006) while it is almost insoluble in non polar solvents. Due to the conglomerate forming nature of the system it is a candidate for a preferential crystallization process. The molecular structure of the two stereoisomers is given in Figure 19. There are two other isomers, the D- and L-allo-threonine species which lack industrial importance and which are not considered as a target product in this work.

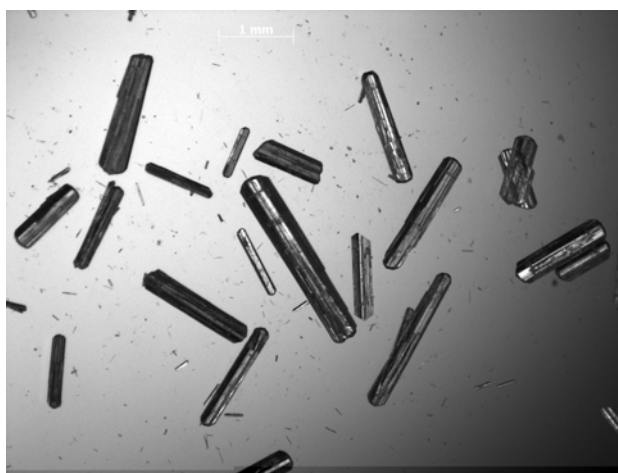


**Figure 17:** Typical DL-threonine crystals harvested from a batch experiment.

The solubilities and the shape of the ternary phase diagram are depicted in Figure 9. The system can be easily identified as of the conglomerate type (see Figure 5). The solubility data are mainly taken from (Sapoundjiev et al., 2006) supplemented by some additional data acquired at higher temperatures.

Threonine crystallizes in needle shape from water. Figure 17 shows typical threonine crystals harvested from a batch experiment. The crystals of the pure enantiomer as well as the racemic mixture are orthorhombic ( $P2_12_12_1$ ) (Janczak et al., 1997) (Shoemaker et al., 1950)). By looking at the shape of the isotherms in Figure 18 it can be seen that the system behaves almost ideal. The solubility of the racemate is nearly twice the solubility of the pure enantiomer. For the solubilities at 40°C the ratio of the solubilities of racemate and enantiomer is 1.84. The ratio for the ideal case would be two. From this analysis it can be stated that for the threonine/water-system no big influence of the counter enantiomer on the solubility of the other enantiomer is observed. The numerical values of the solubilities as well as the specification of the chemicals used can be found in the appendix (Table A 1 and Table A 3). The solid density has been measured in this work to 1.47 g/cm<sup>3</sup> (Helium pycnometer, 35 cm<sup>3</sup> cell volume).

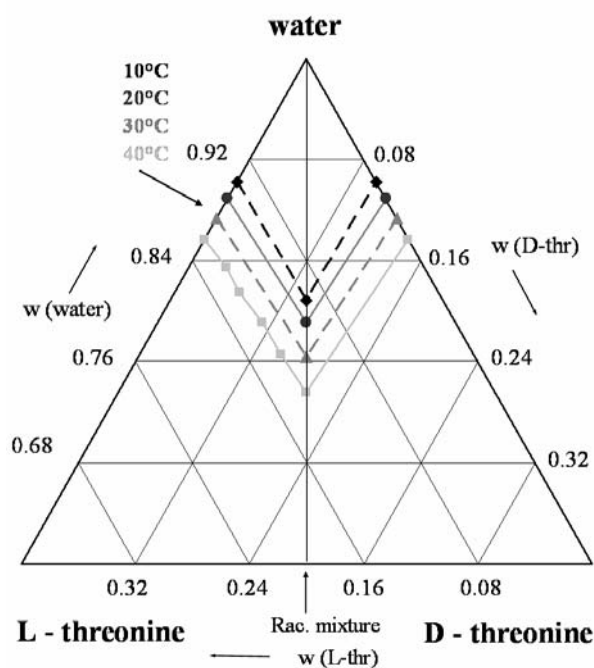


**Figure 18:** Water rich corner (50%) of the ternary phase diagram of DL-threonine/water with a selection of measured solubility isotherms (Sapoundjiev et al., 2006).

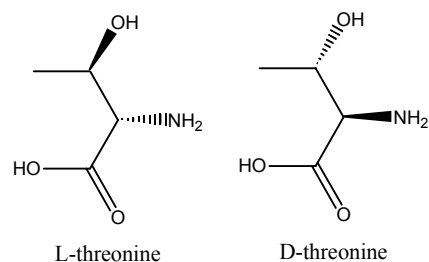


**Figure 19:** The two stereoisomers of the amino acid DL-threonine.

### 3.2 Model system R,S-mandelic acid/water

R,S-mandelic acid is a chiral aromatic alpha hydroxyl acid having two stereoisomers. It has some applications in skin care products and as treatment for urinary tract infections.

In this work it is used as a model system for enantiomer systems of the compound forming type (Jaques et al., 1994). It has a rather high solubility in water and is also soluble in most organic solvents. The molecular structure of the two stereoisomers is given in Figure 22. When crystallized from water the S-enantiomer shows a monoclinic crystalline structure whilst the racemate crystals are orthorhombic. Both crystal types are clear and plate like (see Figure 20 and Figure 21).

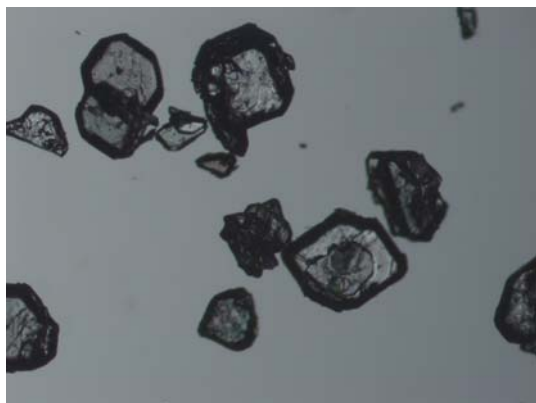


**Figure 20:** Racemate crystals of mandelic acid harvested from a batch run. The picture was taken after filtering and drying.

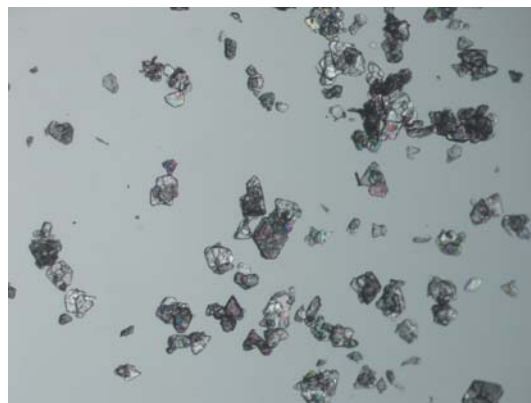


**Figure 21:** R-enantiomer crystals of mandelic acid harvested from a batch run. The picture was taken after filtering and drying.

There exist a metastable modification (Fischer & Profir, 2003; Lorenz et al., 2002; Profir & Rasmuson, 2004) of mandelic acid which is not crystallized during the experimental conditions used in this work.

The two crystalline modifications as well as the polymorph also differ in terms of other properties such as solid density etc.. A very good overview over the system properties can be found in (Perlberg, 2006).

The solubility data in water has been measured in the range of 10-40° C (Lorenz et al., 2002) and is depicted for a number of isotherms in a ternary phase diagram in Figure 23. From the phase diagram it can be seen, that the eutectic composition is nearly independent of temperature. It is fixed with a ratio of 0.31 parts of one enantiomer to 0.69 parts of the other enantiomer for both sides of the phase diagram (symmetric system). The numerical values of the solubility as well as the specification of the chemicals used can be found in the appendix (Table A 2 and Table A 4).

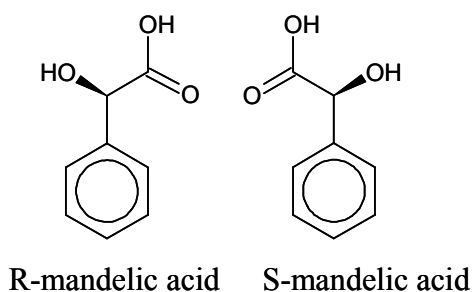


**Figure 22:** The two stereoisomers of mandelic acid.

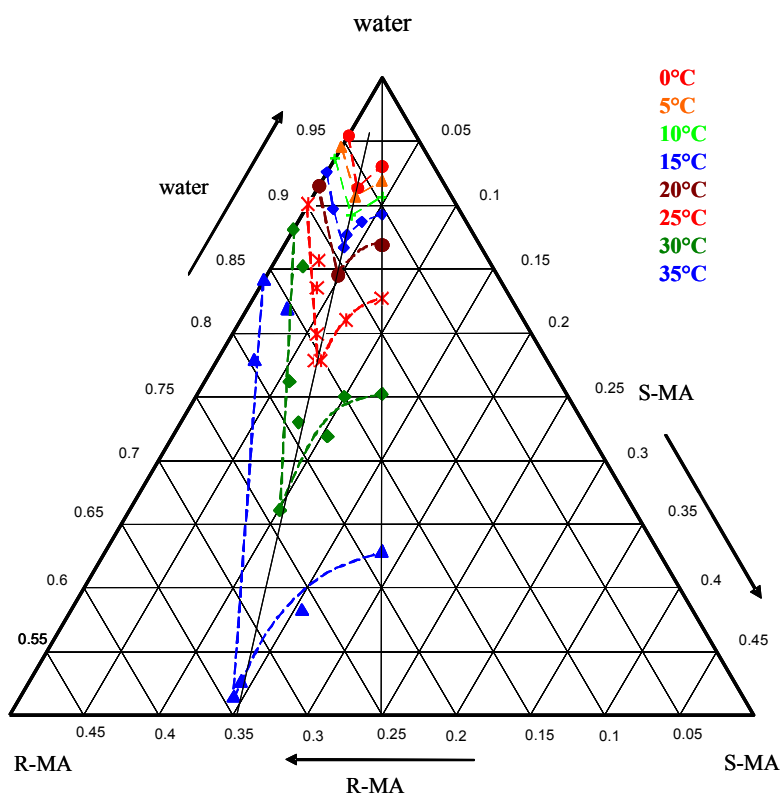


**Figure 23:** Water rich corner (50%) of the ternary phase diagram of R,S-mandelic acid/water with a selection of solubility isotherms.

### 3.3 Experimental setup

The major part of the experiments was performed in a 1.5 Liter lab scale crystallizer filled with 1 liter of solution. The details of the setup and the inline, online and offline analytical instruments used are presented in the following chapters. The basic setup has been already presented in Alvarez Rodrigo et al. (2004) and was improved as shown in Elsner et al. (2005). It was further modified to be suitable for a polythermal process mode during the experimental work for this thesis. One major change of the concept was the addition of probes to monitor the solid phase (FBRM and PVM, see below for details). The setup is depicted schematically in Figure 24.

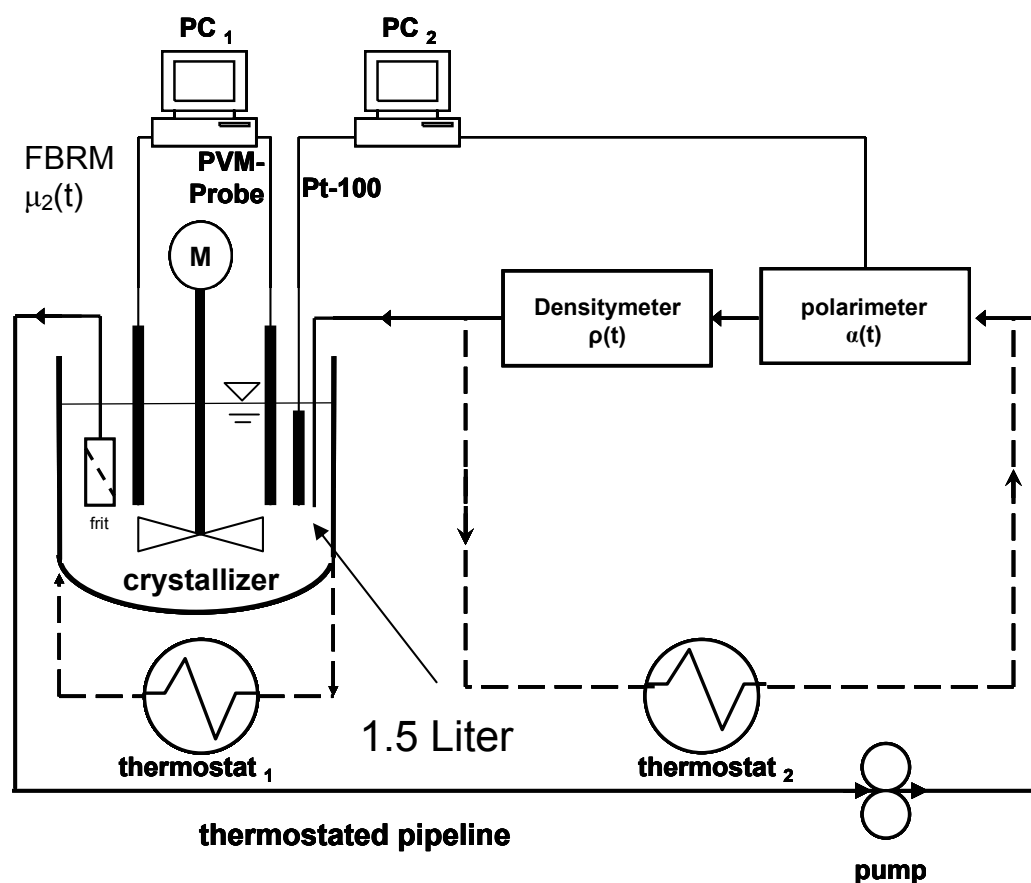


Figure 24: Experimental setup for the 1.5 liter plant.

The main part of the setup is the double walled glass vessel labeled as “crystallizer”. It is equipped with a Teflon® coated propeller stirrer (3 blades, 72mm diameter) and thermostated with the programmable thermostat<sub>1</sub> (Lauda, edition 2000). For the online analysis a solid free sample is drawn through a porous frit (0.45 $\mu\text{m}$  pore size) and

pumped with a peristaltic pump (Heidolph, 5201) through a Polarimeter (Polarmonitor, IBZ Messtechnik GmbH, Hannover, 50 mm cell) and a densitometer (DE40, Mettler-Toledo) and then back into the vessel. The insulated pipeline is thermostated with thermostat<sub>2</sub> (Julabo, F32) at 54°C for all experimental runs in the DL-threonine/water system. The volumetric flow rate of the solution in this measurement circuit was set at 10ml/min and kept constant during all experimental runs. The stirring speed was also kept constant for all experimental runs at 500 rpm.

### **3.4 Online monitoring and analytical methods**

#### **3.4.1 Fluid phase monitoring**

Here the principle of the measuring devices and the analytical methods used during the experiments will be briefly described.

##### *Density measurement*

The density of the solution is measured online using a DE40 Densitometer from Mettler-Toledo GmbH. The densitometer is of the U-tube type and can be operated with a flowing liquid if the lowest accuracy is set for the measurement. Usually the instrument is used for static density measurements. The measurement temperature was set at 50°C for all experimental runs.

##### *Polarimetry*

With a polarimeter the optical rotation of a liquid sample can be measured. Since enantiomers show an optical activity a non racemic solution containing one enantiomer in excess will result in an optical rotation. Usually the optical rotation of the light is randomly. Therefore the change after passing an enriched solution would not be detectable. If polarized light is used instead the optical rotation is changed after passing a sample containing an enantiomeric excess. The typical setup for a polarimeter is depicted schematically in Figure 25.

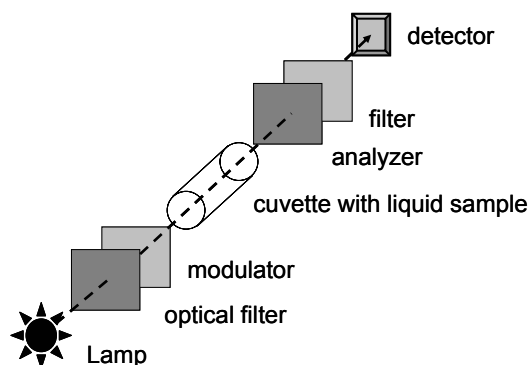


**Figure 25:** Schematic setup of a Polarimeter

Light emitted from the lamp passes the optical filter and the modulator. Afterwards it is linearly polarized. After passing the sample the optical rotation has changed. The change in the optical rotation can be detected with the analyzer. It is transferred into an electronic signal with the help of the detector. A very detailed description of polarimetry can be found e.g. in the book by Busch and Busch (2006).

### *Chiral HPLC*

For an independent method to determine the composition of a solution in terms of the L- to D- ratio chiral HPLC (High performance liquid chromatography) is used. For this a chiral stationary phase is needed in order to separate the very similar molecules. The concrete method used for the separation of DL-threonine is given in the Appendix (Table A 5). The determination of composition is based on peak area calculations.

### **3.4.2 Solid phase monitoring**

Product properties, especially size and shape, play an important role in industrial practice (Rohani et al., 2005; Yu et al., 2007) and in this thesis. Therefore a special chapter is dedicated to different methods of particle size analysis. Depending on the method and measurement principle used, different aspects of a particle characteristic length or other property can be obtained (Stieß, 1995). Bearing this in mind the knowledge of the underlying principles of each analytical method is crucial when using gathered data to feed a model. For process monitoring two inline technologies were used: A D600 L FBRM field unit from Lasentec/Mettler-Toledo GmbH and a V800 L PVM field unit also from Lasentec/Mettler-Toledo GmbH.

### *Focused Beam Reflectance Measurement (FBRM)*

The FBRM-technique is a laser based measurement technique (Monnier et al., 1996; Sparks & Dobbs, 1993). For the measurements performed a D600 L field unit was used (Diameter 19 mm, Length 406 mm). The probe is placed inside the vessel near the tip of the stirrer. The rotating laser beam is focused near the probe tip window. Whenever a particle is crossed by the rotating laser beam a reflection is generated. From the crossing time and the intensity of the reflection a Chord Length Distribution is generated. Depending on the size, shape, orientation and material properties of the solid different reflection intensities and patterns can be obtained (Ruf et al. 2000, Worlitschek 2003, (Kail et al., 2007; Kail et al., 2008a)). The relation between the measured Chord length distribution and the actual particle size distribution (PSD) is usually very complex. There are a number of publications dealing with the subject (see for example, Nandkishor 2007, Worlitschek et al. 2005, Heath et al. 2002), but a general approach for a reconstruction has not yet been found.

### *Particle Vision and Measurement*

A PVM V800 L probe was used during the experiments carried out in the 1.5 Liter vessel. The probe is placed inside the vessel near the tip of the stirrer. The device consists basically out of a high speed camera with very low shutter time taking pictures at 10 times magnification. The illumination is provided by 6 laser diodes at the probe tip circulating the probe window. The pictures taken have a resolution of 826x619 $\mu\text{m}$ . The smallest detectable particle size is 5 $\mu\text{m}$ . Depending on the particle orientation in the measurement field particles with a length up to 1032  $\mu\text{m}$  can be measured. Obviously a more realistic limitation is given by the small side of the measurement window. Based on the pictures a particle size distribution can be calculated with the help of an image analysis algorithm provided by the Software (Mettler-Toledo). The settings for the measurement of DL-threonine/water are given in the Appendix (Table A 6).

During all measurements the spherical equivalent diameter data is sorted into 100 linearly spaced channels in the range from 0 to 500  $\mu\text{m}$ . From this a  $q_0$  distribution (Stieß, 1995) of the particles is obtained.

### Microscopic image analysis

A different technique to analyze particle sizes offline is by taking microscopic pictures of a sample. Based on the pictures a particle size distribution can be generated using an appropriate software package or algorithm. For the samples investigated in this thesis a Zeiss Microscope with an attached camera is used (Zeiss Stemi 2000-C mit Axio Cam MRc). The pictures are then analyzed with the software Axio Vision 4.1 or 4.6 (Zeiss). The settings of the software are each time adapted to the appearance of the pictures so that no fixed setting can be given. However it was always taken care to provide pictures with a high contrast particle to background. From the image analysis the Feret-max and Feret-min values are taken for the particle length and width respectively. The particles are then sorted into 50 classes with varying width. Based on the probability distribution a probability density function can be calculated. Usually the  $q_0$  distribution (number based probability density) is used (Stieß 1995).

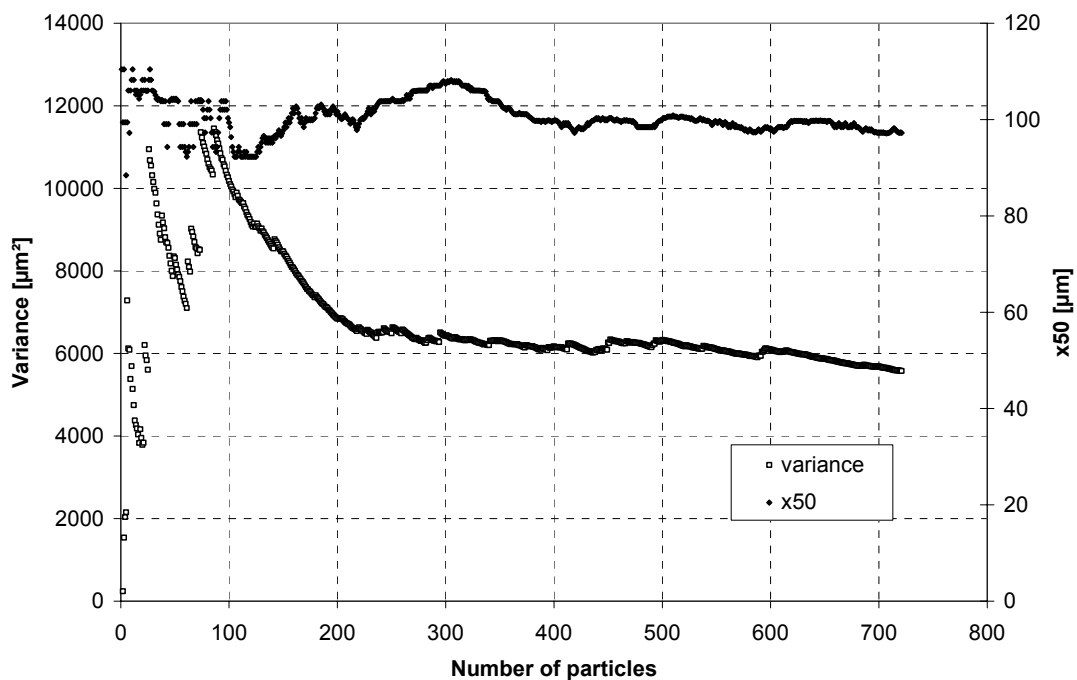


**Figure 26:** Variance and  $x_{50}$  of a sample of particles analyzed by microscopic image analysis over number of measured particles in the sample.

Figure 26 shows the effect of sample size on the mean diameter and the variance of a measured distribution. The measurement was carried out on a typical sample of threonine crystals. It can be seen that the mean diameter as well as the variance do not change significantly beyond 400 measured particles. Therefore, whenever a particle

analysis was undertaken it was taken care that the sample size was at least 400 particles.

### *Comparison of the methods for particle size analysis*

The three methods presented above are used for particle size analysis. The reason for using three more or less independent techniques is that each of the techniques has its advantages and disadvantages (Greaves et al., 2008). The microscopic measurement can only be done offline and the investigated samples have been filtered and dried before the analysis, which could alter the particle size distribution to a small extent. The FBRM technique has its own artifacts as well as the picture based algorithm for the determination of the particle size distribution that is used in the PVM measurement technique. In Figure 27 measurements for a sieved fraction (90-150 $\mu\text{m}$ ) using all three methods are displayed. It can be seen that all methods deliver different particle size distributions.

Hereby the chord length distribution of the FBRM measurement is shifted to smaller particles compared with the microscopic image analysis.

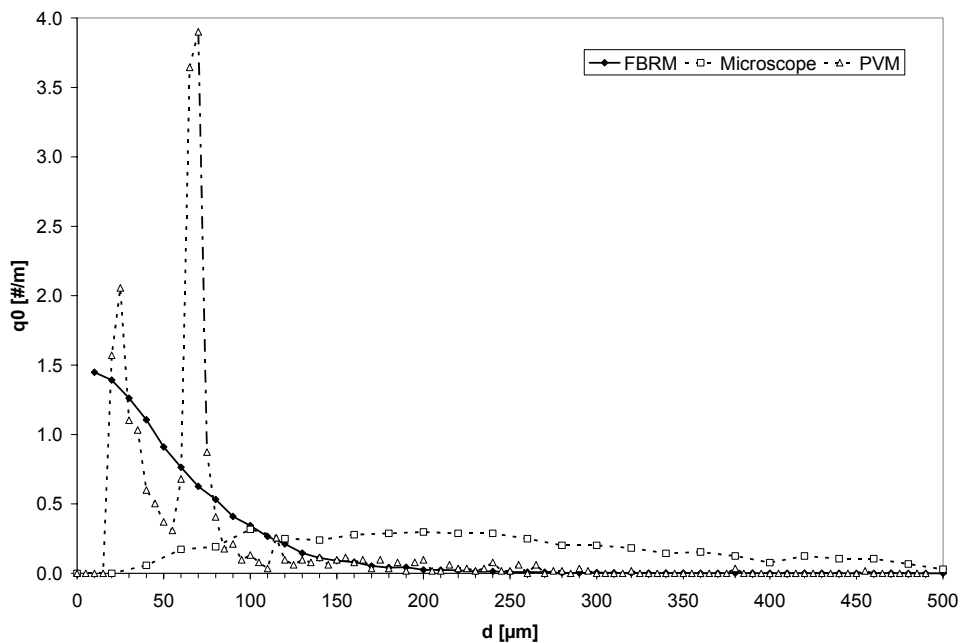


**Figure 27:** Comparison of the particle size distribution or chord length distribution respectively (number density) of the sieve fraction 90-150 $\mu\text{m}$  measured with different measurement techniques (FBRM, PVM, Microscope).

### 3.5 Experimental reproducibility

Reproducibility of experiments is a key issue in crystallization. The underlying physico chemical phenomena are quite complex. Especially when primary nucleation is involved (which is supposed to be a stochastic process) small changes in the experimental conditions can have large effects. If the data can not be reproduced, or the measurement devices are unreliable, the parameterization of kinetic models with the data obtained is futile.

Another fact is that the operation scheme of the preferential crystallization concept requires a reproducibility of single batches in order to design and run the process in a cyclic mode where individual batches are repeated many times.

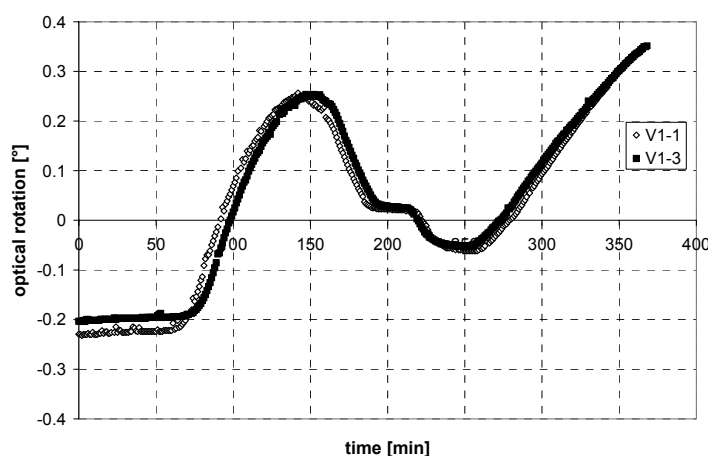


**Figure 28:** Optical rotation over time for two repeated experimental runs of the process concept “nucleation seeded” performed under the similar conditions. L-threonine is the target enantiomer.

In Figure 28 the optical rotation monitored with a Polarimeter is depicted for two experimental runs performed under very similar conditions. As it can be seen, the reproducibility is good. The same holds true for the measured particle counts (FBRM) depicted in Figure 29. Small deviations can be seen, but bearing in mind the stochastic nature of the primary nucleation, the general reproducibility is rather good.

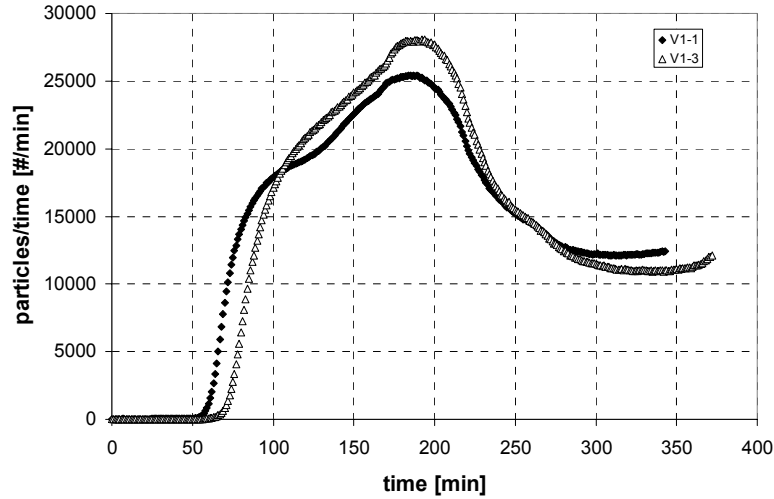


**Figure 29:** Particle counts measured by the FBRM probe over time. L-threonine is the target enantiomer of the process concept “nucleation seeded”.

In Figure 30 two complete cycles are depicted. Although the starting conditions of the four batches vary slightly no larger deviations are detectable. Therefore the general process concept of the “nucleation” strategy seems to be feasible, controllable and robust. All data depicted in the diagrams 28-33 are taken from (Klukas, 2008).

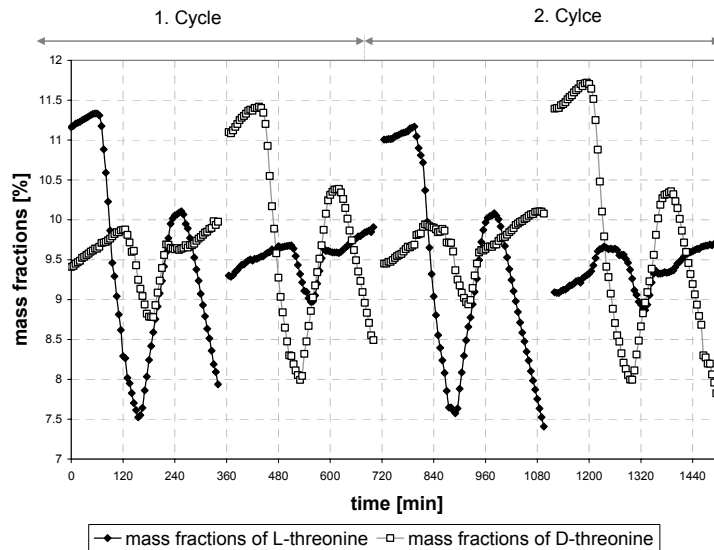


**Figure 30:** Mass fractions of consecutive cycles of the process concept “nucleation seeded” in which L-threonine and D-threonine are crystallized alternating.

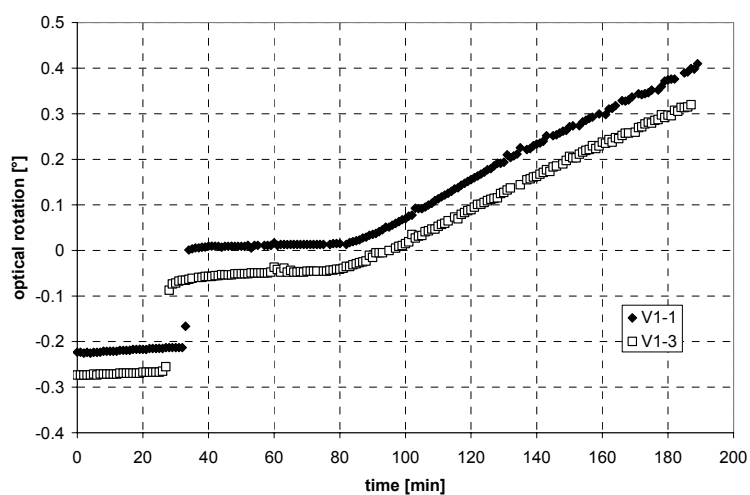


**Figure 31:** Optical rotation over time for two experimental runs of the process concept “milled seeds” performed under similar conditions. L-threonine is the target enantiomer.

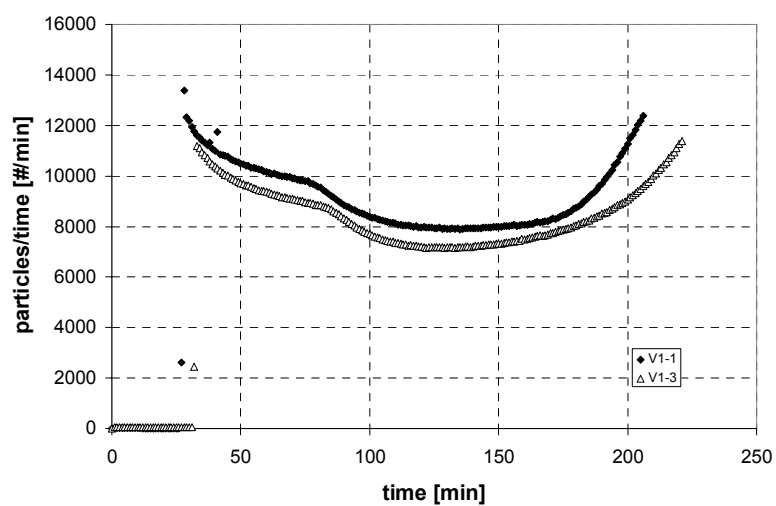


**Figure 32:** Particle counts of the process concept “milled seeds” measured by the FBRM probe over time. L-threonine is the target enantiomer.

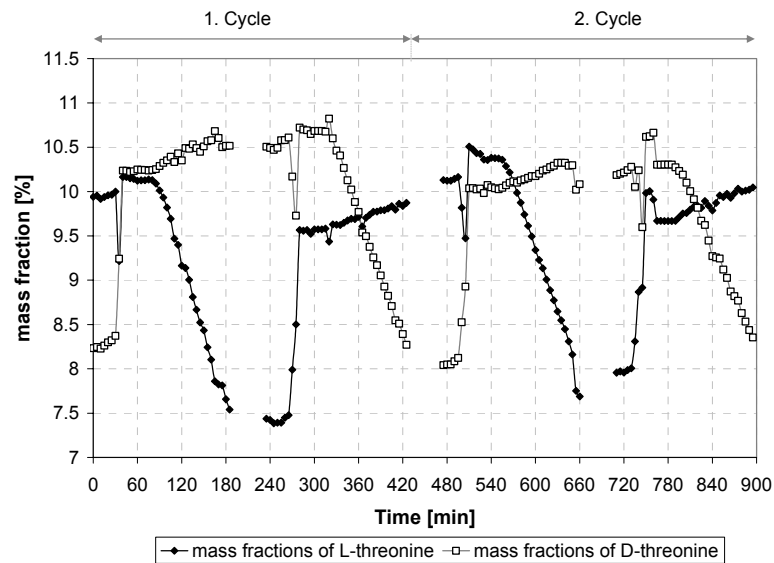


**Figure 33:** Mass fractions of sequel cycles of the process concept “milled seeds” in which L-threonine and D-threonine are crystallized respectively.

The trajectory of the optical rotation for two runs of the process concept “milled seeds” is depicted in Figure 31. The starting conditions vary slightly but still the reproducibility of these repeated runs is good. The same holds true for the particle counts measured with the FBRM-probe given in Figure 32. Two complete cycles where L- and D-threonine are harvested, are depicted in Figure 33.

To summarize, it can be said, that reproducibility for the two investigated process concepts is rather good. However, there exist clear experimental limitations regarding the measurement devices used. The effect of the experimental error will be discussed in more detail, when the reliability of estimated parameters is discussed (see chapter 4).

### 3.6 Preparation of seed crystals

The seeds for the seeded experiments are prepared separately by crystallization from a pure L-threonine solution. The crystallization is carried out as a cooling crystallization in a 500 ml double walled thermostated glass vessel. A double bladed plastic stirrer is used and ran at 150 rpm. No seeds are used for the cooling crystallization. Instead the solution is cooled down with a cooling rate of 1K/h. When the metastable zone width of the solution is crossed primary nucleation occurs and these crystals grow in the supersaturated solution. At the end of the cooling step the temperature is kept constant

for 8h in order to totally desupersaturate the solution. Then a solid-liquid separation is performed and the crystals are washed with 10ml each of ice water and ethanol. The temperature profile applied is illustrated in Figure 34. The experimental conditions for the seed preparation are summarized in Table 1.

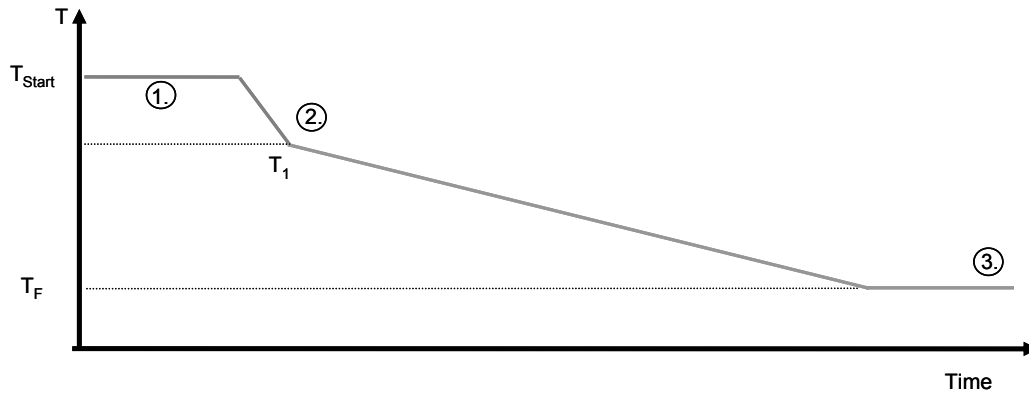


**Figure 34:** Temperature profiles for the preparation of seed material. 1. Dissolution; 2. Fast cooling to the saturation temperature; 3. Slow cooling (1K/h) to the final temperature  $T_F$ .

**Table 1:** Experimental parameters for the seed preparation.

$w_{L,0}$	stirring rate	cooling rate 2.	cooling rate 3.	$T_{Start}$	$T_1$	$T_F$	$m_{Batch}$
0.1198	150 rpm	20 K/h	1 K/h	55 °C	50 °C	10 °C	300 g

In Figure 35 the obtained particle size distributions of five repeated runs for seed preparation are shown. It can be seen that the reproducibility in terms of the particle size distribution is not very good. This was to a certain extent expected due to the stochastic nature of the primary nucleation mechanism.

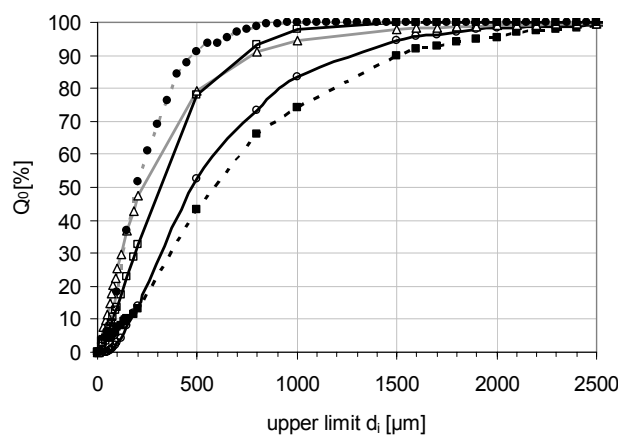


**Figure 35:** Particle size distribution of five repeated experimental runs for seed preparation.

Nevertheless in this way pure L-threonine crystals were obtained that have quite similar size distributions. The crystals could be subsequently sieved in order to narrow the particle size distribution. However, this would lead to adhering dust and surface modifications of the crystals which are also usually unwanted. Thus, no sieving was performed.

### 3.7 Summary of data sets used in further analysis

For the parameter estimation studies a data set of nine experiments was used. The experimental conditions of these experiments are summarized in Table 2. There are five experiments carried out using the variant “defined seeding” (experiments 1-4, see chapter 2.2.3 for the process concept), four experiments using the variant “nucleation seeded” (experiments 5-8, see chapter 2.2.1) and one experiment from the variant “milled seeds” (experiment 9, see chapter 2.2.2). All experiments were carried out using the experimental setup presented in chapter 3.3 or Figure 24 respectively.

**Table 2:** Experimental conditions of the experimental data set used for the parameter estimation procedure. The temperatures and cooling rates correspond with the time points given in Figure 10 and Figure 14.

Exp	$w_{L\text{-thr}}$ [g/g <sub>Lsg</sub> ]	$w_{D\text{-thr}}$ [g/g <sub>Lsg</sub> ]	$m_{\text{Seed}}$ [g]	$k_v$ [-]	$T_0$ [°C]	$(dT/dt)_1$ [K/h]	$T_1$ [°C]	$t_{\text{annealing}}$ [min]	$(dT/dt)_3$ [K/h]	$T_{\text{Final}}$ [°C]
“Defined seeding”										
1	0.1114	0.1099	5.0	0.165	30	0	30	30	-13.3	28
2	0.1219	0.1214	2.2	0.165	55	0	55	30	-16	39
3	0.097	0.0973	1.0	0.397	39	0	39	30	-1.8	25
4	0.1192	0.1205	1.4	0.047	50	0	50	30	-13	40
“Nucleation seeded”										
			$T_{\text{Start}}$ [°C]	$(dT/dt)_0$ [K/h]						
5	0.1173	0.0993	55	-23.3	4	28	39	30	-15	4
6	0.1128	0.0946	55	-23.3	4	28	39	30	-20	4
7	0.1128	0.0946	55	-23.3	4	28	39	30	-25	4
8	0.1116	0.094	55	-23.3	4	28	39	30	-	-
“Milled seeds”										
9	0.0974	0.0794	55	-	-	-28	39	30	-20	4

## 4 Results and discussion

To test the presented process model (chapters 2.1.5 and 2.2.4) and the mathematical tools for the parameter estimation and analysis of the results (chapter 2.3) a suitable chemical model system had to be chosen. The essential amino acid system DL-threonine/water was selected as a model system for the different process concepts of preferential crystallization (chapter 3.1). The main reasons for choosing the system are its non toxicity, the conglomerate forming nature of the system, the rather high solubility in water and the ease of crystallization (see (Elsner et al., 2005) for an example of preliminary research).

As a simple alternative to the rather detailed dynamic model also a short-cut process evaluation approach is introduced in chapter 4.4 for the conglomerate forming system DL-threonine as well as for the compound forming system R,S-mandelic acid.

### 4.1 Calibration of polarimeter and densitometer

To be of use for quantitative process monitoring the online analytics have to be calibrated and tested within the range of relevant process conditions. For the polarimeter and the densitometer this is obvious since the mass fractions of the two molecular species have to be calculated from these combined signals, according to equations 62-64. Hereby Equation 62 defines mass fractions. Equations 63-64 illustrate how the mass fractions can be calculated based on the measured liquid density and optical rotation signals (Alvarez et al. 2004).

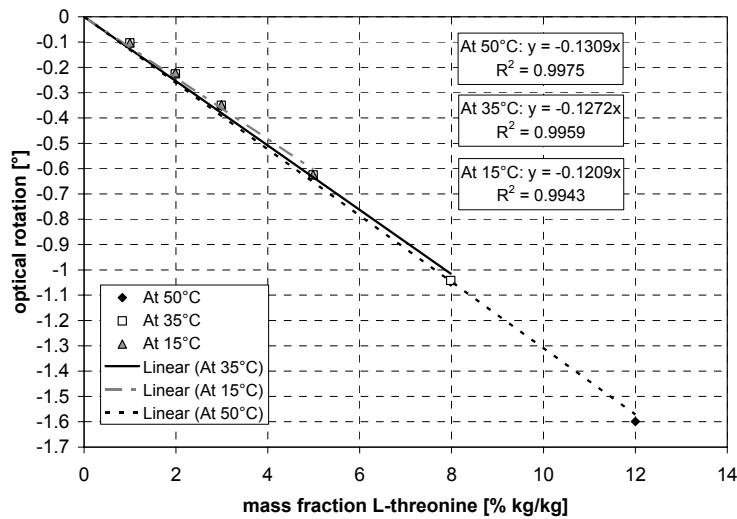
$$w_i = \frac{m_i}{m_i + m_{i\pm 1} + m_w} \quad \text{Equation 62}$$

$$w_i = \frac{1}{2} \left( \frac{\rho(t) - \rho_0}{k_\rho} - \frac{\alpha(t)}{k_{pol}} \right) \quad \text{Equation 63}$$

$$w_{i\pm 1} = \frac{1}{2} \left( \frac{\rho(t) - \rho_0}{k_\rho} + \frac{\alpha(t)}{k_{pol}} \right) \quad \text{Equation 64}$$

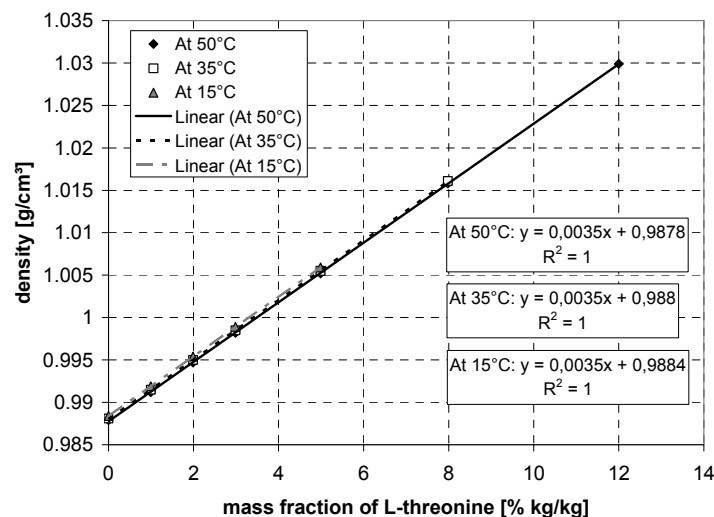
During calibration the parameters  $\rho_0$ ,  $k_\rho$  and  $k_{pol}$  have to be determined. The corresponding correlations for the optical rotation and the liquid density are given in Figure 36 and Figure 37. The setup for the calibration is the apparatus depicted in

Figure 24. The measurement points were obtained by step wise addition of L-threonine to the vessel.



**Figure 36:** Measurements and correlation trend lines for the polarimeter signal (optical rotation) taken at three different vessel temperatures. The polarimeter itself was thermostated at 54°C for all measurements.

The corresponding density of the samples and correlations can be found in Figure 37. Since no significant changes of the calibration correlations due to changes in the vessel temperature occurred it was possible to use one calibration function for samples drawn from the vessel at different temperatures. For all experiments the correlations obtained at 50°C vessel temperature were used.



**Figure 37:** Calibration of the densitometer at three different vessel temperatures. The measurement temperature of the internal cell was set to 50°C.

## 4.2 FBRM-probe calibration

In this work it was assumed that the moments of the chord length distribution (CLD) are related to moments of the PSD measured with image analysis of microscopic pictures. During all measurements the CLD data are sorted into 90 logarithmic channels in the range from 1 to 1000  $\mu\text{m}$ . Experiments were carried out in order to “calibrate” the probe (Vaccaro et al., 2007; Wynn, 2003). A goal of this calibration procedure was to find a correlation between CLD-moments and the real moments of a particle size distribution for the model system DL-threonine. To find this calibration three experiments have been carried out. The experiments were done in the same 1.5 liter vessel used for the crystallization experiments. Instead of using a DL-threonine solution sieved fractions of L-threonine crystals were suspended in ethanol. DL-threonine is almost insoluble in ethanol. This way crystallization phenomena such as crystal growth, dissolution, ripening and nucleation which might alter the particle size distribution are prevented. The stirring rate was set to 500 rpm for all experiments. The sieve fractions used were 63-90 $\mu\text{m}$ , 90-150 $\mu\text{m}$  and 150-212 $\mu\text{m}$ . The particle size distribution of these three fractions obtained with microscopic image analysis are given in Figure 38.

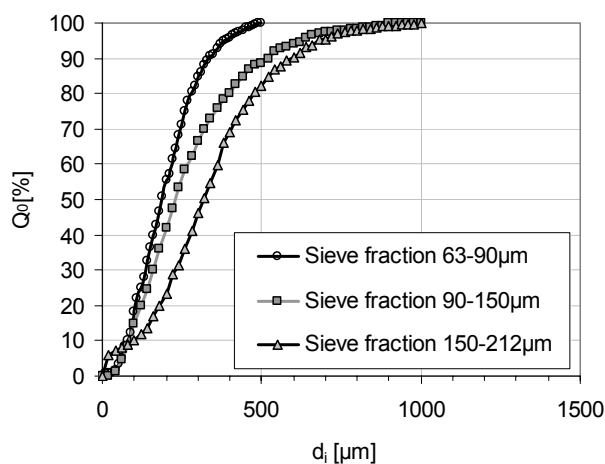


**Figure 38:** Particle size distributions obtained from microscopic image analysis of the three sieve fractions used for the “calibration” of the FBRM-probe.

The crystals of each of the sieve fractions were added in portions of approximately 5g to the vessel. The exact amounts added are given in Table 3.

**Table 3:** Masses of ethanol and crystals used in the three experiments.

Versuch	Ethanol [g]	Zugabe 1 [g]	Zugabe 2 [g]	Zugabe 3 [g]
1	750	5.01	5	5.02
2	750.15	5.01	5.01	5
3	750	5	5.01	5.02

In the stirred vessel the chord length distribution was measured by a FBRM-probe. Additionally a sample of each of the sieve fractions was sized using microscopic image analysis. The moments obtained by the two analytical techniques were compared assuming a direct proportionality of the moments according to Equation 65 and Equation 66:

$$\mu_{0, \text{Microscope}, \text{Exp1}} = A \cdot \mu_{0, \text{FBRM}, \text{Exp1}} = B \cdot \mu_{1, \text{FBRM}, \text{Exp1}} = C \cdot \mu_{2, \text{FBRM}, \text{Exp1}} = D \cdot \mu_{3, \text{FBRM}, \text{Exp1}} \quad \text{Equation 65}$$

$$\mu_{0, \text{Microscope}, \text{Exp2}} = E \cdot \mu_{0, \text{FBRM}, \text{Exp2}} = F \cdot \mu_{1, \text{FBRM}, \text{Exp2}} = G \cdot \mu_{2, \text{FBRM}, \text{Exp2}} = H \cdot \mu_{3, \text{FBRM}, \text{Exp2}} \quad \text{Equation 66}$$

$$\frac{\mu_{i, \text{Microscope}, \text{Exp1}}}{\mu_{i, \text{Microscope}, \text{Exp2}}} = \frac{\mu_{a, \text{FBRM}, \text{Exp1}}}{\mu_{a, \text{FBRM}, \text{Exp2}}} \quad \text{Equation 67}$$

To verify the proportionality Equation 67 has to be fulfilled. In order to check the assumed proportionality the scaled moments from the zeroth to the third moment are displayed along with the scaled moment obtained from the microscopic image analysis for the three investigated sieve fractions (Figure 39 to Figure 41). The scaling of the different moments was done by dividing the value of a measurement through the maximum of that moment.

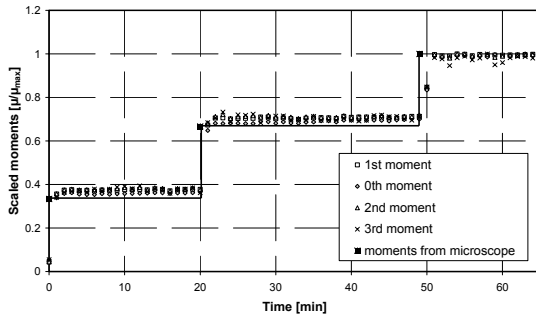


**Figure 39:** Scaled zeroth to third moment of the chord length distribution measured by a FBRM-probe compared with the scaled moments measured by an optical microscope and image analysis of the sieve fraction 63-90µm.

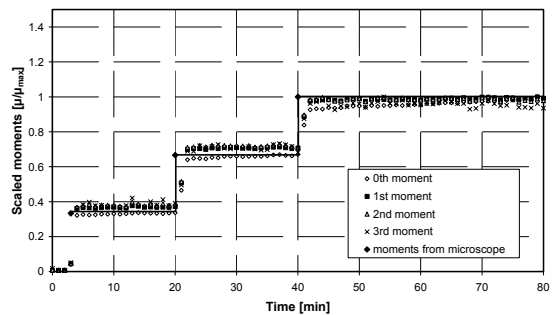


**Figure 40:** Scaled zeroth to third moment of the chord length distribution measured by a FBRM-probe compared with the scaled moments measured by an optical microscope and image analysis of the sieve fraction 90-150µm.

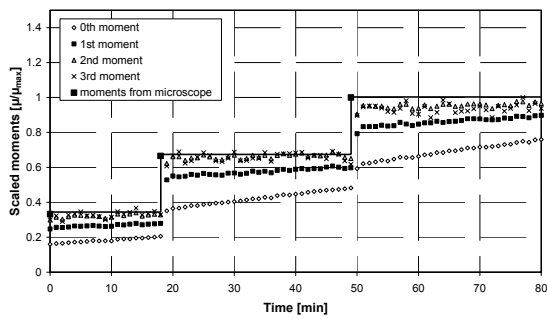


**Figure 41:** Scaled zeroth to third moment of the chord length distribution measured by a FBRM-probe compared with the scaled moments measured by an optical microscope and image analysis of the sieve fraction 150-212 $\mu\text{m}$ .

Accordingly the moments scale proportional to the added amount of seeds (5-15g). The chord length based moments scale proportional to the moments measured by the automated image analysis. Only for the largest sieve fraction (150-212 $\mu\text{m}$ ) significant deviations for the zeroth moment can be seen. This might result from breakage of these larger crystals due to the heavy stirring in the vessel.

When Equation 67 is evaluated for all measurements and all moments the results given in Table A 10 to Table A 12 (Appendix) are obtained.

Numerical values of the measured moments that are the basis for the analysis can be found in Table A 7 to Table A 8 (Appendix).

From the analysis one can see, that the direct proportionality is only satisfied between the second moment of the microscopic image analysis and the zeroth moment of the chord length distribution measured by the probe. An explanation for this finding could be the fact that the laser beam is rotating in a plane. Thus, a particle will produce a reflection proportional to its sectional area in that plane. Therefore the obtained proportionality of the FBRM counts to the second moment of the distribution might have its roots. A perfect proportionality could not be obtained. It is assumed that the deviations essentially result from model errors. The proposed direct proportionality (Equation 67) will be used when parameters for the dynamic models have to be estimated (see chapter 4.6).

## 4.3 Solubility and metastable zone width

### 4.3.1 DL-threonine/water

The essential basis for a reliable modeling and design of a preferential crystallization process is the knowledge of the solubility of the two enantiomers in the solvent of choice depending on composition.

Here a simple approach based on an activity coefficient model and the Schröder van Laar equation (Jaques et al., 1994) is applied to the system DL-threonine/water (see chapter 2.1.4). It has to be differentiated between the two- and the three-phase regions (Indices II and III) and the two crystallizing species (Index  $r=1,2$ ). The basic equations to model the solubility in the two-phase region are given in Equation 68 for the two-phase region (pure enantiomer and solvent) and in Equation 69 for the three-phase region (both enantiomers and solvent):

$$w_{sat,1,II} = \frac{1}{\gamma_{1,II}} \cdot \left( \exp \left[ \frac{\Delta h_{m,II}^0}{R} \cdot \left( \frac{1}{T_{m,II}} - \frac{1}{T} \right) \right] \right) \quad \text{Equation 68}$$

In Equation 68  $\gamma_{1,II} = f(x_2)$  is modelled very similar as in the one constant Margules equation (see for example (Prausnitz et al., 1986)):

$$\gamma_{1,II} = \exp \left( \frac{\varphi \cdot \frac{m_2}{(m_2 + m_{water})}}{RT} \right) \quad \text{Equation 69}$$

The solubility of the racemic composition is modelled in a similar fashion, except that here in order to keep the model simple, it is assumed that  $\gamma_{rac} = constant$ . Using a temperature dependent activity coefficient similar to the one formulated in Equation 69 did not significantly improve the representation of the measured data.

$$w_{sat,rac,III} = \frac{1}{\gamma_{rac}} \cdot \left( \exp \left[ \frac{\Delta h_{m,rac}^0}{R} \cdot \left( \frac{1}{T_{m,rac}} - \frac{1}{T} \right) \right] \right) \quad \text{Equation 70}$$

Obviously the solubility of a single enantiomer in the three phase region is then half this solubility (Equation 71).

$$w_{sat,1,2,III} = 0.5 \cdot w_{sat,rac,III} \quad \text{Equation 71}$$

A plot of the measured data and calculations performed with the presented model equations are given below in Figure 42 for the two phase region of the phase diagram

and in Figure 43 for the eutectic composition. In case of the conglomerate forming system DL-threonine that is the racemate. As it can be seen the model is capable of describing the solubility measurements with relative small deviations.

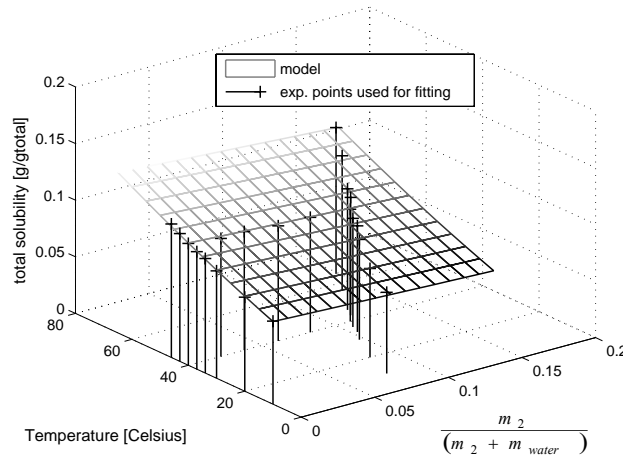


**Figure 42:** Solubility of DL-threonine/water in the two phase region. (+) are measured data points. The grid represents the model calculations.

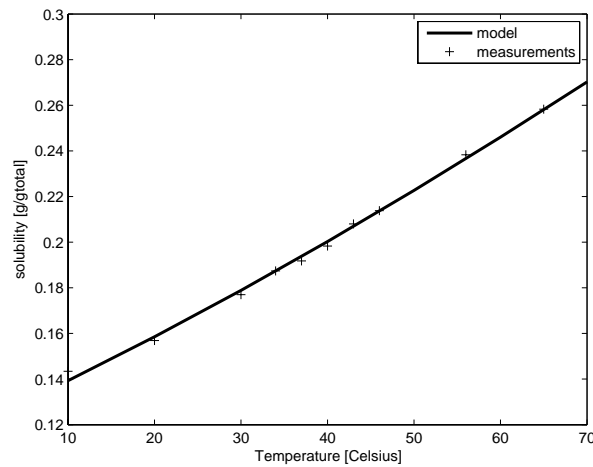


**Figure 43:** Eutectic solubility as function of temperature. (+) are the measured data points. The solid line represents the model calculations.

Additionally, in order to model the preferential crystallisation process, a mathematical representation of the not well defined metastable solubility inside the three phase region is needed. The metastable solubility is the limit of the attainable entrainment in the three phase region as illustrated in Figure 44. The metastable solubility mass fractions of each enantiomer are calculated using Equation 72 and Equation 73 respectively.

$$w_{sat,1,III} = \frac{m_{1,eq}}{m_{1,eq} + \underbrace{m_2 + m_{water}}_{\text{"solvent"}}}$$

**Equation 72**

$$w_{sat,2,III} = \frac{m_{2,eq}}{m_{2,eq} + \underbrace{m_1 + m_{water}}_{\text{"solvent"}}}$$

**Equation 73**

Herein  $m_{r,eq}$  is the equilibrium solubility mass of a single species at the eutectic composition at a defined temperature (resulting from Equation 71).  $m_{r\pm 1}$  is the mass of the counter species that is assumed to be constant as long as a perfectly selective preferential crystallization can be realized. The principle of the chosen modeling approach is further illustrated in Figure 44.

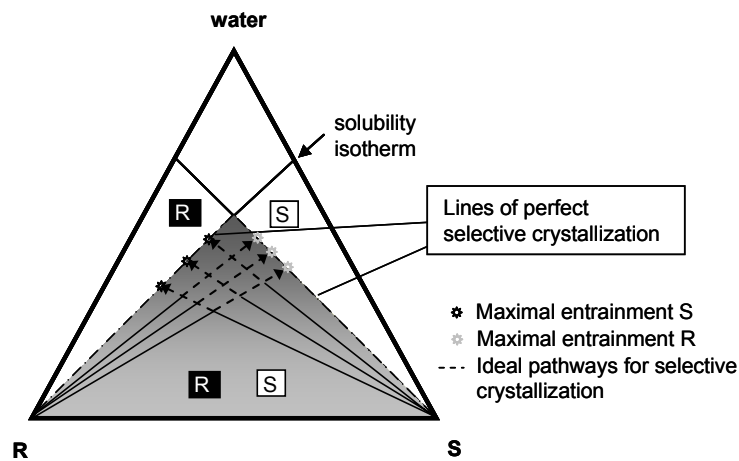


**Figure 44:** Illustration of the chosen metastable solubility model inside the three phase region of a conglomerate forming system (for example DL-threonine/water).

Following lines of “perfect selective crystallization” the solubility of the preferentially crystallizing species is also constant. The “solvent” is in this case the actual solvent (water) plus the counter enantiomer present in the liquid phase. If the second species also crystallizes the metastable solubilities will change, since the solvent composition changes due to the decrease of the liquid phase mass of the counter enantiomer. This way the metastable solubility eventually ends up at the equilibrium solubility of the eutectic (Equation 70) which is usually the end of a preferential crystallization run that is not stopped via a solid liquid separation. This way the presented model is capable of describing the actual system behavior that is observed experimentally. The model presented can be also found in (Czapla et al., 2008c).

A correlation to calculate the measured metastable zone width of the system DL-threonine/water is formulated by a linear regression of experimental data (Lorenz et al., 2006b) as given in Equation 74. The metastable zone width given in Equation 74 has been determined in a previous work (Polenske, 2003) based on turbidity measurements using the polythermal method from Nyvilt (Garside et al., 2002) for nucleation of the racemate (DL-threonine) in the presence of 0.01 (g/300g solution) of L-threonine crystals. The experimental setup should reflect the situation in the process where a nucleation of the unwanted enantiomer or racemate respectively in the presence of crystals of the target enantiomer should be avoided (secondary nucleation).

$$MSZW[K] = -0.205 \cdot T[^\circ C] + 0.971 \cdot \frac{dT}{dt}[K/h] + 13[K] \quad \text{Equation 74}$$

The correlation given in Equation 74 consists of two parts accounting for the influence of solution temperature and cooling rate. The influences of the two factors have been determined separately and then composed into one empirical linear correlation function. The influence of the cooling rate has been determined by varying the cooling rate at a constant initial concentration (2.5 K/h, 5 K/h and 10 K/h at 40°C). The influence of the concentration has been determined by an extrapolation of the subcooling to a cooling rate of 0 K/h for five different saturation temperatures (34, 37, 40, 43, 46 °C). The resulting metastable solubility curves can be found in (Lorenz et al., 2006a).

The free estimated parameters to be used in the different solubility models for the different compositions/species are given in Table B 1 (Appendix).

### **4.3.2 *R,S-mandelic acid/water***

The solubility data used as a basis for process evaluation for the system R,S-mandelic acid/water has been taken from literature (Lorenz et al., 2002). The system is of the compound forming type (Jaques et al., 1994), what means that three different crystalline species exist in different regions of the phase diagram: Racemate, R- and S-crystals. The racemate contains molecules of both enantiomers in a one to one ratio whereas the enantiomer crystals contain only molecules of one optical modification.

In order to use the evaluation approach to be presented the solubility in the ternary system should be modeled with simple thermodynamic correlation functions based on

the Schröder van Laar equation (Jaques et al., 1994). In the case of the system studied and the simplified process design procedure the solubility of three selected parts/points of the phase diagram are needed as a function of temperature and composition (two-phase region):

- a) The solubility at the eutectic composition
- b) The solubility of the racemate
- c) The solubility in the two-phase region (pure enantiomer)

The model has been described in detail in (Czapla et al., 2008c). The correlation function valid for calculating the solubility in the two-phase region is given in Equation 75.

$$w_{sat,1,II} = \frac{1}{\gamma_{1,II}} \cdot \left( \exp \left[ \frac{\Delta h_{m,II}}{R} \cdot \left( \frac{1}{T_{m,II}} - \frac{1}{T} \right) \right] \right) \quad \text{Equation 75}$$

Wherein  $\gamma_{1,II} = f(m_2)$  is modelled very similar to the approach of the one constant Margules equation (Prausnitz et al., 1986) as:

$$\gamma_{1,II} = \exp \left( \frac{\varphi \cdot \frac{m_2}{(m_2 + m_{water})}}{RT} \right) \quad \text{Equation 76}$$

The solubilities of the racemate and the eutectic composition are modeled as presented in Equation 77 and Equation 78:

$$w_{sat,rac} = \frac{1}{\gamma_{rac}} \cdot \left( \exp \left[ \frac{\Delta h_{m,rac}}{R} \cdot \left( \frac{1}{T_{m,rac}} - \frac{1}{T} \right) \right] \right) \quad \text{Equation 77}$$

$$w_{sat,eut} = \frac{1}{\gamma_{eut}} \cdot \left( \exp \left[ \frac{\Delta h_{m,eut}}{R} \cdot \left( \frac{1}{T_{m,eut}} - \frac{1}{T} \right) \right] \right) \quad \text{Equation 78}$$

In contrast to the aforementioned approach here it is assumed that the activity coefficient  $\gamma$  is constant. Using a temperature dependent activity coefficient similar to the one formulated in Equation 76 did not significantly improve the representation of the measured data. The free parameters  $\gamma$ ,  $T_m$ ,  $\varphi$  and  $\Delta h_m$  have been adjusted using a suitable optimisation scheme (fminsearchbnd.m, Nelder-mead Simplex (Lagarias et al., 1998)) in order to represent the measured data points. The results of the fittings

are shown in Figure 45 (racemate), Figure 46 (eutectic composition) and Figure 47 (two-phase region).

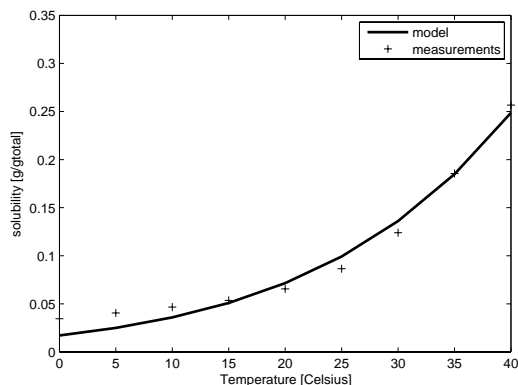


**Figure 45:** Measured and calculated solubility for the racemate of mandelic acid in water.

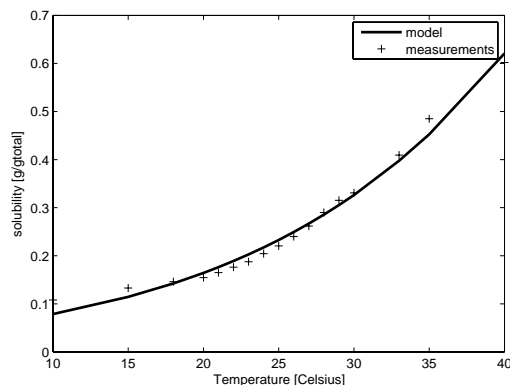


**Figure 46:** Measured and calculated solubility for the eutectic composition of mandelic acid in water.

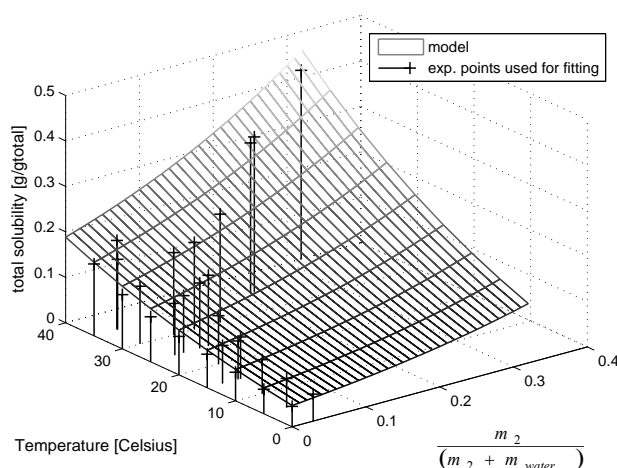


**Figure 47:** Measured and calculated solubility of mandelic acid in the two-phase region of the phase diagram as a function of solvent composition (fraction of the counter enantiomer with respect to the liquid phase mass) and temperature (Czapla et al., 2008c).

It should be noted, that the eutectic composition is assumed to be temperature independent with a fixed ratio of 0.69 to 0.31 parts of the enantiomers respectively. As can be seen the chosen model equations are able to represent the measured data quite accurately within the temperature range of interest (10-40°C).

The free estimated parameters to be used in the different solubility models for the different composition/species are given in Table B 2 (Appendix) again based on Nyvilt's method.

In order to support a dynamic process model (e.g. population balance model) again metastable solubilities of the two crystallizing species are needed. In contrast to the

aforementioned conglomerate forming system here the two species are the racemate and the pure enantiomer. Keeping this in mind the equations presented above (Equation 72 and 72) can also be used to calculate metastable solubilities for compound forming systems. In this case the index 1 labels the enantiomer whereas the index 2 labels the crystalline racemate.

The approach to model the metastable solubility is illustrated for a compound forming system in Figure 48. However, in this work no dynamic model is applied to crystallization processes in compound forming systems. Nevertheless the presented approach for the metastable solubility could be used inside a dynamic process model for compound forming systems.

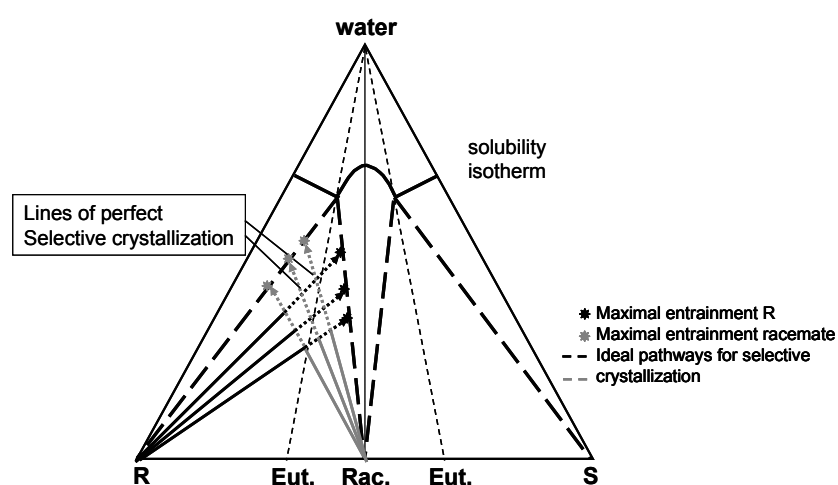


**Figure 48:** Illustration of the chosen metastable solubility model inside the three phase region of a compound forming system (for example R,S-mandelic acid).

The metastable zone width for primary as well as secondary nucleation has been determined as for threonine based on turbidity measurements using the polythermal method from Nyvilt (Garside et al., 2002) (Lorenz et al., 2006a; Perlberg, 2006).

The experimental setup should reflect the situation in the process where a nucleation of the unwanted enantiomer or racemate respectively in the presence of crystals of the target enantiomer/racemate should be avoided (secondary nucleation). For the cooling from a clear solution at  $T_{Start}$  (1) and  $T_l$  (5) a correlation for the primary heterogeneous nucleation is used (Perlberg, 2006).

$$MSZW_{prim} = 0.5155 \cdot T_{annealing} + 0.0526 \cdot \dot{T} - 3.3K \quad \text{Equation 79}$$

$$MSZW_{sec} = -0.3015 \cdot T_{annealing} + 0.2003 \cdot \dot{T} + 12.5K \quad \text{Equation 80}$$

The correlations given in Equation 79 and Equation 80 consist of two parts accounting for the influence of solution temperature and cooling rate. The influences of the two factors have been determined separately and then composed to one linear correlation function. The influence of the cooling rate has been determined by varying it at different initial concentrations and three compositions (pure enantiomer, racemate, eutectic) (1 K/h (eutectic only), 2.5 K/h, 5 K/h, 7.5 K/h (racemate only) and 10 K/h). The influence of the concentration has been determined by an extrapolation of the subcooling to a cooling rate of 0 K/h for up to five different saturation temperatures (15 (racemate only), 20, 25 (racemate only), 35 (racemate only) and 40 °C). The resulting metastable solubility curves can be found in (Lorenz et al., 2006a) or (Perlberg, 2006).

When the metastable zone width has been determined the end times of the crystallization runs can be calculated for a fixed cooling rate (see chapter 4.4.4).

#### **4.4 Short-cut process evaluation**

For the engineer faced with the task to evaluate or design a preferential crystallization process it is at the start often not possible to parameterize and use a kinetic process model without deep knowledge about the system to study or a set of initial experiments to rely on. Even when experiments are performed the estimation of the involved kinetic parameters is often difficult and needs expert knowledge (Elsner et al., 2005; Heinrich, 2008; Wang & Ching, 2006).

Generally the limit for the yield of a preferential crystallization process is the metastable boundary of the unwanted species (the counter enantiomer in case of DL-threonine/water and the racemate or enantiomer in case of R,S-mandelic acid) that is usually a function of cooling rate and saturation temperature or solubility mass fraction respectively.

However, if only solubility data for the system studied are available a simple and short approach for process evaluation can be undertaken. If the starting and end temperature as well as the fluid phase composition are chosen the maximal yield of a hypothetical process can be calculated based on a simple mass balance. A similar approach has been introduced by (Kaspereit, 2006), (Perlberg et al., 2005), (Chen et al., 2008) and (Wang & Chen, 2008) for crystallization processes in the two phase region of ternary systems. Here the approach is extended to an application on preferential crystallization that takes place inside the three phase region.

If additionally metastable zone width measurements for the unwanted species in the three phase region are provided the predictive power of the evaluation approach is enhanced. In this second approach the starting temperature and the cooling rate have to be chosen. With these inputs the metastable limit of the unwanted species can be calculated. The resulting metastable limit defines the endpoint of the process. Using the value of the cooling rate besides the process yield also process productivities can be calculated. The two approaches are outlined schematically in Figure 49.

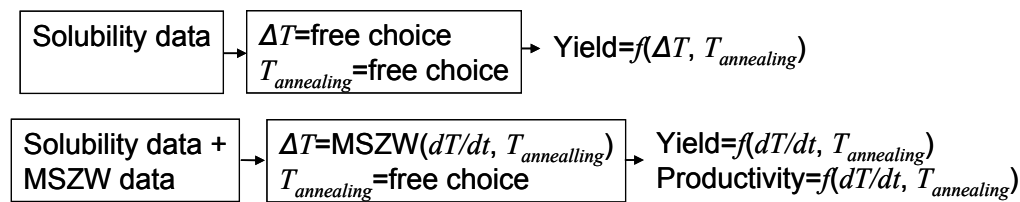


**Figure 49:** Illustration of the course of the two principle process evaluation approaches presented.

If the input values are varied, regions of potential high yield and/or productivity can be identified before actual separation runs are performed. The two different approaches are exemplified in the following subchapters using the two systems DL-threonine/water and R,S-mandelic acid/water. For illustration purposes species masses have been chosen according to Table 4.

**Table 4:** Masses of the two species that are used to illustrate the process short-cut evaluation approach for the two process runs.

System type	$m_{L(R),Start}$ [kg]	$m_{D(S),Start}$ [kg]	$m_{water, Start}$ [kg]
conglomerate (DL-threonine)	0.12	0.1	0.78
compound (R,S-mandelic acid)	0.16	0.06	0.78

#### 4.4.1 Equilibrium analysis DL-threonine

The presented selection on crystallization processes (chapter 2.2) can be evaluated in a first approach assuming that during each process step the thermodynamic equilibrium is reached. Based on this assumption and available solubility data below a short-cut procedure is developed for a first evaluation of a preferential crystallization with respect to achievable yield. If the starting and end temperature and fluid phase composition are chosen the maximal yield can be calculated based on a simple mass balance. The course of the evaluation procedures will be illustrated in the following

on the example of the “nucleation seeded” process concept of the AS3PC process (see chapter 2.2.1).

The procedure for process evaluation is illustrated on an arbitrarily chosen numeric example (starting masses normalized to 1 kg ( $m_L$ ,  $m_D$ ,  $m_{water}$ ), Table 4) in the following. A graphical representation of the simulated run is given in Figure 50.

A constraint for the process is that in order to be run in cyclic operation mode the final enantiomeric excess in the mother liquor should be equal to the initial enantiomeric excess on a mass basis. Additionally, it is assumed that the mass of water stays constant during the whole process. Therefore the amount of crystalline material harvested at the end of a batch has to be exactly double of the mass of the initial enantiomeric excess in order to be replaced by an addition of racemate. These constraints are formulated in Equation 81:

$$\begin{aligned} m_{L,end} &= m_{L,Start} - m_{ee,Start} \\ m_{D,end} &= m_{D,Start} \\ m_{water} &= m_{water,Start} \end{aligned} \quad \text{Equation 81}$$

In this way it is guaranteed that, with an addition of exactly twice the mass of the initial enantiomeric excess as racemic mixture, the process can be started in the same fashion, now crystallizing the other enantiomer. The mass fractions can be calculated as illustrated in Equation 82:

$$w_i = \frac{m_i}{(m_i + m_{i+1} + m_{water})} \quad \text{Equation 82}$$

The initial mass fraction of the target enantiomer is inserted into Equation 83 in order to calculate the starting temperature of the process based on the solubility correlation (Equation 78) plus a security limit of 1 Kelvin to ensure total dissolution in a reasonable time and to compensate for uncertainties in the solubility estimation.

$$T_{Start} = \frac{-\Delta h_{m,eut}}{\ln(2 \cdot w_{L,Start} \cdot \gamma) - \frac{\Delta h_{m,eut}}{R \cdot T_m}} + 1 \quad \text{Equation 83}$$

As already stated in chapter 4.3.1, the enthalpy  $\Delta h_m$  and temperature of melting  $T_m$  needed to apply the equation, were estimated based on fitting Equation 78 to experimental solubility data (see chapter 4.3.1).

Equation 84 illustrates how the annealing temperature can be calculated in the same manner by inserting into the solubility correlation the corresponding liquid phase mass fractions of both species (racemate) present at the annealing temperature. Here

an ideal situation is assumed where the complete initial excess of the target enantiomer has crystallized (corresponding to point (5) in Figure 9) providing the seed material for the following cooling crystallization. Again, to compensate for uncertainties, a security limit of 1 Kelvin is added to the annealing temperature.

$$T_{annealing} = \frac{-\Delta h_{m,eut}}{\ln(2 \cdot w_{L,annealing} \cdot \gamma) - \frac{\Delta h_{m,eut}}{R \cdot T_m}} + 1 \quad \text{Equation 84}$$

$$w_{annealing} = \frac{2 \cdot m_{D,Start}}{(2 \cdot m_{D,Start} + m_{water})} \quad \text{Equation 85}$$

In Equation 86 the end temperature of the process is calculated based on the assumption of a symmetric process that reaches the defined end masses specified in Equation 87 ( $T_{Final}$  in Figure 9).

$$T_{Final} = \frac{-\Delta h_{m,eut}}{\ln(2 \cdot w_{L,Final} \cdot \gamma) - \frac{\Delta h_{m,eut}}{R \cdot T_m}} \quad \text{Equation 86}$$

$$w_{L,Final} = \frac{m_{L,Final}}{(m_{L,Final} + m_{D,Start} + m_{water})} \quad \text{Equation 87}$$

$$w_{D,Final} = \frac{m_{D,Start}}{(m_{L,Final} + m_{D,Start} + m_{water})}$$

With the help of Equation 88 the temperature for the nucleation step ( $T_0$ ) can be calculated based on the final temperature of the process ( $T_{Final}$ ). In the simulated example illustrated in Figure 50 it is assumed that the value of the subcooling ( $\Delta T$ ) is 5 Kelvin below the final temperature of the process. That way it should be assured, that primary nucleation of both enantiomers occurs. The corresponding mass fractions are calculated using Equation 89.

$$T_0 = T_{Final} - \Delta T \quad \text{Equation 88}$$

$$w_{L,0} = w_{D,0} = \frac{1}{\gamma} \cdot \exp\left(\frac{\Delta h}{R \cdot T_m} - \frac{\Delta h}{T_0}\right) \quad \text{Equation 89}$$

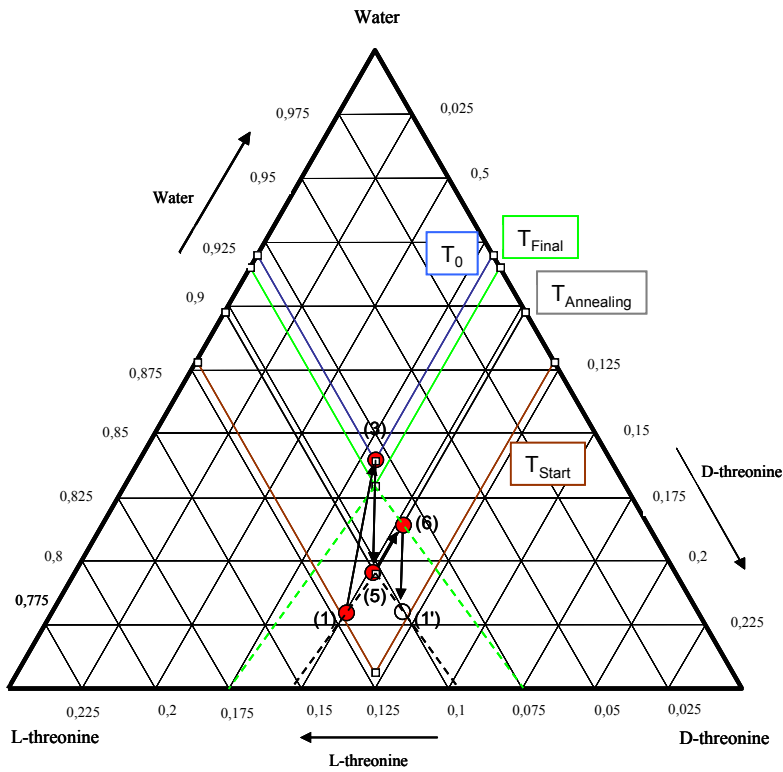


**Figure 50:** Illustration of the sample process simulated using equations (81) - (89). The points in the Figure correspond to the numbered points in Figure 9 (see also Table A 13, A 14 and A 15 in the Appendix for point values). The axes are labeled according to mass fractions.

The example illustrated in Figure 50 is solved with the values given in Table A 13 in the Appendix using the presented equations 81-89 and the values given in Table B1 and B2 for the solubility model. The numeric results of the sample evaluation can be found in Tables A 14 and A 15 (Appendix). In Figure 50 the corresponding solubility isotherms are shown. The numbers at the given points correspond to the numbers in Figure 9 and Figure 10 respectively. A point 1' is added to show the starting point of the batch where the D-enantiomer would be crystallized in the sequel batch of a cycle. This point is a mirror image of point 1. Obviously the yield of such a process, as defined in Equation 90, is only a function of the solubility and the final subcooling of the process:

$$yield_L = \frac{(m_{L,Start} - m_{L,Final})}{1kg} \quad \text{Equation 90}$$

The resulting relationship is illustrated in Figure 51. As it can be seen, it seems to be beneficial to run the process at high temperatures and cool down as far as possible.

The short-cut approach described does not use any crystallization kinetics. Therefore the absolute numbers for the yield are not very reliable. Nevertheless if the width of the metastable zone is assumed to be independent of temperature the generic principle of running the process at high temperatures and cool down as far as possible can be considered to be valid.

The cooling rate should be chosen as fast as possible since usually the metastable zone widens with increasing cooling rate (Garside et al., 2002).

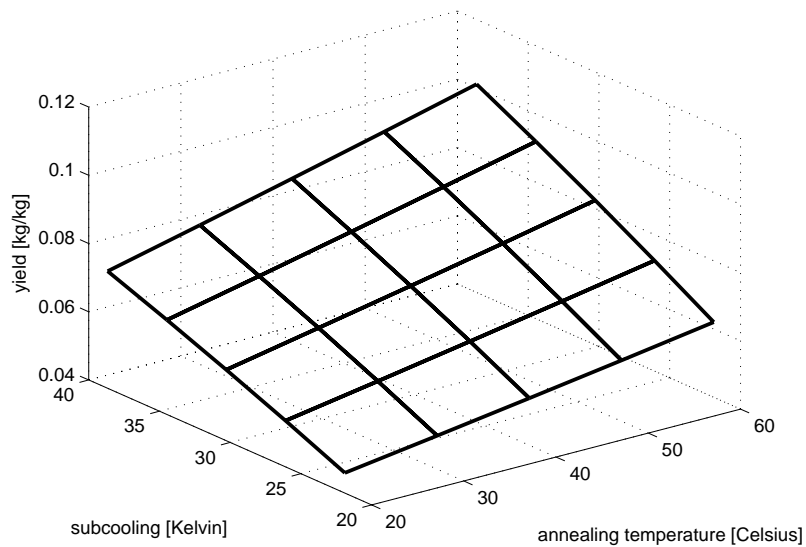


**Figure 51:** Yield of a DL-threonine preferential crystallization run (see Equation 9) as a function of annealing temperature and subcooling. As predicted by the equilibrium based short-cut method.

#### 4.4.2 Evaluation using MSZW-data (DL-threonine)

The first process approach presented above can be extended, if information with respect to the width of the metastable zone is incorporated for a calculation of the final subcooling  $\Delta T$  during the crystallization step. For the DL-threonine/water system measured metastable zone width data is available (Lorenz et al., 2006a; Polenske, 2003). Using this data allows a simultaneous estimation of yield *and* productivity of the process for a given cooling rate and annealing temperature. Using this approach it is assumed, that the metastable boundary of the system with respect to secondary nucleation defines the final temperature  $T_{Final}$ , where the batch is harvested. Equation

91 is then used as an alternative to Equation 86 to calculate the end temperature of the batch  $T_{Final}$ :

$$T_{Final} = T_{annealing} - MSZW \quad \text{Equation 91}$$

The overall process duration time is calculated assuming a constant cooling rate during all heating/cooling steps of the process. With that and the obtained mass of product the process productivity can be calculated according to Equation 92.

$$productivity = \frac{m_{product}}{m_{batch} \cdot t_{process}} \text{ kg / (kg h)} \quad \text{Equation 92}$$

The results of this evaluation procedure are shown in Figure 52 (yield as a function of cooling rate and  $T_{annealing}$ ) and Figure 53 (productivity as a function of cooling rate and annealing temperature  $T_{annealing}$ ).

From the analysis of the graphs it can be derived that the yield increases with increasing cooling rate. The effect of an increase in annealing temperature is twofold: At low cooling rates the yield of the process actually decreases as the metastable zone narrows with increasing annealing temperature. At higher cooling rates however this effect is compensated for and the yield increases. Theoretically an optimal yield can be obtained if the process is run at high cooling rates. In order to obtain an optimal productivity the process has to be run at high temperatures and high cooling rates in order to obtain high process productivities.

However, it has to be kept in mind that the predictions of Equation 79 are considered to be very uncertain due to known difficulties in reproducing nucleation events (Mullin, 2001). From the linear regression of the metastable zone width data confidence intervals of up to +4K have been obtained. Therefore, to check the reliability and predictive power of the method an experiment was performed with the experimental conditions given in Table 6. Details of the experimental setup can be found in (Czapla et al., 2009). The resulting yield and productivity of the experiment have been plotted as a grey dot into Figure 52 and Figure 53 for means of comparison to the predicted values. The corresponding numerical values are given in Table 7.

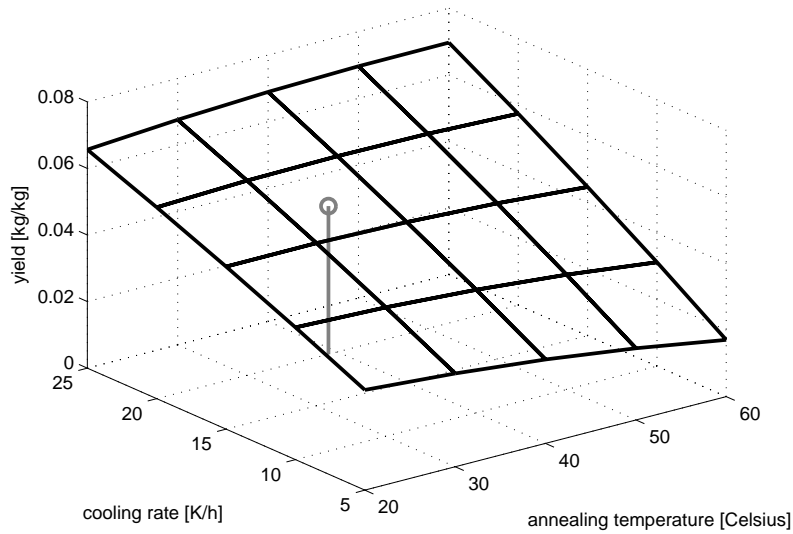


**Figure 52:** Obtainable yield with respect to annealing temperature and cooling rate for preferential crystallization in the DL-threonine/water system.

**Table 5:** Conditions for the designed process.

$T_{Start}$ [°C]	$T_0$ [°C]	$T_{annealing}$ [°C]	$T_{Final}$ [°C]	$w_{L,0}$ [%]	$w_{D,0}$ [%]
42	6	38	11	10.1	9.6

In order to generate model predictions of yield and productivity the corresponding input values as outlined in Figure 49 taken from the experiment performed have been inserted ( $dT/dt$ ,  $T_{annealing}$  for the MSZW approach and  $\Delta T$ ,  $T_{annealing}$  for the equilibrium approach). When comparing the model predictions and experimental values it can be stated that the equilibrium model underestimates the obtainable amount of product e.g. yield only to a small extent. However it has to be kept in mind that the purity of the experimentally obtained product is usually less than 100% (99.1% L-threonine content, determined with chiral HPLC). Additionally there are the previously mentioned uncertainties concerning the solubility data and metastable zone width data. The process evaluation approach incorporating the metastable zone width data (Equation 79) overestimates the obtainable yield and productivity to a small extent. The reason for the overestimation of the productivity is the very careful choice of the process temperatures when the experiment was planned. In the experiment the temperatures  $T_{start}$  and  $T_{annealing}$  have been chosen much higher than the saturation temperatures in order to run the process safely. Therefore the time necessary for heating and cooling is increased.

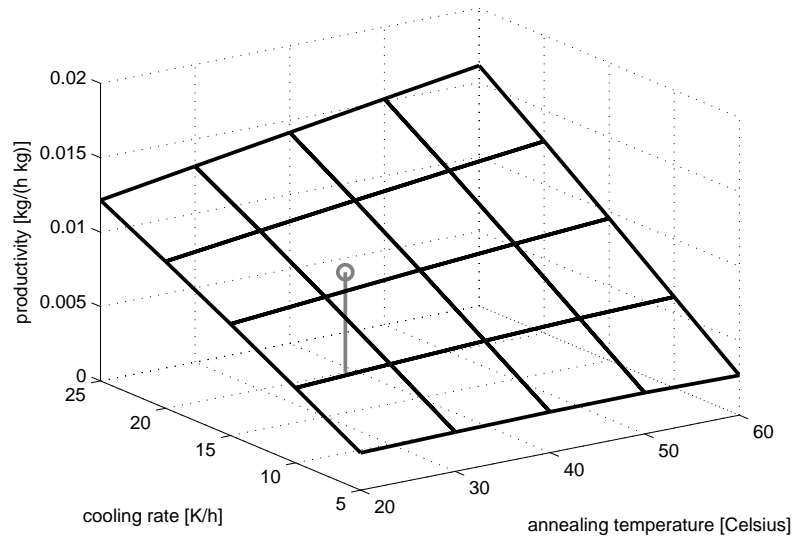


**Figure 53:** Obtainable productivity with respect to annealing temperature and cooling rate for preferential crystallization in the DL-threonine/water system.

Additionally the higher predicted yield of the MSZW-model can be attributed to the fact that the exact symmetry of the process was not given in the experimental run. The product harvested due to the entrainment effect contributed more than fifty percent to the final mass of the product. Therefore the initial enantiomeric excess was not high enough in order to run the process cyclic. Due to that obviously less product is harvested compared to the calculated idealized process, where the initial enantiomeric excess is exactly half of the obtained product on a mass basis.

**Table 6:** Experimental conditions of a sample experiment.

$T_{\text{Start}}$ [°C]	$T_0$ [°C]	$T_{\text{annealing}}$ [°C]	$T_{\text{Final}}$ [°C]	$w_{L,0}$ [%]	$w_{D,0}$ [%]
55	10	39	10	10.1	9.6

**Table 7:** Comparison of calculated yield and productivity with experimentally obtained values.

	Equilibrium Model	MSZW Model	Experiment
yield [kg/kg], (Eq. 90)	0.036	0.0630	0.039
productivity [kg/(kg h)], (Eq. 92)	-	0.0112	0.0068

#### 4.4.3 Equilibrium analysis R,S-mandelic acid

The approaches for process evaluation introduced in the preceding two chapters can also be applied to evaluate a preferential crystallization process for compound forming systems as introduced in chapter 2.2.1. In order to adopt the approach additional equations have to be introduced. This is mainly due to the fact that in contrast to the process applied to conglomerate forming systems here two different batches have to be performed. In one batch the enantiomer is crystallized whereas in the sequel batch the racemic compound has to be crystallized in order to restart the cycle after an addition of fresh eutectic material.

As before the starting masses of the enantiomer batch ( $(m_R, m_S, m_{water,0})$ , Table 4) are chosen in such a way that they add up to 1 kg. The initial mass fractions of the two enantiomers are calculated according to Equation 93 based on the initial masses (Table 4).

$$w_{R,Start} = \frac{m_{R,Start}}{m_{R,Start} + m_{S,Start} + m_{water}} \quad \text{Equation 93}$$

$$w_{S,Start} = \frac{m_{S,Start}}{m_{R,Start} + m_{S,Start} + m_{water}}$$

Inserting the resulting mass fraction of the R-enantiomer the starting temperature of the enantiomer batch is calculated (Equation 94).

$$T_{Start} = \frac{\varphi \cdot SC}{R} + \frac{\frac{\Delta h_m}{R \cdot T_m}}{\left( \frac{\Delta h_m}{R \cdot T_m} - \ln(w_{R,Start}) \right)} \quad \text{Equation 94}$$

Equation 94 is deduced from the solubility correlation presented in Equation 75. In general the course of the temperature profile and the respective masses/mass fractions are calculated based on the solubility model developed for the system R,S-mandelic acid/water (chapter 4.3).

$$T_{annealing} = \frac{-\frac{\Delta h_{m,eut}}{R \cdot T_{m,eut}}}{\ln(w_{eut,annealing} \cdot \gamma) - \frac{\Delta h_{m,eut}}{R \cdot T_{m,eut}}} + 1 \quad \text{Equation 95}$$

Equation 95 illustrates how the annealing temperature can be calculated in the same manner. For the calculation of the corresponding mass fraction it is assumed that the complete enantiomeric excess present at the beginning of the batch has crystallized

providing the seed material for the following preferential cooling crystallization. Therefore the mass fractions at the annealing temperature are assumed to be equal to the solubility mass fractions of the eutectic composition (Equation 96). For the system studied the eutectic composition  $c_{eut}$  is assumed to be fixed with a ratio of 0.31 parts of one enantiomer with respect to the total R,S-mandelic acid content.

$$w_{eut,annealing} = m_{S,Start} \cdot \frac{1}{c_{eut}} \cdot \frac{1}{\left( m_{S,Start} \cdot \frac{1}{c_{eut}} + m_{water} \right)} \quad \text{Equation 96}$$

A graphical representation of a sample run using the numeric values given in Table 4 is illustrated in Figure 54. The points in the Figure correspond to the points in Figure 11, where the basic concept of the process is illustrated. Some solubility isotherms for characteristic temperatures are included in the diagram in order to further illustrate the sample process run.

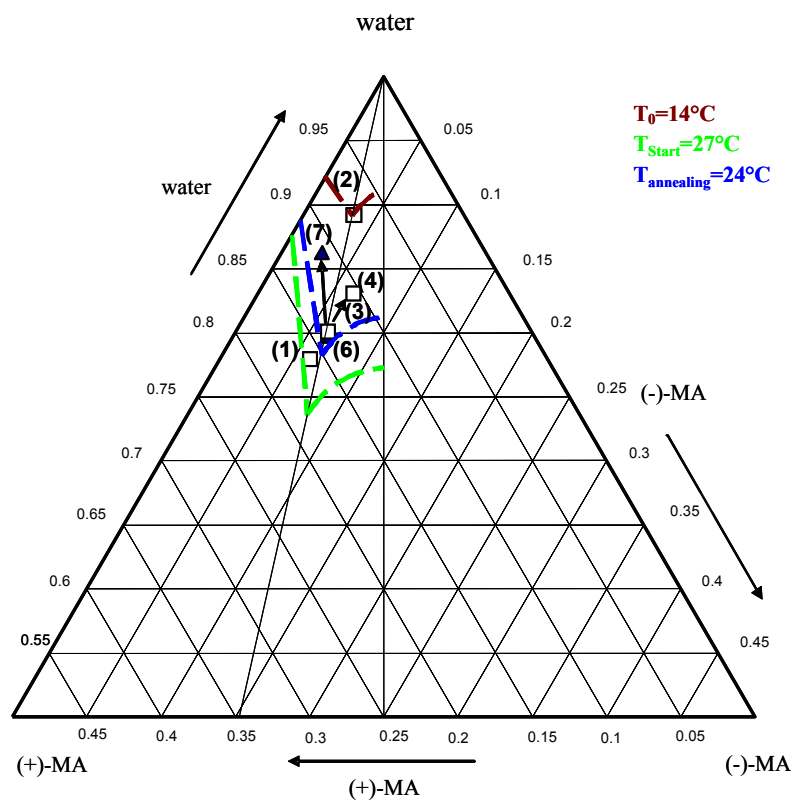


**Figure 54:** Illustration of the described process scheme exemplified with the numeric values given in Table 4. The numbers by the points correspond to the process steps introduced in Figure 11 and Figure 12. The points 5 and 1' are omitted to clarify the illustration. The axes labels are given in mass fractions.

It is assumed that the mass of water stays constant during the sample run. In Equation 97 the temperature  $T_0$  where nucleation is induced is calculated based on the value of the annealing temperature  $T_{annealing}$  calculated previously.

$$T_0 = T_{annealing} - \Delta T_{sub,0} \quad \text{Equation 97}$$

$$T_{final} = T_{annealing} - \Delta T_{sub,1} \quad \text{Equation 98}$$

The value of the subcooling ( $\Delta T_{sub,0}$ ) should be chosen large enough in order to make sure that nucleation takes place out of the clear solution (primary heterogeneous nucleation of racemate and enantiomer). For the example illustrated in Figure 54 a subcooling of 10 K was chosen. However after the temperature  $T_0$  is reached the batch is heated up again to  $T_{annealing}$ . Afterwards the batch is cooled down to a temperature  $T_{final}$ .  $T_{final}$  should be chosen in such a way that the metastable boundary of the racemate is not crossed. This way an enantiopure product can be harvested. In the simulated example using the presented equilibrium approach  $T_{final}$  was chosen to be 5 Kelvin below the calculated annealing temperature (Equation 98).

With the help of Equation 99 the end temperature of the enantiomer batch ( $T_1$ ) is calculated. In Equation 99 the value of  $\Delta T_{sub,2}$  is chosen in such a way that  $T_1$  is 5 Kelvin higher than the annealing temperature in order to provide a sufficient undersaturation for the dissolution of the added eutectic material.

$$T_1 = T_{annealing} + \Delta T_{sub,2} \quad \text{Equation 99}$$

After  $T_1$  is reached eutectic material is added and completely dissolved. Afterwards the solution is cooled back down again to  $T_{annealing}$ .

While  $T_1$  is reached the racemate should have nucleated so that point 6 in Figure 54 is reached. The nucleated racemate crystals now act as seeds for the cooling crystallization towards  $T_3$ , where the racemate is harvested (point 7 in Figure 54). The mass fractions corresponding to the chosen temperatures can be calculated using Equation 100 and Equation 101 respectively.

$$w_{sat,2,eut} = \frac{1}{\gamma_{eut}} \cdot \exp\left(\frac{\Delta h_{m,eut}}{R \cdot T_1} - \frac{\Delta h_{m,eut}}{R \cdot T_{annealing}}\right) \quad \text{Equation 100}$$

$$w_{sat,2,rac} = \frac{1}{\gamma_{rac}} \cdot \exp\left(\frac{\Delta h_{m,rac}}{R \cdot T_1} - \frac{\Delta h_{m,rac}}{R \cdot T_{annealing}}\right) \quad \text{Equation 101}$$

That way it is assured, that primary nucleation of both enantiomers occurs. The end temperature of the racemate batch  $T_2$  is calculated based on the value of the annealing temperature. Relying on the fact that the process is cyclic and should return to the starting point of the enantiomer batch after performing two batches, eutectic material is added. The amount of eutectic material needed can be calculated using Equation 104. The corresponding mass fraction is calculated using Equation 103.

$$T_2 = T_{annealing} - \Delta T_{sub,3} \quad \text{Equation 102}$$

$$w_{3,sat,eut} = \frac{1}{\gamma_{eut}} \cdot \exp\left(\frac{\Delta h_{m,eut}}{R \cdot T_2} - \frac{\Delta h_{m,eut}}{R \cdot T_{annealing}}\right) \quad \text{Equation 103}$$

In order to close the cycle the initial mass fractions of the enantiomer batch have to be reached (Equation 104).

$$\begin{aligned} w_{R,end} &= w_{R,0} \\ w_{S,end} &= w_{S,0} \\ m_{eut,add} &= m_{R,end} - m_{R,3} + (m_{S,end} - m_{S,3}) \end{aligned} \quad \text{Equation 104}$$

Obviously the yield of the enantiomer batch as defined in Equation 105:

$$yield = \frac{(m_{R,0} - m_{R,1,eut,sat})}{1kg} \quad \text{Equation 105}$$

is only a function of the solubility that is assumed to be reached after the final subcooling of the enantiomer batch.

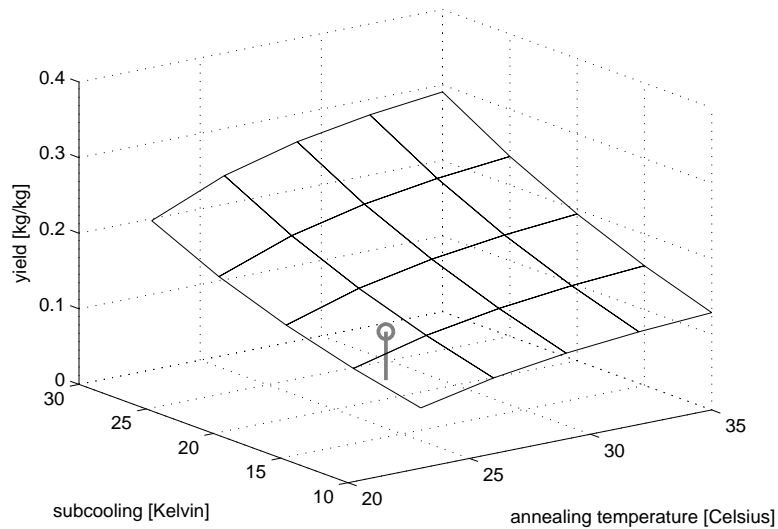


**Figure 55:** Yield of a preferential crystallization run as a function of annealing temperature and subcooling based on the presented equilibrium approach for the system of R,S-mandelic acid/water.

The resulting relationship between yield, annealing temperature and subcooling is illustrated in Figure 55. As can be derived from the plot it seems to be beneficial to run the process at high temperatures and cool down as far as possible. However, based on the equilibrium design approach the effect of the annealing temperature on yield is not as pronounced as the effect of the subcooling. In practice the maximal achievable subcooling is limited by the metastable boundary. Therefore, if experimental data for the metastable limit of the system is available the predictive capacity of the modeling

approach can be significantly enhanced. This approach is further discussed in chapter 4.4.4. In order to validate the predictive capacity of the chosen modeling approach the theoretical forecast is compared to an experimentally obtained value plotted as a grey dot in Figure 55. The numeric values corresponding to the experimental point can be found in Table 9 at the end of the following chapter.

#### 4.4.4 Evaluation using MSZW-data (*R,S*-mandelic acid)

Since a measurement of the metastable zone width for the studied system is available (Equation 79 and Equation 80) it can be used to enhance the quality of the forecast in terms of yield and additionally provide a forecast of process productivity as defined in Equation 92. Here, it can be differentiated between the productivity of the enantiomer batch only and the overall productivity of a single cycle including the process time of the racemate batch. The difference is the difference in the process time  $t_{process}$  used in the equation (Equation 92).

The resulting functional relationships with respect to cooling rate and annealing temperature are depicted in Figure 56 for the yield and Figure 57 for the productivity of the enantiomer batch.

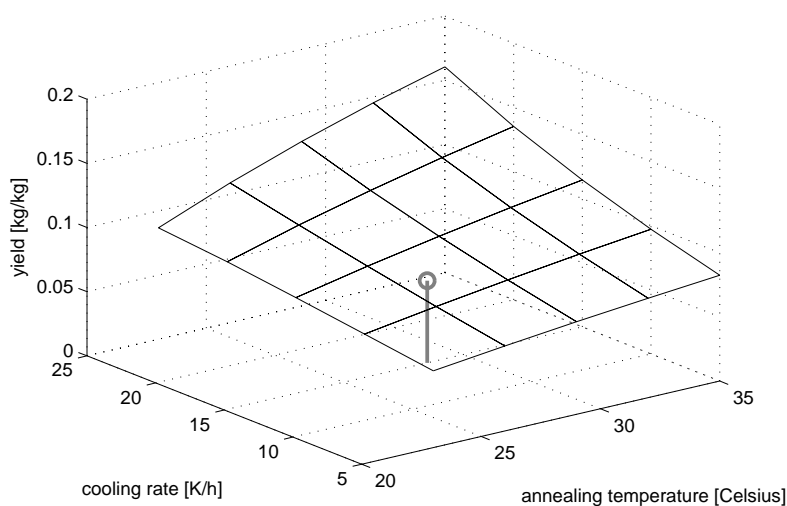


**Figure 56:** Yield of a preferential crystallization run as a function of annealing temperature and cooling rate based on the approach using the metastable zone width for a preferential crystallization in the system *R,S*-mandelic acid/water.

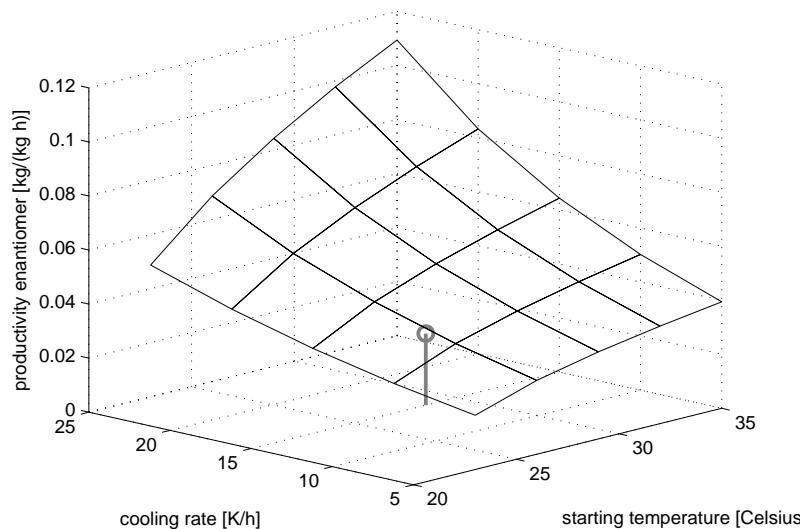


**Figure 57:** Productivity of the enantiomer batch of the cyclic process scheme as a function of starting temperature and cooling rate (MSZW approach) for a preferential crystallization in the system R,S-mandelic acid/water.

The overall productivity including the process time of the racemate batch is depicted in Figure 58. In order to calculate the process times it is assumed that the individual heating and cooling steps (see Figure 12) are undertaken with a fixed cooling rate for the individual steps. The cooling rate of the cooling crystallization steps (4. and 7. in Figure 12) is varied in order to obtain the functional relationships illustrated. Meanwhile the cooling and heating rates of the other process steps are kept fixed during the variation to a value of 20 K/h.

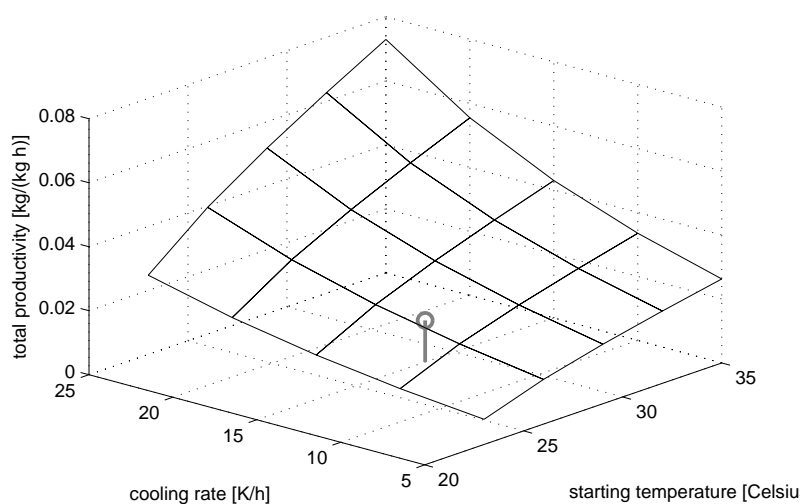


**Figure 58:** Total productivity of one complete cycle of the cyclic process scheme as a function of starting temperature and cooling rate (MSZW approach) assuming the product of the racemate batch as purge for a preferential crystallization in the system R,S-mandelic acid/water.

For the functional relationship to calculate the yield with respect to cooling rate and annealing temperature the previously obtained result of the equilibrium approach is supported. High annealing temperatures combined with high cooling rates lead to high process yield. In order to validate the chosen evaluation approach a comparison with experimental data has been done. The grey dot in Figure 56 represents the yield of a sample experiment. Two sample runs for enantiomer and racemate crystallization were performed in order to obtain data that can be compared with the predicted values (Michaluk, 2007). Important experimental conditions of the runs are given in Table 8.

**Table 8:** Experimental conditions for the enantiomer and racemate batch used for validation purposes.

Enantiomer batch:					
$T_{Start}$ [°C]	$T_0$ [°C]	$T_{annealing}$ [°C]	$T_{Final}$ [°C]	$w_{R,0}$ [%]	$w_{S,0}$ [%]
40	10	28.5	6	15.8	7.9
Racemate batch:					
$T_{Start}$ [°C]	$T_0$ [°C]	$T_{annealing}$ [°C]	$T_{Final}$ [°C]	$w_{R,0}$ [%]	$w_{S,0}$ [%]
40	10	27.5	6	20.54	11.06

The numeric values for the calculated and experimentally obtained yield and productivity can be found in Table 9.

**Table 9:** Calculated and experimentally obtained values for yield and productivity.

	Equilibrium Model	MSZW Model	Experiment
yield [kg/kg], Eq. 105	0.1517	0.0805	0.064
productivity enantiomer batch [kg/(kg h)], Eq. 92	-	0.0331	0.0265
total productivity [kg/(kg h)], Eq. 92 modified	-	0.0197	0.013

As can be seen from the data the predicted yield using the equilibrium approach overestimates the experimentally obtained yield to quite a large extent. Obviously the experimental run had not reached the thermodynamic equilibrium when the batch was harvested. However, the yield predicted with the MSZW-approach is quite close to the experimentally obtained one.

Since the metastable width is intrinsically dependent on the maximal supersaturation level of the counter species that can be reached before the process should be harvested the predicted values can also be used for a forecast of productivity and yield of runs

that do not reach the thermodynamic equilibrium. If more seeds would be used maybe the process could be run closer to the solubility line. Then the equilibrium based approach should also deliver a more precise forecast of the yield.

The presented approaches deliver results that can be used to identify zones of potential high yield and productivity. Nevertheless a dynamic model using actual process kinetics should be able to deliver more accurate and realistic forecasts.

#### **4.5 Model solution strategies**

In the preceding chapters two process evaluation approaches have been introduced and discussed that are able to forecast the yield and productivity of a preferential crystallization run based solely on solubility and metastable zone width data.

However, when compared to actual separation runs deviations between the predicted values and the experiments occurred. In order to provide a more precise forecast of yield, productivity, process trajectories and additionally the particle size distribution of the product a dynamic process model is needed. Usually, to model crystallization processes the population balance framework is used (Randolph & Larson, 1988). If a dynamic model is used the resulting integro-differential equations (Equation 13, Equation 15) have to be solved applying a suitable numeric solution strategy. Nowadays several sophisticated schemes are available to solve the resulting equations (see for example (Qamar et al., 2007)). In this thesis four different solution strategies are used to solve the population balance model together with the fluid phase mass balance as presented in chapter 2.1.5:

- a.) Finite discretization; discretized in the time domain by “ode23” (Matlab<sup>®</sup>) using a linear grid for the particle length
- b.) h,p-moving grid Galerkin approach (Parsival<sup>®</sup>)
- c.) Method of characteristics (MOC); discretized in the time domain by “ode23” (Matlab<sup>®</sup>) using a linear grid for the particle length
- d.) Reduced Model: Method of moments (MOM), discretized in the time domain by “ode23” (Matlab<sup>®</sup>), see chapter 2.1.6

All strategies use different numerical techniques. In this chapter the three most typical techniques (finite differences (Matlab<sup>®</sup>), h,p-moving grid Galerkin scheme

(Parsival<sup>®</sup>), moment model (Matlab<sup>®</sup>)) are compared in terms of calculation times and the actual model solutions (particle size distributions, mass fraction trajectories). The method of characteristics is only applied as long as only one distribution is present. When the second distribution would nucleate the method of characteristics becomes a rather inefficient solution strategy due to the necessary regridding for both populations (Kumar & Ramkrishna, 1997).

The fully discretized model (a.) as introduced in chapter 2.1.5 delivers mass fractions, moment trajectories and particle size distributions at every time point. It is used as a reference model for the reduced model (d.), MOM) as well as the h,p-moving grid Galerkin scheme (b.) implemented in Parsival<sup>®</sup>.

Parsival<sup>®</sup> represents a commercial program for solving population balance equations. Trajectories of mass fractions as well as the particle size distribution can be calculated at every time point. Figure 59 and Figure 60 show comparisons of model solutions obtained with Parsival and the finite discretized solution scheme implemented in Matlab<sup>®</sup> (see chapter 2.1.5). The kinetic parameters used for the calculations can be found in Table B11 in Appendix B. In Figure 59 the solutions are compared with respect to the mass fractions of both enantiomers for a typical experiment of the “nucleation seeded” variant of the auto seeded polythermal preferential crystallization. Figure 60 shows a comparison of the simulated particle size distribution of the L-threonine crystals at the end of the simulation run for both implementations of the population balance.

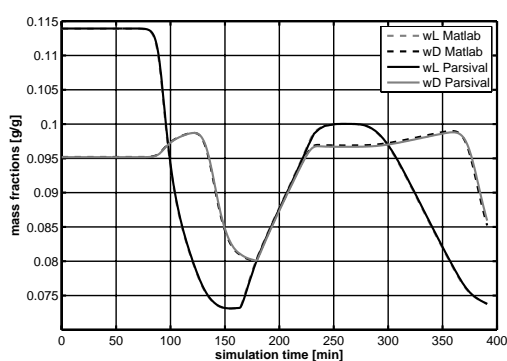


**Figure 59:** Comparison of a model solution with the commercial program Parsival<sup>®</sup> and a finite discretization scheme using  $n=1000$  points on a linear grid from 0-2mm for the mass fractions of the two enantiomers (Matlab<sup>®</sup>).

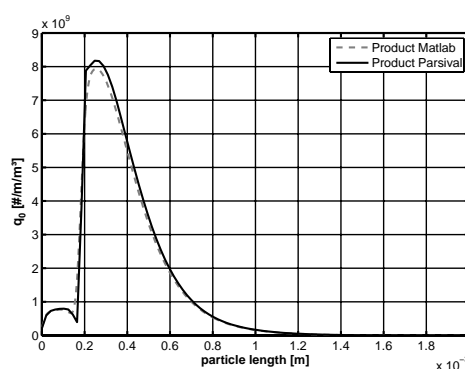


**Figure 60:** Comparison of the final particle size distribution of L-threonine crystals calculated with the commercial program Parsival<sup>®</sup> and a finite discretization scheme using  $n=1000$  points on a linear grid from 0-2mm (Matlab<sup>®</sup>).

Both solutions have a good accordance. Therefore in the following it is assumed that results obtained with one of the two model solution strategies (e.g. estimated kinetic parameters) can be used without a significant loss of accordance in the other and vice versa.

The method of characteristics is a very elegant approach for solving the population balance equations though it is limited to models containing growth and simple nucleation laws. A main advantage of the method is that no numerical dispersion occurs. Therefore the properties of the calculated particle size distributions are preserved along the time coordinate. The method is applied in chapter 4.6.2 to calculate very accurate particle size distributions that are then transformed into chord-length distributions using a model of the applied FBRM-probe. Here the accuracy of the method of characteristics regarding the calculation of particle size distributions is of great benefit. Unfortunately it is unclear how a numerical error incorporated into the calculated particle size distribution would effect the resulting chord length distribution that is obtained after the highly nonlinear mathematical transformation. A comparison between solutions obtained with the method of characteristics and Parsival regarding mass fraction trajectories and particle size distributions is given in Figure 61 and Figure 62 for a seeded preferential crystallization run (process concept “defined seeding”; kinetic parameters taken from Table B 11 from the Appendix). The agreement between the two methods is rather good.

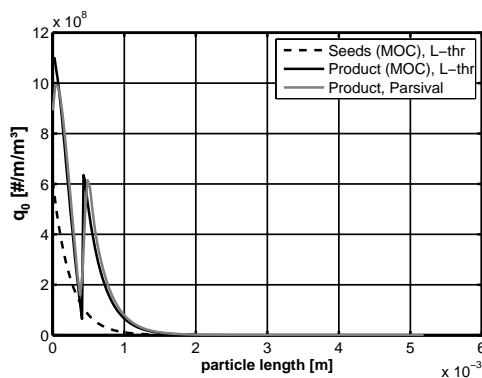


**Figure 61:** Comparison of a model solution with the commercial program Parsival® and a method of characteristics solution (MOC, linear grid using  $n=100$  grid points from 0-2mm, Matlab®.) for the final particle size distribution of L-threonine crystals.

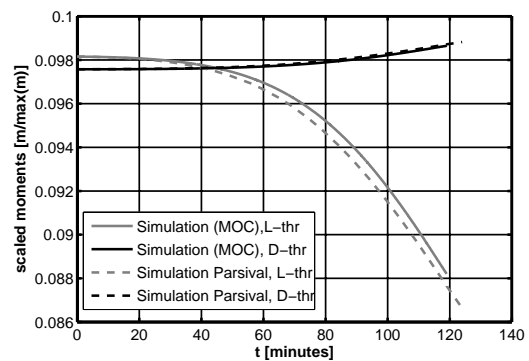


**Figure 62:** Comparison of a model solution for the mass fractions of L- and D-threonine using Parsival® and the method of characteristics (MOC, linear grid using  $n=100$  grid points from 0-2mm, Matlab®).

When the particle size distributions of seed and product as given in Figure 61 are observed it can be seen that the distribution calculated with Parsival® suffers from

numerical dispersion which is not the case for the distribution calculated with the method of characteristics. This explains also the small deviations regarding the mass fraction trajectories presented in Figure 62.

The reduced model (MOM) accounting only for the mass balance and changes in the moments of the particle size distribution was introduced in chapter 2.1.6. It was developed because it could significantly decrease the calculation time compared with the finite discretized full population balance model and the model solution using Parsival<sup>®</sup>. This is especially beneficial for optimization and parameter estimation applications, where the model has to be solved many times (see Table 12). Therefore this model solution strategy is mainly used for parameter estimation applications (chapter 4.6).

The numerical values of the scaling factors  $A$  used in this study for the reduced model (see Equation 21) are given below in Table 10.

**Table 10:** Scaling factors for the moment equations.

Scaling factor	Value
$A_0$	$10^{-6}$ [-]
$A_1$	$10^{-2}$ [1/m]
$A_2$	$10^2$ [1/m <sup>2</sup> ]
$A_3$	$10^4$ [1/m <sup>3</sup> ]

Their values have been chosen to decrease the numerical differences between the moments during calculations. The third moment for example usually has a value in the range of  $10^{-4}$  m<sup>3</sup> while the zero moment, the total particle number, can easily reach values of up to  $10^6$ . If the scaling factors are chosen carefully, the scaled moments will have values between zero and ten.

To check the accordance a test calculation under typical conditions using representative values for the kinetics (Table 11 and chapter 2.2.4) is performed and presented in the Figures 63-65 below. The optical rotation, the mass fraction of the two species and the summed zero moments of the two crystal populations are taken as a means for checking the accordance. These outputs are chosen because they are measurable with the employed devices and play an important role in the following chapters on parameter estimation and model identifyability.

**Table 11:** Values of the kinetic constants used for the model calculations presented in Figures 63 to 65.

parameter	value	parameter	value
$b$	3.4 [-]	$k_{prim}$	0.43 [-]
$k_{b, sek, pre}$	$3.2 \cdot 10^9$ [#/(m <sup>3</sup> s)]	$k_{prim2}$	$2.27 \cdot 10^{-10}$ [-]
$g$	1.4 [-]	$E_g$	-47.9 [kJ/mol]
$k_{g, pre}$	$1.63 \cdot 10^{-9}$ [m/s]	$E_d$	-57.4 [kJ/mol]
$E_{b, sek}$	-102.6 [kJ/mol]	$k_d$	0.996 [kg/(s m <sup>2</sup> )]
$k_b$	$2.24 \cdot 10^4$ [#s]	$k_v$	0.048
$T_{mean}$	30 [°C]	-	-

From the plots it can be seen that with the assumed “Ansatz” for the particle size distribution in the dissolution part a good accordance between the two solution strategies can be achieved. Small deviations can be seen (especially for the zero moment) but compared to the experimental reproducibility (chapter 3.5) these differences can be neglected.

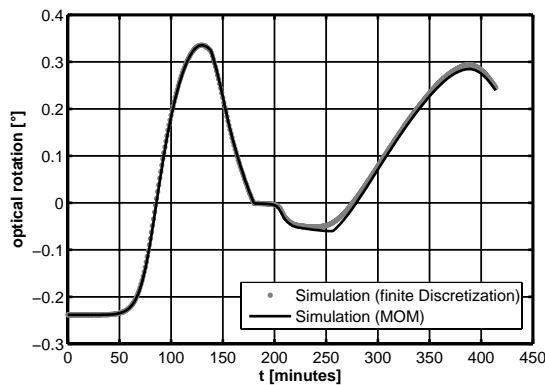


**Figure 63:** Comparison of a model solution with the method of moments and a finite discretization scheme using  $n=500$  points on a linear grid from 0-2mm for the optical rotation.

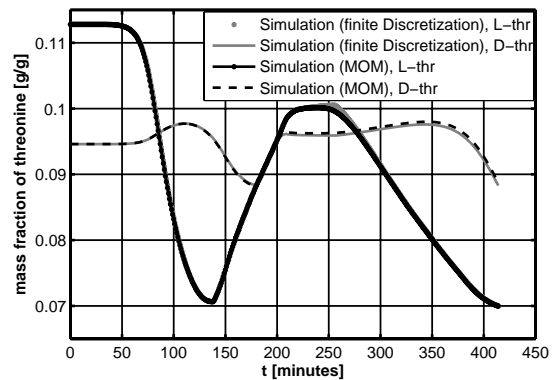


**Figure 64:** Comparison of a model solution with the method of moments and a finite discretization scheme using  $n=500$  points on a linear grid from 0-2mm for the mass fractions of both enantiomers.

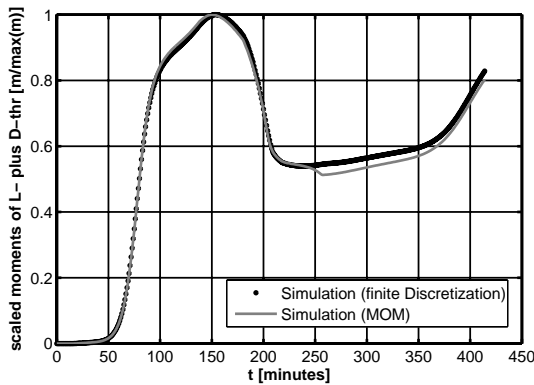


**Figure 65:** Comparison of a model solution with the method of moments and a finite discretization scheme using  $n=500$  points on a linear grid from 0-2mm for the total zero moments (L- plus D-threonine).

When comparing the model solution strategies (Table 12) and software implementations apart from calculation times Parsival performs superior in terms of user friendliness. On the other hand it lacks the wide variety of mathematical operators and functions e.g. optimization routines, graphical outputs and transformation functions which the Matlab® environment provides. The simulation strategy

can be chosen according to the type of problem to be solved (e.g. process optimization) and the experimental data that is available (e.g. Moments, particle size distributions).

**Table 12:** Comparison of the reduced model and the full model in terms of calculation times

	Reduced model solved with ode23	Fully discretized model solved with ode23	Fully discretized model solved with h,p-moving grid Galerkin method (Parsival®)
Calculation time [sec]	1	59	117
Information regarding the particle size	Moments only	Particle size distribution at every time point	Particle size distribution and online graphs at every time point
Feature	many functionalities		user friendly

Then, for the model to be of any use the free kinetic parameters have to be determined. Typically this is done by fitting the model to experimental data (parameterization). The procedure of identifying and evaluating these parameters will be covered in detail in the following chapters.

## 4.6 Parameterization of the model

A process model is only of value to the user if it is capable of predicting the behaviour of the modelled process. In order to guarantee the predictive power of the model, the free kinetic model parameters have to be identified and evaluated in terms of their reliability. The task is therefore to minimize the difference between model (chapter 2.1.5 and chapter 2.2.4, Equation 13 and Equation 15, Equation 28-Equation 35) and experiment by a variation of the free parameters. The process of identifying these free kinetic parameters is called parameterization (see chapter 2.3 for theoretic details).

Three different approaches for model parameterization are taken in this work and presented in this chapter.

The first approach is to use a reduced model (chapter 2.1.6), solve it using Matlab® and estimate the kinetic parameters by a minimization of the goal function  $F_{goal,1}$  (Equation 107) based on experimental data of three seeded preferential crystallization runs (experiments 1 to 3 from Table 2). Additionally the model is fitted to experiments of the process concept “nucleation seeding” (experiments 6-8 from Table 2; see chapter 2.2.1 for more information regarding the process concept).

The second approach is to use chord length distribution data measured by a FBRM probe along with optical rotation data (goal function  $F_{goal,2}$ , Equation 109, experiments 1 to 3 from Table 2) to parameterize a fully discretized model that is solved using the method of characteristics implemented into Matlab® (see chapter 4.6.2 for the results). The method of characteristics is used there because of its accuracy regarding the particle size distribution calculation. Initial experiments are carried out for testing the probe model. The experiments used for the actual model parameterization are of the process concept “defined seeding” (see chapter 2.2.3).

The third approach is to use the commercial software package Parsival® (M.Wulkow, 2001) and its built in solver along with the module for parameter estimation to solve the parameterization problem for a fully discretized model. Here the fitting is done using the available data of the fluid phase mass fractions and measured particle size distributions (typically seeds and product). In Parsival® a very efficient numerical solver is available. Therefore it is convenient to compare calculated particle size distributions to measured ones at defined time points of the process. Experiments 1 to

3, 5-8 and 10 from Table 2 are used for the comparison between model and experiment (see chapter 4.6.3 for the results).

The general course of action concerning parameterization of the model is illustrated in Figure 15. The approach proposes an iterative procedure for model parameterization that includes simulation and experiments. The task of identifying a suitable model structure (e.g. choosing kinetic equations) is left out but could be inserted easily into the scheme (Chen & Asprey, 2003).

The basic course of the three different approaches is presented in short in Table 13.

Using the first parameter estimation approach additionally the effect of a reparameterization of the model kinetics is studied (see chapter 4.6.1; theory on reparameterization is given in chapter 2.3.5).

For parameterization a suitable optimization scheme is needed to minimize the proposed goal function (see Equation 106 for a general formulation). Several optimizers implemented into the Matlab<sup>®</sup> optimization suite have been tested. Among those the solver “fminsearchbnd.m” that is based on “fminsearch.m” was finally elected to be used for the first two approaches because of its stochastic nature and robustness (bounded Nelder-Mead Simplex (Lagarias et al., 1998)). Optimization schemes based on derivative approximations were not able to deliver satisfying results for the problems studied.

**Table 13:** Overview over the different parameterization approaches followed in the thesis. The different model solution strategies are introduced and compared in chapter 4.5.

<b>Data used (x,y), see Eq. 106</b>	$\mu_2, \alpha$	$\mu_{0,CLD}, \alpha$	$w_b, PSD$
<b>Model solution strategy</b>	MOM (Matlab <sup>®</sup> )	MOC (Matlab <sup>®</sup> )	h,p-Galerkin approach (Parsival <sup>®</sup> )
<b>Optimization scheme</b>	Bounded Nelder Mead simplex (fminsearchbnd.m)	Bounded Nelder Mead simplex (fminsearchbnd.m)	Simulated annealing + damped Gauss Newton scheme
<b>chapter</b>	4.6.1	4.6.2	4.6.3

For the model implemented into Parsival<sup>®</sup> a simulated annealing stochastic optimization scheme combined with a damped Gauss-Newton method have been used. Both schemes are “built in” into the software package and are specifically adapted to parameter estimation problems in the context of population balance problems.

After the model is defined and a suitable optimizer has been chosen the formulation of the optimization goal function and, afterwards, the evaluation of the estimated parameters are eminent. In this context also the quality and type of the available experimental data is an issue of importance.

Typically a goal function is formulated as the sum of squares of the difference between measured and experimental data. As often different types of data with different units or range of numerical values are measured a suitable scaling has to be undertaken. Additionally, weights  $w_i$  can be applied to different terms of the goal function in order to modify their impact onto the results. A quite general formulation of an optimization goal function is given in Equation 106 for two signals  $x$  and  $y$  using scaling factors  $A$  and  $B$ :

$$F_{goal} = \sum_{i=1}^{N_{exp}} \sum_{j=1}^{N_{data}} \left( w_{i,x} \cdot \left( \frac{x(i,j)_{measured}}{A_{i,scal,measured}} - \frac{x(i,j)_{calculated}}{A_{i,scal,calculated}} \right)^2 + w_{i,y} \cdot \left( \frac{y(i,j)_{measured}}{B_{i,scal,measured}} - \frac{y(i,j)_{calculated}}{B_{i,scal,calculated}} \right)^2 \right) \quad \text{Equation 106}$$

#### 4.6.1 Parameter estimation using second moments and optical rotation

A parameter estimation for the crystallization kinetics presented in chapter 2.2.4 was used to estimate the eleven free model parameters  $b$ ,  $k_{b,sek,pre}$ ,  $g$ ,  $k_{g,pre}$ ,  $E_{sek}$ ,  $k_b$ ,  $k_{prim}$ ,  $k_{prim2}$ ,  $E_g$ ,  $E_d$  and  $k_d$  based on optical rotation data and second moment trajectories. For means of simplification the volumetric shape factor  $k_v$  is considered a system dependent constant. The goal function to minimize for the parameter estimation is given in Equation 107.

$$F_{goal,1} = \sum_{i=1}^{N_{exp}} \sum_{j=1}^{N_{data}} \left( \left( \frac{\alpha(i,j)_{measured} - \alpha(i,j)_{calculated}}{\alpha(i,0)_{measured}} \right)^2 + \left( \frac{\mu(i,j)_{2,measured}}{\max(\mu(i)_{2,measured})} - \frac{\mu(i,j)_{2,calculated}}{\max(\mu(i,j)_{2,calculated})} \right)^2 \right) \quad \text{Equation 107}$$

The scaling of the different measured properties is done by dividing through the maximum of the trajectory of the second moment or the initial optical rotation respectively. This approach is chosen because in the experiments where no seed material is used (“nucleation seeding”) the maximum of the second moment trajectory defines a setpoint to relate the moment measured by the FBRM probe to the simulated moment trajectory.

The different conduction of the experiments allows a separate estimation of the parameters governing certain kinetics.

Experiments 1 to 3 from Table 2 have been used as a basic data set to fit the model to experimental data. The chosen experiments were carried out using seeds. The experimental conditions were chosen in such a way that a broad range of sensible operating conditions (temperatures, mass fractions, amount of seeds, cooling rates) were covered. The goal of this initial fitting was to estimate the six free model parameters of the growth and secondary nucleation laws  $b$ ,  $k_{b,sek,pre}$ ,  $g$ ,  $k_{g,pre}$ ,  $E_{sek}$ , and  $k_b$ . In the experiments 1 to 3 used here no primary nucleation and dissolution occurs (see also chapter 2.2.4 for the formulation of the different kinetic expressions used in the model). Therefore the kinetic parameters governing these equations cannot be estimated. The fitting results of the first fitting are shown in the Figures 66-69. There the model outputs and measured trajectories for the optical rotation, the scaled second moment of the particle size distribution and the mass fractions of the two enantiomers are displayed. The estimated parameters are given in Table B 3 (Appendix) along with measures for the quality of the estimates (confidence intervals, condition number of the Fisher information matrix and collinearity index).

The confidence intervals given in the table have been estimated based on the evaluation of the Fisher information matrix (*FIM*) (see chapter 2.3.2 for details on the method). The quality of the fit and the reliability of the parameters can be quantified based on the condition and collinearity index of the *FIM* that are also given in the table. Based on these results one can state that the chosen model is in principle capable of describing the experiments performed. There are some deviations which have to be attributed to the experimental error on the one hand and the uncertainty of the model structure on the other hand (may be there actually is some (insignificant) agglomeration, breakage, inhomogeneity of the fluid phase, etc....).

However, based on the evaluated numbers of the condition and collinearity index it can be seen that the solution of the estimation problem is far from being unique. The condition should be below 100, the collinearity index below 20 (Brun, 2002). So according to the proposed scheme (Figure 15) there are three routes of action to take:

- a.) Model reduction
- b.) Reparameterization of the kinetics
- c.) Perform additional (designed) experiments

A model reduction in a systematic manner can be done by a comparison of the calculated sensitivity measures (Equation 39, chapter 2.3.1) of the parameters. If the sensitivity measure of a parameter is very low compared to the sensitivity measure of other parameters the parameter is difficult to estimate based on the available data and should be fixed to a reasonable value. Afterwards by performing a new parameter estimation with the now fixed parameter it should be checked, if a good fitting can be obtained with the remaining set of parameters.

In the case presented here the sensitivity measures of the parameters have more or less the same order of magnitude and therefore a model reduction using the method of sensitivity measures cannot be applied.

**Table 14:** Parameters, confidence intervals, sensitivity measures and measures for quality of fit for the second estimation using reparameterized kinetics based on experiment 1-3 (“defined seeding”, DL-threonine/water, Table 2). The corresponding model equations can be found in the chapters 2.1.5 (model), 2.2.4 (kinetics) and 2.3.4 (reparameterization). The original parameters with confidence intervals obtained from resubstitution are also given. Temperature mean centering (see Eq. 56) is applied using the reference temperature  $T_{mean}$  given.

Parameter	Estimated value	Confidence [%] (95%), Eq. 48	Sensitivity measure [-], Eq. 41
$G_1$	$1.853 \cdot 10^{-9}$ [-]	2	77
$G_2$	$4.51 \cdot 10^{-9}$ [-]	3	221
$B_1$	$3.82 \cdot 10^4$ [-]	6	53
$B_2$	$7.98 \cdot 10^6$ [-]	6	82
$E_{b, sek}$	-68.8 [kJ/mol]	1	172
$E_g$	-105.9 [kJ/mol]	1	460
$b$	1.85 [-]	0.1	-
$k_{b, sek, pre}$	$1.9 \cdot 10^8$ [#/ (m <sup>3</sup> s)]	7	-
$g$	0.3 [-]	1.4	-
$k_{g, pre}$	$7.65 \cdot 10^{-9}$ [m/s]	4	-
<i>Condition</i>	$9.46 \cdot 10^5$ [-]		
<i>Collinearity index <math>\gamma</math></i>	491 [-]		
<i>Goal function</i>	140.4 [-]		
$s_1$	0.01 [-]		
$s_2$	0.18 [-]		
$T_{mean}$	30 [°C]		

A reparameterization of the kinetics is feasible using the approach taken from Ratkowsky (Ratkowsky, 1989) which is introduced in detail in chapter 2.3.5.

If this approach is followed and a parameter estimation is performed new estimates for the reparameterized kinetics are obtained (Table 14).

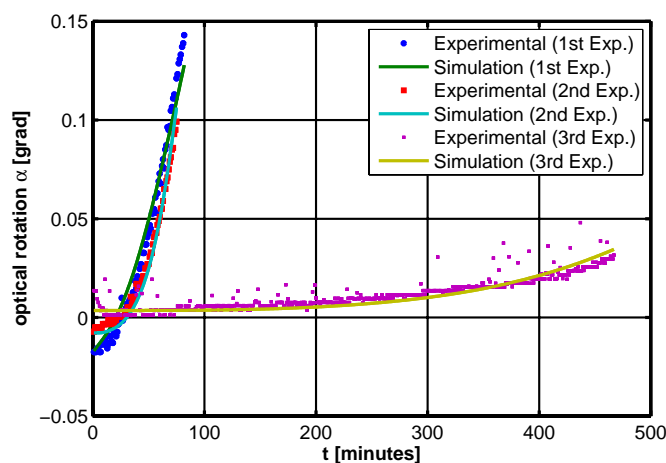


**Figure 66:** Model calculations and experimental data for the optical rotation over time (Experiments 1 to 3, Table 2).

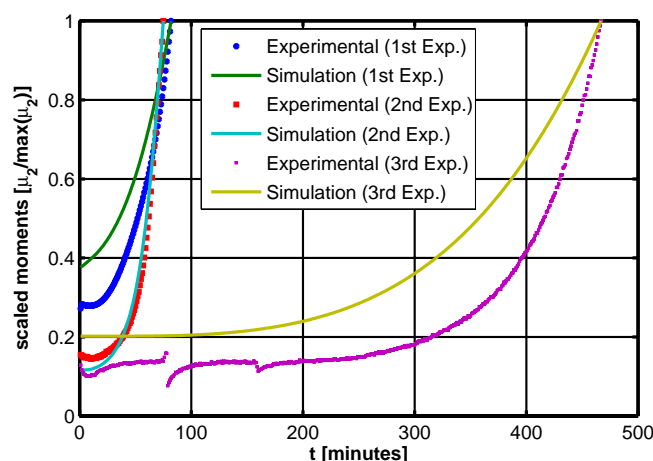


**Figure 67:** Model calculations and experimental data for the scaled second moments over time (Experiments 1 to 3, Table 2). Experimental moments are obtained from FBRM-data.

The results show that it is possible to reduce the condition and the collinearity index of the estimation problem significantly by using a reparameterization of the kinetics. Along with this the residuum is significantly lowered leading to a better fit of the model to the experiment. Since the principle model behavior has not been altered by the reparameterization the value changes can be explained by local minima resulting mainly from parameter cross correlation. The cross correlation of individual parameter pairs can be evaluated using the omega matrix (Equation 46).

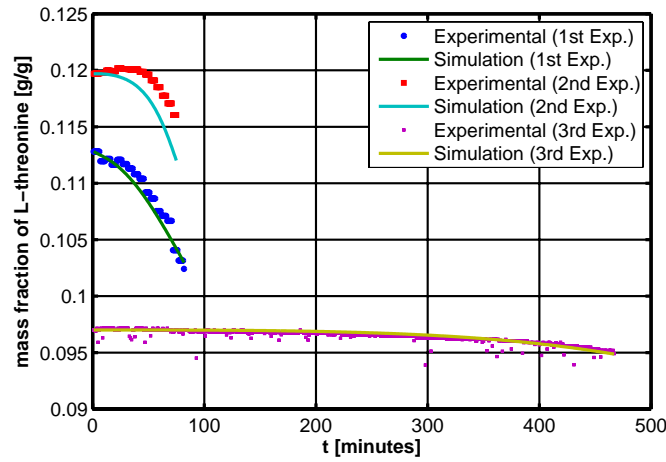


**Figure 68:** Model calculations and experimental data for the mass fractions of L-threonine over time (Experiments 1 to 3, Table 2).

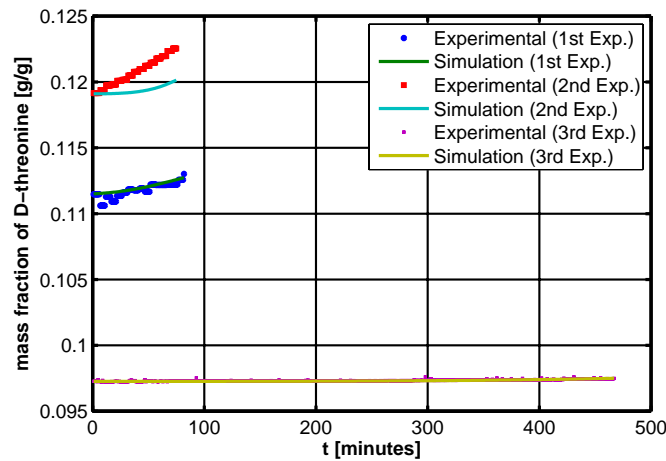


**Figure 69:** Model calculations and experimental data for the mass fractions of D-threonine over time (Experiments 1 to 3, Table 2).

To compare the original set of parameters and the reparameterized kinetics both omega matrices are given in Table B 4 and Table B 5 (Appendix). The matrix coefficients have values between zero and one. One meaning total correlation zero no correlation at all. A value above  $\pm 0.95$  shows significant correlation. That means that it is hard to estimate reliable values of the parameters in question. From a comparison of the coefficients of the original estimation problem with the estimation using reparameterized kinetics it can be seen that the reparameterization has significantly reduced the correlation between prefactors and power coefficient of the power law kinetics for secondary nucleation and crystal growth. Although the new values of the

kinetics especially for the crystal growth and nucleation laws are quite untypical (for example  $g = 0.3$ ) the parameter set in total should provide a better representation of the actual process behaviour as the initial one obtained before reparameterization.

Nevertheless the condition of the *FIM* and the collinearity index are still too high. Therefore additional experimental data is needed. The sequel experiments are designed based on the methods introduced in chapter 2.3.4. The hope is that the amount of additional experiments can be reduced significantly by the application of a dynamic experimental design. The effect of this design of experiments is presented and discussed in detail in chapter 4.8.

The numerical values obtained for the individual parameters lie in the range of values found in literature (compare for example (Elsner et al., 2005; Garside & Shah, 1980)).

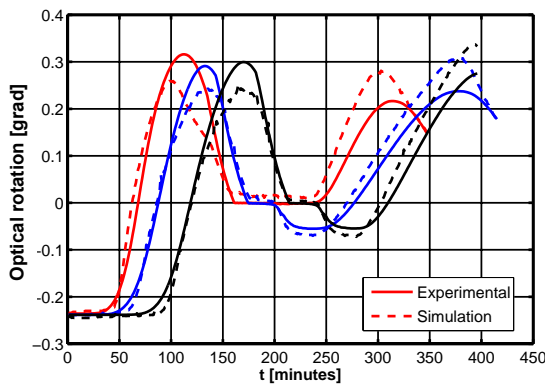


**Figure 70:** Measured and calculated optical rotation trajectories for experiments (5-7, Table 2).

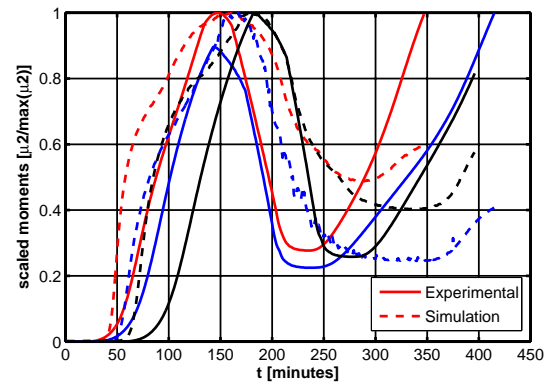


**Figure 71:** Measured and calculated second moment trajectories (experiments 5-7, Table 2).

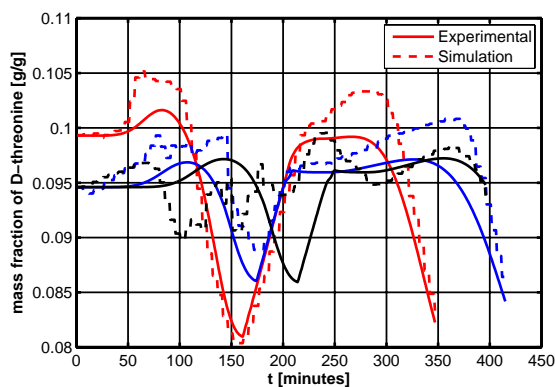


**Figure 72:** Measured and calculated trajectories for the D-threonine mass fractions (experiments 5-7, Table 2).

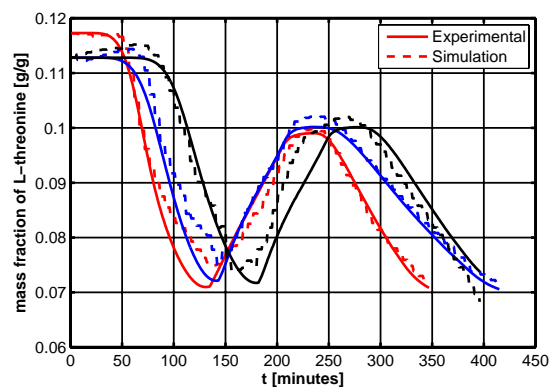


**Figure 73:** Measured and calculated trajectories for the L-threonine mass fractions (experiments 5-7, Table 2).

Additionally a parameter estimation and evaluation of the parameter quality is undertaken for three experimental runs carried out using the process concept “nucleation seeding” (experiments 5-7 from Table 2, see also chapter 2.2.1). As starting values for the parameter estimation the values of the parameters from Table 14 were chosen accompanied with the three parameters  $k_b$ ,  $k_{prim}$ ,  $k_{prim2}$  governing the kinetics of primary nucleation (Equation 30) and the parameters  $k_d$  and  $E_d$  describing the dissolution kinetics (Equation 29).

The fit of the model to the experimental data is shown in the graphics from Figure 70 to Figure 73. The parameters that result from the fitting procedure are given in Table 15.

**Table 15:** Parameters, confidence intervals, sensitivity measures and measures for quality of fit for the estimation using reparameterized kinetics based on experiment 5-7 (DL-threonine/water, Table 2) run in the “nucleation seeding” process mode. The corresponding model equations can be found in the chapters 2.1.5 (model), 2.2.4 (kinetics) and 2.3.4 (reparameterization). The original parameters with confidence intervals obtained from resubstitution are also given. Temperature mean centering (see Eq. 56) is applied using the reference temperature  $T_{mean}$  given.

Parameter	Estimated value	Confidence [%] (95%), Eq. 48	Sensitivity measure [-], Eq. 41
$G_1$	$8.0916 \cdot 10^{-9}$ [-]	0.8	21
$G_2$	$2.99 \cdot 10^{-7}$ [-]	0.2	111
$B_1$	59.77 [-]	2	14
$B_2$	2.9424 [-]	0.2	97
$E_{b, sek}$	-14.33 [kJ/mol]	1.6	12
$E_g$	-55.0 [kJ/mol]	0.14	12
$b$	2.14 [-]	0.01	-
$k_{p, sek, pre}$	$1.26 \cdot 10^8$ [#/(m <sup>3</sup> s)]	0.02	-
$g$	1.25 [-]	0.03	-
$k_{g, pre}$	$2.5 \cdot 10^{-8}$ [m/s]	0.1	-
$k_p$	$2.96 \cdot 10^4$ [#/(m <sup>3</sup> s)]	0.8	7
$k_{prim}$	0.37 [-]	3	4
$k_{prim2}$	$1.3 \cdot 10^{-10}$ [-]	$1.6 \cdot 10^8$	0
$k_d$	1.28 [kg/(s m <sup>2</sup> )]	11.6	0.4
$E_d$	-53.1	25	0.1
$k_v$	0.113 [-]		
Condition	$\infty$ [-]		
Collinearity index $\gamma$	$3.7 \cdot 10^8$ [-]		
Goal function	77 [-]		
$s_1$	0.01 [-]		
$s_2$	0.18 [-]		
$T_{mean}$	30 [°C]		

Unfortunately it was not possible to use the same parameters already estimated for the crystal growth and secondary nucleation rates based on other experimental data as given in Table 14 to model the experimental runs including the kinetics of dissolution and primary nucleation.

The estimation problem based on the three runs of the “nucleation seeding” strategy is badly set as the condition of the sensitivity matrix turns to infinity. Also the collinearity index is very high. The main reason for the incapacity to accurately estimate the parameters is the parameter  $k_{prim2}$  which has a comparably very high confidence interval ( $1.6 \cdot 10^8\%$ ) and a sensitivity measure of nearly zero. This parameter should be fixed to a reasonable value or calculated using a theoretically derived expression.

The sensitivities of the parameters governing the dissolution kinetics are also quite low. In order to handle the estimation problem properly these parameters should also be fixed to reasonable values. It seems appropriate and relatively easy to obtain the dissolution kinetics from individual experimental runs (Saenz de Jubera, 2006).

Nevertheless the numeric values of the estimated parameters lie in the range of parameters found in literature and therefore seem reasonable (see again (Elsner et al., 2005; Garside & Shah, 1980)).

#### **4.6.2 Parameter estimation using FBRM data and optical rotation**

The conclusions of chapter 4.2 stated that the correlation between the second moment of the particle size distribution and the counts of the FBRM-probe is prone to errors introduced by the simplifying assumptions made when using the presented probe calibration procedure.

Nevertheless some information regarding the particle size distribution or moments thereof is needed in order to correctly estimate nucleation *and* growth rate kinetic parameters. The question arising when using the FBRM-technique for this task is whether the CLD-data can be used directly to parameterize a kinetic model of the process. Such a way the process model could be used for an accurate prediction of productivity and/or particle properties such as size or size distribution. The strategy used here (others are possible, see (Heinrich, 2008) for a recent overview) is outlined in the following.

The model introduced in chapter 4.5 is used to calculate the particle size distribution at every time point using the method of characteristics as presented in (Kumar &

Ramkrishna, 1997) to solve the model. The method of characteristics (MOC) can be easily applied when no nucleation of the counter enantiomer takes place (see also chapter 4.5). It offers the advantage of no numerical dispersion along with high numerical stability using a defined grid with just a small number of nodes. 50 nodes on a linearly discretized grid from 0-1 mm are used here.

There are two established approaches to utilize the calculated particle size distributions and/or chord-length distributions for parameterization of a population balance model. One approach is to use the chord length distribution data directly to estimate CLD-based kinetics (Togkalidou et al., 2004; Trifkovic et al., 2008; Yu et al., 2008). However, then the model can also only be used to predict CLDs. Further on the coupling of the population balance to the mass balance can only be realized on an empirical basis. Another and in a way superior option is to use a suitable model to transfer the calculated particle size distribution into a chord length distribution or vice versa. Then the CLD resulting from the transformation of the PSD can be adjusted to the measured CLD by a variation of the free kinetic model parameters. This way the model should be capable of predicting properties of the particle size distribution along with the composition of the fluid phase.

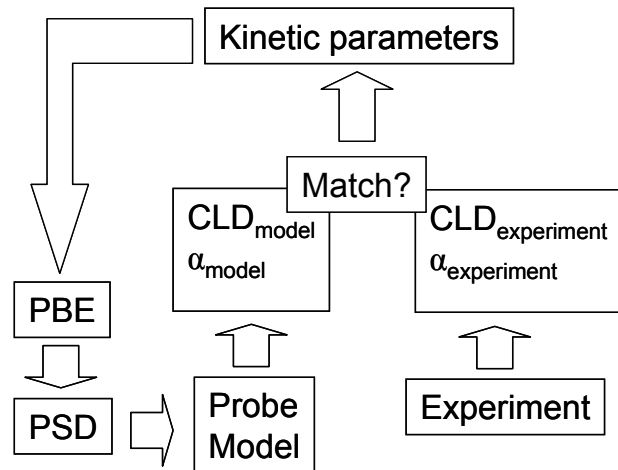


**Figure 74:** Illustration of the chosen method for parameter estimation.

There are different methods available to transform a particle size distribution into a chord length distribution and vice versa. However the back transformation from CLD to PSD is usually mathematically ill posed (A.Ruf, 2000; Worlitschek, Hocker & Mazzotti, 2005). A different and in some aspects more efficient way is to use a forward model as formulated in (Kail et al., 2007; Kail et al., 2008b) in order to relate model calculations to FBRM-data. This approach is investigated further in this work

and illustrated schematically in Figure 74. The approach circumvents the ill-posed character of the transformation of CLD to PSD which makes the method more robust with respect to measurement errors of the CLD-data.

The recently developed model for the FBRM probe (Kail et al., 2007; Kail et al., 2008b) is used as a means of a forward transformation of the calculated PSD to a CLD (Kail 2009). The FBRM probe model relies on the implemented geometry of the particles to be measured. All necessary inputs to the model are illustrated in Figure 75 in order to give an overview. To illustrate the method and the problem of the implementation of a particle geometry typical crystals of the amino acid DL-threonine are depicted in Figure 17. The crystals are modeled as a simple elongated rectangle which should provide a good representation of their actual appearance. Important in this context is the ratio between length and width of the crystals. As can be seen in the pictures the particles are usually quite elongated. For the sieved crystals an average ratio of length to width of approximately three to one has been measured. For the actual seed crystals and crystals inside the process an average length to width ratio of approximately six to one has been found. These geometries are an important input to the model. Another input variable that has to be provided is the refractive index of the medium. For the calibration experiments (see next chapter) the refractive index of ethanol, used as the liquid phase, has been inserted ( $n=1.36$ ). For the crystallization system the refractive index depends on the mass fraction of threonine in solution. It has been set to a value of  $n=1.36$  corresponding to a mass fraction of 15% DL-threonine dissolved in water, measured at 30° Celsius (Mettler-Toledo refractometer). Luckily here the refractive index of the calibration system is quite similar to the actual crystallization system (actual values: Ethanol: 1.3614, Threonine/water (15% threonine content): 1.358).

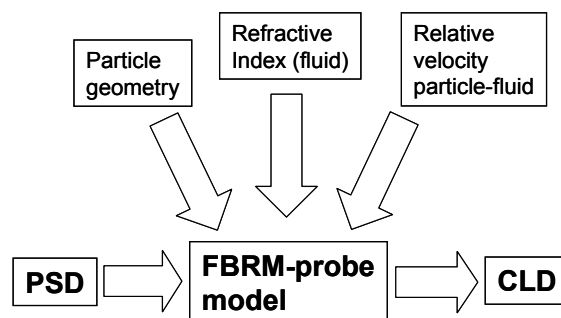


**Figure 75:** Illustration of the necessary input data for the probe model in order to transform a measured PSD into a CLD.

The ratio of length to width can be quantified by use of the volumetric shape factor  $k_v$ :

$$V_{solid} = k_v \cdot L^3 \quad \text{Equation 108}$$

Apart from the implementation of the crystal geometry and the setting of the refractive index there are not many further possibilities to adjust the FBRM probe model. The remaining free parameter inside the probe model is a velocity factor accounting for the relative velocity between laser (2m/s nominal scanning speed) and crystals suspended in the vessel. Since the stirring speed in the experiments performed is quite high (500 rpm) calculations have been performed in order to estimate the average crystal velocity in the stirred vessel. A standard CFD-calculation has been performed using FLUENT with ten crystals of different size (500  $\mu\text{m}$  and 1mm length respectively) inserted at random points inside the vessel in order to approximate the average crystal velocity. The resulting velocity distributions are given in Figure 76 and Figure 77. From the calculations an average particle velocity in the vessel of 1m/s can be estimated. Therefore the velocity factor is set to 0.5 as the particle velocity is approximately half of the nominal laser rotational velocity.

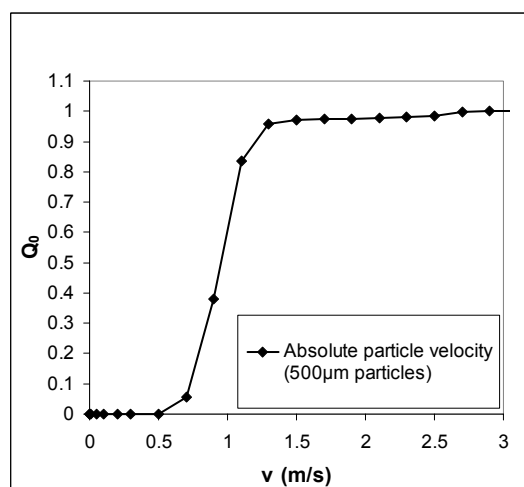


**Figure 76:** Cumulative absolute velocity distribution of particles of 500  $\mu\text{m}$  length in a stirred vessel (calculation with FLUENT, based on 10 randomly inserted particles, 3.5 seconds calculation time, 3 blade propeller stirrer at 500 rpm).

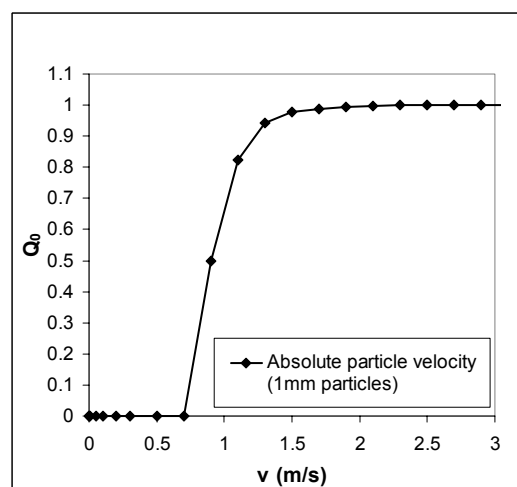


**Figure 77:** Cumulative absolute velocity distribution of particles of 1000  $\mu\text{m}$  length in a stirred vessel (calculation with FLUENT, based on 10 randomly inserted particles, 3.5 seconds calculation time, 3 blade propeller stirrer at 500 rpm).

In order to check the basic validity of the approach for the investigated system some preliminary experiments using L-threonine crystals suspended in ethanol are performed. Since threonine is nearly insoluble in ethanol the particle size distribution

of the suspended crystals should not be altered significantly after their introduction into the vessel. After some time breakage of the crystals due to crystal-stirrer or crystal-crystal collisions could alter the particle size distribution. However this fact was neglected due to the fact that the measured CLD-moments did not change significantly over time (except for the largest sieve fraction).

During all measurements the CLD data provided by the FBRM-probe is sorted into 50 linear channels in the range from 1 to 1000  $\mu\text{m}$ . The corresponding settings of the model parameters of the FBRM probe are given in Table A 16 in the Appendix.

Experiments were carried out in order to “calibrate” the probe similar to the procedures presented in (Vaccaro et al., 2007; Wynn, 2003). A goal of this calibration procedure was to find a correlation between the measured CLD and the CLD resulting from a transformation of the PSD measured with the optical microscope using the probe model.

To find this calibration three additional experiments have been carried out. The experiments were done in the same 1.5 liter vessel used for the crystallization experiments. Instead of using a DL-threonine solution sieved fractions of L-threonine crystals were suspended in ethanol. The stirring rate was set to 500 rpm for all experiments. The sieve fractions used were 63-90 $\mu\text{m}$ , 90-150 $\mu\text{m}$  and 150-212 $\mu\text{m}$ . The particle size distributions of these three fractions obtained with microscopic image analysis are given in Figure 38.

The crystals of each of the sieve fractions were added in portions of approximately 5g to the vessel. The exact amounts added are given in Table 3.

In the stirred vessel the chord length distribution was measured by the inserted FBRM-probe. Additionally a sample of each of the sieve fractions was measured using microscopic image analysis. The measured particle size distribution (PSD) for the three sieve fractions is given in Figure 85. The measured CLD of the suspended crystals and the CLD resulting from the model transformation of the measured PSD after the first addition of crystals are displayed in Figure 78. A scaling based on total particle number was done in order to compare the added samples with the measured samples (same number of particles).

The resulting CLDs after the subsequent additions of crystalline material are given in Figure 79 and Figure 80. When comparing the resulting CLDs with the measured CLDs it is obvious that the fit is unsatisfying. Thus, the model is not capable of describing the chord length distribution for all three fractions and for the different

amounts of crystals added (5, 10, 15g). The size region of the chord sizes is predicted quite accurately, but the weighting of the chord counts is shifted towards larger sized crystals. In order to solve this problem it was assumed that the particles are mainly transparent and only generate a reflection around the edges. This phenomenon is sometimes referred to as chord splitting (Tadayyon & Rohani, 1998). It was incorporated into the model assuming that the particles are a quarter as thin as the actual particles. The approach followed is illustrated in Figure 81. Thereby more elongated particles are incorporated into the model in order to generate reflections at the particle edges only.

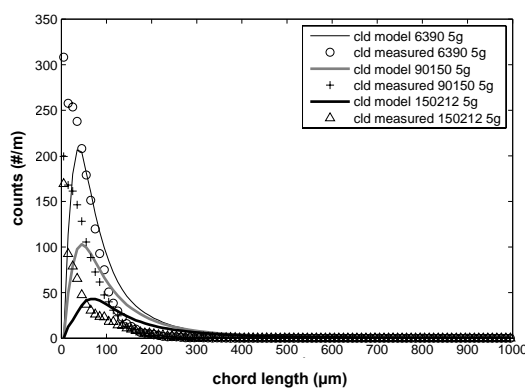


**Figure 78:** Measured and calculated scaled CLDs using the model from (Kail et al., 2008b) after the first addition of crystalline material.

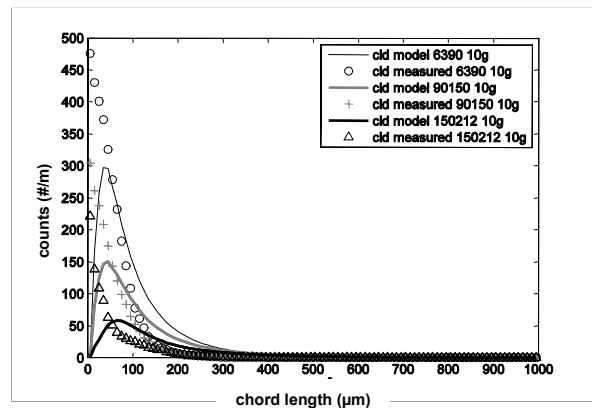


**Figure 79:** Measured and calculated scaled CLDs using the model from (Kail et al., 2008b) after the second addition of crystalline material.

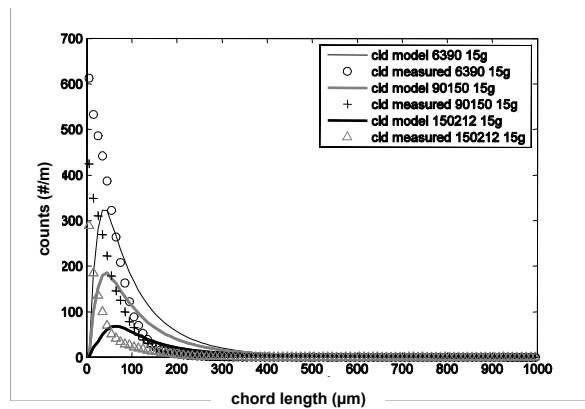


**Figure 80:** Measured and calculated scaled CLDs using the model from (Kail et al., 2008b) after the third addition of crystalline material.

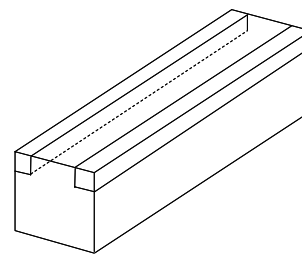


**Figure 81:** Illustration of implemented alternative geometry that is used to simulate chord splitting. The small particles on the edges are the substitute for the original particle.

Therefore for every particle two reflections are generated with a smaller size as the original particle which simulates a particle that is half transparent with respect to its surface area. Due to the scaling the effect of generating two chords per particle can be neglected.

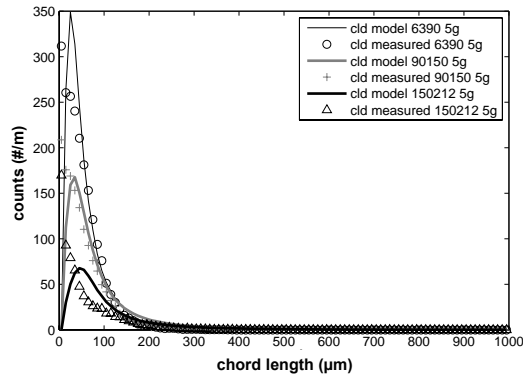


**Figure 82:** Measured and calculated scaled CLDs using the model from (Kail et al., 2008b) after the first addition of crystalline material. It was assumed that the particles are measured twice in order to simulate chord-splitting.

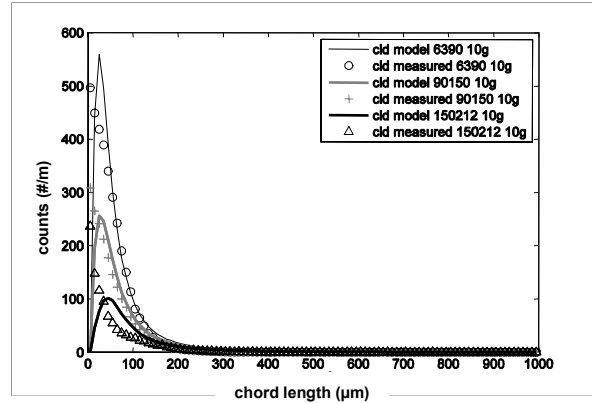


**Figure 83:** Measured and calculated scaled CLDs using the model from (Kail et al., 2008b) after the second addition of crystalline material. It was assumed that the particles are measured twice with an opaque center in order to simulate chord-splitting.

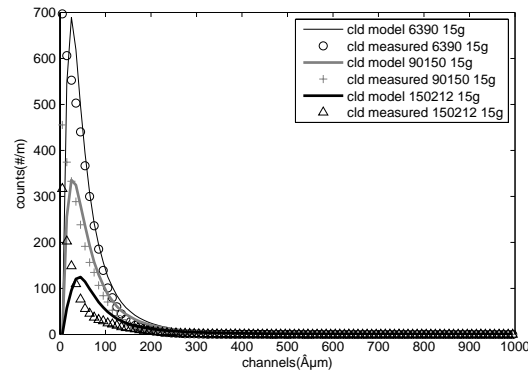


**Figure 84:** Measured and calculated scaled CLDs using the model from (Kail et al., 2008b) after the third addition of crystalline material. It was assumed that the particles are measured twice with an opaque center in order to simulate chord-splitting.

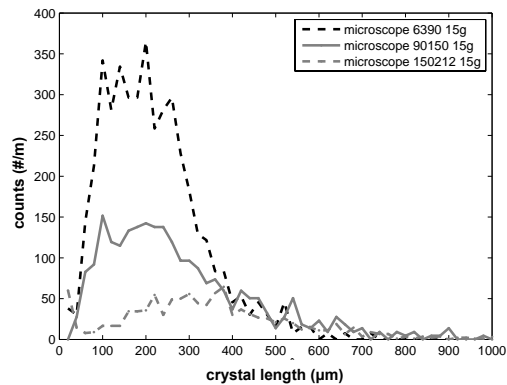


**Figure 85:** PSDs for the three sieve fractions used for probe calibration. The distributions were scaled to a mass of 15g.

Comparing the quality of the fits from Figure 82 to Figure 84 the agreement gets slightly worse with an increase in particle size. This can be attributed to the fact that the further used assumption of exactly half opaque particles might hold for the smaller particles but not for the larger particles. There the edges already have significant

widths which might be too large in comparison to the actual edge widths seen by the laser. The results of this modified approach of correlating CLD and PSD are displayed in Figure 82, Figure 83 and Figure 84 for the three fractions investigated. The fit of the model to the experimental data has significantly improved so that the model can be tested for analyzing the three actual crystallization experiments in order to estimate kinetic parameters.

The chosen objective function used for the parameter estimation (Equation 109) incorporates two parts to be minimized. One part of the objective function presented in Equation 109 consisted of the difference between calculated and measured CLDs. A second additive part of the objective function consisted of the difference between the optical rotation values  $\alpha$  also measured in the three runs and the corresponding values calculated using the model and a polarimeter calibration function.

In Figure 86 the measured CLD trajectories for the seeded experiment 1 (see Table 2) were plotted over time and channel length. From the course of the CLD-distribution it can be seen that the process is dominated by nucleation. The number of counts increases heavily along the experimental run.

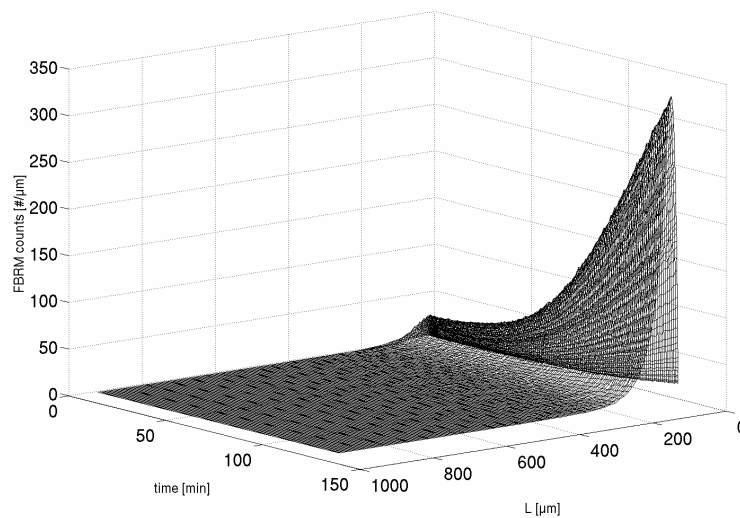


**Figure 86:** Measured CLD trajectories for the seeded experiment 1 from Table 2.

Figure 87 shows the chord length distribution fitted to the experimentally determined one using Equation 109 as the objective function. Instead of using the full CLD-distribution the zero moment of the CLD-distribution is used in order to fit the model to the experimental data. It showed that using the zero moment of the chord length distribution gave a comparable quality of the fit of the model to the experiment. This

is far superior to fitting the whole distribution in terms of calculation times and assignment of weights to the objective function. Additionally, the assignment of weights to the objective function, which would have been necessary in order to scale the two parts when using full distributions, would have been more complicated and would result in introducing additional parameters.

$$F_{goal} = \sum_{j=1}^{N_{data}} \left( \left( \frac{\alpha(i, j)_{measured} - \alpha(i, j)_{calculated}}{\alpha(i, 0)_{measured}} \right)^2 + \left( \frac{\mu(i, j)_{0,scal,CLD,measured}}{\max(\mu(i)_{0,scal,CLD,measured})} - \frac{\mu(i, j)_{0,scal,CLD,calculated}}{\max(\mu(i, j)_{0,scal,CLD,calculated})} \right)^2 \right) \quad \text{Equation 109}$$

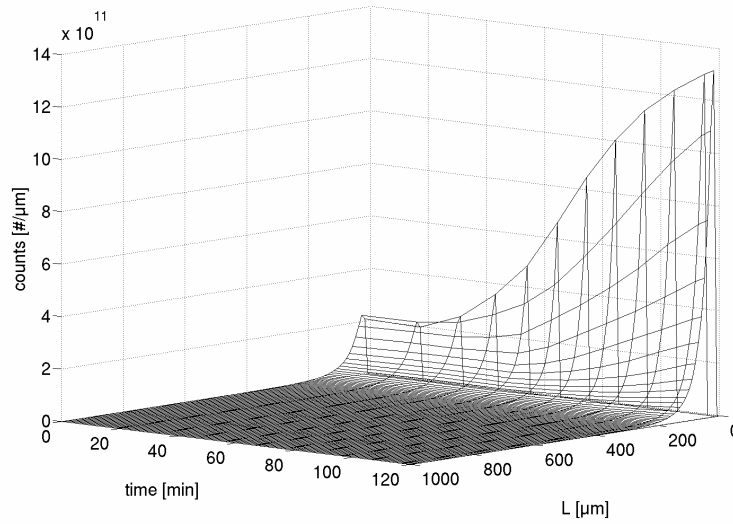


**Figure 87:** Calculated best fit CLD trajectories for the seeded experiment 1 from Table 2.

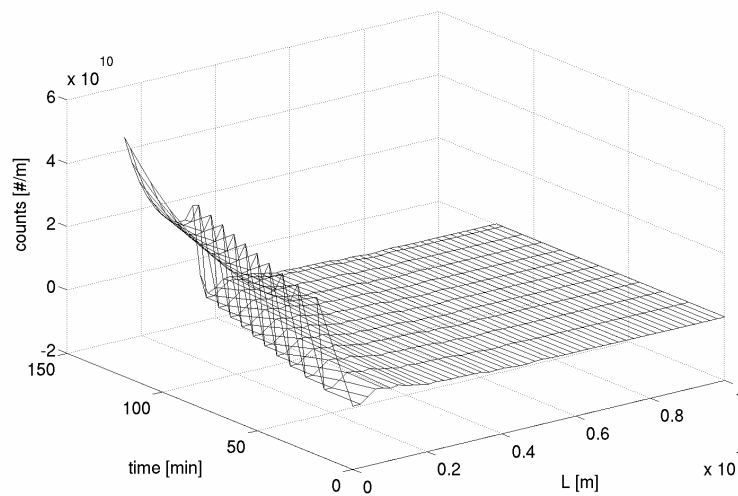


**Figure 88:** Calculated best fit PSD trajectories for experiment 1 from Table 2.

In Figure 89 the measured and calculated CLD-distributions at the end of the batch are compared. In Figure 90 the measured and calculated optical rotation trajectories are displayed. For both trajectories a relatively good agreement between model and experiment is obtained. The calculated PSD, that is the basis for the determination of the CLD presented in Figure 87, is given in Figure 88. A significant occurrence of secondary nucleation can be seen. In order to evaluate the quality of the estimated parameters and of the method applied the fit was made using all three experiments performed at different conditions (Table 2) simultaneously. The calculated and measured CLD-distributions at the end of the individual runs are plotted in Figure 90.

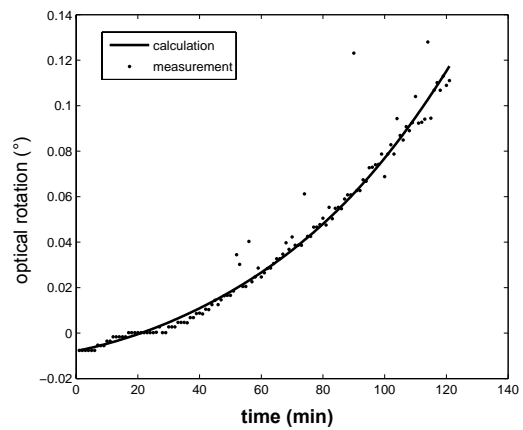
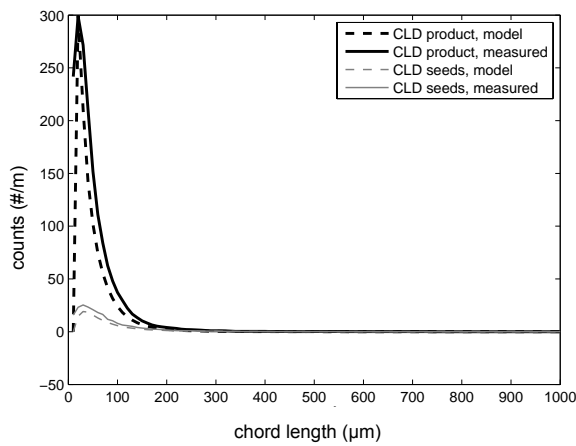


**Figure 89:** Comparison of calculated and measured chord length distributions at the end of the first experimental run.

**Figure 90:** Comparison between calculated and measured optical rotation for experimental run 1.

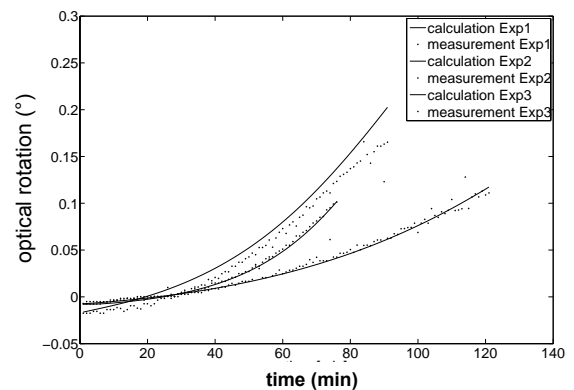
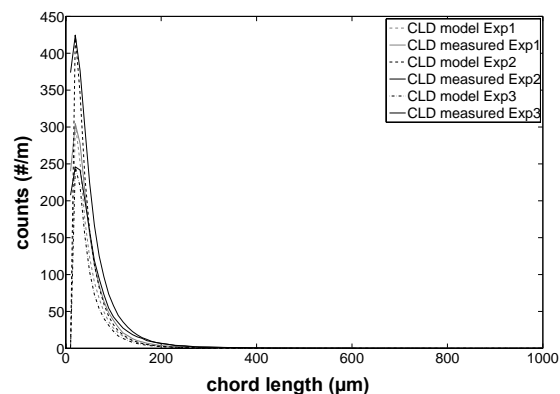


**Figure 91:** Calculated and measured chord length distribution for three seeded experiments (experiment 1 to 3 from Table 2) at the end of the experimental run.

**Figure 92:** Comparison between calculated and measured optical rotation (experiment 1 to 3 from Table 2).

For an easy illustration of the course of the chord lengths of the particle population along the three experimental runs also the zero moments based on the measured chord length distributions are plotted in Figure 93.

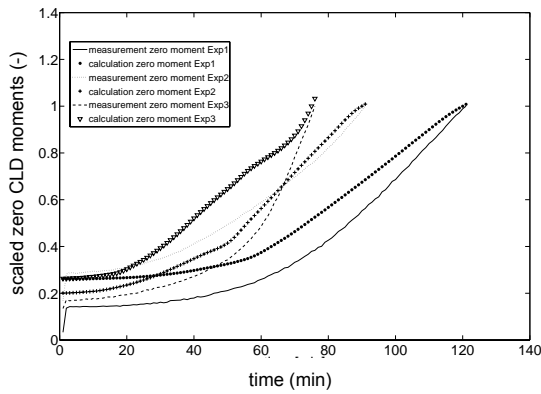


**Figure 93:** Comparison of calculated and measured zero moments of the chord length distributions for three seeded experiments (experiment 1 to 3 from Table 2).

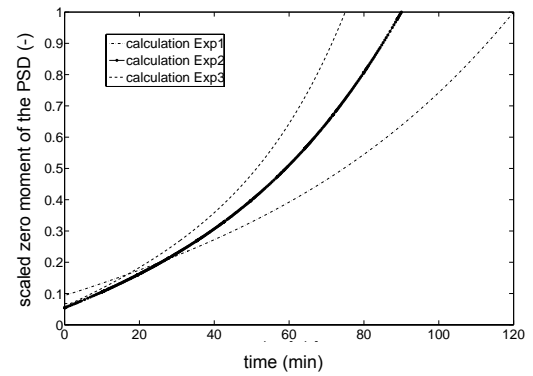


**Figure 94:** Comparison between calculated and measured zero moments of the particle size distribution.

Obviously there is still some potential for improvement. For this reason it was tried to improve the implementation of the geometry further by considering the exact morphology of a DL-threonine crystal as presented in (Kumar et al., 2006). However, it turned out, that the performance of the model could not be improved significantly by the addition of two edges.

**Table 16:** Resulting kinetic parameters after fitting the model simultaneously to the data provided by experiment 1-3 (DL-threonine/water, Table 2). The corresponding model equations can be found in the chapters 2.1.5 (model), 2.2.4 (kinetics). Temperature mean centering (see Eq. 56) is applied using the reference temperature  $T_{mean}$  given.

Parameter	Estimated value
$b$	2.9 [-]
$k_{b, sek, pre}$	$2.1 \cdot 10^{16}$ [#/(m <sup>3</sup> s)]
$g$	1 [-]
$k_{g, pre}$	$5.6 \cdot 10^{-8}$ [m/s]
$E_{b, sek}$	-11 [kJ/mol]
$E_g$	-319 [kJ/mol]
$T_{mean}$	30 [°C]

When a closer look is taken on the numerical values of the parameters obtained after fitting the model simultaneously to the data obtained from experiments 1 to 3 (Table 16), parameter values are obtained for the orders and prefactors that lie in the range expected (compare for example (Garside & Shah, 1980) and (Elsner et al., 2005) for values on the system DL-threonine water). However, as often the case in crystallization experiments, the physical significance of the parameters is not fully convincing. Especially the values for the activation energies appear to be less reliable. In particular  $E_g$  is atypically high. Confidence intervals of the estimated parameters were not determined in the presented case study.

The presented approach using FBRM-data along with a suitable probe model and information regarding the fluid phase composition seems to be feasible to identify parameter values.

If the probe model could be further improved using a better representation of the optical properties of the particles, the presented method should provide an excellent tool for parameter estimation, process monitoring, process control and particle design applications.

#### **4.6.3 Parameter estimation using mass fractions and PSDs**

For means of comparison the commercially available software package (Parsival<sup>®</sup>, (Wulkow, 1996; Wulkow, 2001; Wulkow, 2007; Wulkow et al., 2001b; Wulkow et al., 2001a)) is used to model the preferential crystallization processes presented in this work. It contains a package for parameter estimation that is used to estimate the free model parameters (chapter 2.2.4) and analyze the estimates with similar methods as introduced in chapter 2.3. The numerical solver used in the package is a h,p-moving grid Galerkin scheme (Wulkow, 1996), (Wulkow et al., 2001a). Different methods to estimate free parameters are available in the software package. The methods used in this work are a simulated annealing stochastic optimizer (Kirkpatrick et al., 1983) and the so called “automatic projection” routine which uses a damped Gauss-Newton procedure (Wulkow, 2007), (Telgmann, 2007), (Deuflhard, 2004). Several parameters can be estimated based on experimental data. The quality of the parameters is evaluated using an approach based on sensitivity calculation giving confidence intervals for the individual parameters and the determinant and condition for the

corresponding sensitivity matrix of the whole problem (similar to the methods presented in chapter 2.3.2.).

However in contrast to the previously presented goal function (Equation 107) here the parameter estimation is undertaken based on the mass fraction trajectories of the two enantiomers and the particle size distribution at defined time points (usually seeds and product). The particle size distributions were measured using microscopy in combination with an automated image analysis software (see chapter 3.4.2).

Similar to the estimation routine used in chapter 4.6.1 the estimation problem is split up into different blocks. One block uses experiments 1-4 of Table 2 to estimate the free kinetic parameters for secondary nucleation and crystal growth. Experiments 6-9 are used to estimate the free parameters for the primary nucleation kinetics. Experiment ten is used to model the process concept “milled seeds”.

In order to use multiple experiments as a basis for the parameter estimation the model has to be formulated in “concentration mode”. In this simulation mode the initial particle size distribution can be implemented as a mathematical function instead of measured data points. Then the function can be manipulated by a variation of the free parameters of the function to account for differences in mass of seeds or shape of the particle size distribution. Several functions were tested in order to model the particle size distribution of the seed crystals used in experiments 1-4 and 10. It was found that among the tested models (Bernstein polynomials, gamma distribution, log normal distribution, exponential distribution) a modified exponential distribution (Equation 110) gave an optimal fit to the measured data (on the topic of fitting distributions see also (John et al., 2007), (Motz, 2004)). The goal function used for the fitting is given in Equation 111 and accounts not only for the difference in number distribution but also weighs the moments of the particle size distribution. This addition is done in order to conserve mass, surface and length as well as the total number of crystals. In Parsival the estimated parameters  $k_1$ ,  $k_2$  and the  $x_{50}$  can be inserted into a measured data file (.mdf-File) along with other data (e.g. mass fractions, temperature,...).

Figure 95 shows the result of a typical seed crystal number distribution and the model used to fit the distribution.

$$F(x) = k_1 \cdot e^{\left(\frac{-x}{x_{50}^2}\right)} + k_2 \quad \text{Equation 110}$$

$$F_{goal} = \sum_{i=1}^{N_{data}} (F(x)_{measured} - F(x)_{calc})^2 +$$

$$10^9 \cdot (\mu_{1,measured} - \mu_{1,calc}) + 10^{11} \cdot (\mu_{2,measured} - \mu_{2,calc}) + 10^{13} \cdot (\mu_{3,measured} - \mu_{3,calc})$$

Equation 111

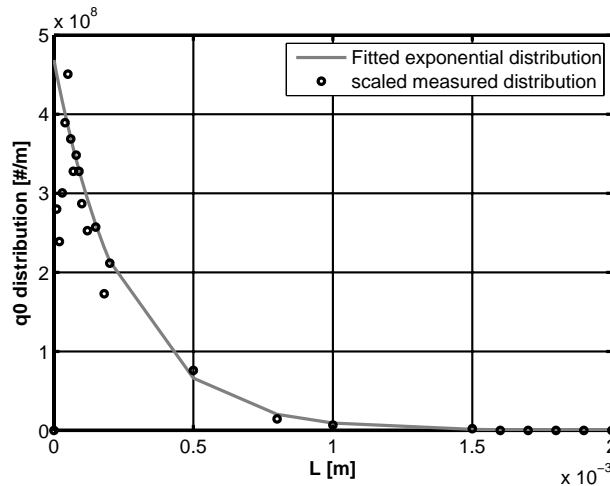


Figure 95: Model and measured number of seed crystals. Parameters:  $k_1=1.1973e5 \text{ \#/m}$ ;  
 $k_2=9.3e3 \text{ \#/m}$ ;  $x_{50}=255 \text{ \mu m}$ ;  $mass=2.2 \text{ g}$ .

The routine for the estimation of the parameters is to first use a simulated annealing run using 100 steps to obtain a good fit between model and experiment. Then the automated projection routine is used to improve the fit and obtain information about the reliability of the fitting via condition of the *FIM* and confidence intervals of the parameters.

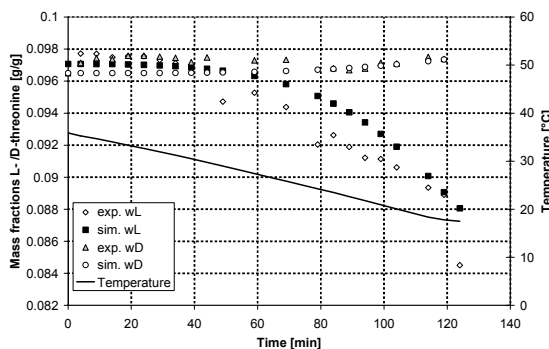


Figure 96: Measured and simulated mass fractions and temperature trajectories for an experiment using seeds (“Defined seeding”). The experimental data is taken from experiment 2 in Table 2.

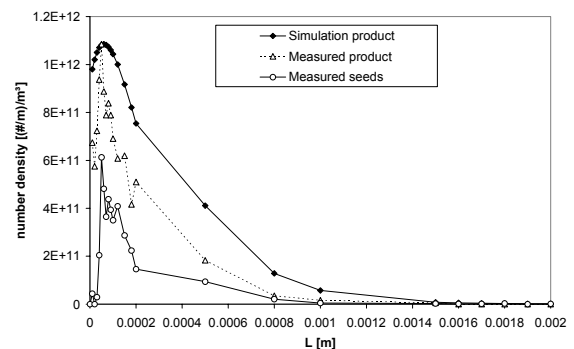
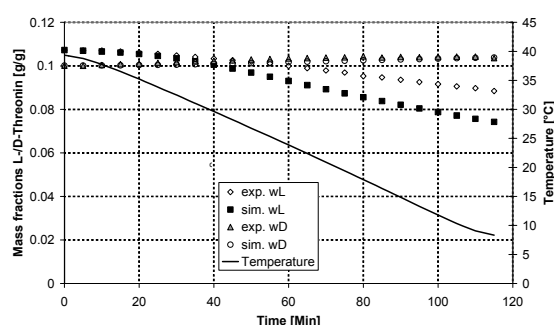


Figure 97: Measured and simulated particle size distributions for an experiment using seeds (“Defined seeding”). Measurements are taken from experiment 2 in Table 2.

The performance of the final, parameterized model is shown in Figure 96 for a seeded run (Experiment 2, Table 2). The parameterized model and the measured data agree fairly well with each other. The same can be stated for the measured and simulated particle size distributions of the product crystals (see Figure 97).

In Figure 98 to Figure 99 the results for exemplary runs of the process concepts “Milled seeding” and “Nucleation seeding” are shown. Also for these two cases the accordance between model and experiment is good.



**Figure 98:** Measured and simulated mass fractions and temperature trajectories for an auto seeded run (“Milled seeding”). The experimental data is taken from experiment 10 in Table 2.

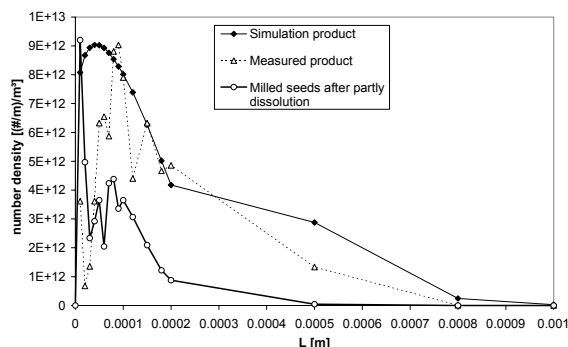


**Figure 99:** Measured and simulated particle size distributions for the product of an auto seeded run (“Milled seeding”). Measurements are taken from experiment 10 in Table 2. The particle size distribution of the seeds refers to the crystals that remain after partly dissolution of the racemic feed (see chapter 2.2.2).

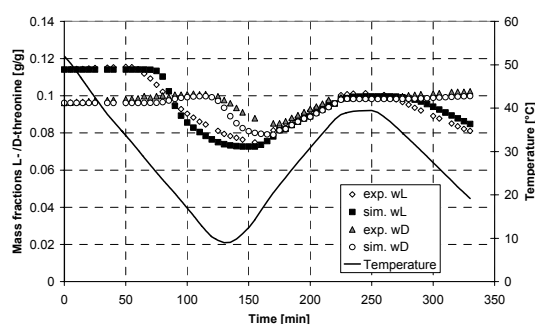


**Figure 100:** Measured and simulated mass fractions and temperature trajectories for an auto seeded run (“Nucleation seeding”). The experimental data is taken from experiment 6 in Table 2.

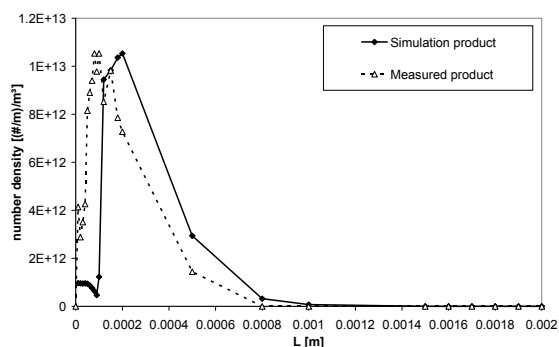


**Figure 101:** Measured and simulated particle size distributions for the product of an auto seeded run (“Nucleation seeding”). Measurements are taken from experiment 6 in Table 2.

The deviations between the individual model calculations and the measurements can be attributed to the experimental errors, the uncertainty of the kinetic parameters and the idealizations incorporated into the model structure.

The resulting set of kinetic parameters is given in Table 17. Some parameters have been fixed because they were determined by independent measurements ( $k_v$ ,  $E_d$ ,  $k_d$  (Saenz de Jubera, 2006)). Others were fixed to reasonable values because they could not be determined based on the available experimental data ( $E_{b,sek}$ ,  $E_g$ ) (Diaz, 2005).

**Table 17:** Optimal values for the estimated kinetic parameters for the three investigated process concepts based on experiments 1-3 (“Defined seeding”), 5-8 (“nucleation seeding”) and 9 (“milled seeding”) for the system DL-threonine/water. The corresponding model equations can be found in the chapters 2.1.5 (model), 2.2.4 (kinetics).

Parameter	“Nucleation” and “Defined seeding”		“Milled process”	
	Estimated value	Confidence interval (95%) [%], Eq. 48	Estimated value	Confidence interval (95%) [%], Eq. 48
$b [-]$	5.8	22.6	7.6	50.8
$k_{b,sek,pre} [\#/(m^3s)]$	$1.1 \cdot 10^{28}$	137.6	$2.1 \cdot 10^{28}$	156.8
$g [-]$	2.5	15.1	2.2	39.4
$k_{g,pre} [m/s]$	140.2	58	21.1	129
$k_b [\#/(m^3s)]$	$4 \cdot 10^8$	n.a.	-	-
$k_{prim} [-]$	6.9	n.a.	-	-
$E_{b,sek} [kJ/mol]$	92.6	0 (fixed)	92.6	0 (fixed)
$E_g [kJ/mol]$	40.7	0 (fixed)	40.7	0 (fixed)
$E_d [kJ/mol]$	57	0 (fixed)	57	0 (fixed)
$k_{prim2} [-]$	$3.6 \cdot 10^{-7}$	0 (fixed)	-	-
$k_d [kg/(s m^2)]$	$1.7 \cdot 10^9$	0 (fixed)	$1.7 \cdot 10^9$	0 (fixed)
$k_v [-]$	0.113	0 (fixed)	0.113	0 (fixed)

#### 4.6.4 Possible improvements of parameter estimation – experimental design

In chapter 4.6.1 a parameterization of the kinetic process model (chapter 2.1.5) was undertaken but delivered not fully satisfying results. In order to improve the reliability of the estimated parameters additional experimental data are needed.

In order to reduce the amount of experiments necessary for the parameterization of the kinetic model presented (chapter 2.1.5 and chapter 2.2.4, Equation 13 and Equation 15, Equation 28-Equation 35) a dynamic experimental design is undertaken with the design goal of lowering the condition of the *FIM* (modified E-optimal design, Equation 55).

The degrees of freedom for the experiment are the mass of seeds, the initial mass fractions of the two enantiomers, the cooling rate and the endtime of the run. A constraint is put on the temperature difference between starting temperature and end temperature. The difference should be smaller than the metastable zone width of the system. The metastable zone width in Kelvin was approximated using a correlation that is a function of the cooling rate in °C/h taken from (Polenske, 2003) for the system under investigation:

$$MSZW = 0.479 \cdot \dot{T} + 6.3 \quad \text{Equation 112}$$

The constraint has to be introduced since it is assumed that no primary nucleation of the counter enantiomer takes place during the experiments.

To illustrate the effect of the number and quality of experiments used to estimate the kinetic parameters the estimation has been done using the data of the first experiment, than the data from the first and second experiment and so on. The results of the procedure in terms of the condition of the *FIM* and the collinearity index are shown in Figure 102 and Figure 103.

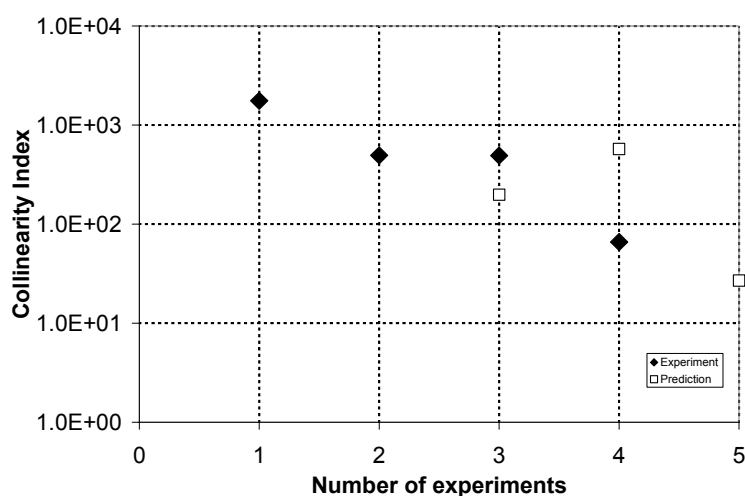


**Figure 102:** Collinearity index of the *FIM* for the designed (calculated) and the actual experiment.

One can see that the condition of the *FIM* decreases after each additional experiment performed. When comparing the predicted value of the *FIM* and the resulting value after a refitting of the model to the obtained experimental data deviations of the calculated and measured condition are obtained. These differences can be attributed to the uncertainty of the model parameters and should decrease more and more with the number of experimental runs performed.

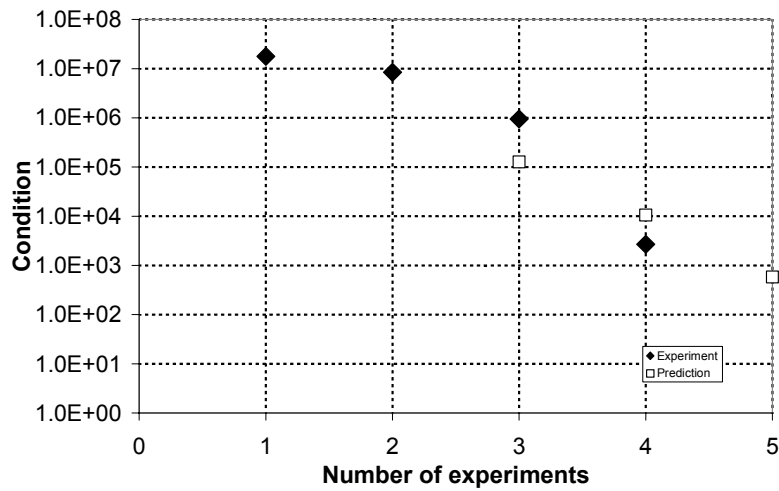


**Figure 103:** Condition of the *FIM* for the designed (calculated) and the actual experiment.

The course of the collinearity index is not as pronounced as that for the condition. This is due to the condition being the design goal function of the dynamic design undertaken. Obviously the smallest eigenvalue can vary while the condition is still monotone decreasing (see Equation 49).

**Table 18:** Parameters for the designed experiments 3, 4 and 5. Only experiments 3 and 4 were actually performed.

Experiment	Seedmass [g]	$w_{rac,0}$ [-]	$dT_1$ [K/h]	$t_{end}$ [min]	$T_0$ [°C]	$T_{end}$ [°C]
3	1	0.194	1.8	467	39	25
4	1.4	0.2156	1	407(135)	46	39(43)
(5)	15	0.2054	4	228	42	15

After the fourth experiment the condition is still too high ( $\gg 1000$ ) indicating that the estimated parameter set is unreliable. When looking at the fit of the model to the experimental data (Figure 104, Figure 105) it can be seen that the quality of the fit in terms of the residuum is quite satisfying.

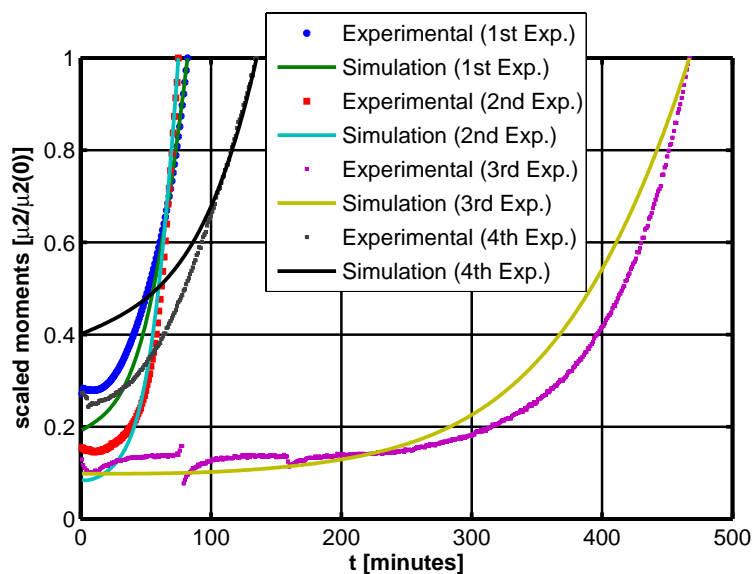


**Figure 104:** Calculated and measured scaled trajectories of the second moment of the particle size distribution compared with the scaled counts of the FBRM-probe (experiments 1 to 3 plus the designed experiment).

**Table 19:** Parameters, confidence intervals, sensitivity measures and measures for quality of fit for the estimation using reparameterized kinetics based on experiment 1 to 3 and the designed experiment 4 (Table 2). The original parameters with confidence intervals obtained from resubstitution are also given. Temperature mean centering (see Eq. 56) is applied using the reference temperature  $T_{mean}$  given.

Parameter	value	confidence [%] (95%)	Sensitivity measure [-]
$G_1$	$3.9221 \cdot 10^{-10}$ [-]	0.24	1700
$G_2$	$1.9508 \cdot 10^{-8}$ [-]	0.15	2705
$B_1$	$1.633 \cdot 10^5$ [-]	0.3	82
$B_2$	$5.04 \cdot 10^7$ [-]	0.2	402
$E_{b, sek}$	-43 [kJ/mol]	0.2	532
$E_g$	-116.3 [kJ/mol]	0.1	11500
$b$	1.98 [-]	0.01	-
$k_{b, sek, pre}$	$1.51 \cdot 10^9$ [#/(m <sup>3</sup> s)]	0.21	-
$g$	1.35 [-]	0.02	-
$k_{g, pre}$	$1.98 \cdot 10^{-7}$ [m/s]	0.1	-
<i>Condition</i>	$2.687 \cdot 10^3$ [-]		
<i>Collinearity index <math>\gamma</math></i>	66 [-]		
<i>Goal function</i>	206 [-]		
$s_1$	0.01 [-]		
$s_2$	0.18 [-]		
$T_{mean}$	30 [°C]		

The fourth experiment was only analyzed up to a time point (135 minutes) where two of the employed analytical devices (densitometer and FBRM) were not anymore measuring data of sufficient quality.

The fifth experiment was designed using the model parameterized after experiment 4. After the fifth experiment the condition should have been below a value of 1000 indicating a parameter set that should be reliable to a certain extent. The experiment was not carried out due to a lack of time and resources.

The kinetic parameters resulting from the fit after experiment 4 are given in Table 19. All values obtained lie in the range expected from literature. Only the activation energy of the crystal growth kinetic seems to be relatively high.

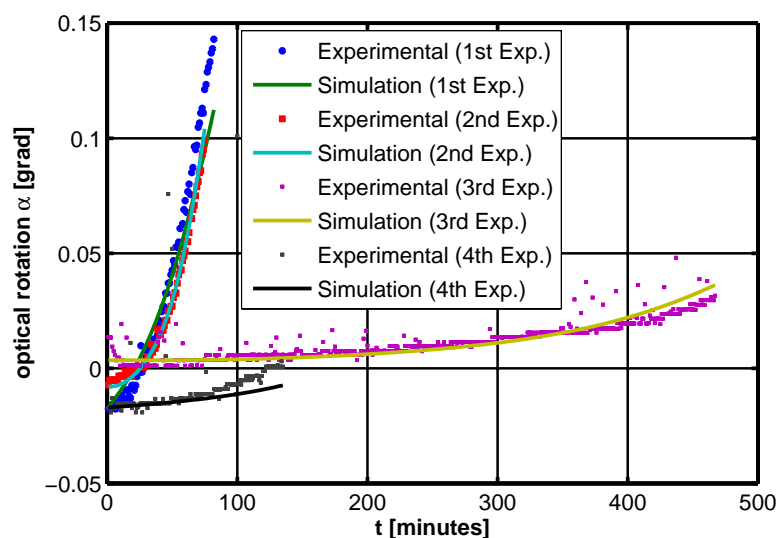


**Figure 105:** Calculated and measured trajectories of the optical rotation (experiments 1 to 3 plus the designed experiment).

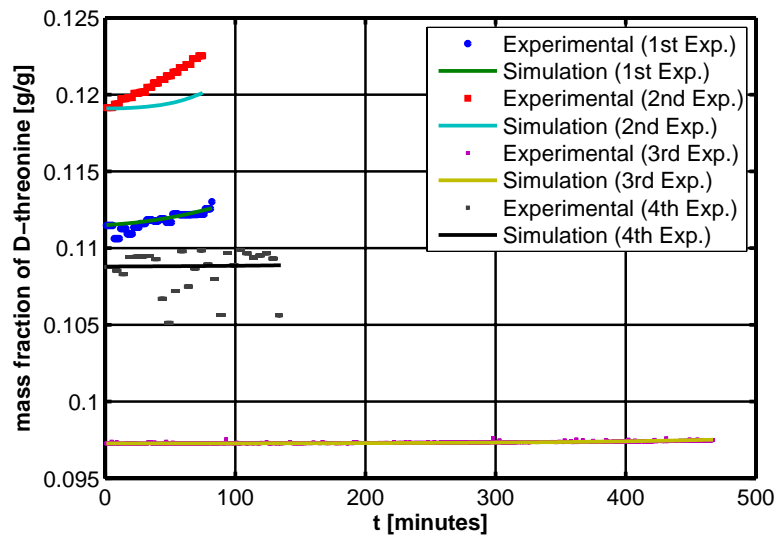


**Figure 106:** Calculated and measured trajectories of the D-threonine mass fractions (experiments 1 to 3 plus the designed experiment).

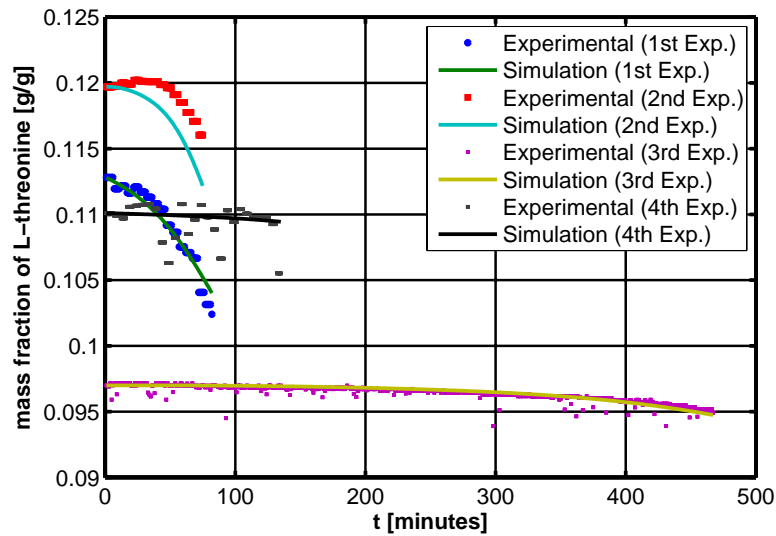


**Figure 107:** Calculated and measured trajectories of the L-threonine mass fractions (experiments 1 to 3 plus the designed experiment).

#### 4.6.5 Comparison of parameter estimation approaches

In the preceding chapters three different approaches for parameter estimation of the kinetic model parameters have been presented (chapters 4.6.1 to 4.6.3, see Table 13 for an overview over the different approaches). The corresponding model and the kinetics used can be found in chapters 2.1.5, 2.1.6 and 2.2.4 respectively.

To compare and evaluate the different kinetics in terms of the numerical values obtained is difficult. Some values as for example the activation Energy of crystal growth taken from Table 16 as of -319 [kJ/mol] seem very high compared with literature values (Garside, 1980). However, as one result of the evaluation and comparison of the presented parameter estimation approaches it has to be stated that it is very difficult to evaluate individual parameters. Instead, the obtained parameters have to be seen as a set that should be used as a whole. The reason for this is the significant cross correlation of the individual parameters. In this context the interested reader should look into chapter 2.3.1 for theory on parameter cross correlation and chapter 4.6.1 or Tables B 4 and B 5 for some correlation coefficients of the parameter sets used. The cross correlation could be partly reduced by the reparameterization of the crystallization coefficients. Nevertheless it could not be annealed totally. A second aspect is the type and quality of the experimental data used (see once more Table 13 for an overview). A set of kinetic parameters estimated based on optical rotation data and moments is not necessarily of good use for predicting the particle size distribution of an experiment.

To illustrate this the trajectories of a seeded experimental run (process concept “defined seeding”) have been predicted using the three different sets of kinetic parameters finally obtained (Table 16, Matlab<sup>®</sup>, optical rotation and CLD; Table 17, Parsival<sup>®</sup>, mass fractions and PSD; Table 19, Matlab<sup>®</sup>, optical rotation and moments).

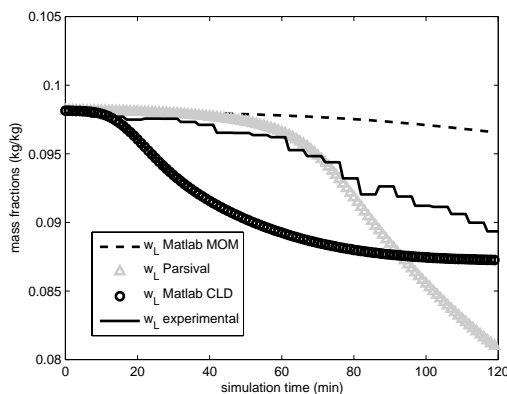


**Figure 108:** Simulated and measured mass fractions. The simulation runs were carried out using three different kinetics sets obtained from the three investigated parameter estimation approaches (Table 16, Matlab<sup>®</sup>, optical rotation and CLD; Table 17, Parsival<sup>®</sup>, mass fractions and PSD; Table 19, Matlab<sup>®</sup>, optical rotation and moments)

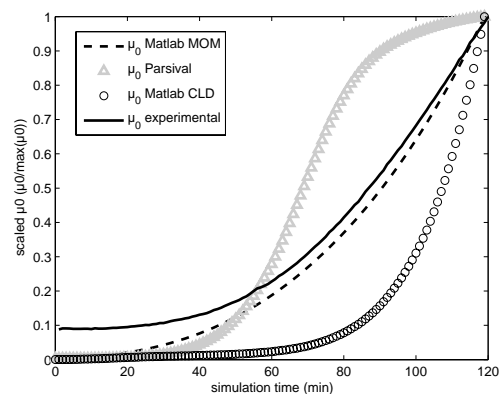


**Figure 109:** Simulated and measured scaled zero moments. The simulation runs were carried out using three different kinetics sets obtained from the three investigated parameter estimation approaches (Table 16, Matlab<sup>®</sup>, optical rotation and CLD; Table 17, Parsival<sup>®</sup>, mass fractions and PSD; Table 19, Matlab<sup>®</sup>, optical rotation and moments)

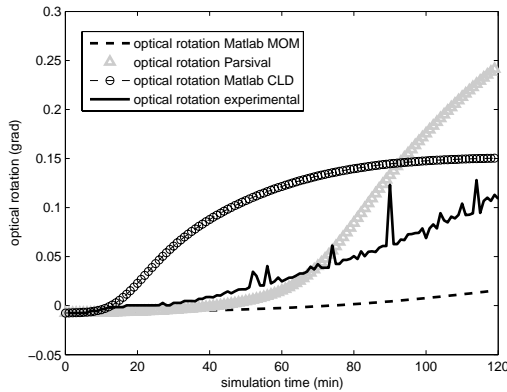


**Figure 110:** Simulated and measured optical rotation trajectories. The simulation runs were carried out using three different kinetics sets obtained from the three investigated parameter estimation approaches (Table 16, Matlab<sup>®</sup>, optical rotation and CLD; Table 17, Parsival<sup>®</sup>, mass fractions and PSD; Table 19, Matlab<sup>®</sup>, optical rotation and moments)

As can be seen in the Figures 102-104 no parameter set is capable of predicting the trajectory of zero moments, optical rotation or mass fraction of the target enantiomers in a perfect manner. Nevertheless all sets describe the trend of the two signals in a qualitative manner. The conditions of the experiment used for the test are given below in Table 20.

**Table 20:** Experimental conditions of the experimental data set used for comparison of the different parameter estimation approaches investigated in the thesis.

Exp.	$w_{L-thr}$ [g/g <sub>L.sg</sub> ]	$w_{D-thr}$ [g/g <sub>L.sg</sub> ]	$m_{Seed}$ [g]	$k_v$ [-]	$T_0$ [°C]	$(dT/dt)_1$ [K/h]	$T_1$ [°C]	$t_{annealing}$ [min]	$(dT/dt)_3$ [K/h]	$T_{Final}$ [°C]
Test experiment “Defined seeding”										
1	0.09815	0.09757	3.5	0.08	-	-	36	30	-9	18

#### 4.6.6 Comparison of confidence intervals obtained with different methods

One important aspect within parameter estimation is to obtain confidence intervals on the parameter estimates (Dochain & Vanrolleghem, 2001). Two alternative methods are used in this work. A very popular method is based on an evaluation of the Fisher information matrix as introduced in chapter 2.3.2 (Peterson, 2000). However this

method only provides an estimation of the *lower boundary* of the parameter estimates (Ljung, 1999). An alternative method that provides a distribution of the estimated parameters and actual confidence intervals of the parameters is the so called Bootstrap method introduced in chapter 2.3.3 (Efron, 1979; Efron & Tibshirani, 1993). Comparing the two methods different results can be obtained depending on the model under investigation and the model structure used (Joshi, 2007; Kay, 1993). Also the effect of a reparameterization of the kinetic expressions can be evaluated further based on the distribution histograms of individual parameters.

Using the parameter set given in Table 19 a Bootstrap run is performed. The experimental standard deviation needed in Equation 50 is estimated using Equation 51. As a basis for the difference between model and experiment the three first experiments given in Table 2 along with the designed experiment 4 are used. In order to estimate the number of parameter estimation runs that need to be performed in order to obtain a representative distribution of a parameter the variance of the kinetic parameter  $kg_1$  is plotted exemplarily over the number of fittings (Figure 111).

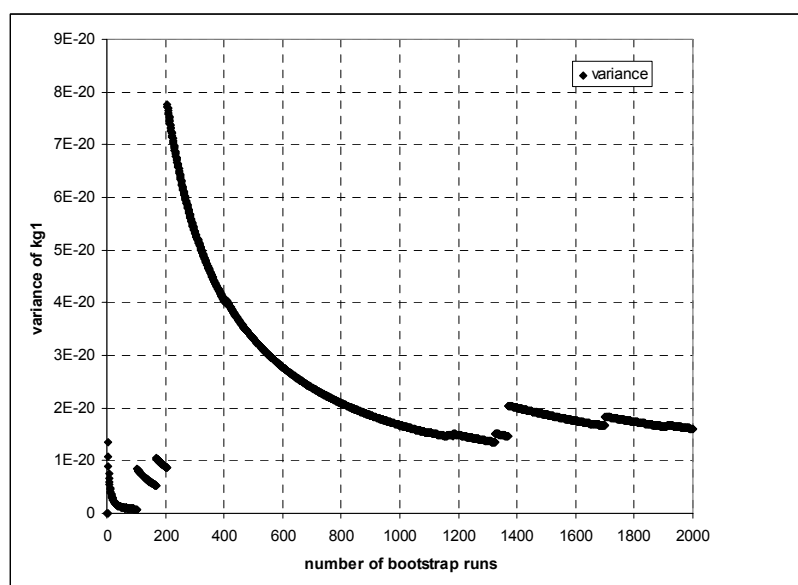


**Figure 111:** Variance of the kinetic parameter  $kg_1$  over number of bootstrap runs.

After a small number of fittings the variance of the distribution is oscillating highly. After approximately 2000 bootstrap runs the variance is more or less stable. Therefore in order to obtain representative confidence intervals at least 2000 bootstrap runs should be performed as a basis for the subsequent statistical analysis. This illustrates the drawback of the Bootstrap approach compared with the analysis of the Fisher information matrix: Very time consuming calculations have to be performed

(approximately three days calculation time on a Intel(R) Core(TM)2 Duo CPU E8400 @ 3.00GHz). As a prerequisite for the analysis of the resulting parameter distributions outliers have to be removed. The criteria for the identification of an outlier can be found in (Joshi, 2007) or (Montgomery et al., 2001). The parameter confidence intervals obtained from the procedure are given in Table 21.

**Table 21:** Confidence intervals obtained from bootstrap simulation runs (2000 fittings) of original free parameters, reparameterized kinetics and of the back transformed parameters.

Original kinetics:	Parameter	[±%]	Reparameterized kinetics:	Parameter	[±%]	Back transformation:	[±%]
	$kg$	117		$kg_1$	68	$kg$	57
	$kb$	264		$kb_1$	315	$kb$	229
	$g$	31		$kg_2$	10	$g$	9
	$b$	40		$kb_2$	62	$b$	91
	$Eg$	32		$Eg$	20	$Eg$	20
	$Eb$	147		$Eb$	689	$Eb$	689

When comparing the size of the confidence intervals obtained from the analysis of the Fisher Information (see Table 8 and chapter 2.3.2) obviously the confidence intervals obtained from the Bootstrap runs are much larger than the ones calculated using the Fisher information. However the numeric values of the confidence intervals delivered by the bootstrap approach are much more realistic than the values obtained from the analysis of the Fisher Information matrix.

Keeping in mind that the confidence intervals obtained from the analysis of the Fisher Information are only a lower boundary of the real confidence intervals the results of the Bootstrap analysis seem to be more appropriate to judge the size of the parameter confidence region.

When the size of the confidence intervals obtained from a fitting of the original kinetic parameters is compared with the size of the confidence intervals of a fitting of the reparameterized kinetics it can be seen that the confidence intervals of the reparameterized kinetics are significantly smaller. That stresses the fact that a reparameterization of the kinetic equations should be done wherever applicable (see also chapter 2.3.5).

The actual distributions of the individual parameters are given in the histograms from Figure 112 to Figure 121. From the distributions of the parameters it can be seen that the assumption of a normally distributed parameter which is frequently applied (Bard, 1974) is often not applicable. The reason for the strong bias of the parameter

distributions is the nonlinearity of the model (see the kinetic equations in chapter 2.2.4). The result in terms of model identifyability based on the *FIM* is supported by the results obtained from the bootstrap analysis. The number of experiments is insufficient to estimate all kinetic parameters reliably. Therefore the confidence intervals are quite large. The distribution of the parameters and correlation plots of parameter pairs can be used to evaluate the parameter cross correlation by analyzing the shape and size of the resulting correlation plots (Joshi, 2007). However this analysis is skipped here. Another recently developed method is the so called sigma point method (Schenkendorf et al., 2009) which provides realistic confidence intervals compared to the analysis of the Fisher information while the calculation times are significantly smaller than the ones of a typical bootstrap simulation run.

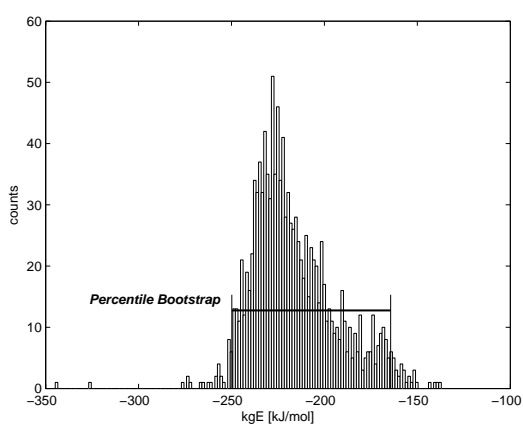


**Figure 112:** Distribution histogram of the kinetic parameter  $E_g$ .

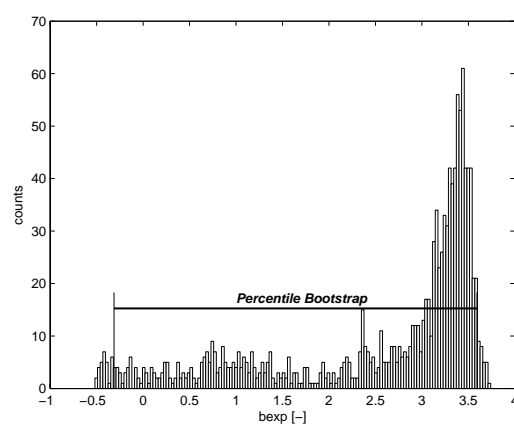


**Figure 113:** Distribution histogram of the kinetic parameter  $b$ .

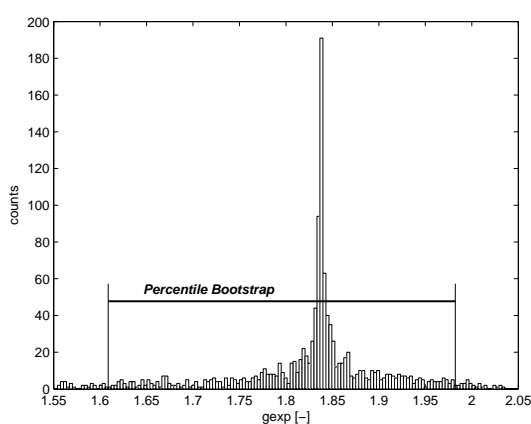


**Figure 114:** Distribution histogram of the kinetic parameter  $g$ .

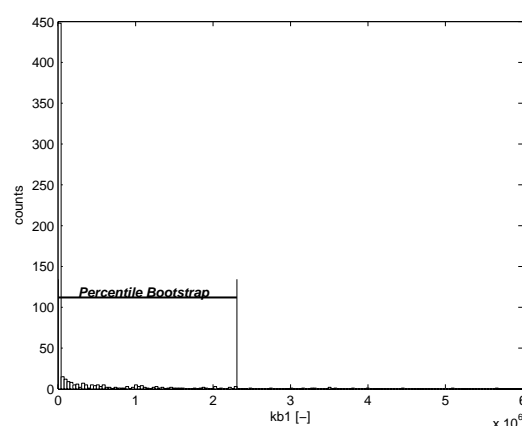


**Figure 115:** Distribution histogram of the kinetic parameter  $kb_I$ .

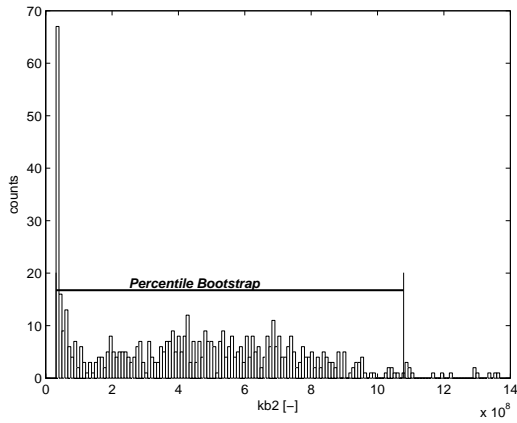


**Figure 116:** Distribution histogram of the kinetic parameter  $kb_2$ .

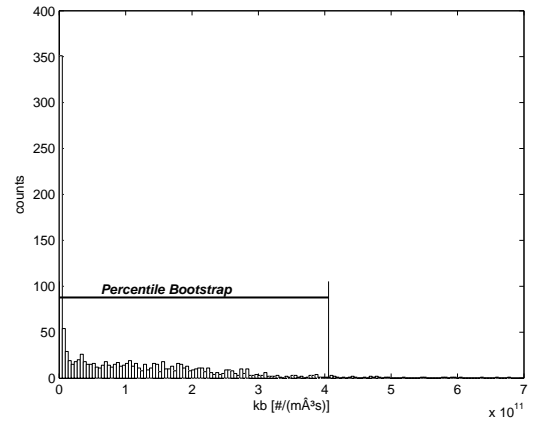


**Figure 117:** Distribution histogram of the kinetic parameter  $kb$ .

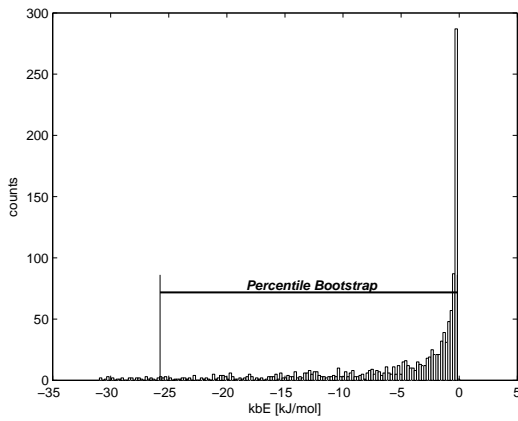


**Figure 118:** Distribution histogram of the kinetic parameter  $E_b$ .

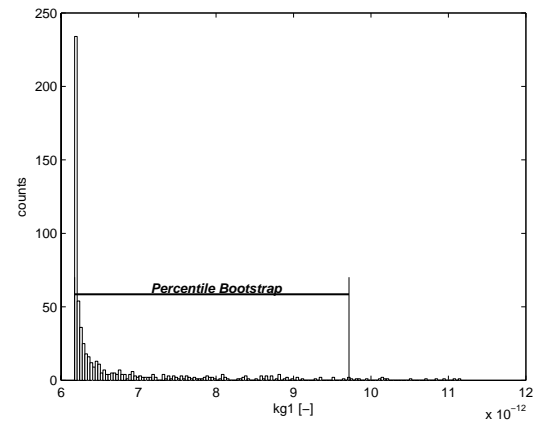


**Figure 119:** Distribution histogram of the kinetic parameter  $kg_1$ .

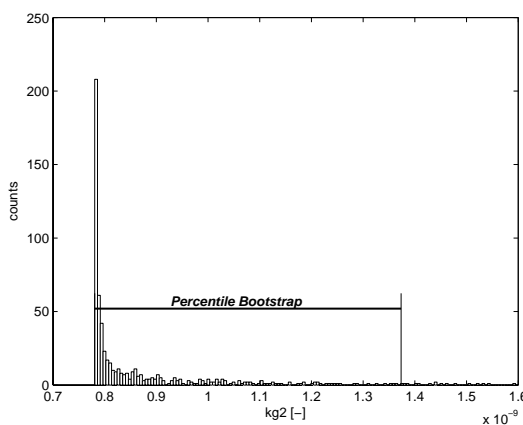


**Figure 120:** Distribution histogram of the kinetic parameter  $kg_2$ .

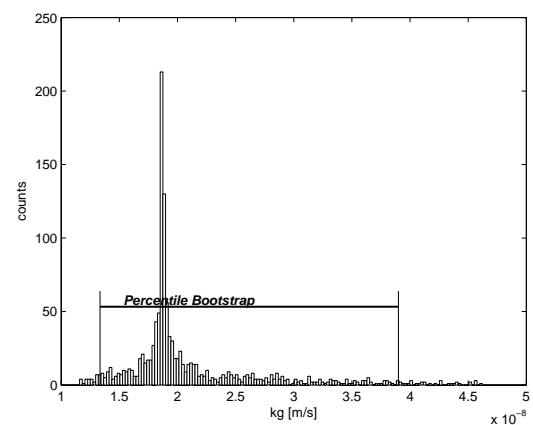


**Figure 121:** Distribution histogram of the kinetic parameter  $k_g$ .

## 4.7 Parametric studies – Trends for product design

In pharmaceutical crystallization the most important aspects of the product are the product purity and crystalline structure (polymorph type, composition) (Chow et al., 2008; Cussler & Moggridge, 2001; Rohani et al., 2005). The exact shape of the particle size distribution is a secondary but nevertheless important issue (Yu et al., 2007). Once a model has been approved and validated it can be used to optimize the process productivity under the required purity constraints (see chapter 4.8). Additionally the model can be used to calculate process conditions under which the particle size distribution or characteristic properties of the particle size distribution such as the median or the variance of the distribution can be achieved.

At first it has to be checked whether the parameterized model is in principle capable of predicting the particle size distribution of the product crystals (Braun et al., 2004). Afterwards a particle design can be undertaken. One of the questions arising in this context is whether the particle size distribution can be designed without any loss in yield or productivity.

Usually when looking at product design not the complete particle size distribution is designed or modified characteristic values of the distribution are looked at. Very often the mean particle size ( $L_{50}$ ) and the variance ( $\sigma^2$ ) of the particle size distribution are taken as characteristic parameters of a distribution (John et al., 2007; Ward et al., 2006). Sometimes also other characteristic diameters such as the  $L_{10}$  or  $L_{90}$  or a quotient thereof are used to characterize a particle size distribution (Stieß, 1995).

When looking at the presented system DL-threonine/water a goal for product design could be to reduce the fines content in the product and harvest bigger crystals, which is a typical design goal in crystallization (Braun et al., 2004).

When looking at the presented process concepts there are two main options to influence the particle size distribution of the product crystals (see Figure 122). One option is to use a different seed particle size distribution. This way, while applying identical cooling profiles as well as initial mass fractions of the enantiomers, different product particle size distributions can be obtained. The second option is to use similar seed particle size distributions while modifying the temperature trajectory or the initial mass fractions of the batch run. Obviously the two ways of modifying the particle properties can also be combined.

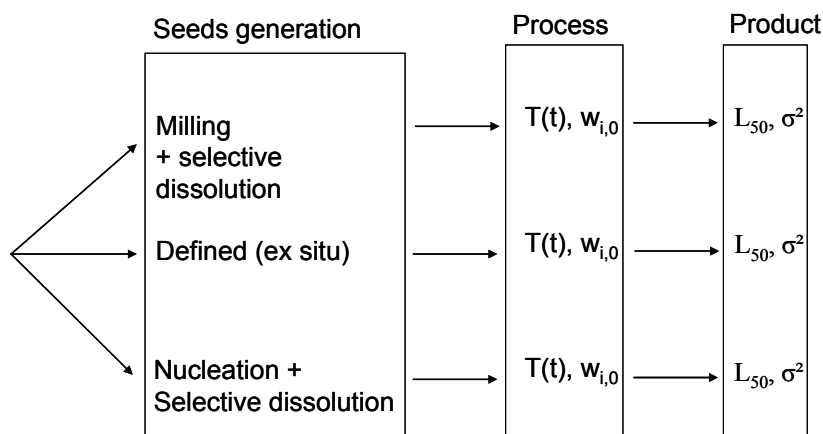


**Figure 122:** Illustration of different routes to product design for a preferential crystallization process.

A problematic aspect in this context is the multivariate optimization problem that arises when certain particle properties are wanted along with high purity and yield or productivity respectively (Bhat & Huang, 2009; Ward et al., 2006).

The process concept “nucleation seeding” offers the possibility to modify the particle size of the seed crystals and the product in situ. Thus compared with other process strategies it offers the possibility of an optimization of productivity and yield as well as particle properties within a single batch. Using the previously developed process model implemented in Parsival<sup>®</sup> (chapter 4.6.3) a parameter variation study is performed for the seeding part of this process concept in order to investigate the influences of the initial enantiomeric excess and the temperature profile on the  $L_{50}$  and variance of the produced seed crystals. For the calculations the kinetics given in Table 17 are used. While varying the temperature profiles it showed that only the cooling rate of the first cooling step ( $dT_1$ ) and the initial enantiomeric excess had a significant influence on the resulting mean particle size and variance. Interestingly the end temperature of the first cooling step (varied with 5, 10 and 15 °C) as well as the heating rate of the dissolution step ( $dT_2$ ) had no significant influence on the seed crystal properties. For the calculations the sum of the initial mass fractions of both species was set fixed to a value of 0.253 kg/kg, which is the value obtained after the optimization of the process concept in terms of productivity as shown in chapter 4.8. The results of the parameter variation are displayed for the  $L_{50}$  of the seed crystals in Figure 123. The influence on the variance is displayed in Figure 124. The varied parameters and results are given in Table A 17 in the Appendix. By varying the initial cooling rate the mean size of the seed crystals can be modified from 160 $\mu$ m to

254 $\mu\text{m}$ . The variance as a measure of the width of the particle size distribution varies within a range of  $2.06 \cdot 10^4 \mu\text{m}^2$  to  $3.37 \cdot 10^4 \mu\text{m}^2$ . Therefore it can be stated that for the seed crystals with a high enantiomeric excess and a slow cooling rate large particles are obtained while the width of the particle size distribution is small. For a low enantiomeric excess combined with high cooling rates the opposite can be stated. However the influence of the initial enantiomeric enrichment on the variance of the particle size distribution seems to be negligible.

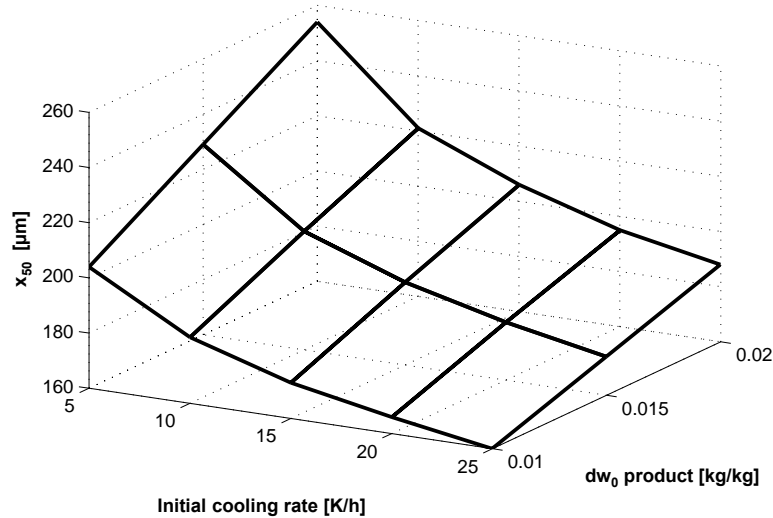


**Figure 123:** Influence of the cooling rate of the nucleation step and the initial enantiomeric enrichment onto the mean particle size ( $L_{50}$ ) of the seed crystals at the end of the annealing phase.

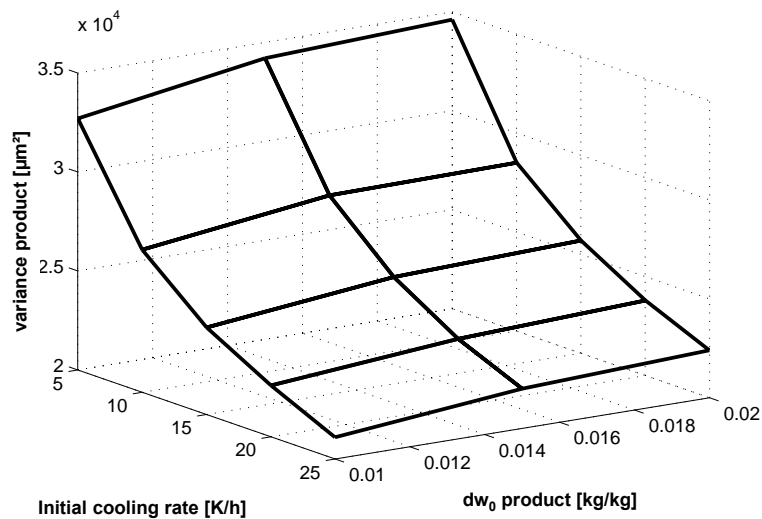


**Figure 124:** Influence of the cooling rate of the nucleation step and the initial enantiomeric enrichment onto the variance of the particle size distribution of the seed crystals at the end of the annealing phase.

Obviously, if different seed crystals are used also different products are obtained when similar cooling rates for the crystallization step are chosen. Nevertheless the resulting productivity of the runs might differ, which in turn leads to a challenging optimization problem (Bhat & Huang, 2009).

To investigate the effect of the different seed particle size distributions simulations have been carried out using the same parameter field as for the seed production processes in order to obtain the mean diameter and variance for the particle size distribution of the product crystals. The results of the simulations are given in Figure 125 and Figure 126. The results in terms of the maximal and minimal values to achieve are however a little different for the product.

The maximal mean particle size in the investigated range is 378  $\mu\text{m}$ . It is obtained using an initial excess of 0.02 kg/kg and a cooling rate of 5 K/h for the initial cooling leading to primary nucleation. The smallest particle size is obtained for an initial excess of 0.02 kg/kg and a cooling rate of 25 K/h. On the contrary the highest variance of the particle size distribution is obtained for an initial excess of 0.01 kg/kg and a cooling rate of 5 K/h.

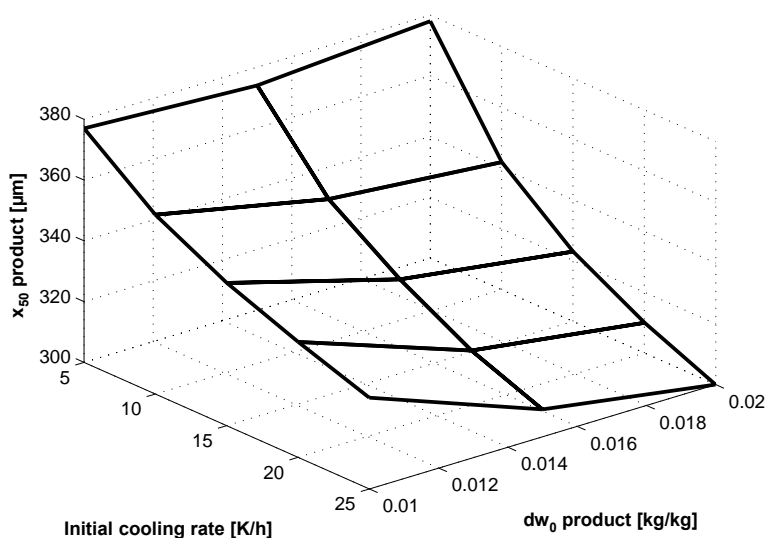


**Figure 125:** Influence of the cooling rate of the nucleation step and the initial enantiomeric enrichment onto the mean diameter of the particle size distribution of the product crystals at the end of the cooling crystallization using a fixed cooling rate and time for the cooling crystallization step.

The smallest variance is obtained for an initial excess of 0.02 kg/kg and 25 K/h cooling rate. Therefore the usual goal of particle design of obtaining rather large particles with a small width of the distribution can not be accomplished. Another interesting fact is that the initial enantiomeric excess does not seem to have a

significant influence on the mean particle size of the product. Therefore it should be possible to modify the particle properties of the product while still obtaining an optimal process yield. Obtaining an optimal productivity as well might be difficult due to a possibly slow cooling rate for the initial nucleation step.

Future work in this field could be the use of a 2 dimensional model in order to obtain a more realistic representation of the needle like threonine crystals and try to modify the particle elongation by choosing appropriate process conditions.

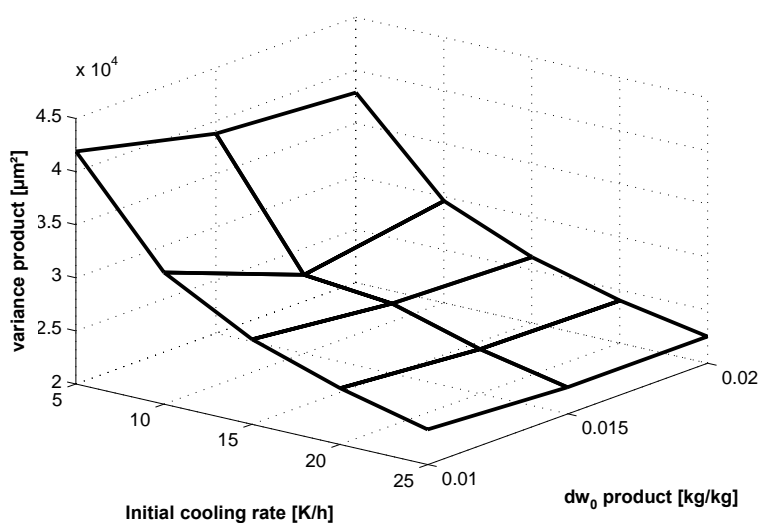


**Figure 126:** Influence of the cooling rate of the nucleation step and the initial enantiomeric enrichment onto the variance of the particle size distribution of the product crystals at the end of the cooling crystallization using a fixed cooling rate and time for the cooling crystallization step.

## 4.8 Illustration of process optimization

The model parameterized and validated using the simulation software Parsival<sup>®</sup> can be used to design the specific process concepts or optimize certain process objectives like productivity, or properties of the particle size distribution (e.g.  $x_{50}$ ). In the case study presented in this chapter for illustration the process productivity of the different process concepts is optimized using the previously developed model. The calculations are then compared with actual experiments to check the predictive capacity of the model.

For each of the process concepts the process productivity has to be defined individually to account for the different process modifications. The definitions of the optimization constraints and the productivity are given in Equations 66 to 71. In Equation 113 the constraints for the process concept “defined seeding” are

formulated. A product purity above 98% on a mass basis has been set as a constraint. Additionally it has been assumed that the processes are run in cyclic mode (see chapter 2.2). Therefore the goal of the optimization is not only to optimize the productivity of a single batch but also to assure that the mass of product is approximately equal to the mass of the target enantiomer present at the beginning of the batch as initial enantiomeric excess. This is necessary to smoothly run the process in a cyclic operation mode. In the cyclic process scheme, after solid-liquid separation, an amount of racemate is added to the recycled mother liquor that is twice the mass of the harvested product. This concept has to be applied to all process concepts in one form or the other. For the process concept “milled seeds” (see chapter 2.2.2) half of the added racemate is dissolved, the other half acts as seed material. Therefore for this process concept the mass of the product has to equal the mass of the obtained seed material (Equation 113, Equation 114). Equation 115 and Equation 116 are applied as constraints for the optimization of the productivity of the process concept “defined seeding”. Finally for the process concept “nucleation seeding” Equation 117 and Equation 118 are used as optimization constraints.

$$\begin{aligned}
 t &\sim t_{End} \\
 Pur &\geq 0.98 \\
 m_D - m_L &\geq m_{Seeds}
 \end{aligned}
 \tag{Equation 113}$$

$$Prod = \frac{\mu_{3,L} \cdot \rho \cdot k_v - \mu_{3,D} \cdot \rho \cdot k_v}{m_{Batch} \cdot (t_{End} + 0.5[h])}
 \tag{Equation 114}$$

$$\begin{aligned}
 t &\sim t_{End} \\
 Pur &\geq 0.98 \\
 m_D - m_L &\geq m_{Seeds}
 \end{aligned}
 \tag{Equation 115}$$

$$Prod = \frac{\mu_{3,L} \cdot \rho \cdot k_v - \mu_{3,D} \cdot \rho \cdot k_v - m_{Seeds}}{m_{Batch} \cdot (t_{End} + 0.5[h])}
 \tag{Equation 116}$$

$$\begin{aligned}
 t &\sim t_{End} \\
 Pur &\geq 0.98 \\
 m_D - m_L &\geq m_{ee,0}
 \end{aligned}
 \tag{Equation 117}$$

$$Prod = \frac{\mu_{3,L} \cdot \rho \cdot k_v - \mu_{3,D} \cdot \rho \cdot k_v}{m_{Batch} \cdot (t_{End} + 0.5[h])}
 \tag{Equation 118}$$

The original purpose of the parameter estimation module of the Parsival<sup>®</sup> suite is not an optimization using special goal functions like the ones given in Equation 113 to

Equation 118. However this problem can be overcome by the introduction of a measured data file with artificially generated experimental data for the process productivity. Then the parameters that can be modified in order to increase the productivity of the batch can be “estimated” using the parameter estimation software by fitting the obtained productivity to the “measured” productivity. Of course the artificially generated productivity has to be chosen within a reasonable range closely above the assumed optimal productivity of the process.

**Table 22:** Manipulated parameters for the optimization of the different process concepts along with the resulting optimal values for the productivity.

Process concept:	"defined seeding"	"milled seeds"	"nucleation seeding"
Parameters:	$dT_1$	$dT_1$	$dT_3$
	$t_{cooling}$	$t_{cooling}$	$t_{cooling}$
	$w_{L,D,0}$	$w_{L,D,0}$	$w_{L,D,0}$
	$m_{ee0}$	$m_{seed}$	$m_{ee0}$
	$m_{seed}$	-	$m_{seed}$
Optimized productivity [kg/(h kg)]:	0.0121	0.0256	0.00414

The parameters that are manipulated in order to optimize the process productivity differ slightly, depending on the process scheme under investigation. They are listed along with the productivities introduced into the measured data files in Table 22. The resulting values for the optimal experiments are given in Table 23.

**Table 23:** Experimental conditions for the optimal runs of the individual process concepts.

Process concept:		"defined seeding"	"milled seeds"	"nucleation seeding"
Parameters:	$T_0$	57	40	65
	$T_{End}$	37	10	37
	$dT$	12	16	18
	$t_{cooling}$	170	116	70
	$w_{L,D,0}$	0.2334	0.21	0.25314
	$ee_0$	0.018281	-	0.0081785
	$m_{seed}$	8.55	11.8	-
Optimized productivity [kg/(h kg)]:		0.0121	0.0256	0.00414

As can be seen from the definition of the goal functions half an hour of preparation time is assumed for each of the different process schemes. This time accounts for the preparation of the added racemate, tempering of the vessel etc..

Under these assumptions the best process concept in terms of productivity is the process concept “milled seeds”. However the results given in Table 22 are based on calculations. To check for the predictive power of the model experiments are performed under the calculated optimal conditions given in Table 23. The temperature of the vessel has been controlled by the built in controller of the thermostat. The comparison between model calculations and the actual experiments is illustrated in Figure 127 to Figure 129. It can be seen that the temperature control of the thermostat worked fine for the different process concepts. The comparison of the calculations with the measured data shows that all process concepts can be predicted with an acceptable deviation. The deviations are not large but can have a significant influence on the product purity. If the counter enantiomer has already nucleated inside the vessel (nucleation shower) the product will not match the desired purity requirements. The model proved its predictive quality, but could not be used to perfectly match the outcome of the experiments. Therefore the model should be used to calculate suitable process conditions for the optimal batch of a cyclic run.

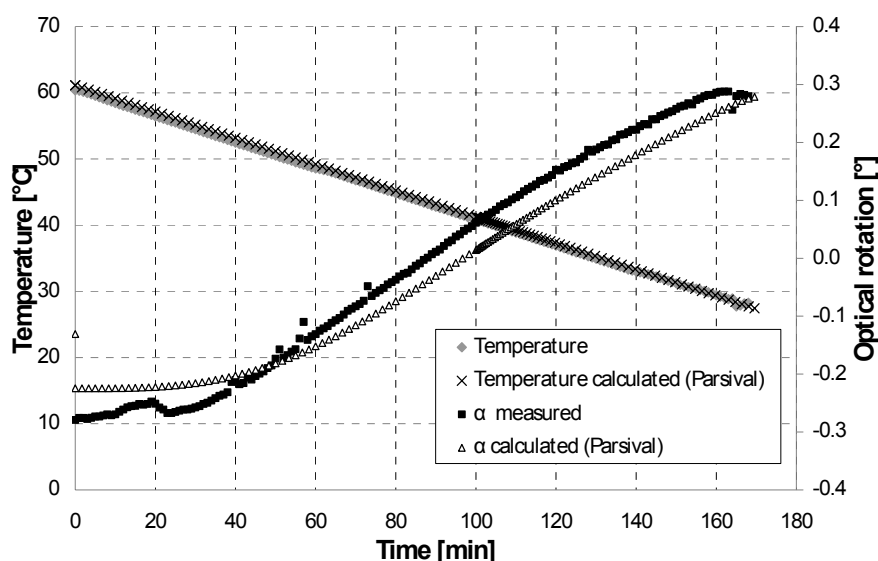


**Figure 127:** Comparison of the measured and calculated values for the optical rotation and temperature trajectories of a batch of the optimized cycle. The investigated process concept is “defined seeding”.

Due to the deviations some test runs should be undertaken in order to determine the optimal stop point of the experiments. It would be beneficial to modify the constraints given in Equation 113, Equation 115 and Equation 117 in such a way that the purity constraint would be set to 100%. In practice the purity will be lowered anyway due to

adhering mother liquor and the deviations between calculation and experiment resulting from errors and uncertainties.

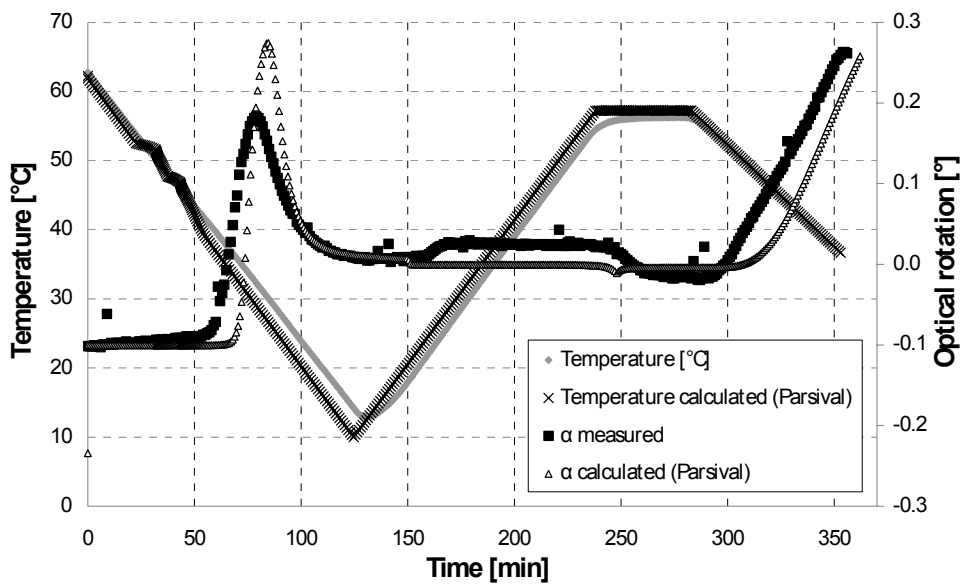


**Figure 128:** Comparison of the measured and calculated values for the optical rotation and temperature trajectories of a batch of the optimized cycle. The investigated process concept is “nucleation seeding”.

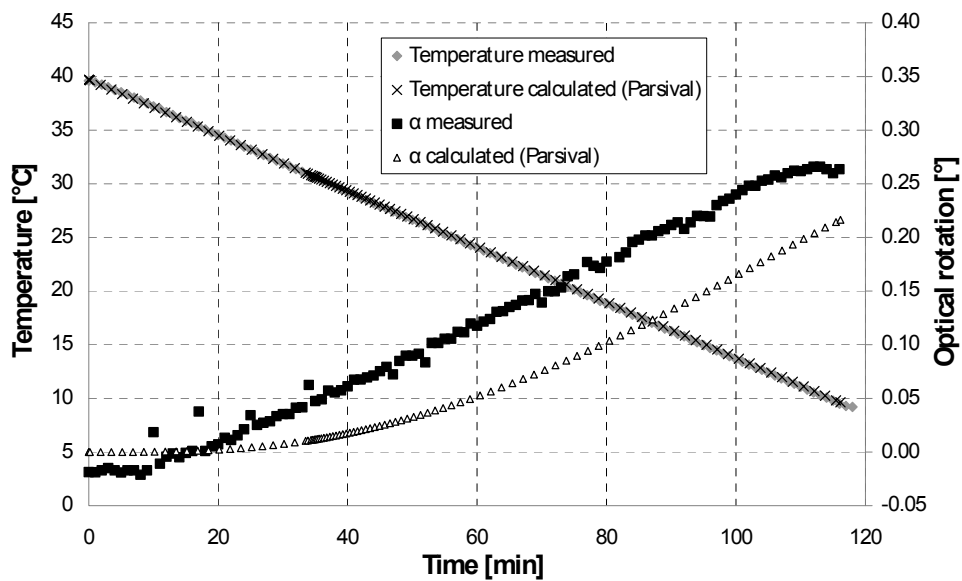


**Figure 129:** Comparison of the measured and calculated values for the optical rotation and temperature trajectories of a batch of the optimized cycle. The investigated process concept is “milled seeding”.

In all three cases the experimental productivity (based on the measured optical rotation) is higher than the calculated one. This shows that the model underestimates the obtainable productivities to a small extent.

When the productivities given in Table 23 are compared with the results of the design procedure based on equilibrium data or metastable zone width respectively (chapter 4.4) it can be stated that the obtained productivities are much lower than the expected ones (Figure 53). One of the reasons for this result is that for the calculation of the productivities presented in Figure 59 only the final cooling step of the process has been considered. Therefore the time for seed preparation of the individual process concepts has not been considered at all. These times however differ significantly and are highest for the process concept “nucleation seeding”. Therefore there the productivity is lowest.

Nevertheless the concept “nucleation seeding” offers other advantages apart from productivity considerations. If, for example, the design of a specific particle size distribution is required the process concept “nucleation seeding” offers additional degrees of freedom for modifying the particle size distribution by a manipulation of the temperature profile and initial concentrations. Another obvious advantage is that no seeds have to be introduced into the vessel. Using the presented model (chapters 2.1.5 and 2.2.4 respectively other optimization functions can be thought of and corresponding regimes can be designed. This was outside the scope of this thesis.

## 5 Conclusions and outlook

In the thesis three different process variants of preferential crystallization were introduced and successfully applied for enantioseparation of DL-threonine and R,S-mandelic acid. These are mainly differentiated by their seeding strategy as “defined seeding”, “nucleation seeded” and “milled seeding”. In order to evaluate, design and optimize the different process variants, and thus fully exploit the potential of the separation method, reliable models were needed. Depending on the gathered experimental data models with different levels of complexity were used.

Based on solubilities and metastable zone width data short-cut process evaluations were used to identify operating regions where high process yields or productivities can be expected. This short-cut approach was applied to the conglomerate forming system DL-threonine as well as to the compound forming system R,S-mandelic acid. Based on the results for these two representative systems, the procedure has the potential to evaluate a preferential crystallization process for a wide range of different systems. However, the predictive power of the short-cut methods is limited due to the simplifying assumptions made.

Therefore a time resolved dynamic model using the population balance framework was developed. This model could be used to describe runs of all three preferential crystallization process variants studied.

After the formulation of a suitable kinetic process model the free parameters had to be determined. Differing in the data used three suitable approaches were applied.

The first approach exploited experimentally determined second moments of the particle size distribution in the vessel and the optical rotation to parameterize a reduced model (moment model).

The second approach used chord-length distributions measured with a FBRM-probe along with optical rotation data to parameterize a full population balance model solved with the method of characteristics. A model for the FBRM-probe taken from recent literature was needed for the approach to work.

The third approach used measured data of the particle size distribution at defined discrete times along with trajectories of the mass fractions of the two species to

parameterize a full population balance model solved with the h,p-moving grid Galerkin method that is built in into Parsival<sup>®</sup>.

All model solution strategies had been chosen and adapted based on the experimental data used for the individual approaches. As a result three kinetic parameter sets were derived that are able to describe the measured data rather adequately. Most estimated parameters lie in a reasonable range of parameter values found in literature. However the numerical parameter values derived from the different estimation approaches differ partly in a significant manner. The third estimation approach provided a statistically unique parameter set which is therefore favorized for future applications of the model.

When the three approaches were compared in terms of quality of the resulting parameter sets and their predictive power the approach using the commercial software package Parsival<sup>®</sup> proved to be superior to the other two methods tested. Nevertheless for future research the FBRM-probe model applied in the second approach has high potential to be used as a valuable tool for quality control and product design.

The reliability of the kinetic parameters can be enhanced by the use of additional experimental data. To provide additional data with a high information content a dynamic experimental design was undertaken. As a result of the experimental design the reliability of the parameter set determined beforehand using a reduced moment model was enhanced. The presented method potentially reduces the number of experiments needed for the reliable estimation of kinetic parameters.

An outlook is given on the potential use of the derived model for product design purposes. The process variant “nucleation seeding” had the potential of modifying the particle size distribution by a simple variation of the temperature profile and the initial conditions. It could be shown theoretically that a slight modification of the product properties  $x_{50}$  and variance  $\sigma^2$  was possible.

Finally to test and use the parameterized model a process optimization in terms of productivity was undertaken for the three different process variants introduced. The calculated setups could be experimentally validated. Therefore the predictive capability of the model and parameter set resulting from the third estimation approach was proved.

A future working field could be the use of additional measuring devices. In this context the use of measured data provided by the Particle vision and Measurement-probe (PVM, Mettler Toledo GmbH) is promising. However the data measured by the

PVM need to be processed carefully to generate reliable particle size distribution data from the microscopic pictures taken.

In general the methods and tools presented should be of use for engineers working in industry that need to design or evaluate preferential crystallization processes.

The problems discussed can also act as examples for practical cases where data from production runs are used to parameterize kinetic models. For such cases the tested statistical tools can be of large value.

## 6 Nomenclature

### Latin

$B$	nucleation rate, (#/s)
$Bern$	Bernstein polynomial series
$b$	exponent for the nucleation law, (-)
$B_{1,2}$	reparameterized nucleation rate constants
$C$	variance covariance matrix
$CLD$	chord length distribution
$w$	mass fraction, (kg/kg)
$w_{sat}$	saturation mass fraction, (kg/kg)
$D$	dissolution rate, (m/s)
$ee$	enantiomeric excess, (kg/kg)
$E_{b,sec}$	activation energy for secondary nucleation, (kJ/mol)
$E_d$	activation energy for dissolution, (kJ/mol)
$E_g$	activation energy for crystal growth, (kJ/mol)
$Elo$	Elongation, (-)
$F$	number density of the crystals, (#/m)
$F_{goal}$	goal function for optimization calculations
$FIM$	Fisher information matrix
$G$	growth rate, (m/s)
$G_{1,2}$	reparameterized growth rate constants
$g$	exponent for the growth law, (-)
$\Delta h$	enthalpy of melting, (J/kg)
$k_b$	nucleation constant for primary nucleation, (#/s)
$k_{b,sec}$	nucleation constant for secondary nucleation, (#/(s m <sup>3</sup> ))
$k_{b,sec,pre}$	nucleation prefactor for secondary nucleation, (#/(s m <sup>3</sup> ))
$k_d$	dissolution constant, (kg/(m <sup>2</sup> s))

$k_{d,pre}$	dissolution constant prefactor, (kg/(m <sup>2</sup> s))
$k_g$	growth constant, (m/s)
$k_{g,pre}$	growth constant prefactor, (m/s)
$k_{prim}$	factor influencing primary nucleation
$k_v$	shape factor, (-)
$L$	characteristic coordinate for crystal size, (m)
$m_l$	mass of the enantiomers in the liquid phase, (kg)
$MSZW$	metastable zone width
$p$	parameter
$Prod$	Productivity, (kg/(h kg))
$PSD$	particle size distribution
$q$	weighting factor
$R$	gas constant, (8.314 J/(mol K))
$S$	sensitivity
$s$	supersaturation, (-)
$sd$	standard deviation
$T$	temperature, (°C)
$t$	time, (s)
$V$	Volume, (m <sup>3</sup> )
$x$	Measured quantities

### **Greek**

$\alpha$	optical rotation, (°)
$\delta$	sensitivity measure
$\varphi$	parameter for solubility correlation
$\gamma$	collinearity index
$\lambda$	eigenvalue
$\mu_i$	i-th moment of the population, (m <sup>i</sup> )
$\rho$	density, (kg/m <sup>3</sup> )
$\Omega$	correlation measure
$\zeta$	significance level, (-)
$\sigma$	relative supersaturation

## Indices

<i>r</i>	enantiomer $r=1,2$
<i>k</i>	distribution moment of the order $k$
<i>mean</i>	average or reference value
<i>measured</i>	experimental data
<i>calculated</i>	data resulting from simulations
<i>p</i>	referring to the parameter vector
<i>x</i>	referring to the measured values
<i>i,j</i>	counter

## 7 Literature

- Abrams, D. S. & Prausnitz, J. M. (1975). Statistical Thermodynamics of Liquid-Mixtures - New Expression for Excess Gibbs Energy of Partly or Completely Miscible Systems. *AIChE Journal*, 21(1), 116-128.
- Amiard, G. (1956). Sur Le Dedoublement Direct De La Threonine, Par Entrainement. *Bulletin De La Societe Chimique De France*, (3), 447-447.
- Angelov, I., Raisch, J., Elsner, M. P. & Seidel-Morgenstern, A. (2006). Optimization of initial conditions for preferential crystallization. *Industrial & Engineering Chemistry Research*, 45(2), 759-766.
- Angelov, I., Raisch, J., Elsner, M. P. & Seidel-Morgenstern, A. (2008). Optimal operation of enantioseparation by batch-wise preferential crystallization. *Chemical Engineering Science*, 63, (5), 1282-1292.
- Arellano-Garcia, H., Schoneberger, J. & Korkel, S. (2007). Optimal design of experiments in the chemical engineering. *Chemie Ingenieur Technik*, 79(10), 1625-1638.
- Ariens, E. J. (1984). Stereochemistry, a Basis for Sophisticated Nonsense in Pharmacokinetics and Clinical-Pharmacology. *European Journal of Clinical Pharmacology*, 26(6), 663-668.
- Bard, Y. (1974). *Nonlinear parameter estimation*. New York and London: Academic press.
- Beck, J. V. (1977). *Parameter estimation in engineering and science*. John Wiley and Sons.
- Bhat, S. A. & Huang, B. (2009). Preferential Crystallization: Multi-Objective Optimization Framework. *AIChE Journal*, 55(2), 383-395.
- Bock, H. G. (Ed.). (1981). *Numerical treatment of inverse problems in chemical reaction kinetics*. Heidelberg: Springer.
- Box, G. E. P., Hunter, W. G. & Hunter, J. S. (1978). *Statistics for experimenters; An introduction to design, data analysis and model building* New York: Wiley.
- Braun, B., Groen, H. & Tschernjaew, J. (2004). Production-scale particle design of a pharmaceutical intermediate. *Crystal Growth & Design*, 4(5), 915-920.
- Brun, R. (2002). *Learning from data: Parameter identification in the context of large environmental simulation models*. Zürich: ETH Zürich, Phd-thesis.
- Burton, W. K., Cabrera, N. & Frank, F. C. (1951). The Growth of Crystals and the Equilibrium Structure of Their Surfaces. *Philosophical Transactions of the Royal Society of London Series a-Mathematical and Physical Sciences*, 243(866), 299-358.
- Caner, H., Groner, E., Levy, L. & Agranat, I. (2004). Trends in the development of chiral drugs. *Drug Discovery Today*, 9(3), 105-110.
- Chen, A. M., Wang, Y. L. & Wenslow, R. M. (2008). Purification of partially resolved enantiomeric mixtures with the guidance of ternary phase diagram. *Organic Process Research & Development*, 12(2), 271-281.
- Chen, B. H. & Asprey, S. P. (2003). On the design of optimally informative dynamic experiments for model discrimination in multiresponse nonlinear situations. *Industrial & Engineering Chemistry Research*, 42(7), 1379-1390.
- Chen, B. H., Bermingham, S., Neumann, A. H., Kramer, H. J. M. & Asprey, S. P. (2004). On the design of optimally informative experiments for dynamic

- crystallization process modeling. *Industrial & Engineering Chemistry Research*, 43(16), 4889-4902.
- Chow, K., Tong, H. H. Y., Lum, S. & Chow, A. H. L. (2008). Engineering of pharmaceutical materials: An industrial perspective. *Journal of Pharmaceutical Sciences*, 97(8), 2855-2877.
- Chung, S. H., Ma, D. L. & Braatz, R. D. (2000). Optimal model-based experimental design in batch crystallization. *Chemometrics and Intelligent Laboratory Systems*, 50(1), 83-90.
- Collins, A. N., Sheldrake, G. N. & Crosby, J. (1997). *The commercial manufacture and applications of optically active compounds*. Chichester: Wiley.
- Collins, A. N., Sheldrake, G. N. & Crosby, J. (2000). *The commercial manufacture and applications of optically active compounds*. Chichester: Wiley.
- Coquerel, G., Petit, M.-N. & Bouaziz, R. (2000) United States Patent, Patent Number: 6,022,409.
- Cussler, E. & Moggridge, G. D. (2001). *Chemical product design*. Cambridge: Cambridge university press.
- Czapla, F., Haida, H., Elsner, M. P., Lorenz, H. & Seidel-Morgenstern, A. (2008a). Parameterization of population balance models for polythermal auto seeded preferential crystallization of enantiomers. *Chemical Engineering Science*, 64(4), 753-763.
- Czapla, F., Lorenz, H. & Seidel-Morgenstern, A. (2008c): Efficient design of preferential crystallization processes. In "*17<sup>th</sup> International Symposium on Industrial Crystallization*" - ISIC 17<sup>th</sup>, Maastricht, 803-810.
- Czapla, F., Lorenz, H. & Seidel-Morgenstern, A. (2009). Modellierung und Vergleich von polythermen autoseeded Prozessvarianten der Bevorzugten Kristallisation. *Chemie Ingenieur Technik*, 6, 839-848.
- Deuflhard, P. (2004). *Newton methods for nonlinear problems. Affine invariance and adaptive algorithms*. New York, Heidelberg: Springer.
- Diaz, L. I. (2005). *Experimentelle und modellbasierte Studien zur Untersuchung von Einflußfaktoren auf die Kinetik der "Bevorzugten Kristallisation" von Threonin*. Magdeburg: Otto-von-Guericke University, Diploma-thesis.
- Diez, M. D., Fjeld, M., Andersen, E. & Lie, B. (2006). Validation of a compartmental population balance model of an industrial leaching process: The Silgrain (R) process. *Chemical Engineering Science*, 61(1), 229-245.
- Dochain, D. & Vanrolleghem, P. (2001). *Dynamical Modelling and estimation in wastewater treatment processes*. London: IWA publishing.
- Efron, B. (1979). 1977 Rietz Lecture - Bootstrap Methods - Another Look at the Jackknife. *Annals of Statistics*, 7(1), 1-26.
- Efron, B. & Tibshirani, R. J. (1993). *An introduction to the bootstrap*. Chapman and Hall/CRC.
- Elsner, M. P., Menendez, D. F., Muslera, E. A. & Seidel-Morgenstern, A. (2005). Experimental study and simplified mathematical description of preferential crystallization. *CHIRALITY*, 17, S183-S195.
- Fischer, A. & Profir, V. M. (2003). A metastable modification of (RS)-mandelic acid. *Acta Crystallographica Section E-Structure Reports Online*, 59, O1113-O1116.
- Garside, J., Mersmann, A. & Nyvilt, J. (2002). *Measurement of crystal growth and nucleation rates*. Rugby: Institution of chemical engineers.

- Garside, J. & Shah, M. B. (1980). Crystallization Kinetics from Msmpr Crystallizers. *Industrial & Engineering Chemistry Process Design and Development*, 19(4), 509-514.
- Gerstlauer, A., Gahn, C., Zhou, H., Rauls, M. & Schreiber, M. (2006). Application of population balances in the chemical industry - current status and future needs. *Chemical Engineering Science*, 61(1), 205-217.
- Greaves, D., Boxall, J., Mulligan, J., Montesi, A., Creek, J., Sloan, E. D. & Koh, C. A. (2008). Measuring the particle size of a known distribution using the focused beam reflectance measurement technique. *Chemical Engineering Science*, 63(22), 5410-5419.
- Grosche, G., Zeidler, E., Ziegler, D. & Ziegler, V. (Eds.). (1995). *Teubner-Taschenbuch der Mathematik part II*. Stuttgart: Teubner.
- Heinrich, J. (2008). *Determination of crystallization kinetics using in situ measurement techniques and model-based experimental design & analysis*. Halle: Martin-Luther University, Phd-thesis.
- Hintermaier, J. C. (1948). Foundations for Experimental Design. *Analytical Chemistry*, 20(12), 1144-1146.
- Hu, Q., Rohani, S. & Jutan, A. (2005). New numerical method for solving the dynamic population balance equations. *AIChE Journal*, 51(11), 3000-3006.
- Hulburt, H. M. & Katz, S. (1964). Some Problems in Particle Technology - a Statistical Mechanical Formulation. *Chemical Engineering Science*, 19(8), 555-574.
- Ito, A. & Matsuoka, M. (2008). Nucleation behavior of D-threonine on different faces of L-threonine crystals. *Crystal Growth & Design*, 8(8), 2716-2720.
- Janczak, J., Zobel, D. & Luger, P. (1997). L-threonine at 12 K. *Acta Crystallographica Section C-Crystal Structure Communications*, 53, 1901-1904.
- Jaques, J., Collet, A. & Wilen, S. H. (1994). *Enantiomers racemates and resolutions*. Malabar: Krieger publishing Company.
- John, V., Angelov, I., Oncul, A. A. & Thevenin, D. (2007). Techniques for the reconstruction of a distribution from a finite number of its moments. *Chemical Engineering Science*, 62(11), 2890-2904.
- Joshi, A., Kremling, A. & Seidel-Morgenstern, A. (2006). Model based statistical analysis of adsorption equilibrium data. *Chemical Engineering Science*, 61(23), 7805-7818.
- Joshi, M. (2007). *statistical analysis of models and parameters in chemical and biochemical reaction networks*. Magdeburg: Otto-von-Guericke University, Phd-thesis.
- Kail, N., Briesen, H. & Marquardt, W. (2007). Advanced geometrical modeling of focused beam reflectance measurements (FBRM). *Particle & Particle Systems Characterization*, 24(3), 184-192.
- Kail, N., Briesen, H. & Marquardt, W. (2008a). Analysis of FBRM measurements by means of a 3D optical model. *Powder Technology*, 185(3), 211-222.
- Kail, N., Briesen, H. & Marquardt, W. (2008b): Model based reconstruction of particle size distributions from FBRM measurements. In "17<sup>th</sup> International Symposium on Industrial Crystallization" - ISIC 17<sup>th</sup> Maastricht, 533-540.
- Kashiev, D. (2000). *Nucleation : basic theory with applications*. Oxford Butterworth-Heinemann: Butterworth-Heinemann.

- Kaspereit, M. (2006). *Separation of enantiomers by a process combination of chromatography and crystallisation*. Magdeburg: Otto-von-Guericke University Magdeburg, Phd-thesis.
- Kay, S. M. (1993). *Fundamentals of statistical processing, Volume I: Estimation theory*. Prentice Hall.
- Kirkpatrick, S., Gelatt, C. D. & Vecchi, M. P. (1983). Optimization by Simulated Annealing. *Science*, 220(4598), 671-680.
- Klamt, A. (1995). Conductor-Like Screening Model for Real Solvents - a New Approach to the Quantitative Calculation of Solvation Phenomena. *Journal of Physical Chemistry*, 99(7), 2224-2235.
- Klukas, L. (2008). *Systematische Untersuchung der polythermen zyklischen Bevorzugten Kristallisation am Beispiel des Stoffsystems DL-Threonin/Wasser*. Magdeburg: FH Magdeburg-Stendal, Phd-thesis.
- Knabe, J. (1989). On the Enantioselectivity of Drugs. *Arzneimittel-Forschung/Drug Research*, 39-2(11), 1379-1384.
- Kumar, G. R., Raj, S. G., Mohan, R. & Jayavel, R. (2006). Influence of isoelectric pH on the growth linear and nonlinear optical and dielectric properties of L-threonine single crystals. *Crystal Growth & Design*, 6(6), 1308-1310.
- Kumar, S. & Ramkrishna, D. (1997). On the solution of population balance equations by discretization - III. Nucleation, growth and aggregation of particles. *Chemical Engineering Science*, 52(24), 4659-4679.
- Lagarias, J. C., Reeds, J. A., Wright, M. H. & Wright, P. E. (1998). Convergence properties of the Nelder-Mead simplex method in low dimensions. *Siam Journal on Optimization*, 9(1), 112-147.
- Ljung, L. (1999). *Systems identification: theory for the users*. Prentice Hall.
- Lorenz, H., Perlberg, A., Sapoundjiev, D., Elsner, M. P. & Seidel-Morgenstern, A. (2006a). Crystallization of enantiomers. *Chemical Engineering and Processing*, 45(10), 863-873.
- Lorenz, H., Perlberg, A., Sapoundjiev, D., Elsner, M. P. & Seidel-Morgenstern, A. (2006b). Crystallization of enantiomers. *Chemical Engineering and Processing*, 45(10), 863-873.
- Lorenz, H., Polenske, D. & Seidel-Morgenstern, A. (2006c). Application of preferential crystallization to resolve racemic compounds in a hybrid process. *CHIRALITY*, 18(10), 828-840.
- Lorenz, H., Sapoundjiev, D. & Seidel-Morgenstern, A. (2002). Enantiomeric mandelic acid system-melting point phase diagram and solubility in water. *Journal of Chemical and Engineering Data*, 47(5), 1280-1284.
- M. Wulkow, A. G. U. N. (2001). Modeling and simulation of crystallization processes using parsival. *Chemical Engineering Science*, 56, 2575-2588.
- Maier, N. M., Franco, P. & Lindner, W. (2001). Separation of enantiomers: needs, challenges, perspectives. *Journal of Chromatography A*, 906(1-2), 3-33.
- Marquardt, W. (2005). Model-based experimental analysis of kinetic phenomena in multi-phase reactive systems. *Chemical Engineering Research & Design*, 83(A6), 561-573.
- Mersmann, A. (1995). *Crystallization technology handbook*. New York: Marcel Dekker Inc.
- Mersmann, A., Braun, B. & Löffelmann, M. (2002). Prediction of crystallization coefficients of the population balance. *Chemical Engineering Science*, 57(20), 4267-4275.
- Meyberg, K. & Vachenaer, P. (1991). *Höhere Mathematik I*. München: Springer.

- Mezaki, R. & Kittrell, J. R. (1967). Parametric Sensitivity in Fitting Nonlinear Kinetic Models. *Industrial and Engineering Chemistry*, 59(5), 63-&.
- Michaluk, N. (2007). *Inline- und Online-Prozessanalyse der Bevorzugten Kristallisation am Beispiel der Stoffsysteme Threonin und Mandelsäure*. Magdeburg: Hochschule Magdeburg/Stendal (FH), Diploma-thesis.
- Mollá, G. & Padilla, G. (2002) Universidad Politecnica de Valencia, Spain.
- Monnier, O., Klein, J. P., Hoff, C. & Ratsimba, B. (1996). Particle size determination by laser reflection: Methodology and problems. *Particle & Particle Systems Characterization*, 13(1), 10-17.
- Montgomery, D. G., Runger, G. C. & Humbele, N. F. (2001). *Engineering statistics*. New York: John Wiley and Sons.
- Morgan, E. D. (1995). *Chemometrics: Experimental Design*. New York: Wiley.
- Motz, S. (2004). *Reduktion populationsdynamischer Modelle*. Stuttgart: University of Stuttgart, Phd-thesis.
- Motz, S., Mitrovic, A. & Gilles, E. D. (2002). Comparison of numerical methods for the simulation of dispersed phase systems. *Chemical Engineering Science*, 57(20), 4329-4344.
- Mullin, J. W. (2001). *Crystallization*. Oxford: Butterworth-Heinemann.
- Myerson, A. S. (Ed.). (2002). *Handbook of industrial crystallization*. Boston: Butterworth-Heinemann.
- O'Hara, M. & Reid, M. C. (1973). *Modelling crystal growth rates from solution*. Upper Saddle River: Prentice Hall.
- Orye, R. V. & Prausnitz, J. M. (1965). Multicomponent Equilibria with Wilson Equation. *Industrial and Engineering Chemistry*, 57(5), 18-&.
- Park, T. Y. & Froment, G. F. (2001). Kinetic modeling of the methanol to olefins process. 2. Experimental results, model discrimination, and parameter estimation. *Industrial & Engineering Chemistry Research*, 40(20), 4187-4196.
- Perlberg, A. (2006). *Untersuchungen zum Einfluß des Gegenenantomers bei der enantioselektiven Kristallisation aus Lösungen*. Magdeburg: Otto-von Guericke University, Phd-thesis.
- Perlberg, A., Lorenz, H. & Seidel-Morgenstern, A. (2005). Crystal growth kinetics via isothermal seeded batch crystallization: Evaluation of measurement techniques and application to mandelic acid in water. *Industrial & Engineering Chemistry Research*, 44(4), 1012-1020.
- Peterson, B. (2000). *Calibration, identifiability and optimal experimental design of activated sludge models*. Gent: University of Gent, Phd-thesis.
- Polenske, D. (2003). *Untersuchungen zur Racemattrennung von Threonin mit Hilfe der "Preferential Crystallization"*. Magdeburg: Hochschule Magdeburg-Stendal (FH), Phd-thesis.
- Prausnitz, J. M., Lichtenthaler, R. N. & Azevedo, E. G. d. (1986). *Molecular thermodynamics of fluid-phase equilibria*. Englewood Cliffs: Prentice Hall.
- Predel, B. (1982). *Heterogene Gleichgewichte: Grundlagen und Anwendungen*. Darmstadt: Steinkopff.
- Profir, V. M. & Rasmuson, A. C. (2004). Influence of solvent and the operating conditions on the crystallization of racemic mandelic acid. *Crystal Growth & Design*, 4(2), 315-323.
- Qamar, S., Ashfaq, A., Angelov, I., Elsner, M. P., Warnecke, G. & Seidel-Morgenstern, A. (2008). Numerical solutions of population balance models in preferential crystallization. *Chemical Engineering Science*, 63(5), 1342-1352.

- Qamar, S., Ashfaq, A., Warnecke, G., Angelov, I., Elsner, M. P. & Seidel-Morgenstern, A. (2007). Adaptive high-resolution schemes for multidimensional population balances in crystallization processes. *Computers & Chemical Engineering*, 31(10), 1296-1311.
- Qamar, S., Elsner, M. P., Angelov, I. A., Warnecke, G. & Seidel-Morgenstern, A. (2006). A comparative study of high resolution schemes for solving population balances in crystallization. *Computers & Chemical Engineering*, 30(6-7), 1119-1131.
- Ramkrishna, D. (2000). *Population balances: Theory and applications to particulate systems in engineering*. New York: Academic press Inc.
- Ramkrishna, D. & Mahoney, A. W. (2002). Population balance modeling. Promise for the future. *Chemical Engineering Science*, 57(4), 595-606.
- Randolph, A. D. & Larson, M. A. (1988). *Theory of particulate processes*. San Diego: Academic Press Inc.
- Ratkowsky, D. A. (1989). *Handbook of nonlinear regression models*. New York and Basel: Marcel Dekker.
- Renon, H. & Prausnitz, J. M. (1968). Local Compositions in Thermodynamic Excess Functions for Liquid Mixtures. *AIChE Journal*, 14(1), 135-&.
- Rohani, S., Horne, S. & Murthy, K. (2005). Control of product quality in batch crystallization of pharmaceuticals and fine chemicals. Part 1: Design of the crystallization process and the effect of solvent. *Organic Process Research & Development*, 9(6), 858-872.
- Saenz de Jubera, A. M. (2006). *Dissolution kinetics of threonine in H2O: Experimental investigation, parameter estimation and statistical data analysis*. Magdeburg: OvG University Magdeburg, Diploma-thesis.
- Sakai, K. & Coquerel, G. (2007). *Novel optical resolution techniques*. Berlin: Springer.
- Sandler & Stanley, I. (1999). *Chemical and engineering thermodynamics*. New York: Wiley.
- Sapoundjiev, D., Lorenz, H. & Seidel-Morgenstern, A. (2006). Solubility of chiral threonine species in water/ethanol mixtures. *Journal of Chemical and Engineering Data*, 51(5), 1562-1566.
- Schenkendorf, R., Kremling, A. & Mangold, M. (2009). Optimal experimental design with the sigma point method. *Iet Systems Biology*, 3(1), 10-23.
- Shampine, L. F. & Reichelt, M. W. (1997). The MATLAB ODE suite. *Siam Journal on Scientific Computing*, 18(1), 1-22.
- Shoemaker, D. P., Donohue, J., Schomaker, V. & Corey, R. B. (1950). The Crystal Structure of Ls-Threonine. *Journal of the american chemical society*, 72(6), 2328-2349.
- Smallwood, H. M. (1947). Design of Experiments in Industrial Research. *Analytical Chemistry*, 19(12), 950-952.
- Sparks, R. G. & Dobbs, C. L. (1993). The use of laser backscatter instrumentation for the online measurement of the particle-size distribution of emulsions. *Part. Part. Syst. Charact.*, 10, 279-289.
- Stieß, M. (1995). *Mechanische Verfahrenstechnik 1*. Berlin, Heidelberg, New York: Springer.
- Tadayyon, A. & Rohani, S. (1998). Determination of particle size distribution by Par-Tec (R) 100: Modeling and experimental results. *Particle & Particle Systems Characterization*, 15(3), 127-135.
- Telgmann, R. (2007). *Computer aided modeling*. FU Berlin, Phd-thesis.

- Togkalidou, T., Braatz, R. D., Johnson, B. K., Davidson, O. & Andrews, A. (2001). Experimental design and inferential modeling in pharmaceutical crystallization. *AIChE Journal*, 47(1), 160-168.
- Togkalidou, T., Tung, H. H., Sun, Y., Andrews, A. T. & Braatz, R. D. (2004). Parameter estimation and optimization of a loosely bound aggregating pharmaceutical crystallization using in situ infrared and laser backscattering measurements. *Industrial & Engineering Chemistry Research*, 43(19), 6168-6181.
- Trifkovic, M., Sheikhzadeh, M. & Rohani, S. (2008). Kinetics estimation and single and multi-objective optimization of a seeded, anti-solvent, isothermal batch crystallizer. *Industrial & Engineering Chemistry Research*, 47(5), 1586-1595.
- Vaccaro, A., Sefcik, J. & Morbidelli, M. (2007). Modeling focused beam reflectance measurement and its application to sizing of particles of variable shape. *Particle & Particle Systems Characterization*, 23(5), 360-373.
- van Ness, H. C. & Abbott, M. M. (1982). Classical thermodynamics of non-electrolyte solutions: With applications to phase equilibria.
- Walter, E. & Pronzato, L. (1990). Qualitative and Quantitative Experiment Design for Phenomenological Models - a Survey. *Automatica*, 26(2), 195-213.
- Walter, E. & Pronzato, L. (1997). *Identification of parametric models from experimental data*. London: Springer.
- Wang, X. J. & Ching, C. B. (2006). A systematic approach for preferential crystallization of 4-hydroxy-2-pyrrolidone: Thermodynamics, kinetics, optimal operation and in-situ monitoring aspects. *Chemical Engineering Science*, 61(8), 2406-2417.
- Wang, Y. L. & Chen, A. M. (2008). Enantioenrichment by crystallization. *Organic Process Research & Development*, 12(2), 282-290.
- Ward, J. D., Mellichamp, D. A. & Doherty, M. F. (2006). Choosing an operating policy for seeded batch crystallization. *AIChE Journal*, 52(6), 2046-2054.
- Wulkow, M. (1996). The simulation of molecular weight distributions in polyreaction kinetics by discrete Galerkin methods. *Macromolecular Theory and Simulations*, 5(3), 393-416.
- Wulkow, M. (2001). PARSIVAL simulation package for particle balances. *Software handbook*.
- Wulkow, M. (2007). Advanced parameter estimation in Predici, Parsival and Presto-Kinetics. *Software handbook*.
- Wulkow, M., Gerstlauer, A. & Nieken, U. (2001a). Modeling and simulation of crystallization processes using parsival. *Chemical Engineering Science*, 56(7), 2575-2588.
- Wulkow, M., Gerstlauer, A. & Nieken, U. (2001b). Modeling and simulation of crystallization processes using parsival. *Chemical Engineering Science*, 56, 2575-2588.
- Wynn, E. J. W. (2003). Relationship between particle-size and chord-length distributions in focused beam reflectance measurement: stability of direct inversion and weighting. *Powder Technology*, 133(1-3), 125-133.
- Yu, Z. Q., Chew, J. W., Chow, P. S. & Tan, R. B. H. (2007). Recent advances in crystallization control - An industrial perspective. *Chemical Engineering Research & Design*, 85(A7), 893-905.
- Yu, Z. Q., Chow, P. S. & Tan, R. B. H. (2008). Interpretation of focused beam reflectance measurement (FBRM) data via simulated crystallization. *Organic Process Research & Development*, 12(4), 646-654.

## Appendix A - Data and settings

**Table A 1:** Chemicals used to setup the experiments for crystallization in the DL-threonine/water system.

	DL-threonine	L-threonine	D-threonine
Product name	DL-Threonine	L-Threonine for biochemistry	D-Threonine
Supplier	SIGMA-Aldrich Inc.	Merck KGaA	SIGMA-Aldrich
Purity	≥98%	≥99%	≥98%

**Table A 2:** Chemicals used to setup the experiments for crystallization in the R,S-mandelic acid/water system.

	S-mandelic acid	R,S-mandelic acid
Product name	(S)-(+)-Mandelsäure	R,S-Mandelsäure
Supplier	Merck KGaA	Merck KGaA
Purity	≥98%	≥98%

**Table A 3:** Solubility data for the system DL-threonine/water in a temperature range from 10-65°C measured at different compositions.

Water [g]	L-threonine [g]	D-threonine [g]	Temperature [°C]
0.8566	0.0717	0.0717	10
0.9266	0.0000	0.0734	
0.9271	0.0729	0.0000	
0.8431	0.0785	0.0785	20
0.9169	0.0000	0.0831	
0.9166	0.0834	0.0000	
0.8230	0.0885	0.0885	30
0.9051	0.0000	0.0949	
0.9048	0.0952	0.0000	
0.8126	0.0937	0.0937	34
0.8988	0.0000	0.1012	
0.8082	0.0959	0.0959	37
0.8962	0.0000	0.1038	
0.8017	0.0992	0.0992	40
0.8924	0.0000	0.1076	
0.8760	0.0198	0.1042	
0.8612	0.0341	0.1047	
0.8434	0.0549	0.1017	
0.8240	0.0745	0.1015	
0.8929	0.1071	0.0000	
0.7920	0.1040	0.1040	43
0.8871	0.0000	0.1129	
0.7862	0.1069	0.1069	46
0.8821	0.0000	0.1179	
0.7617	0.1192	0.1192	56
0.7417	0.1292	0.1292	65

**Table A 4:** Solubility data for the system R,S-mandelic acid/water in a temperature range from 5-40°C measured at different compositions (pure enantiomer, eutectic composition and racemate).

Temperature [°C]	(S)-MS [g/100g]	RS- MS_(rac.) [g/100g]	RS- MS_(eut.) [g/100g]	(S)- MS_(eut.) [g/100g]	RS- MS_(eut.) [g/100g]	(S)-MS [g/100g]	RS- MS_(rac.) [g/100g]	RS- MS_(eut.) [g/100g]
5	5.42	8.10	9.30	-	-	10.15	28.73	20.94
10	6.30	9.32	10.80	-	-	8.66	19.05	14.94
15	7.40	10.70	13.30	-	-	8.14	13.84	13.17
18	8.20	12.49	14.60	10.22	8.76	8.28	12.87	14.13
20	8.44	13.10	15.45	10.82	9.27	8.57	13.12	15.61
21	9.02	13.85	16.49	11.54	9.90	8.78	13.51	16.61
22	-	-	17.62	12.33	10.57	9.02	14.09	17.77
23	8.96	14.66	18.76	13.13	11.26	9.30	14.84	19.10
24	9.79	16.37	20.43	14.30	12.26	9.61	15.77	20.60
25	9.90	17.30	22.06	15.44	13.24	9.97	16.88	22.27
26	10.41	18.12	24.00	16.80	14.40	10.36	18.17	24.11
27	11.16	-	26.19	18.33	15.71	10.80	19.63	26.12
28	11.16	20.56	28.99	20.29	17.39	11.27	21.28	28.30
29	-	-	31.54	22.08	18.92	11.78	23.11	30.64
30	11.90	25.20	33.07	23.15	19.84	12.33	25.12	33.16
31	-	-	-	-	-	12.91	27.30	35.84
32	-	-	-	-	-	13.54	29.66	38.69
33	13.94	31.44	40.93	28.65	24.56	14.20	32.21	41.71
35	15.83	38.51	48.50	33.95	29.10	15.64	37.83	48.26
40	22.56	51.33	60.18	-	-	19.92	55.03	67.58

**Table A 5:** HPLC-method used for threonine.

Column	Chirobiotic T, 250x4.6 mm, 5 µm particles
Eluent	80% Ethanol 20% Water
Temperature	20°C
Flow	0.5 mL/min
Pressure	136bar
Injection	5µl
Detector wavelength	220nm

**Table A 6:** Settings for the image analysis algorithm of the PVM-software (Particle Vision and Measurement, Mettler-Toledo).

<u>Pre-processing:</u>	Decimation factor:5 Filter type: Median 5x5 Edge Filter: Sobel
<u>Thresholding:</u>	Lower threshold: 8 Upper threshold: 254
<u>Particle acceptance Criteria:</u>	Minimum Pixel size: 10 Reject particles with ellipsoidity smaller: 25 Output Distribution: Diameter (Spherical Eq.)

**Table A 7:** Moments for experiment 1 (sieve fraction 63-90 $\mu$ m).

FBRM measurement

PSD analysis

Sieve fraction 63-90 $\mu$ m

Add [g]	5.01E+00	5.01E+00	5.00E+00
M0 [#]	7.84E+02	1.51E+03	2.19E+03
M1 [m]	3.90E-02	7.40E-02	1.05E-01
M2 [m <sup>2</sup> ]	3.38E-06	6.40E-06	8.91E-06
M3 [m <sup>3</sup> ]	4.34E-10	8.30E-10	1.14E-09

Add [g]	5.01E+00	5.01E+00	5.00E+00
M0 [#]	1.57E+06	3.14E+06	4.71E+06
M1 [m]	3.40E+02	6.81E+02	1.02E+03
M2 [m <sup>2</sup> ]	9.41E-02	1.88E-01	2.82E-01
M3 [m <sup>3</sup> ]	3.14E-05	6.27E-05	9.40E-05

**Table A 8:** Moments for Experiment 2 (Sieve fraction 90-150 $\mu$ m).

FBRM measurement

PSD analysis

Sieve fraction 90-150 $\mu$ m

Add [g]	5.01E+00	5.00E+00	5.02E+00
M0 [#]	6.33E+02	1.26E+03	1.80E+03
M1 [m]	3.30E-02	6.35E-02	8.84E-02
M2 [m <sup>2</sup> ]	3.20E-06	6.05E-06	8.28E-06
M3 [m <sup>3</sup> ]	4.78E-10	8.90E-10	1.20E-09

Add [g]	5.01E+00	5.00E+00	5.02E+00
M0 [#]	6.26E+05	1.25E+06	1.88E+06
M1 [m]	1.78E+02	3.55E+02	5.33E+02
M2 [m <sup>2</sup> ]	7.23E-02	1.44E-01	2.17E-01
M3 [m <sup>3</sup> ]	3.92E-05	6.27E-05	1.18E-04

**Table A 9:** Moments for experiment 3 (Sieve fraction 150-212  $\mu\text{m}$ ).

FBRM measurement

PSD analysis

Sieve fraction 150-212  $\mu\text{m}$

Add [g]	5.00E+00	5.01E+00	5.02E+00
M0 [#]	2.52E+02	5.46E+02	8.15E+02
M1 [m]	1.46E-02	3.05E-02	4.44E-02
M2 [m <sup>2</sup> ]	1.84E-06	3.85E-06	5.54E-06
M3 [m <sup>3</sup> ]	3.68E-10	7.57E-10	1.09E-09

Add [g]	5.00E+00	5.01E+00	5.02E+00
M0 [#]	1.29E+05	2.59E+05	3.88E+05
M1 [m]	4.64E+01	9.29E+01	1.39E+02
M2 [m <sup>2</sup> ]	2.32E-02	4.65E-02	6.98E-02
M3 [m <sup>3</sup> ]	1.53E-05	3.06E-05	4.59E-05

**Table A 10:** Moment analysis according to Equation 67 for the sieve fractions 63-90 $\mu\text{m}$  compared with sieve fraction 90-150 $\mu\text{m}$ .

Moment fractions based on microscope analysis			Moment fractions from FBRM measurements		
$\mu_{0,2}/\mu_{0,1}$			$\mu_{0,2}/\mu_{0,1}$		
0.40	0.40	0.40	0.81	0.83	0.82
$\mu_{1,2}/\mu_{1,1}$			$\mu_{1,2}/\mu_{1,1}$		
0.52	0.52	0.52	0.85	0.86	0.85
$\mu_{2,2}/\mu_{2,1}$			$\mu_{2,2}/\mu_{2,1}$		
0.77	0.77	0.77	0.95	0.95	0.93
$\mu_{3,2}/\mu_{3,1}$			$\mu_{3,2}/\mu_{3,1}$		
1.25	1.00	1.25	1.10	1.07	1.05

**Table A 11:** Moment analysis according to Equation 67 for the sieve fractions 63-90 $\mu\text{m}$  compared with sieve fraction 150-212 $\mu\text{m}$ .

Moment fractions based on microscope analysis			Moment fractions from FBRM measurements		
$\mu_{0,3}/\mu_{0,1}$			$\mu_{0,3}/\mu_{0,1}$		
0.08	0.08	0.08	0.32	0.32	0.37
$\mu_{1,3}/\mu_{1,1}$			$\mu_{1,3}/\mu_{1,1}$		
0.14	0.14	0.14	0.37	0.41	0.42
$\mu_{2,3}/\mu_{2,1}$			$\mu_{2,3}/\mu_{2,1}$		
0.25	0.25	0.25	0.55	0.60	0.62
$\mu_{3,3}/\mu_{3,1}$			$\mu_{3,3}/\mu_{3,1}$		
0.49	0.49	0.49	0.85	0.91	0.96

**Table A 12:** Moment analysis according to Equation 67 for the sieve fractions 90-150 $\mu\text{m}$  compared with sieve fraction 150-212 $\mu\text{m}$ .

Moment fractions based on microscope analysis			Moment fractions from FBRM measurements		
$\mu_{0,3}/\mu_{0,2}$			$\mu_{0,3}/\mu_{0,2}$		
0.21	0.21	0.21	0.40	0.43	0.45
$\mu_{1,3}/\mu_{1,2}$			$\mu_{1,3}/\mu_{1,2}$		
0.26	0.26	0.26	0.44	0.48	0.50
$\mu_{2,3}/\mu_{2,2}$			$\mu_{2,3}/\mu_{2,2}$		
0.32	0.32	0.32	0.58	0.64	0.67
$\mu_{3,3}/\mu_{3,2}$			$\mu_{3,3}/\mu_{3,2}$		
0.39	0.49	0.39	0.77	0.85	0.91

**Table A 13:** Data corresponding to the calculated process run depicted in Figure 50.

	Solubility racemate [g/g <sub>total</sub> ]	w <sub>L,sat</sub> [g/g]	w <sub>D,sat</sub> [g/g]	Temperature [°C]
Start	0.244	0.122	0.122	59
Nucleation	0.160	0.080	0.080	21
Annealing	0.205	0.102	0.102	42
cooling crystallization	0.171	0.085	0.085	26

**Table A 14:** Liquid phase composition corresponding to the calculated process run depicted in Figure 50.

Liquid phase						
	m <sub>L</sub> [g]	m <sub>D</sub> [g]	m <sub>water</sub> [g]	w <sub>L</sub> [g/g]	w <sub>D</sub> [g/g]	w <sub>water</sub> [g/g]
Start	0.120	0.100	0.780	0.120	0.100	0.780
Nucleation	0.074	0.074	0.780	0.080	0.080	0.840
Annealing	0.100	0.100	0.780	0.102	0.102	0.796
cooling crystallization	0.078	0.103	0.780	0.083	0.104	0.812

**Table A 15:** Solid phase composition corresponding to the calculated process run depicted in Figure 50.

Solid phase			
	m <sub>L</sub> [g]	m <sub>D</sub> [g]	w <sub>L</sub> [g/g]
Start	0.000	0.000	1.000
Nucleation	0.046	0.026	1.778
Annealing	0.020	0.000	1.000
Cooling crystallization	0.042	0.000	1.000

**Table A 16:** Model parameters for the FBRM-model used to transform the calculated particle size distribution into a chord-length distribution.

Model parameters		
variable	value	description
w1	2.5mm	lens radius
f1	12mm	focal length first lens
f2	25mm	focal length second lens
L	50mm	lens distance
sigmar,min	1.6 $\mu$ m	minimal laser radius
rfib	31.25 $\mu$ m	fiber radius
zmax	4000 $\mu$ m	maximum detection depth
y <sub>max</sub>	sigma r(z <sub>max</sub> )	maximum detection width
vlas	2m/s	nominal laser velocity
etawat	1.33	refractive index of water
delta offset	8.00E-05	threshold offset
delta space	8.00E-05	threshold spacing
delta scatter	1	scattered light fraction
vp	0.3m/s	particle velocity
teta max,lac	17.7°	maximum indication angle lactose
teta max,pol	90.0°	maximum inclination angle polystyrene
tolTau	e-5	iteration tolerance discrimination threshold
tolEps	e-3	iteration tolerance chord line concentration
velfac	2	relative velocity of the laser beam with respect to the fluid velocity

**Table A 17:** Fixed and varied parameters for the variation calculations performed with Parsival<sup>®</sup>.

ee <sub>0,1</sub> [kg/kg]	0.01	dT <sub>1,1</sub> [K/h]	5	T <sub>1</sub> [°C]	dT <sub>2</sub> [K/h]	T <sub>annealing</sub> [°C]	t <sub>annealing</sub> [min]	W <sub>D,L,0</sub> [kg/kg]
ee <sub>0,2</sub> [kg/kg]	0.015	dT <sub>1,2</sub> [K/h]	10	10	10	58.2 (ee <sub>0,1</sub> )	30	0.25314
ee <sub>0,3</sub> [kg/kg]	0.02	dT <sub>1,3</sub> [K/h]	15			58.5 (ee <sub>0,2</sub> )		
		dT <sub>1,4</sub> [K/h]	20		dT <sub>3</sub> [K/h]	58.9 (ee <sub>0,3</sub> )	t <sub>cooling</sub> [min]	
		dT <sub>1,5</sub> [K/h]	25		15		70	

## Appendix B - Parameter estimates

**Table B 1:** Parameters resulting from the fit of Equation 68 to solubility data of the system DL-threonine/water (see Figure 18). The Table is cited in chapter 4.3.

Parameter	Estimated value (Eutectic)	Estimated value (Enantiomer)
$\gamma[-]$	0.1905	-
$\frac{\Delta h}{R \cdot T_m} \left[ \frac{mol}{kg} \right]$	0.16	1.485
$\frac{\Delta h}{R} \left[ \frac{mol \cdot K}{kg} \right]$	1.07E3	1.1624E3
$\phi[-]$	-	189.086

**Table B 2:** Parameters resulting from the fit of Equation 68 to solubility data of the system DL-threonine/water (see Figure 18). The Table is cited in chapter 4.3.

Parameter	Estimated value (Eutectic)	Estimated value (Enantiomer)	Estimated value (racemate)
$\gamma[-]$	3.9165E-6	-	9.963
$\frac{\Delta h}{R \cdot T_m} \left[ \frac{mol}{kg} \right]$	6.5636	7.8239	19.17
$\frac{\Delta h}{R} \left[ \frac{mol \cdot K}{kg} \right]$	6.1036E3	2.9729E3	5.72E3
$\phi[-]$	-	-872.9	-

**Table B 3:** Parameters, confidence intervals, sensitivity measures and measures for quality of fit for the first estimation based on experiment 1 to 3 (Table 2). The corresponding model equations can be found in the chapters 2.1.5 (model), 2.2.4 (kinetics) and 2.3.4 (reparameterization). The Table is cited in chapter 4.6.1.

Parameter	Estimated value	Confidence [%] (95%), Eq. 48	Sensitivity measure [-], Eq. 41
$b$	4 [-]	5	210
$k_{b, sek, pre}$	$1.23 \cdot 10^8$ [#/(m <sup>3</sup> s)]	35	22
$g$	2.1 [-]	1.4	490
$k_{g, pre}$	$1.472 \cdot 10^{-6}$ [m/s]	8	102
$E_{b, sek}$	-94.6 [kJ/mol]	3	37.7
$E_g$	-111.2 [kJ/mol]	0.3	126
Condition	$5.9 \cdot 10^6$ [-]		
Collinearity index $\gamma$	$1.27 \cdot 10^3$ [-]		
Goal function	122 [-]		

**Table B 4:** Omega matrix for the estimation problem using the original kinetics (see Equation 46). The Table is cited in chapter 4.6.1.

	$k_{g,pre}$	$g$	$E_g$	$k_{b,sek,pre}$	$b$	$E_{b,sek}$
$k_{g,pre}$	1.000	-0.999	0.627	0.810	-0.870	0.948
$g$	-0.999	1.000	-0.643	-0.801	0.860	-0.934
$E_g$	0.627	-0.643	1.000	0.824	-0.796	0.495
$k_{b,sek,pre}$	0.810	-0.801	0.824	1.000	-0.993	0.792
$b$	-0.870	0.860	-0.796	-0.993	1.000	-0.857
$E_{b,sek}$	0.948	-0.934	0.495	0.792	-0.857	1.000

**Table B 5:** Omega matrix for the estimation problem using the reparameterized kinetics (see Equation 46). The Table is cited in chapter 4.6.1.

	$G_1$	$G_2$	$E_g$	$B_1$	$B_2$	$E_{b,sek}$
$G_1$	1.000	0.358	-0.241	-0.818	-0.305	0.352
$G_2$	0.358	1.000	0.273	-0.792	-0.984	-0.091
$E_g$	-0.241	0.273	1.000	-0.176	-0.140	-0.980
$B_1$	-0.818	-0.792	-0.176	1.000	0.715	0.004
$B_2$	-0.305	-0.984	-0.140	0.715	1.000	-0.040
$E_{b,sek}$	0.352	-0.091	-0.980	0.004	-0.040	1.000

## List of Figures

Figure 1: Overview of different nucleation mechanisms adapted from (Mersmann, 1995). .....	19
Figure 2: Schematic illustration of the different metastable zone widths (MSZW) for different types of nucleation. ....	21
Figure 3: Different types of enantiomer systems represented by binary phase diagrams. (a): conglomerate, (b): compound forming systems, (c): the three types of solid solution forming systems. ....	23
Figure 4: Schematic 3D-representation of a ternary system of two enantiomers labeled D and L and the solvent S. ....	24
Figure 5: The two types of ternary systems investigated in this thesis: (a), conglomerate, (b) racemic compound. The rectangles designate the thermodynamically stable solid phases in certain parts of the phase diagram. ...	24
Figure 6: Evaluation of the mass fractions of all three components (D,L, solvent) in a ternary phase diagram. ....	25
Figure 7: Schematic illustration of a periodically operated preferential crystallization process in a ternary phase diagram for a conglomerate forming system. ....	32
Figure 8: Schematic illustration of a periodically operated preferential crystallization process in a ternary phase diagram for a compound forming system. ....	33
Figure 9: Process concept of auto seeded polythermal preferential crystallization. The seeds are generated by primary nucleation followed by dissolution of the crystals of the unwanted enantiomer. Ternary phase diagrams are used to illustrate the process concept. ....	35
Figure 10: Schematic temperature profile for the Process concept „nucleation seeding“ .....	36
Figure 11: Illustration of the AS3PC nucleation process concept “Nucleation seeding” in a series of ternary phase diagrams. The seeds of the pure enantiomer are generated through primary nucleation followed by dissolution of the crystals of the racemate. The seeds for the racemate batch are generated by primary nucleation only. ....	39
Figure 12: Schematic illustration of the temperature profile corresponding to the process illustrated in Figure 11. The temperature profile illustrates one complete cycle with an enantiomer and a racemate batch. ....	40
Figure 13: Illustration of the process concept „milled seeds“ in two ternary phase diagrams. ....	41
Figure 14: Schematic illustration of the temperature profile for the Process concept „milled seeds“ .....	41
Figure 15: Schematic illustration of an approach to model parameterization (adapted from (Brun, 2002)) .....	44
Figure 16: Illustration of the procedure to obtain confidence intervals for parameters estimated based on the bootstrap approach. ....	49
Figure 17: Typical DL-threonine crystals harvested from a batch experiment. ....	53
Figure 18: Water rich corner (50%) of the ternary phase diagram of DL-threonine/water with a selection of measured solubility isotherms (Sapoundjiev et al., 2006). ....	54
Figure 19: The two stereoisomers of the amino acid DL-threonine. ....	55
Figure 20: Racemate crystals of mandelic acid harvested from a batch run. The picture was taken after filtering and drying. ....	55

Figure 21: R-enantiomer crystals of mandelic acid harvested from a batch run. The picture was taken after filtering and drying. ....	55
Figure 22: The two stereoisomers of mandelic acid. ....	56
Figure 23: Water rich corner (50%) of the ternary phase diagram of R,S-mandelic acid/water with a selection of solubility isotherms. ....	56
Figure 24: Experimental setup for the 1.5 liter plant. ....	57
Figure 25: Schematic setup of a Polarimeter ....	59
Figure 26: Variance and $x_{50}$ of a sample of particles analyzed by microscopic image analysis over number of measured particles in the sample. ....	61
Figure 27: Comparison of the particle size distribution or chord length distribution respectively (number density) of the sieve fraction 90-150 $\mu\text{m}$ measured with different measurement techniques (FBRM, PVM, Microscope). ....	62
Figure 28: Optical rotation over time for two repeated experimental runs of the process concept “nucleation seeded” performed under the similar conditions. L-threonine is the target enantiomer. ....	63
Figure 29: Particle counts measured by the FBRM probe over time. L-threonine is the target enantiomer of the process concept “nucleation seeded” ....	64
Figure 30: Mass fractions of consecutive cycles of the process concept “nucleation seeded” in which L-threonine and D-threonine are crystallized alternating. ....	64
Figure 31: Optical rotation over time for two experimental runs of the process concept “milled seeds” performed under similar conditions. L-threonine is the target enantiomer. ....	65
Figure 32: Particle counts of the process concept “milled seeds” measured by the FBRM probe over time. L-threonine is the target enantiomer. ....	65
Figure 33: Mass fractions of sequel cycles of the process concept “milled seeds” in which L-threonine and D-threonine are crystallized respectively. ....	66
Figure 34: Temperature profiles for the preparation of seed material. 1. Dissolution; 2. Fast cooling to the saturation temperature; 3. Slow cooling (1K/h) to the final temperature $T_F$ . ....	67
Figure 35: Particle size distribution of five repeated experimental runs for seed preparation. ....	67
Figure 36: Measurements and correlation trend lines for the polarimeter signal (optical rotation) taken at three different vessel temperatures. The polarimeter itself was thermostated at 54 $^{\circ}\text{C}$ for all measurements. ....	70
Figure 37: Calibration of the densitometer at three different vessel temperatures. The measurement temperature of the internal cell was set to 50 $^{\circ}\text{C}$ . ....	70
Figure 38: Particle size distributions obtained from microscopic image analysis of the three sieve fractions used for the “calibration” of the FBRM-probe. ....	71
Figure 39: Scaled zeroth to third moment of the chord length distribution measured by a FBRM-probe compared with the scaled moments measured by an optical microscope and image analysis of the sieve fraction 63-90 $\mu\text{m}$ . ....	72
Figure 40: Scaled zeroth to third moment of the chord length distribution measured by a FBRM-probe compared with the scaled moments measured by a optical microscope and image analysis of the sieve fraction 90-150 $\mu\text{m}$ . ....	72
Figure 41: Scaled zeroth to third moment of the chord length distribution measured by a FBRM-probe compared with the scaled moments measured by a optical microscope and image analysis of the sieve fraction 150-212 $\mu\text{m}$ . ....	73
Figure 42: Solubility of DL-threonine/water in the two phase region. (+) are measured data points. The grid represents the model calculations. ....	75

Figure 43: Eutectic solubility as function of temperature. (+) are the measured data points. The solid line represents the model calculations.....	75
Figure 44: Illustration of the chosen metastable solubility model inside the three phase region of a conglomerate forming system (for example DL-threonine/water)....	76
Figure 45: Measured and calculated solubility for the racemate of mandelic acid in water.....	79
Figure 46: Measured and calculated solubility for the eutectic composition of mandelic acid in water. ....	79
Figure 47: Measured and calculated solubility of mandelic acid in the two-phase region of the phase diagram as a function of solvent composition (fraction of the counter enantiomer with respect to the liquid phase mass) and temperature (Czapla et al., 2008b). ....	79
Figure 48: Illustration of the chosen metastable solubility model inside the three phase region of a compound forming system (for example R,S-mandelic acid). ....	80
Figure 49: Illustration of the course of the two principle process evaluation approaches presented. ....	82
Figure 50: Illustration of the sample process simulated using equations (81) - (89). The points in the Figure correspond to the numbered points in Figure 9 (see also Table A 13, A 14 and A 15 in the Appendix for point values). The axes are labeled according to mass fractions. ....	85
Figure 51: Yield of a DL-threonine preferential crystallization run (see Equation 9) as a function of annealing temperature and subcooling. As predicted by the equilibrium based short-cut method.....	86
Figure 52: Obtainable yield with respect to annealing temperature and cooling rate for preferential crystallization in the DL-threonine/water system.....	88
Figure 53: Obtainable productivity with respect to annealing temperature and cooling rate for preferential crystallization in the DL-threonine/water system.....	89
Figure 54: Illustration of the described process scheme exemplified with the numeric values given in Table 4. The numbers by the points correspond to the process steps introduced in Figure 11 and Figure 12. The points 5 and 1' are omitted to clarify the illustration. The axes labels are given in mass fractions. ....	91
Figure 55: Yield of a preferential crystallization run as a function of annealing temperature and subcooling based on the presented equilibrium approach for the system of R,S-mandelic acid/water.....	93
Figure 56: Yield of a preferential crystallization run as a function of annealing temperature and cooling rate based on the approach using the metastable zone width for a preferential crystallization in the system R,S-mandelic acid/water. ....	94
Figure 57: Productivity of the enantiomer batch of the cyclic process scheme as a function of starting temperature and cooling rate (MSZW approach) for a preferential crystallization in the system R,S-mandelic acid/water.....	95
Figure 58: Total productivity of one complete cycle of the cyclic process scheme as a function of starting temperature and cooling rate (MSZW approach) assuming the product of the racemate batch as purge for a preferential crystallization in the system R,S-mandelic acid/water.....	95
Figure 59: Comparison of a model solution with the commercial program Parsival <sup>®</sup> and a finite discretization scheme using n=1000 points on a linear grid from 0-2mm for the mass fractions of the two enantiomers (Matlab <sup>®</sup> ). ....	98
Figure 60: Comparison of the final particle size distribution of L-threonine crystals calculated with the commercial program Parsival <sup>®</sup> and a finite discretization scheme using n=1000 points on a linear grid from 0-2mm (Matlab <sup>®</sup> ). ....	98

Figure 61: Comparison of a model solution with the commercial program Parsival <sup>®</sup> and a method of characteristics solution (MOC, linear grid using $n=100$ grid points from 0-2mm, Matlab <sup>®</sup> .) for the final particle size distribution of L-threonine crystals. ....	99
Figure 62: Comparison of a model solution for the mass fractions of L- and D-threonine using Parsival <sup>®</sup> and the method of characteristics (MOC, linear grid using $n=100$ grid points from 0-2mm, Matlab <sup>®</sup> ).	99
Figure 63: Comparison of a model solution with the method of moments and a finite discretization scheme using $n=500$ points on a linear grid from 0-2mm for the optical rotation. ....	101
Figure 64: Comparison of a model solution with the method of moments and a finite discretization scheme using $n=500$ points on a linear grid from 0-2mm for the mass fractions of both enantiomers. ....	101
Figure 65: Comparison of a model solution with the method of moments and a finite discretization scheme using $n=500$ points on a linear grid from 0-2mm for the total zero moments (L- plus D-threonine). ....	102
Figure 66: Model calculations and experimental data for the optical rotation over time (Experiments 1 to 3, Table 2). ....	108
Figure 67: Model calculations and experimental data for the scaled second moments over time (Experiments 1 to 3, Table 2). Experimental moments are obtained from FBRM-data. ....	108
Figure 68: Model calculations and experimental data for the mass fractions of L-threonine over time (Experiments 1 to 3, Table 2). ....	109
Figure 69: Model calculations and experimental data for the mass fractions of D-threonine over time (Experiments 1 to 3, Table 2). ....	109
Figure 70: Measured and calculated optical rotation trajectories for experiments (5-7, Table 2). ....	110
Figure 71: Measured and calculated second moment trajectories (experiments 5-7, Table 2). ....	110
Figure 72: Measured and calculated trajectories for the D-threonine mass fractions (experiments 5-7, Table 2). ....	110
Figure 73: Measured and calculated trajectories for the L-threonine mass fractions (experiments 5-7, Table 2). ....	110
Figure 74: Illustration of the chosen method for parameter estimation. ....	113
Figure 75: Illustration of the necessary input data for the probe model in order to transform a measured PSD into a CLD. ....	114
Figure 76: Cumulative absolute velocity distribution of particles of 500 $\mu\text{m}$ length in a stirred vessel (calculation with FLUENT, based on 10 randomly inserted particles, 3.5 seconds calculation time, 3 blade propeller stirrer at 500 rpm). ..	115
Figure 77: Cumulative absolute velocity distribution of particles of 1000 $\mu\text{m}$ length in a stirred vessel (calculation with FLUENT, based on 10 randomly inserted particles, 3.5 seconds calculation time, 3 blade propeller stirrer at 500 rpm). ..	115
Figure 78: Measured and calculated scaled CLDs using the model from (Kail et al., 2008b) after the first addition of crystalline material. ....	117
Figure 79: Measured and calculated scaled CLDs using the model from (Kail et al., 2008b) after the second addition of crystalline material. ....	117
Figure 80: Measured and calculated scaled CLDs using the model from (Kail et al., 2008b) after the third addition of crystalline material. ....	117

Figure 81: Illustration of implemented alternative geometry that is used to simulate chord splitting. The small particles on the edges are the substitute for the original particle.....	117
Figure 82: Measured and calculated scaled CLDs using the model from (Kail et al., 2008b) after the first addition of crystalline material. It was assumed that the particles are measured twice in order to simulate chord-splitting. ....	118
Figure 83: Measured and calculated scaled CLDs using the model from (Kail et al., 2008b) after the first addition of crystalline material. It was assumed that the particles are measured twice with an opaque center in order to simulate chord-splitting. ....	118
Figure 84: Measured and calculated scaled CLDs using the model from (Kail et al., 2008b) after the first addition of crystalline material. It was assumed that the particles are measured twice with an opaque center in order to simulate chord-splitting. ....	118
Figure 85: PSDs for the three sieve fractions used for probe calibration. The distributions were scaled to a mass of 15g.....	118
Figure 86: Measured CLD trajectories for the seeded experiment 1 from Table 2. ...	119
Figure 87: Calculated best fit CLD trajectories for the seeded experiment 1 from Table 2. ....	120
Figure 88: Calculated best fit PSD trajectories for experiment 1 from Table 2. ....	120
Figure 89: Comparison of calculated and measured chord length distributions at the end of the first experimental run. ....	121
Figure 90: Comparison between calculated and measured optical rotation for experimental run 1. ....	121
Figure 91: Calculated and measured chord length distribution for three seeded experiments (experiment 1 to 3 from Table 2) at the end of the experimental run. ....	121
Figure 92: Comparison between calculated and measured optical rotation (experiment 1 to 3 from Table 2). ....	121
Figure 93: Comparison of calculated and measured zero moments of the chord length distributions for three seeded experiments (experiment 1 to 3 from Table 2)...	122
Figure 94: Comparison between calculated and measured zero moments of the particle size distribution. ....	122
Figure 95: Model and measured number of seed crystals. Parameters: $k_1=1.1973e5$ #/m; .....	125
Figure 96: Measured and simulated mass fractions and temperature trajectories for an experiment using seeds (“Defined seeding”). The experimental data is taken from experiment 2 in Table 2. ....	125
Figure 97: Measured and simulated particle size distributions for an experiment using seeds (“Defined seeding”). Measurements are taken from experiment 2 in Table 2.....	125
Figure 98: Measured and simulated mass fractions and temperature trajectories for an auto seeded run (“Milled seeding”). The experimental data is taken from experiment 10 in Table 2. ....	126
Figure 99: Measured and simulated particle size distributions for the product of an auto seeded run (“Milled seeding”). Measurements are taken from experiment 10 in Table 2. The particle size distribution of the seeds refers to the crystals that remain after partly dissolution of the racemic feed (see chapter 2.2.2). ....	126

Figure 100: Measured and simulated mass fractions and temperature trajectories for an auto seeded run (“Nucleation seeding”). The experimental data is taken from experiment 6 in Table 2. ....	126
Figure 101: Measured and simulated particle size distributions for the product of an auto seeded run (“Nucleation seeding”). Measurements are taken from experiment 6 in Table 2. ....	126
Figure 102: Collinearity index of the <i>FIM</i> for the designed (calculated) and the actual experiment. ....	128
Figure 103: Condition of the <i>FIM</i> for the designed (calculated) and the actual experiment. ....	129
Figure 104: Calculated and measured scaled trajectories of the second moment of the particle size distribution compared with the scaled counts of the FBRM-probe (experiments 1 to 3 plus the designed experiment). ....	130
Figure 105: Calculated and measured trajectories of the optical rotation (experiments 1 to 3 plus the designed experiment). ....	131
Figure 106: Calculated and measured trajectories of the D-threonine mass fractions (experiments 1 to 3 plus the designed experiment). ....	132
Figure 107: Calculated and measured trajectories of the L-threonine mass fractions (experiments 1 to 3 plus the designed experiment). ....	132
Figure 108: Simulated and measured mass fractions. The simulation runs were carried out using three different kinetics sets obtained from the three investigated parameter estimation approaches (Table 16, Matlab <sup>®</sup> , optical rotation and CLD; Table 17, Parsival <sup>®</sup> , mass fractions and PSD; Table 19, Matlab <sup>®</sup> , optical rotation and moments).....	133
Figure 109: Simulated and measured scaled zero moments. The simulation runs were carried out using three different kinetics sets obtained from the three investigated parameter estimation approaches (Table 16, Matlab <sup>®</sup> , optical rotation and CLD; Table 17, Parsival <sup>®</sup> , mass fractions and PSD; Table 19, Matlab <sup>®</sup> , optical rotation and moments).....	133
Figure 110: Simulated and measured optical rotation trajectories. The simulation runs were carried out using three different kinetics sets obtained from the three investigated parameter estimation approaches (Table 16, Matlab <sup>®</sup> , optical rotation and CLD; Table 17, Parsival <sup>®</sup> , mass fractions and PSD; Table 19, Matlab <sup>®</sup> , optical rotation and moments).....	134
Figure 111: Variance of the kinetic parameter $kg_1$ over number of bootstrap runs. ...	135
Figure 112: Distribution histogram of the kinetic parameter $E_g$ .....	137
Figure 113: Distribution histogram of the kinetic.....	137
Figure 114: Distribution histogram of the kinetic parameter $g$ .....	137
Figure 115: Distribution histogram of the kinetic.....	137
Figure 116: Distribution histogram of the kinetic parameter $kb_2$ . ....	138
Figure 117: Distribution histogram of the kinetic parameter $kb$ .....	138
Figure 118: Distribution histogram of the kinetic parameter $E_b$ .....	138
Figure 119: Distribution histogram of the kinetic.....	138
Figure 120: Distribution histogram of the kinetic parameter $kg_2$ . ....	138
Figure 121: Distribution histogram of the kinetic .....	138
Figure 122: Illustration of different routes to product design for a preferential crystallization process. ....	140
Figure 123: Influence of the cooling rate of the nucleation step and the initial enantiomeric enrichment onto the mean particle size ( $L_{50}$ ) of the seed crystals at the end of the annealing phase. ....	141

Figure 124: Influence of the cooling rate of the nucleation step and the initial enantiomeric enrichment onto the variance of the particle size distribution of the seed crystals at the end of the annealing phase.....	141
Figure 125: Influence of the cooling rate of the nucleation step and the initial enantiomeric enrichment onto the mean diameter of the particle size distribution of the product crystals at the end of the cooling crystallization using a fixed cooling rate and time for the cooling crystallization step.....	142
Figure 126: Influence of the cooling rate of the nucleation step and the initial enantiomeric enrichment onto the variance of the particle size distribution of the product crystals at the end of the cooling crystallization using a fixed cooling rate and time for the cooling crystallization step.....	143
Figure 127: Comparison of the measured and calculated values for the optical rotation and temperature trajectories of a batch of the optimized cycle. The investigated process concept is “defined seeding”.....	146
Figure 128: Comparison of the measured and calculated values for the optical rotation and temperature trajectories of a batch of the optimized cycle. The investigated process concept is “nucleation seeding”.....	147
Figure 129: Comparison of the measured and calculated values for the optical rotation and temperature trajectories of a batch of the optimized cycle. The investigated process concept is “milled seeding”.....	147

## List of Tables

Table 1: Experimental parameters for the seed preparation. ....	67
Table 2: Experimental conditions of the experimental data set used for the parameter estimation procedure. The temperatures and cooling rates correspond with the time points given in Figure 10 and Figure 14. ....	68
Table 3: Masses of ethanol and crystals used in the three experiments. ....	72
Table 4: Masses of the two species that are used to illustrate the process short-cut evaluation approach for the two process runs. ....	82
Table 5: Conditions for the designed process. ....	88
Table 6: Experimental conditions of a sample experiment. ....	89
Table 7: Comparison of calculated yield and productivity with experimentally obtained values. ....	89
Table 8: Experimental conditions for the enantiomer and racemate batch used for validation purposes. ....	96
Table 9: Calculated and experimentally obtained values for yield and productivity. .	96
Table 10: Scaling factors for the moment equations. ....	100
Table 11: Values of the kinetic constants used for the model calculations presented in Figures 63 to 65. ....	101
Table 12: Comparison of the reduced model and the full model in terms of calculation times. ....	102
Table 13: Overview over the different parameterization approaches followed in the thesis. The different model solution strategies are introduced and compared in chapter 4.5. ....	104
Table 14: Parameters, confidence intervals, sensitivity measures and measures for quality of fit for the second estimation using reparameterized kinetics based on experiment 1-3 (“defined seeding”, DL-threonine/water, Table 2). The corresponding model equations can be found in the chapters 2.1.5 (model), 2.2.4 (kinetics) and 2.3.4 (reparameterization). The original parameters with confidence intervals obtained from resubstitution are also given. ....	107
Table 15: Parameters, confidence intervals, sensitivity measures and measures for quality of fit for the estimation using reparameterized kinetics based on experiment 5-7 (DL-threonine/water, Table 2) run in the “nucleation seeding” process mode. The corresponding model equations can be found in the chapters 2.1.5 (model), 2.2.4 (kinetics) and 2.3.4 (reparameterization). The original parameters with confidence intervals obtained from resubstitution are also given. ....	111
Table 16: Resulting kinetic parameters after fitting the model simultaneously to the data provided by experiment 1-3 (DL-threonine/water, Table 2). The corresponding model equations can be found in the chapters 2.1.5 (model), 2.2.4 (kinetics). ....	122
Table 17: Optimal values for the estimated kinetic parameters for the three investigated process concepts based on experiments 1-3 (“Defined seeding”), 5-8 (“nucleation seeding”) and 9 (“milled seeding”) for the system DL-threonine/water. The corresponding model equations can be found in the chapters 2.1.5 (model), 2.2.4 (kinetics). ....	127
Table 18: Parameters for the designed experiments 3, 4 and 5. Only experiments 3 and 4 were actually performed. ....	129

Table 19: Parameters, confidence intervals, sensitivity measures and measures for quality of fit for the estimation using reparameterized kinetics based on experiment 1 to 3 and the designed experiment 4 (Table 2). The original parameters with confidence intervals obtained from resubstitution are also given. ....	130
Table 20: Experimental conditions of the experimental data set used for comparison of the different parameter estimation approaches investigated in the thesis. ....	134
Table 21: Confidence intervals obtained from bootstrap simulation runs (2000 fittings) of original free parameters, reparameterized kinetics and of the back transformed parameters.....	136
Table 22: Manipulated parameters for the optimization of the different process concepts along with the resulting optimal values for the productivity. ....	145
Table 23: Experimental conditions for the optimal runs of the individual process concepts.....	145
Table A 1: Chemicals used to setup the experiments for crystallization in the DL-threonine/water system. ....	162
Table A 2: Chemicals used to setup the experiments for crystallization in the R,S-mandelic acid/water system. ....	162
Table A 3: Solubility data for the system DL-threonine/water in a temperature range from 10-65°C measured at different compositions.....	163
Table A 4: Solubility data for the system R,S-mandelic acid/water in a temperature range from 5-40°C measured at different compositions (pure enantiomer, eutectic composition and racemate). ....	164
Table A 5: HPLC-method used for threonine.....	164
Table A 6: Settings for the image analysis algorithm of the PVM-software (Mettler-Toledo).....	165
Table A 7: Moments for experiment 1 (sieve fraction 63-90µm).....	165
Table A 8: Moments for Experiment 2 (Sieve fraction 90-150µm). ....	165
Table A 9: Moments for experiment 3 (Sieve fraction 150-212 µm).....	166
Table A 10: Moment analysis according to Equation 67 for the sieve fractions 63-90µm compared with sieve fraction 90-150µm. ....	166
Table A 11: Moment analysis according to Equation 67 for the sieve fractions 63-90µm compared with sieve fraction 150-212µm. ....	166
Table A 12: Moment analysis according to Equation 67 for the sieve fractions 90-150µm compared with sieve fraction 150-212µm.....	167
Table A 13: Data corresponding to the calculated process run depicted in Figure 50. ....	167
Table A 14: Liquid phase composition corresponding to the calculated process run depicted in Figure 50. ....	167
Table A 15: Solid phase composition corresponding to the calculated process run depicted in Figure 50. ....	167
Table A 16: Model parameters for the FBRM-model used to transform the calculated particle size distribution into a chord-length distribution. ....	168
Table A 17: Fixed and varied parameters for the variation calculations performed with Parsival®.....	168

Table B 1: Parameters resulting from the fit of Equation 68 to solubility data of the system DL-threonine/water (see Figure 18). The Table is cited in chapter 4.3.	169
Table B 2: Parameters resulting from the fit of Equation 68 to solubility data of the system DL-threonine/water (see Figure 18). The Table is cited in chapter 4.3.	169
Table B 3: Parameters, confidence intervals, sensitivity measures and measures for quality of fit for the first estimation based on experiment 1 to 3 (Table 2). The corresponding model equations can be found in the chapters 2.1.5 (model), 2.2.4 (kinetics) and 2.3.4 (reparameterization). The Table is cited in chapter 4.6.1.	169
Table B 4: Omega matrix for the estimation problem using the original kinetics (see Equation 46). The Table is cited in chapter 4.6.1.	170
Table B 5: Omega matrix for the estimation problem using the reparameterized kinetics (see Equation 46). The Table is cited in chapter 4.6.1.	170

# Lebenslauf

Name: Felix Czapla  
Geburtsdaten: 18.03.1979 in Rinteln

## Schulbildung

1985 – 1989 Grundschole in Rehren  
1989 – 1991 Orientierungsstufe in Obernkirchen  
1991 – 1998 Gymnasium in Rinteln

## Wehrdienst

07/1998 – 05/1999 Nienburg an der Weser

## Studium

10/1999 – 03/2005 Studium im Fach Maschinenbau (Diplom) an der TU Braunschweig. Vertiefungsrichtung: „Energie- und Verfahrenstechnik“  
Diplomarbeit: „Charakterisierung des Stoffübergangs in einer gepackten Blasensäule“

## Berufspraxis

04/2005 – 08/2009 Wissenschaftlicher Mitarbeiter am „Max-Planck-Institut für Dynamik komplexer technischer Systeme“ in Magdeburg.

Seit 09/2009 Wissenschaftlicher Mitarbeiter bei der Nordzucker AG in Braunschweig im Bereich „Produktentwicklung und technischer Service“